Università degli Studi di Firenze

Dipartimento di Fisica
Dottorato di Ricerca in Fisica, **XX** Ciclo
Settore Disciplinare: Fisica Nucleare e Subnucleare (FIS04)

PhD Thesis

Precise measurement of particle energy with the PAMELA space experiment

Elena Taddei

Advisor:
Dr.
Elena Vannuccini

PhD Coordinator:
Prof.
Alessandro Cuccoli

Firenze, 31 12 2007

Introduction

The Earth is continuously hit by particles coming from space with different energies and nature. The study of these particles is related to many fields of the physics research, from cosmology to astrophysics and particle physics. The observed cosmic ray spectra extend up to energies of about $10^{21}\ eV$, decreasing their flux with increasing energy, and can be related to a wide variety of sources.

Although many studies on cosmic rays have been carried out, since from the beginning of the previous century, still some aspects remain to be clarified. For example one of the most interesting items is the presence of antiparticles in cosmic rays, in fact the apparent asymmetry of matter and antimatter in the visible universe is one of the greatest unsolved problems in physics. Antiprotons and positrons have been detected in cosmic rays among the much more consistent background of protons and electrons. These antiparticles can be produced as secondaries in interactions of cosmic ray nuclei with interstellar matter but the observed flux does not agree perfectly with the theoretical expectations based on secondary production. This fact triggered the development of many theories for possible exotic sources of antimatter in the universe, but no conclusion can be addressed on this question because the available measurements are still quite poor. For this purpose some experiments have been designed in order to optimize the antiparticle measurements.

The detection of cosmic rays is complicated by the presence of the atmosphere around the Earth, due to the interaction of cosmic rays with the nuclei of atmospheric gases that makes impossible their direct detection at ground level. For this reason the physicists had to develop experiments at high altitude, first of all with balloon flights. This technique has been

successfully employed in the past but it had some limitations due to the short duration of this kind of missions and the presence of a residual atmospheric burden which increases the uncertainties of the measurements. In order to overcome these problems the PAMELA experiment has been designed to operate out of the atmosphere for a three-year long mission. It has been launched on 15 June 2006 on board of the Resurs-DK1 Russian satellite, which is orbiting at an altitude between 350 and 610 Km, with inclination of 70°. PAMELA is an experiment that takes advantage of many subdetectors. The most important are a permanent magnet spectrometer, providing a rigidity measurement, and a sampling calorimeter, which is a powerful particle identifier. Thanks to its long exposure time and to the advanced experimental techniques employed, PAMELA will measure with unprecedented statistics and sensitivity the abundance and energy spectra of cosmic electrons, positrons, antiprotons and light nuclei over a very large energy range.

The spectrometer and calorimeter calibrations are fundamental items that have to be completed in order to obtain final scientific results. In fact, in order to achieve the main objectives of the experiment, an unbiased measurement of the momentum of charged particles is needed and it is provided by the spectrometer only if a proper treatment of the mechanical misalignments of the detectors is performed. An alignment procedure has already been developed and applied during the previous years to the system on ground. Since the position of the detectors might have changed after the launch a further step of the alignment procedure has to be performed in flight. For this task a measurement of the particle rigidity independent of the spectrometer is needed. One of the most important feature of the PAMELA apparatus is the redundancy, which allows for example to obtain the energy of electrons and positrons also by means of calorimeter information.

The main aim of this work has been to develop a method to determine the energy of electrons and positrons by using the calorimeter measurements. This information can be used to perform a cross calibration between spectrometer and calorimeter, with the final objective to evaluate the alignment parameters necessary for the tracking system analysis.

The first chapter contains an introduction to the general aspects of

cosmic-ray physics, with some details about the antiparticle issue. In the second chapter the PAMELA mission, its objectives, and the sub-systems that compose the apparatus are described, with main focus on the magnetic spectrometer and the calorimeter, which are the detector mainly involved in this work. Some details on the data reduction and calibration procedures, which have been developed for the analysis of the data, are illustrated in chapter 3. Chapter 4 is fully dedicated to the method developed to reconstruct the energy of electrons and positrons by means of calorimeter information. This method has been used to perform the alignment of the spectrometer in flight, which is the argument treated in chapter 5.

Contents

Chapter 1

Cosmic rays

In the first half of the 20^{th} century cosmic rays played a fundamental role in particle physics, since they were the most powerful sources of particles with an energy high enough to create new particles or to study the structure of the nucleus. However, with the advent of more and more powerful accelerator machines, subnuclear physics increasingly employed artificial beams in substitution of the cosmic radiation, and the interest of cosmic-ray physicists turned towards understanding the processes involved in the origin and the propagation of these particles rather than on using them as a source for experiments, thus giving contributions to the fields of astrophysics and cosmology too. Nowadays the astrophysics community is particularly interested in studying the antimatter component in cosmic rays in order to understand the nature of dark matter and the apparent unbalance between matter and antimatter.
This chapter provides a brief review of the features of cosmic-ray spectrum and composition, together with the main theories on their origin and propagation, with particular focus on antiparticles. Then the current experimental situation is presented with the description of the open issues to be investigated especially regarding positrons.

1.1 Introduction to cosmic rays

Till 1912 it was believed that the radiation measured in air at sea level was emitted by the surface of the Earth. This view changed when the physicist Victor Hess [1] through experiments on balloon with an electroscope, showed that the intensity of ionising radiation was decreasing up to 1500 m from ground, but increasing continuously after that. It was only in 1926 that Millikan used for the first time the expression "cosmic rays" to indicate the extraterrestrial ionizing radiation. Now the term is usually applied to all the charged particles and nuclei entering the Earth atmosphere from space, and often it is extended to include other components such as high-energy photons or neutrinos.
The observation of single cosmic-ray tracks became possible in 1930, when cloud chambers were invented. In this way many particles have been discovered, starting from the positron in 1932 and the muon in 1937. The discoveries of subatomic particles as a result of cosmic-ray research gave birth to the science of elementary-particle physics and, until the advent of the accelerators, particle physicist used only cosmic rays for their research. Later accelerator based particle physics provided more accurate measurements, but currently only energies, in the center of mass system of reference, up to $E_{CM} \sim 10^{13}\ eV$, which correspond to a cosmic ray of energy $E_{CR} \sim 5 \cdot 10^{16}\ eV$, can be reached. Thus the study of particles at higher energies can be performed only through cosmic rays, since the energy of cosmic particles cover a wide range from $\sim 10^{6}\ eV$ to $\sim 10^{20}\ eV$.
Since the discover of cosmic radiation, the research was performed through balloon experiments. At the altitudes reached by these devices, $\sim 40\ km$, there is still an overburden of $\sim 5\ g/cm^2$ from the residual atmosphere, where particle interactions can occur. The next step in cosmic-ray physics has therefore been to use satellite-borne experiments.

Cosmic rays are conventionally divided into two groups, called primaries and secondaries, according to their origin: primary cosmic rays are created and accelerated by some astrophysical sources and then they propagate through space and reach the Earth, while secondaries are par-

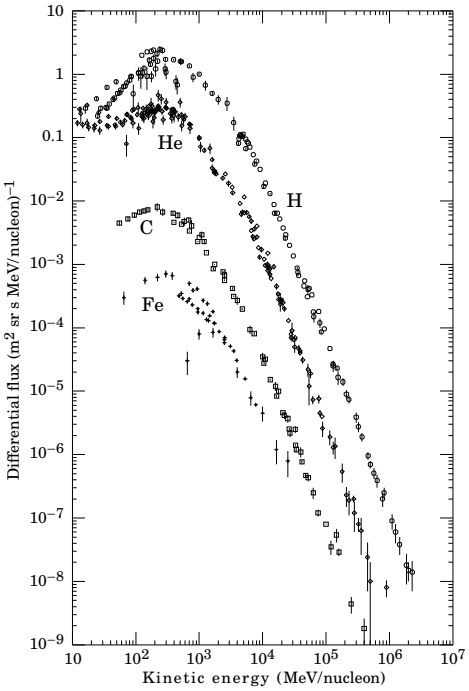

Figure 1.1: Differential flux of the most abundant nuclear components of cosmic rays at the top of the atmosphere (from Ref. [2]).

ticles and nuclei generated by the interaction of the primaries with the interstellar medium along their path.

The chemical composition of cosmic rays depends on the energy range considered. In the energy range below 1 TeV, where direct measurements exist, cosmic rays are composed of about 85% protons and 15% helium nuclei, with less than 1% of electrons and small abundances of heavier nuclei and antiparticles.

The *differential flux* $\Phi(E)$ is defined as the number of cosmic rays per unit area, time, solid angle and energy. This quantity is shown in figure 1.1 as measured at the top of the atmosphere for the most abundant nuclei in cosmic rays and for energies up to some units in 10^6 $MeV/nucleon$. Figure 1.2 shows the so-called "all-particle" spectrum (i.e. the spectra of the different components all added together) up to the highest measured

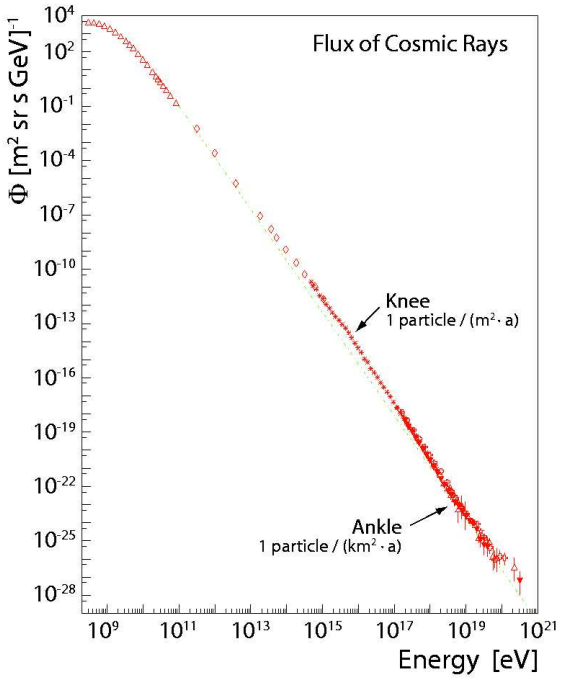

Figure 1.2: Differential all-particle flux of the highest-energy cosmic rays.

energies. The cosmic-ray spectrum is today known with good precision up to $\sim 10^{19}\ eV$. The differential energy spectrum can be represented by a broken power law function:

$$\frac{dN}{dE} \propto E^{-\alpha} \tag{1.1}$$

where E here represents the energy-per-nucleon and α is the differential spectral index, which varies depending on the energy region. At low energy the spectrum is dominated by solar modulation, which explains the presence of a maximum around some hundreds $MeV/nucleon$. In the region between about $10^9\ eV$ and $10^{15}\ eV$ the measured spectral index is about 2.7, then the spectrum steepens for higher energies (spectral index 3) until $5 \cdot 10^{18}\ eV$, and above the spectrum flattens (spectral index 2.8). These two features of the cosmic-radiation spectrum are called the

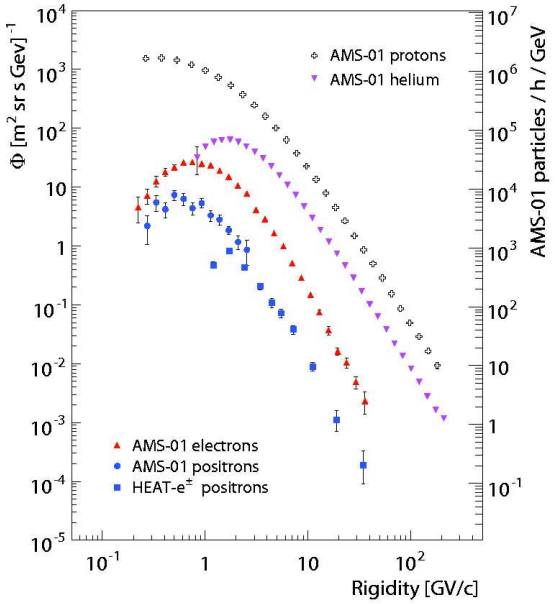

Figure 1.3: Fluxes of some of the most abundant cosmic-ray components as measured by $AMS-01$ and $Heat-e^{\pm}$.

"knee" and the "ankle", respectively, and the reason of their existence is not well understood yet. Probably the changes in the power law is related to different mechanisms of particle acceleration and propagation. Figure 1.3 shows the spectra of protons and helium nuclei together with that of electrons and positrons with energies up to approximately $100\,GeV$. It is apparent that in this energy range protons are by far the most abundant cosmic-ray component. In particular, their flux exceeds that of positrons by a factor of $10^3 \div 10^4$. Moreover, the energy spectra of the leptons ($\alpha \sim 3.4$) are slightly steeper than those of nuclei.

Standard theories on the origin of cosmic rays state that most of the non-solar component is produced by the shock waves existing in the regions around supernovae explosions inside our galaxy. The spectrum and composition of cosmic rays for energies up to the "knee" is compatible with a production of the nuclei in supernovae explosions and with a successive acceleration via the "Fermi mechanism". This mechanism

of acceleration was proposed in 1949 by E.Fermi [3], it is based on the assumption that particles in collisions with macroscopic moving objects, such as magnetic fields in shock waves of supernovae, could undergo repeated finite energy gains. It states that at each interaction a particle gains a fraction of its initial energy and has a certain probability to escape the acceleration region, which is related to the particle velocity. In fact when the speed is too high for the magnetic field to constrain the particles in the acceleration region, they would eventually escape into the galaxy. With the above simple assumption this model naturally predicts the observed spectral shape. Moreover the source would be characterized by a maximum reachable energy, which depends on its size and on the intensity of its magnetic field. According to theory, the maximum energy which the Fermi mechanism can give to a nucleus increases with its charge. As a consequence, cosmic-ray composition becomes heavier around and above the knee, since heavier elements may be accelerated to higher energies. According to this scenario the lower-energy change in the spectral index at the "knee" could reflect the fact that some of the galactic accelerators of cosmic rays have reached the upper limit beyond which the process no longer provides particles in an efficient way.
However the Fermi acceleration model associated to galactic objects, cannot explain particles with energy greater than $10^{18}\ eV$. The origin of the highest portion of the spectrum remains unclear but several possible explanations have been proposed, suggesting that the cosmic rays above the ankle could have origin from extragalactic sources or that they could be the decay products of exotic massive particles such as those predicted by extensions of the Standard Model of particle physics. The types of objects in the Universe that are able to accelerate particles at these high energies are limited in number. In particular, there are only 4 classes of sites able to accelerate particles above $10^{20}\ eV$: high magnetic field neutron stars, Active Galactic Nuclei (AGN), lobes of giant radio galaxies and Gamma-ray bursts. All these sites are characterised either by strong magnetic fields or by large physical dimensions. Recent measurements [4] found a correlation with nearby AGN, favouring these kind of object as sources of cosmic rays with $E > 10^{19}\ eV$.

Due to the wide extension of the cosmic-ray spectrum, and to the

large variation in the number of particles, different kinds of experimental techniques have been used to perform measurements in the different energy regions. Direct measurements of cosmic rays can be done by means of detectors on board of aerostatic balloons or satellites, the highest energy attainable with such techniques is about $10^{15}\ eV$. At higher energy the flux is too low, hence the experimental techniques exploit the showers of particles produced by the interaction of primary cosmic rays with the atmosphere: ground-based large-array detectors and fluorescence detectors are used to investigate the higher energy region.

1.1.1 Propagation

Apart from the solar component, the observed cosmic-ray particles are produced somewhere in the galactic volume and, regarding the extreme energy component maybe also in extragalactic sources. Consequently, on their way to Earth, cosmic rays are involved in many kinds of processes, including scattering off the interstellar medium and interaction with magnetic fields. The result of all these processes is that cosmic rays are isotropized, therefore do not map their origin. Moreover the detected spectrum is modified with respect to the one at the sources. A careful study of the propagation models in the galaxy is needed in order to compare the observed data with those expected according to some theoretical production rate.
Charged particles move under the influence of the galactic magnetic field, at the energies we are interested in the magnetic gyro-radii [1] are quite small, however, the magnetic field is tangled so that particles can jump to nearby field lines and can drastically alter their courses. The process of propagation of charged particles in the galaxy can be modeled as a random walk, which can be described by the following diffusion equation:

$$\frac{\partial N}{\partial t} = \nabla \cdot (D\nabla N - \vec{u}N) - \frac{N}{\tau_{esc}} - \frac{\partial}{\partial E}(b(E)N) + Q \qquad (1.2)$$

[1] The gyro-radius, or radius of gyration, defines the radius of the circular motion of a charged particle in the presence of a uniform magnetic field. It is calculated as $r_g = \frac{mv_\perp}{|q|B}$, where m is the mass of the particle of charge q, $v_\perp$ is the velocity component perpendicular to the direction of the constant magnetic field B.

where $N \equiv N(\vec{r}, t, E)$ is the cosmic-ray number density with energy E at a point $\vec{r}$ and time t and $Q \equiv Q(\vec{r}, t, E)$ is their source number density. The first term on the right hand side contains the diffusion coefficient D and the velocity $\vec{u}$ of convective particle transport in the galaxy. The second term represents the losses of particles by collision and decay with a mean escape time τ_{esc}. The third term describes the energy variation through the energy loss rate $b(E) \equiv dE/dt$. This term depends strictly on the nature of the propagating particle. In fact, while for hadrons the energy loss is mainly due to ionization, electrons and positrons, because of their smaller mass, suffer large radiative losses through Bremsstrahlung emission, inverse-Compton scattering with the ambient photons and synchrotron radiation in the magnetic field. Their relative importance depends on the electron energy expressed through $\gamma = E/m_e c^2$ for relativistic particles, in details

$$b(E) = A_1(3 \ln \gamma) + A_2\gamma + A_3\gamma^2. \tag{1.3}$$

The first term on the right describes ionization losses which have a logarithmic dependence on the energy; the second term accounts for Bremsstrahlung losses and the last for inverse Compton and synchrotron losses. The last processes dominate over ionization and Bremsstrahlung energy losses for electron energy greater than 1 GeV. Since cosmic microwave radiation permeates all the space the process of inverse Compton scattering with this radiation limits the distance that $e^{\pm}$ can travel, with the result that the electrons detected in cosmic radiation have surely a galactic origin. The energy lost by cosmic-ray electrons and positrons is proportional to the square of their energy; therefore, they cannot diffuse for large distances. Their average range is [5] $r \sim 1\ kpc/E(TeV)$. Moreover, the sources of high-energy electrons and positrons must be relatively recent in order not to have important radiative losses, $t_{rad} \sim 2.1 \cdot 10^5\ yr/E(TeV)$. On the contrary the mean free path for hadrons in interstellar space is larger than the typical galactic distances.
Many authors emphasized that the cosmic-ray electron spectrum cannot be considered to be representative of a Galactic average, but it must reflect the recent history of the solar system neighborhood, especially in the highest energy range. Consequently, although the electron compo-

nent constitutes less than 1% of the cosmic rays, it plays an important role in understanding the propagation of cosmic rays in the Galaxy.
The most frequently used models are briefly reviewed in the following:

Leaky box model This is the simplest model of propagation in the galaxy, based on the assumption that the sources of cosmic rays are uniformly distributed in the galactic disk, which is surrounded by the halo, and that they diffuse freely in a confinement volume: at each encounter with its boundary they can be reflected and the probability per unit of time of escaping into intergalactic space is constant.

Diffusion model In this model cosmic-ray sources and matters are located in the galactic disk, then they diffuse through the disk and the halo and escape freely from the boundary. This model is more realistic than the leaky box model to describe cosmic-ray propagation in the Galaxy because the spatial properties, such as structure of the Galaxy, the spatial distributions of the sources, the interstellar radiation and the magnetic fields are taken into account.

1.2 Modulation

In the vicinity of the earth the radiation environment consists of galactic cosmic rays, solar particles and trapped particles, which vary in time and with the geographical position modulated by two processes: the sun solar wind and the Earth magnetic field. The effect of this modulation, which is visible as a maximum in the spectra in figure 1.2, is due to an attenuation of the flux of low-energy galactic cosmic rays reaching the Earth.

The solar wind is a continuous flow of plasma, mainly low-energy electrons and light ionized nuclei, coming out from the sun corona; it travels with a speed of about 350 km/s extending out beyond Pluto (as far as about 100 AU[2]). This plasma originates the interplanetary magnetic field

[2]Astronomical Unit, is approximately the mean distance between the Earth and the Sun: 149598000 kilometers

because it carries the solar magnetic field out into the solar system. The solar activity which causes the solar wind varies with time with a period of 22 years, that is the field varies from a maximum level to a minimum and then returning to a maximum in 11 years, then there is a reversion of the magnetic field.
When the interstellar cosmic rays enter the solar system they interact with the solar wind and the magnetic field deflects the low-energy part of the incoming cosmic radiation. The overall effect is a variation of the flux, which is known as solar modulation, strongly correlated to the activity of the Sun: the higher is the production of solar particles, the lower is the number of galactic cosmic rays capable of reaching the Earth. The level of modulation varies in anticorrelation with solar activity. The PAMELA experiment takes place during a solar minimum.
The effect of solar modulation depends on the energy of the particles, it decelerates the incoming particles and excludes some of them with energies below about 1 GeV, while it becomes negligible above ~ 10 GeV. This solar modulation also exhibits a dependence on the sign of the cosmic-ray particle charge [6]. This feature has not been completely explained and has to be confirmed by more accurate measurements.
Other effects due to the Sun occurs occasionally when bursts of energetic particles are emitted during solar flares or in the course of coronal mass ejections: in such events, particles up to some tens of GeV are sent out into space and they contribute to the cosmic-ray spectrum.

Another contribution to the reduction of the amount of cosmic radiation comes from the Earth influence. In the vicinity of the Earth its magnetic field[3] is well approximated by a dipole field, as shown in figure 1.4. The axis of the field is inclined of about 11° with respect to the Earth rotational axis, and its magnetic north pole is located in the southern hemisphere. The intensity of the field is given approximately by:

$$B(\lambda, r) \simeq \frac{0.31\ Gauss}{(r/r_E)^3}\ \sqrt{1 + 3\ \sin^2 \lambda} \tag{1.4}$$

[3]The terrestrial magnetic field is probably generated by the electric currents connected to the movements of the melted masses inside the planet.

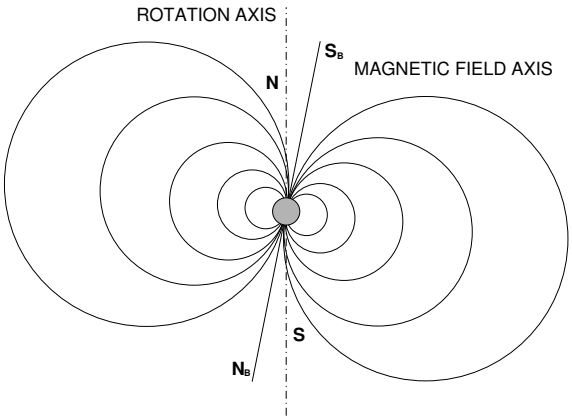

Figure 1.4: Sketch of the magnetic field of the Earth, showing the inclination of the magnetic axis and the location of the magnetic poles N_B and S_B with respect to the geographic ones.

where λ represents the geomagnetic latitude, which depends on both the geographical latitude and longitude, because of the inclination of the axis of the dipole, r_E is the radius of the Earth, and r is the distance between its center and the point of interest. The geometry and the intensity of the terrestrial magnetic field define the so-called geomagnetic cut-off effect which is related to the minimum momentum that an incoming particle needs in order to reach the Earth in spite of the magnetic field deflection. Actually the best quantity to describe the behaviour of charged particles moving inside a magnetic field is not the momentum but the rigidity defined as the ratio between the magnitude of its momentum and its charge, $R = p/q$, because particles with different momentum and charge but identical rigidity are bent in the same direction with the same curvature by the Lorentz force. The vertical geomagnetic cut-off is larger at the equator ($> 10\ GeV$) than in the polar regions ($< 1\ GeV$), its variation with geomagnetic latitude λ can be approximated by the following expression [7]:

$$R_{cut-off} \simeq 14.9 \cdot \cos^4 \lambda\ (GeV/c). \tag{1.5}$$

It is confirmed by the fact that the measured intensity of cosmic radiation

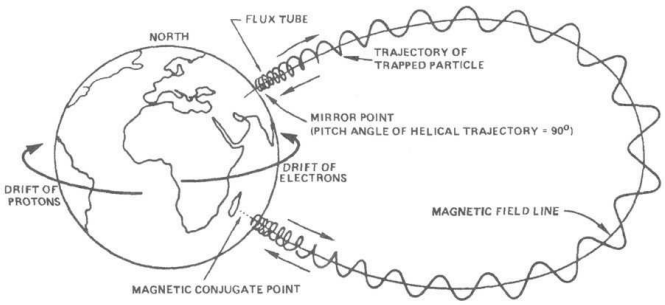

Figure 1.5: Particle drift in the Van Allen belts. The motion of trapped particles consists of three periodic components: gyration around a magnetic field line, movement along the field and longitudinal drift toward west and east for positively and negatively charged particles respectively.

is dependent on latitude, longitude and azimuth.

Particles can become trapped in the dipolar terrestrial field because of mirroring in the "magnetic bottle", this is shown in figure 1.5. There are two stable radiation belts, where trapped particles are confined. The outer belt consists mainly of electrons of energy up to 10 MeV, while the inner belt is populated by protons of energy up to few hundreds of MeV. Due to the fact that the magnetic field and the belts are tilted compared to the Earth rotational axis, there is a region off the coast of Argentina where the inner belt is closer to the Earth Surface, this region is referred to as South Atlantic Anomaly (SAA). The shape and the strength of the radiation belts are modified by the activity of the Sun because it determines the extent of the magnetosphere. As a consequence the intensity of any component of the cosmic rays below a few GeV depends both on the location and on time.

1.3 Antiparticles in cosmic rays

The model of quantum field theory has placed antimatter on an equal footing with matter and opened up speculation as to whether there is an overall balance between the amount of matter and the amount of anti-

matter in the universe.
The Standard Model of particle physics describes the elementary constituents and interactions of matter and is successful in explaining almost all experimental observations in particle physics. However, it is widely assumed that the Standard Model must merely be a part of a superior and more comprehensive theory, in the sense that it could be a low-energy effective theory truly valid only in the energy regime open to current experiments. The Standard Model shows that every particle has an antiparticle, and that they can only be produced in pairs. Antiprotons and positrons have been observed in cosmic rays, while antinuclei heavier than $\bar{p}$ have been looked for but never been observed in space. The number of antiparticles present in cosmic rays is much lower than the number of the corresponding particles, reflecting the fact that we live in a galaxy made mostly of matter. In order to justify a Universe made entirely by matter we must introduce some new physics in the Standard Model and Standard cosmology.

This possibility was proposed in 1967 by Sakharov [8]. According to his model an initially symmetric Universe could dynamically evolve to generate the observed asymmetry if three conditions are satisfied:

1. different interactions of particles and antiparticles, for example violation of C and CP symmetries;

2. deviation from the thermal equilibrium in the early Universe;

3. non-conservation of the baryonic charge.

These conditions were suggested after the discovery of the CP-violation in the neutral kaon system in 1964 and of the C-violation in the pion decay. However the level of CP-violation seems not enough to fulfill the Sakharov conditions. In 1965 the Cosmic Microwave Background Radiation was discovered, this radiation is considered as the best evidence for the Big Bang model of the Universe, from which the second condition arises naturally, since it foresees an expanding Universe. Currently there is no experimental evidence of the violation of the baryonic charge, but this condition is foreseen in the models of Grand Unification at an energy scale of $\sim 10^{16}\ GeV$. Other scenarios with baryon non-conservation

at much lower energies have been developed and include for example supersymmetric particles, topological defects and black-hole evaporation.

Another approach developed to explain the observed local asymmetry between matter and antimatter relies on the hypothesis that baryons may survive as galaxies in some regions of the universe and antibaryons may survive as antigalaxies in other regions. In this case, the matter-antimatter asymmetry should be "local" instead of "global". Unfortunately, it is not possible to look for antimatter galaxies with optical methods, since the photon is its own antiparticle. This hypothesis needs a separation between matter and antimatter domains to justify the fact that they do not annihilate.

There are different ways to investigate the addressed questions. A possibility is to study the γ radiation component in the Universe, since it is connected to annihilation processes of matter and antimatter. Detailed studies of the expected γ-ray background, in the case the universe consists of distinct regions of matter and antimatter, demonstrated that the size of the domain where we live should be at least comparable to the present day cosmological horizon [9], therefore excluding a globally baryon-symmetric universe.
Another possibility, the one studied in this work because it is the aim of PAMELA experiment, is to directly detect a primary antimatter component in cosmic radiation.
The known antimatter cosmic-ray component consists of antiprotons and positrons. They can be produced as secondaries arising from interactions of standard matter in the galaxy.

Antiprotons can be produced as secondaries in collisions of high energy cosmic-ray nuclei with the interstellar medium, through the general reaction $Np \rightarrow \bar{p}X$. The threshold for antiproton production from kinematic constraints is 5.6 GeV and the production cross section is strongly energy dependent. Due to the fact that kinematics predicts the suppression of low-energy secondary antiprotons in the Galactic cosmic rays, the search for a possible primary component of antiprotons at lower energy should be easier, but in this case one has to take into account even the solar modulation, as already explained in section 1.2.

Positrons are produced as secondaries either by pair production ($\gamma\gamma \rightarrow e^+e^-$) and by a multitude of reactions induced by high energy cosmic-ray nuclei interaction with the interstellar medium involving the creation of pions and kaons, which in turn decay in electrons and positrons (via the decay $\pi^\pm, k^\pm \rightarrow \mu^\pm \rightarrow e^\pm$). The muons created through decays of secondary pions and kaons are fully polarized, which results in $e^\pm$ decay asymmetry and consequently a difference in their production spectra. However, since this asymmetry is negligible, the process yields a nearly equal amount of electrons and positrons.
There are systematic differences among various positron flux measurements due for example to solar modulation, consequently, for the task of comparison, it is natural to express the positron flux as the ratio $e^+/(e^+ + e^-)$. The positron fraction measured at the top of the atmosphere is $\simeq 10\%$ at few GeV, thus the majority of the electrons have to be of primary origin. If positrons are instead mainly of secondary origin, their spectrum becomes a valuable tool for judging the validity of propagation models since it decouples the measurements of the propagation products from the measurement of primary electron spectrum. The secondary component can be estimated by using the spectra of cosmic-ray nuclei measured at the top of the atmosphere and models of cosmic-ray propagation in the galaxy.

At present the known antimatter cosmic-ray component does not include antihelium or heavier antinuclei, according to the fact that the probability for them to be generated with secondary production is extremely low. Consequently, if any $\bar{H}e$ is discovered, it can be stated that it has primary origin, either produced during primordial nucleosynthesis or coming from a distant antigalaxy. In figure 1.6 is shown the present experimental limits concerning $\bar{H}e/He$ ratio, no observation of anti-helium has been made to date and so upper limits are shown. The value of this ratio is very important being connected with the baryon antibaryon asymmetry in the Universe. We can reasonably expect that the antimatter-matter ratio in cosmic rays is more or less equal to the (anti-star)-star ratio $N_{\bar{S}}/N_S$, if the antistars are of the same kind as the stars in the Galaxy. The present observational limit in the search of

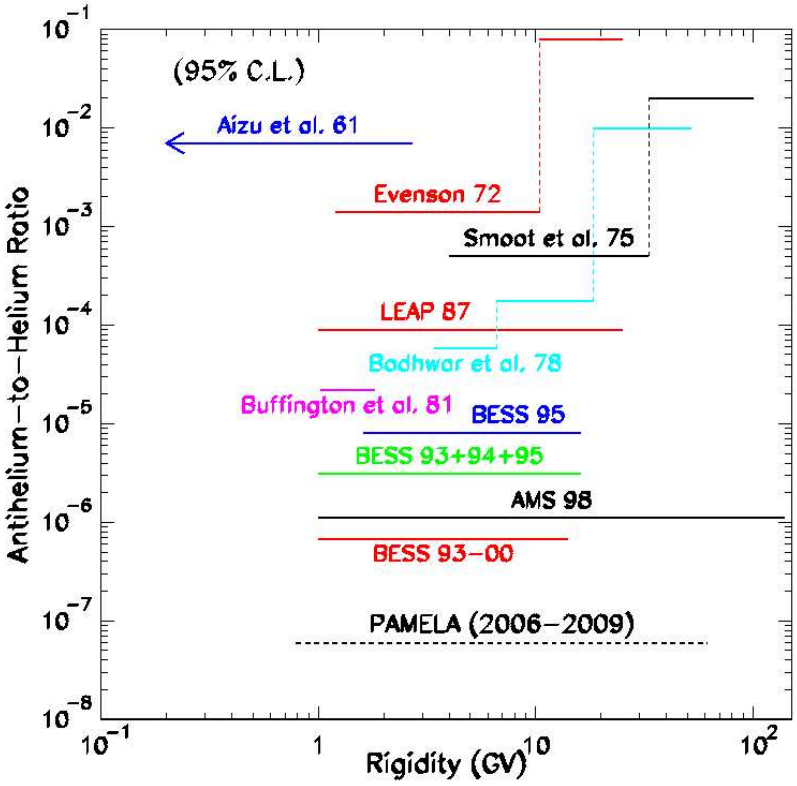

Figure 1.6: Experimental limits on the ratio of anti-helium to helium in the cosmic radiation shown as a function of rigidity [35]. The expectation for PAMELA after a 3 year long mission is shown.

antihelium is of the order of 10^{-6}, leading to the constraint [10]:

$$\frac{N_{\bar{S}}}{N_S} \lesssim \frac{\bar{He}}{He} \lesssim 10^{-6}. \tag{1.6}$$

Considering that the number of ordinary stars in the galaxy is about $N_S \sim 10^{11}$, it follows $N_{\bar{S}} \lesssim 10^5$. In the same figure the expectation for PAMELA after a 3 year long mission is shown, PAMELA should extend this limit to the 10^{-7} level.
On the contrary, since antiprotons and positrons are extensively produced by collisions of cosmic rays with interstellar matter, their existence is not a direct signature for the existence of primary antimatter sources, but their signal might arise anyway as a distortion on the detected secondary production fluxes.

From the current status of antiproton and positron measurements it seems that the observed spectra agrees with a purely secondary production, anyway at high energy the measurement are not quite significant because the statistic is too low. The general behaviour would asses an enhancement of the expected number of antiparticles that could be justified by some primary sources. Apart from antistars there are other possible sources of primary antimatter, first of all the dark matter annihilation. In the following the status of the antiparticle observation and the main hypotheses developed to explain such behaviour are reviewed.

1.3.1 Present antiparticle measurements

Positrons and antiprotons are the only antiparticle species detected in the cosmic radiation until now. Detailed measurements of the antiproton and positron energy spectra can provide valuable information on the structure of the interstellar medium, on cosmic-ray propagation and solar modulation. However, there might also be more exotic contributions to the observed intensities of these particles. To solve this puzzle of hypotheses the study of their flux is fundamental and many experiments have been performed in the past with this aim.

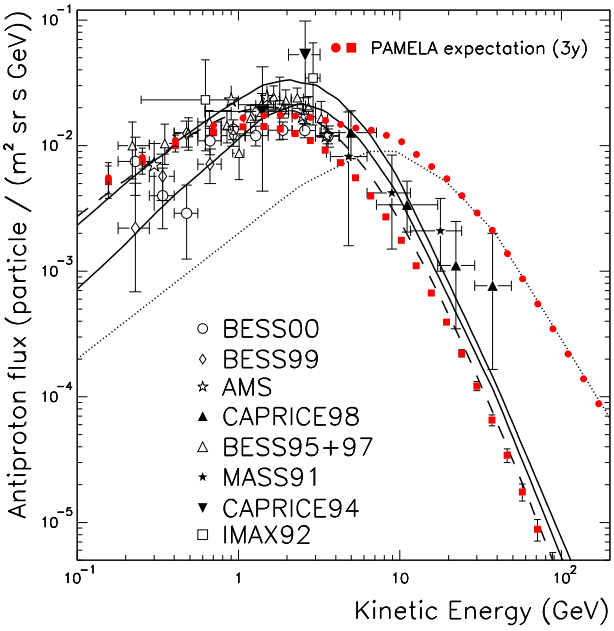

Figure 1.7: Recent experimental spectra (BESS00 and BESS99 [11], AMS [12], CAPRICE98 [13], BESS95+97 [14], MASS91 [15], CAPRICE94 [16], IMAX92 [17]) along with theoretical calculations for pure secondary production (solid lines: [18], dashed line: [19]) and for pure primary production (dotted line: [20], assuming the annihilation of neutralinos of mass 964 GeV/c^2). The expected PAMELA performance, in case of a pure secondary component (full boxes) and of an additional primary component (full circles), are indicated. Only statistical errors are included in the expected PAMELA data.

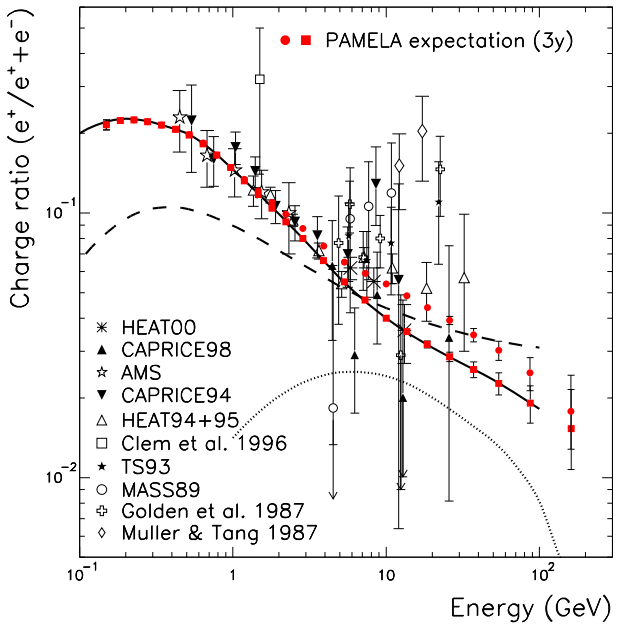

Figure 1.8: The positron fraction as a function of energy measured by several experiments ([21, 22, 23] and MASS89 [24], TS93 [25], HEAT94+95 [26], CAPRICE94 [27] [28], AMS [29], CAPRICE98 [30], HEAT00 [31]). The dashed [32] and the solid [33] lines are calculations of the secondary positron fraction. The dotted line is a possible contribution from annihilation of neutralinos of mass 336 GeV/c^2 [34]. The expected PAMELA performance, for a pure secondary component (full boxes) and of an additional primary component (full circles), are indicated. Only statistical errors are included in the expected PAMELA data.

Figures 1.7 and 1.8 show a summary of the current status of antiproton and positron measurements together with PAMELA expectations. The majority of the data available comes from balloon-borne experiments, with the exception of AMS-01 [36], that flew on a short-duration flight on the Space Shuttle in 1998. At present data exist in the energy range up to 50 GeV for antiprotons and up to 30 GeV for positrons. PAMELA will increase the range for both particle types up to few hundred GeV and will reduce the statistical errors in the range where data exist.

The study of antimatter in cosmic rays is a unique tool to investigate several physics and astrophysical phenomena. In fact, even if the observed antiprotons and positrons are only or mainly of secondary origin, their energy spectra are useful to validate the propagation models. Thus in order to compare the secondary expected flux with the measured one, a careful study of cosmic-ray propagation, following different galactic model, is needed. In this way one can identify the primary contributions in the spectra of secondary antiproton and positron. The dashed and solid lines in figures 1.7 and 1.8 indicate expectations from purely secondary production models.
From figure 1.7 seems that the observed antiproton flux measurements agrees with a purely secondary antiproton production, at least in the energy range where the measurements are statistically significant.
cosmic-ray electrons are probably accelerated by the same engines that accelerate cosmic-ray protons and nuclei (galactic supernova explosions). Positrons, whose flux is 10% of the electron flux above a few GeV, are believed to be produced by the interactions of cosmic rays with the interstellar medium. However few experiments measured a larger positron fraction which lead to speculations about primary sources of positrons.
From figure 1.8 it can be seen that the observed positron fraction below 10 GeV is essentially explained by the secondary origin. For example recent observations with CAPRICE94 [27] show that the observed positron spectrum and the positron fraction below about 10 GeV are consistent with a pure secondary origin in the diffusion model of cosmic-ray propagation.
On the other hand some measurements indicate that there is a significant

excess of positrons at energies around 10 GeV and above, compared to the fraction expected from the secondary sources. The HEAT instrument [4] has detected cosmic-ray electrons and positrons in two balloon flights, at energies between 1 and 50 GeV. The combined data set indicates that the positron fraction does not increase with energy above 10 GeV. However, the results suggest a slight overabundance of positrons at all energies compared with published predictions from secondary production sources, and possibly the hint of a feature in the positron fraction in the energy range $7 \div 20$ GeV.
However, the interpretation of the results at high energy is difficult due to large uncertainties in propagation models and large experimental errors. Moreover a contamination of protons in the positron sample could affect the results, thus more analyses and statistics are needed.

1.3.2 Sources of primary antiparticles

One of the possible explanation of a primary component of antiparticles in cosmic rays comes from the existence of antigalaxies in the Universe, in this case they should produce and accelerate particles in the same way of galaxies and consequently extragalactic cosmic rays made of antimatter could reach our galaxy becoming part of the Milky Way cosmic rays. In case of existence of primordial antimatter, $\bar{He}$ should be the most abundant element apart from anti-hydrogen, while heavier antinuclei could be produced only during stellar nucleosynthesis processes, thus their detection should be the prove of the existence of anti-stars.
The other possibilities are all related to "exotic processes". One of them is the evaporation of primordial black holes (PBH) by the Hawking process. The prediction of PBHs follows from the existence of a hot phase in the early universe that has density fluctuations which can collapse to form PBHs. They evaporate with the emission of gamma rays, antiprotons and antideuterons.
However, the most interesting possibilities consist in antiparticles coming

[4] The High-Energy Antimatter Telescope (HEAT), is based on a balloon borne detector system which includes a superconducting magnet spectrometer. This instrument has been successfully flown in 1994 and 1995 to measure the flux of positrons and electrons over a wide energy range.

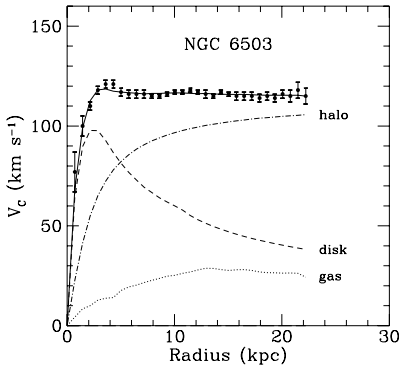

Figure 1.9: Rotation curve of the galaxy NGC6503 [37] with contributions from stars (disk), interstellar gas and the dark matter halo.

from dark matter annihilation.

Dark matter

Evidence for the presence of significant amounts of invisible matter is numerous and apparent from the small to the largest scales. Recent measurements of the cosmic microwave background have revealed that ordinary matter constitutes only 5% of the critical density, which confirms the Big Bang nucleosynthesis prediction. The remaining 95% of the energy density of the Universe consists of 70% "dark energy", a mysterious negative-pressure field responsible for the late acceleration of the Universe, and of 25% "dark matter". There are also many observational evidences of the existence of dark matter, most of them coming from the study of the motions of galaxies. For example, the velocity of rotation of astrophysical objects versus the distance from the galactic center, described by the galactic rotation curves, cannot be explained by only the visible matter. The radial velocity of a star at distance r from the center of the galaxy is expected to be $\propto 1/\sqrt{r}$, outside the luminous galactic disk. This behaviour is indicated by the dashed rotation curve in figure 1.9 for the galaxy NGC6503 [37]. However, the data show that the actual radial velocity is a constant function of the distance from the center. This could be explained with the assumption that the galactic

disk is embedded in a galactic halo of non-luminous dark matter, represented by the dash-dotted line in figure 1.9. The same behaviour has been found in all the galaxies studied up to now [38]. Other observed phenomena consistent with dark matter observations are gravitational lensing of background objects by galaxy clusters, and the temperature distribution of hot gas in galaxies and clusters of galaxies. Dark matter also plays a central role in structure formation and galaxy evolution, and has measurable effects on the anisotropy of the cosmic microwave background.

Regarding its composition, many aspects remain to be clarified. Studies of big bang nucleosynthesis have provided increasingly convincing evidence that dark matter is mostly non-baryonic and can be divided into three different types, namely hot, warm and cold if particles move ultra-relativistically, relativistically or non-relativistically. In the first case an optimum candidate is the neutrino, since it does not interact via either the electromagnetic or the strong nuclear force. However there are bounds on neutrino mass suggesting that neutrinos can provide only a small contribution to the density of dark matter. Therefore most cosmologists favor the cold dark matter theory. It could explain how the Universe went from a smooth initial state at early times, proved by the cosmic microwave background radiation, to the present large-scale structure in the form of a clumpy distribution of galaxies and their clusters. The most commonly proposed particles to be dark matter components are not part of the standard model of particle physics, but they can arise in theories extending the standard model. Among the other proposed particles, the most interesting are the so called **Weakly Interacting Massive Particles (WIMPs)**: they should be massive relic particles created during the Big Bang and diluted during the inflationary era, which interact mainly through gravity, and have a large mass compared to standard particles. Many supersymmetric models naturally give rise to WIMPs. The lightest supersymmetric particle, called "neutralino", is one of the best candidate, because it has the attractive feature of giving a relic density adequate to explain cosmological dark matter in a large region of the parameter space. It arises in supersymmetric models as a linear combination of the superpartners of the neutral gauge and

Higgs bosons (the Bino $\tilde{B}$, the Wino $\tilde{W}^3$ and the two neutral Higgsinos $\tilde{H_1}^0, \tilde{H_2}^0$), the lightest one is:

$$\tilde{\chi_1}^0 = N_{11}\tilde{B} + N_{12}\tilde{W}^3 + N_{13}\tilde{H_1}^0 + N_{14}\tilde{H_2}^0 \tag{1.7}$$

Besides the direct detection of galactic neutralino dark matter in the laboratory, dark matter neutralinos can be detected by looking for the products of their annihilation. Three types of searches can be distinguished according to the place where neutralino annihilations occur. The first is the case of neutralino annihilation in the Sun or the Earth, which gives rise to a signal in high-energy neutrinos; the second is the case of neutralino annihilation in the galactic halo, or in the halo of external galaxies, which generates gamma-rays and other cosmic rays such as positrons and antiprotons; the third is the case of neutralino annihilations around black holes, in particular around the black hole at our Galactic Center. All these annihilation signals share the property of being proportional to the square of the neutralino density. This follows from the fact that the neutralino is a Majorana fermion, i.e. is identical to its antiparticle. Two neutralinos can annihilate to produce standard model particles. Consequently the annihilation rate, being proportional to the product of the densities of the initial particles, is proportional to the square of the neutralino density.

When neutralinos annihilate in the galactic halo, they produce quarks, leptons, gauge bosons, Higgs bosons and gluons which consequently decay or hadronize, producing the same quantity of particles and antiparticles. Consequently the detection of supersymmetric dark matter can be achieved indirectly through its effect on cosmic rays, in particular on the antiparticle spectra of antiprotons and positrons, due to the lower background: this signature should arise as a distortion on their secondary fluxes. Possibilities for neutralino detection in the antiparticles channels depend strongly on its nature that determines the annihilation cross section.
As an example in figure 1.7 the dotted lines, with a maximum around $E \sim 10\ GeV$, show the theoretical prediction of a primary contribution due to neutralino annihilation of mass 964 GeV/c^2, to the antiproton

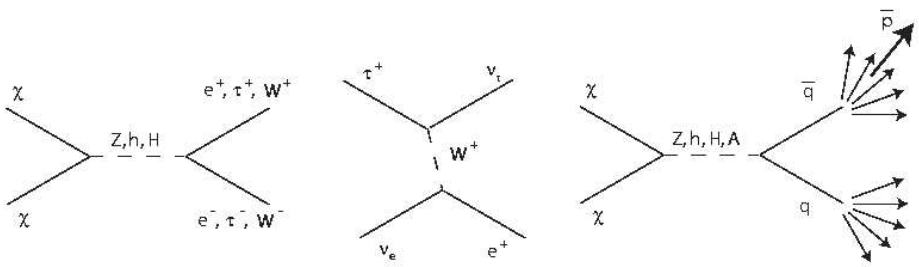

Figure 1.10: Secondary production of antiparticles form neutralino interactions.

flux.

Positrons primary sources

Several theories have explored the idea of primary sources for positrons: they can be divided in astrophysical and new physics sources. In the first group positrons produced by pair creation in the magnetic field near discrete sources such as Galactic γ-ray pulsars can be included, as well as primary black hole annihilation and radioactive decay of ^{56}Co in young supernovae remnants. The second group of theories mainly states that positrons are the products of dark matter annihilation. From this process positrons can be produced either directly or from decaying mesons in hadron jets. We thus expect to get both monochromatic positrons from direct annihilation into electron/positron pair with an energy corresponding to neutralino mass and continuum positrons from the other annihilation channels. In general the branching ratio for the former case is rather small but for some classes of model one can obtain a large enough branching ratio for the line to be observable. The most interesting energy range for this kind of study is the region above $\sim 10\ GeV$ because of the small influence of the solar modulation effects that permits to fully exploit the performances of the PAMELA experiment. In fact interactions with the solar wind and magnetosphere alter the low energy spectrum.
Detailed studies of the expected flux of positrons at the Earth coming

from neutralino annihilation in the halo have been performed. The results of one of these calculations[34] is shown by the dotted line in figure 1.8. In that study the positron propagation is treated in a diffusion model including energy loss, it is a more realistic model then the leaky-box model but still permits an analytic solution. The positron source function which has been used includes contributions from both continuum and monochromatic positrons. The minimal supersymmetric standard model parameters space has been scanned in details and the most recent accelerator results are used to exclude some of the models. The theoretical prediction shown in figure 1.8 is obtained with a neutralino of mass 336 GeV/c^2, but many other models have been investigated.
It may be noted that except in the radioactive decay case, equal amounts of e^+ and e^- are produced in all the above processes. While the total spectrum of $(e^- + e^+)$ can be identified by different experimental techniques, a magnet spectrometer is essential to distinguish between e^- and e^+. The unambiguous detection of positrons is difficult because of the vast background of protons. In fact at high energy the number of protons is about 10^3 times the number of positron, as a consequence a proton rejection factor of at least 10^5 is needed for experiments aimed to measure the antimatter component in cosmic rays with a fraction of background events in the selected sample of antimatter particles less than 1%.

Chapter 2

The PAMELA experiment

The PAMELA experiment has been conceived by the WiZard collaboration, a group that has been involved for many years in cosmic ray research performing several balloon flights. The experimental devices used for the balloon experiments employed a combination of highly sophisticated and new detector systems for space. Taking advantage of this important experience the group was able to conceive the PAMELA experiment, with the aim of improving significantly the physics results obtained with the limited acquisition time and altitude typical of balloon flights. On the contrary PAMELA is hosted by a satellite and should be operative for at least 3 years.

This chapter is dedicated to the explanation of the scientific objectives of the PAMELA experiment and of the technical design developed to accomplish the physics goals. Then a description of the whole apparatus is given, explaining with more details those detectors that in this work have been used for the analysis, namely the tracking system and the calorimeter.

2.1 Mission overview

PAMELA is an acronym for *Payload for Antimatter-Matter Exploration and Light-nuclei Astrophysics*. It is a space-borne experiment, which was launched on board of the Russian Resurs-DK1 Earth-observation

satellite from Baikonur cosmodrome in Kazakhstan on the 15^{th} June 2006. A drawing of the satellite is shown in figure 2.1; it is mainly designed to collect and transmit data on sea surface status, ice coverage and meteorological conditions in the Earth polar region, moreover it takes high resolution images of the Earth surface. In order to perform these observations, it is continuously oriented toward the Earth and it has a large amount of hard disk space, of which 100 GB are reserved for the PAMELA experiment. The PAMELA apparatus is installed inside a pressurized and temperature controlled container on one side of the satellite. Its weight is $\sim$ 470 kg while the total mass of the satellite is $\sim$ 10 *tonnes*. The average power consumption is 2000 W, of which 355 W dedicated to the PAMELA experiment, and it is supplied by solar panels and batteries depending on the satellite position with respect to the Earth shadow. The satellite follows a semi-polar elliptical orbit, varying its altitude from 350 to 600 km, with an inclination of 69.9° compared to the Equator and a period of about 90 minutes. It was planned to stay in orbit for at least three years. This long data-taking time compared to balloon borne experiments, which can fly usually few days, will provide unprecedented statistics. Moreover, thanks to the absence of atmospheric overburden, it will be possible to greatly reduce the systematic errors of the previous experiments. In fact the balloon altitude is about 40 km, so the measured fluxes had to be corrected for the presence of secondary particles produced during cosmic ray interaction in the residual atmospheric layers.

Until now only the advantages of direct detection of cosmic rays from satellite have been discussed. However it has many inconveniences, too, mainly from a technical point of view: there are in fact limitations on the maximum weight and size of the apparatus and on the power available for the instruments. In addition the detectors have to be designed in order to be able to withstand the stresses of the launch as well as the presence of ionizing radiations in the space environment. Another important feature of satellite experiments is the automation of most of the operational procedures, since only minimal interventions from ground are possible.

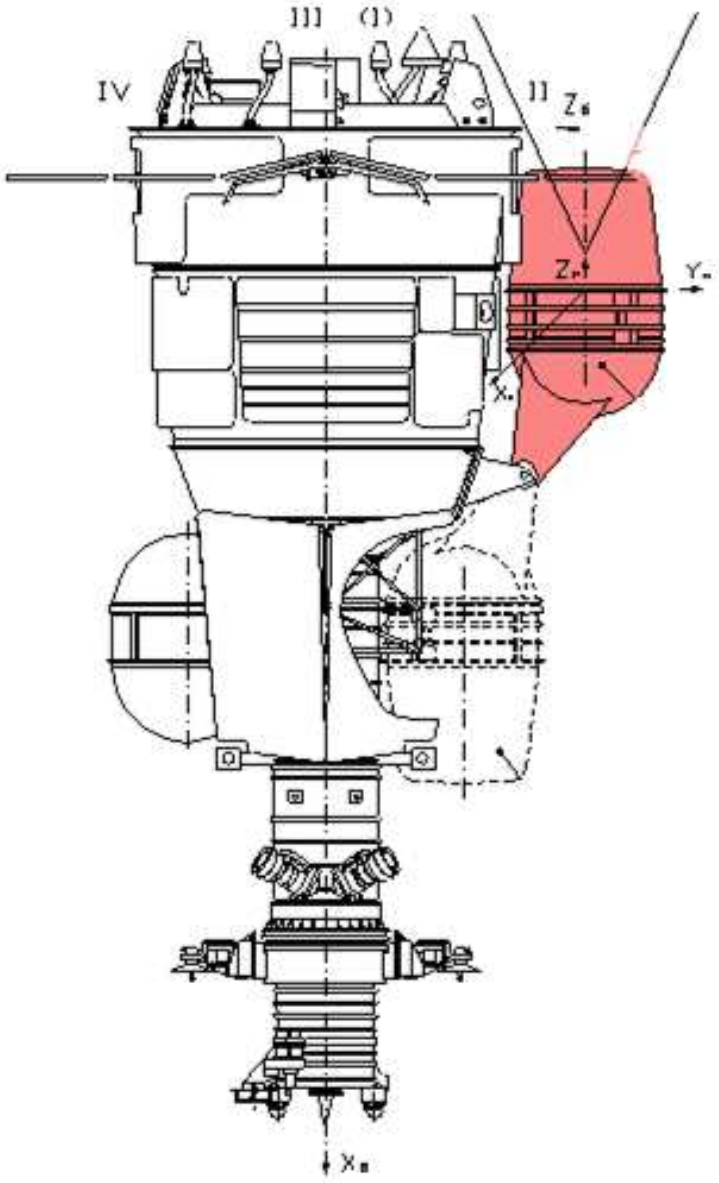

Figure 2.1: Drawing of the Resurs DK1 satellite. The pressurized container of the PAMELA apparatus is shown in red as it is positioned normally during acquisition. The dotted drawing shows instead the position of the container during the launch phase.

2.2 Scientific objectives

The primary scientific objective of the PAMELA experiment is the study of the antimatter component in cosmic rays, which is performed in particular in order to measure the antiproton and positron spectra. In fact as explained in the previous chapter their fluxes are connected to possible new physics and they allow to test cosmic ray propagation models. The principal aims of PAMELA are the increase of the number of detected antiparticles and the extension of the energy range compared to previous experiments. This will be possible because this experiment detects cosmic rays outside the atmosphere and is able to measure their momentum and identify antiparticles in a much larger particle background. Even if PAMELA is optimized for the measurement of rare cosmic rays components, there are additional goals that can be addressed by this experiment thanks to the long exposure time and the characteristics of the orbit. It is possible to study the effects of solar modulation on the lower energy particles and the solar flare events occurring in this period, as well as the study of trapped particles in the radiation belts.

The expected detection capabilities of both the rarest cosmic ray components and the more abundant particles, like protons, electrons and light nuclei, are the following:

- antiproton spectrum from 80 MeV to 190 GeV ($\sim 10^4$ in 3y);
- positron spectrum from 50 MeV to 270 GeV ($\sim 10^5$ in 3y);
- sensitivity in $\bar{He}/He$ of the order of $\cdot 10^{-7}$;
- proton spectrum from 80 MeV to 700 GeV ($\sim 10^8$ in 3 years);
- electron spectrum from 50 MeV to 400 GeV ($\sim 10^6$ in 3 years);
- electron plus positron spectrum up to 2 TeV;
- light nuclei ($Z \leq 6$) spectrum up to 250 GeV per nucleon.

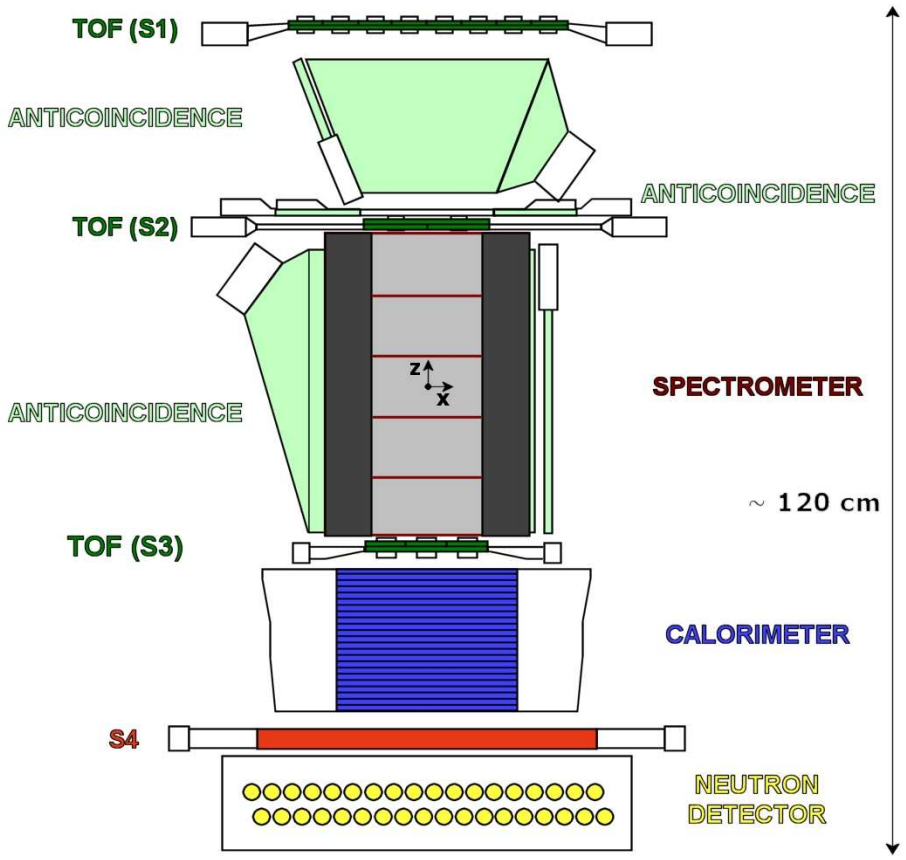

Figure 2.2: Schematic drawing of the PAMELA detectors, showing the sensitive areas of the various subsystems, in a longitudinal section.

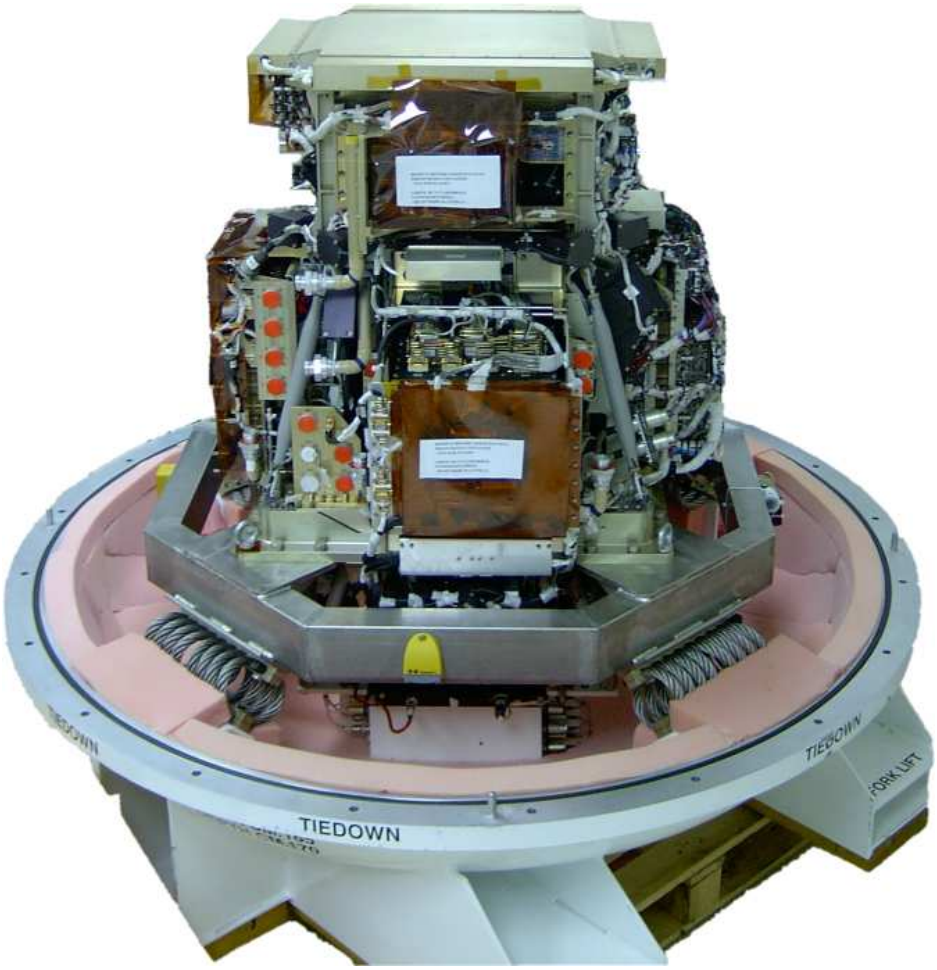

Figure 2.3: A picture of the PAMELA detector laid on the bottom part of the container which has been used to transport it from Italy to Russia, for the assembling on the satellite. The cabled boxes around the body of the detector contain the electronic boards of the various subsystems.

2.3 Detector description

The PAMELA experiment consists of several subdetectors, providing different measurements of the incident particle. The technique employed to accomplish the physical tasks of the mission is to use the information of all the detectors in order to measure the momentum of charged particles, their charge and identity. A drawing of the longitudinal section of the PAMELA detector is shown in figure 2.2, while a picture of the complete instrument is shown in figure 2.3.

The central component of the instrument is a hollow permanent magnet which, together with a tracking system composed of six planes of silicon sensors, forms a magnetic spectrometer used to determine the rigidity ($R = p/q$) and the charge of particles crossing the magnetic cavity. The rigidity and the sign of the charge are determined through the reconstruction of the trajectory based on the impact points on the tracking planes, while the energy loss in the silicon planes is related to the absolute value of the charge, which can be determined approximately up to $Z = 5$. The tracker geometry and its dimensions define the geometric acceptance of the experiment.
An electromagnetic imaging calorimeter is placed under the spectrometer. Its main task is to perform particle identification through the analysis of electromagnetic and hadronic showers, which develop differently in the calorimeter. The calorimeter can also measure the energy of electrons and positrons interacting in its volume, providing an important check for the spectrometer calibration. Due to its wide dynamical range, it is able to determine the absolute value of the charge up to silicon nuclei ($Z = 14$).

The time-of-flight system (TOF) is composed of three groups of fast plastic scintillators (S1, S2 and S3 in figure 2.2). It can measure the velocity of the particles, allowing the discrimination between positrons (electrons) and protons (antiprotons) for momenta up to about 1 GeV/c. Another important task of this device is to produce the main trigger for the experiment, and to determine the arrival direction of particles in order to reject albedo (up-going) particles.
An additional plastic scintillator, S4 in figure 2.2, is placed under the

calorimeter. It can detect charged particles leaking out of the calorimeter and can be used to help the identification when the showers are not completely contained in it. It is used also as a stand alone trigger for the Neutron detector, ND in figure 2.2, which consists of ^{3}He filled counters, located at the bottom of the instrument. The Neutron detector is sensitive to neutrons produced in hadronic interactions, therefore it can give useful information for the discrimination of electromagnetic and hadronic showers in the calorimeter.
Finally the whole detector is surrounded by two sets of scintillators (Anticoincidence). Their information is used during the offline analysis to tag particles entering outside the acceptance of the tracker.

The apparatus has the important feature to be redundant, that is the information provided by the different subdetectors overlaps. In this way, even if one of the detector would fail during the mission, the physics goals should be partly obtained, in addition the system redundancy can allow the cross calibration between the subdetectors.
An example is given by the momentum that is usually calculated from tracker information but also calorimeter can provide this information for electrons and positrons. Another example is the charge of the particle which can be obtained from the tracker or calorimeter or the time of flight system even if not all the detectors cover the same range of measurable charge.

2.3.1 The magnetic spectrometer

The core of the PAMELA apparatus is the magnetic spectrometer, which provides the main information needed to determine the spectrum of charged cosmic rays: the momentum p of the particles and their charge q. In fact this kind of detector measures the *magnetic deflection*, of charged particles passing through a magnetic field, η; it is defined as the inverse of the particle rigidity R:

$$\eta = \frac{1}{R} = \frac{q}{p} \tag{2.1}$$

The principle of the spectrometer measurement is that charged particles moving in a region where a magnetic field is present, undergo the Lorentz force $\vec{F}_L$, which is responsible for the curvature of their trajectories. The intensity and direction of this force depends on the particle velocity $\vec{v}$ and charge q, as well as on the magnetic field $\vec{B}$. The Lorentz force can be expressed in the International System of Units (SI) as:

$$\vec{F}_L \; = \; q \, \vec{v} \times \vec{B} \; . \tag{2.2}$$

Under the effect of this force the equation of motion for relativistic particles with mass m in a non uniform magnetic field can be resolved by means of numerical methods (as will be explained later in section 5.1) and the deflection value can be obtained. With the approximation of constant magnetic field the trajectory of a particle with momentum p (in GeV/c) and charge Z is a helix, with curvature k and pitch angle λ. The radius of curvature $R_c = 1/k$ and the momentum component p perpendicular to $\vec{B}$ are related by [59]:

$$p \cdot cos(\lambda) = 0.3 \cdot Z \cdot B \cdot R_c \tag{2.3}$$

where B is in Tesla and R_c is in meters.

If the direction of motion is fixed (using TOF information as will be clear in section 2.3.3), from the sign of the deflection the sign of the particle charge can be inferred. Finally the momentum is determined from equation 2.1 if the absolute value of the charge is known. This quantity can be determined from the measurement of the energy deposited in the silicon detectors or in the TOF scintillator planes, because is proportional to the square of the charge of the particles.

In order to determine the particle deflection one has to reconstruct the particle trajectory. The tracking system is composed, as shown in figure 2.4, by a set of six detecting planes, segmented in x and y directions, so that we can use the measured coordinates of the impact points of the particles crossing the planes to find the trajectory. Consequently it is fundamental, in order to determine the deflection, that the system provides a very precise measurement of the impact point coordinate and that the magnetic field is precisely known in every point.

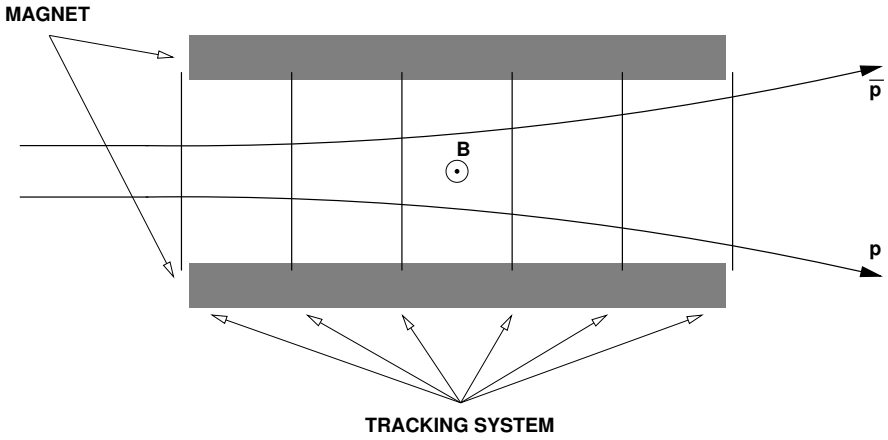

Figure 2.4: Schematic drawing of a magnetic spectrometer, represented in a longitudinal section. Trajectories of particles with different electric charge sign are bent in opposite directions because of the Lorentz force, as they pass inside a cavity where a nearly uniform magnetic field is present. A tracking system measures the passage of particles while crossing a set of six detecting planes.

The design of the spectrometer had to take in account the main objective of the PAMELA experiment, that is the extension of the measured energy range of the antiparticle spectra, so it is important to be able to measure particles with very high energy and to be sure to determine the right sign of its charge. On the other hand, in order to obtain an improvement of the statistics we need also to maximize the instrument acceptance. This requirement is conflicting with the previous one, therefore the dimension and the geometry of the magnetic cavity have been chosen as the best compromise between a sufficiently high number of particles entering the geometric acceptance of the system and the possibility of achieving a precise measurement of their rigidity.
At high energy the main uncertainty comes from the finite spatial resolution σ of the tracking detector in measuring the particle impact points on the detecting planes. In case of a uniform magnetic field, the spec-

trometer resolution can be expressed in the form [59]:

$$\frac{\Delta p_{res}}{p} \propto \frac{\sigma}{B\ L'^2}\ p\ . \tag{2.4}$$

where L' is the length of the track when projected on the bending plane. The precision in the measurement of rigidity becomes worse for higher values of the momentum, since the trajectory of the particle is less affected by the magnetic field and tends toward a straight line. The performances of a magnetic spectrometer for cosmic ray studies are usually expressed by a quantity called MDR, *Maximum Detectable Rigidity*, that is defined as the value of the rigidity which corresponds to 100% uncertainty on its measurement. Therefore it is clear from equation 2.4, that to enhance the MDR, that is reducing $\Delta p/p$ at high energies, one can use a longer magnetic cavity and a bigger magnetic field intensity. On the contrary to obtain an higher acceptance one should increase the cross-section of the cavity, with the consequence that it is more difficult to maintain an high field on a larger area.

The PAMELA spectrometer has been designed to achieve an MDR of at least 740 GeV/c. Besides this optimum performance expected for particle spectra determination, another effect has to be considered when measuring antiparticles, due to their rarity in the cosmic radiation. In fact when at high energies the tracks get closer and closer to a straight line, it is more and more difficult to determine the rigidity, with an higher probability that a particle is wrongly identified as the corresponding antiparticle and vice-versa. This effect is known as *spillover* and is particularly important in the case of the PAMELA experiment, which aims to explore the high-energy spectrum of antiprotons and positrons, since the ratio between the flux of a particle species and the corresponding antiparticle is $\sim 10^4$ for protons and $\sim 10^2$ for electrons. When the number of particles misidentified due to the spillover effect becomes comparable to the antiparticle signal, it happens that no reliable assumptions can be made on the antiparticle abundance. The PAMELA spectrometer has been designed to perform the detection of antiprotons until to about 190 GeV/c and of positrons to about 270 GeV/c, being limited by the spillover effect.

For small values of p the main uncertainty is due to the multiple Coulomb scattering of the particle as it passes through the matter along its path inside the spectrometer. This effect implies that

$$\frac{\Delta p_{ms}}{p} \propto \frac{1}{\beta} = \sqrt{1 + \left(\frac{m\,c^2}{p\,c}\right)^2}, \tag{2.5}$$

the contribution of this error is clearly very important only at low energies, while approaches a constant value, negligible compared to the resolution error, as p increases. In order to reduce this effect, in the design of the tracking system one has to minimize the amount of material along the path of the particles.

In the following I will describe the magnetic configuration and the silicon tracking system used for the PAMELA experiment, showing that the above requirements have been complied with a proper design.

The magnet

As it happens in all the space missions, there are strong constraints on the maximum weight and size of the instrument and on the available power. Therefore a permanent magnet for the spectrometer of PAMELA was chosen instead of a strongly power consuming superconducting magnet. The magnetic material is a Nd-Fe-B alloy, which provides a high residual induction of $(1.32 \pm 0.03)\ T$. For technical reasons it is not possible to create magnetic modules bigger than about $20 \times 100\ mm^3$, so the required intensity of the field of the PAMELA spectrometer is generated by five identical modules positioned one on top of another to form a tower, which is 436 mm high. The modules are located at a vertical distance of 9 mm and are interleaved with six detectors planes, which are inserted in the magnetic tower by means of dedicated slits. The design of the magnetic modules, shown in figure 2.5, has been studied in order to optimize the uniformity and the intensity of the magnetic field inside the cavity. A picture of the whole structure is shown in figure 2.6. The resulting B field in the spectrometer is almost uniform, and it mainly points opposite to the direction chosen as the y axis of the reference frame of PAMELA (see figure 2.2). Due to the Lorentz force the trajectory of cosmic ray

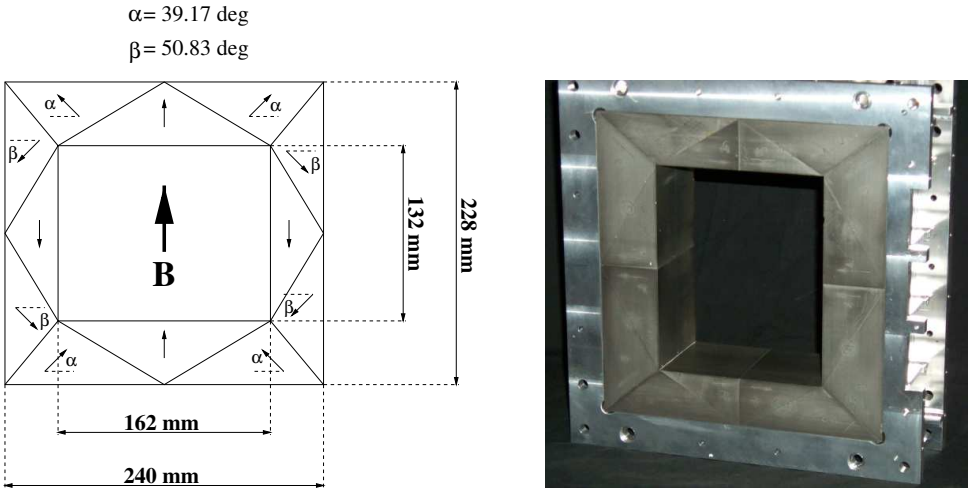

Figure 2.5: One of the magnetic modules of the spectrometer: on the left, a drawing of the yokeless configuration, which shows the direction of the residual induction and the resulting $\vec{B}$ field vector in the cavity; on the right, a picture of a prototype of the magnetic modules surrounded by its aluminium frame.

particles is curved mostly in the x direction, so that the bending plane is identified by the x and z axes. The magnetic field has been measured by sampling its B_{X}, B_{Y} and B_{Z} components on a three-dimensional grid consisting of 67367 points, 5 mm apart, along the three axes, by means of a Hall probe mounted on the moving mechanical arm of an automated precision positioning system. Some of the results which have been obtained are displayed in figure 2.7 and 2.8: they show the shape of the B_{Y} component of the field, which is the main one, on the plane $z = 0$ and along the axis $x = y = 0$, respectively. The average value of the field over the whole volume of the cavity is about 0.43 T.
Even if the residual magnetic field outside the spectrometer is low, ferromagnetic screens, with a thickness of 2 mm, are placed around the tower at a distance of 8 mm. This expedient was necessary to be sure not to interfere with the satellite control system and with the photomultipliers used to detect the light output of the scintillators.

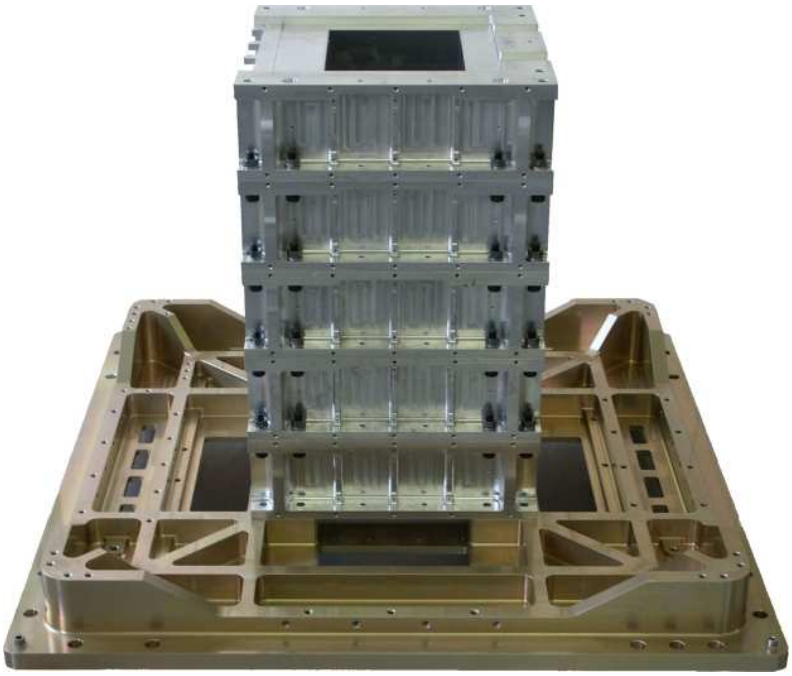

Figure 2.6: The permanent magnet of the spectrometer, composed of five modules encased in their aluminium frame. The tower is mounted over the base plate which connects PAMELA to the satellite structure. On top of it the upper opening of the magnetic cavity can be seen.

The tracking system and the silicon detectors

The tracking system of the PAMELA spectrometer is composed by six planes of silicon sensors, inserted in the slits between the magnetic modules and at both the ends of the spectrometer. The distance between them is 89 mm and the length of the whole tracking volume is 44.5 cm. There is no other additional structure to support the planes, thus minimizing the amount of matter which particles have to cross on their path. In this way the effect of multiple scattering, which worsen the momentum resolution at low energy, is reduced. Each plane contains three independent detecting units, called *ladders*, glued together side by side and fixed inside an aluminium frame, as shown in figure 2.9. Four thin carbon-fiber bars are glued at the sides of the ladders, in order to strengthen the me-

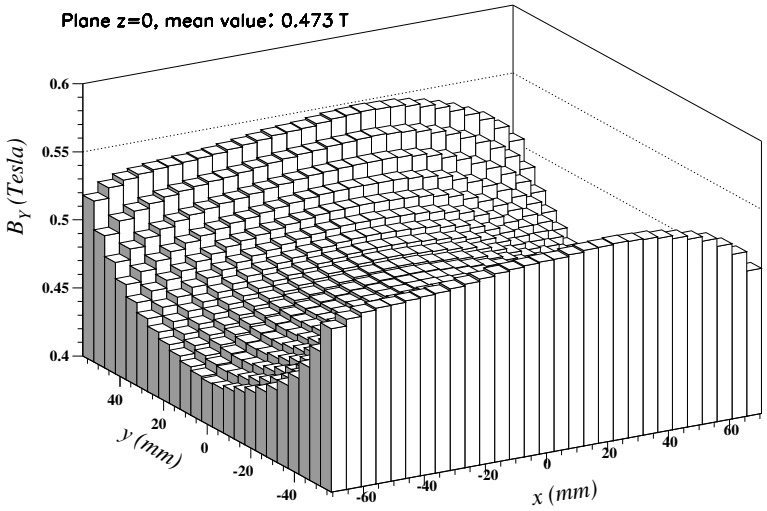

Figure 2.7: Measured values of the main component of the magnetic field over the cross section going through the center of the cavity (plane $z = 0$).

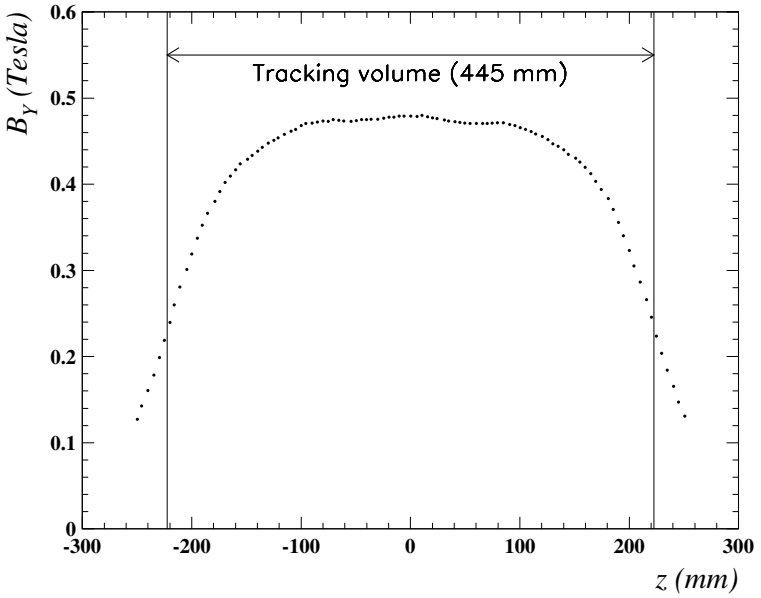

Figure 2.8: Measured values of the main component of the magnetic field along the longitudinal axis going through the center of the cavity (axis $x = y = 0$).

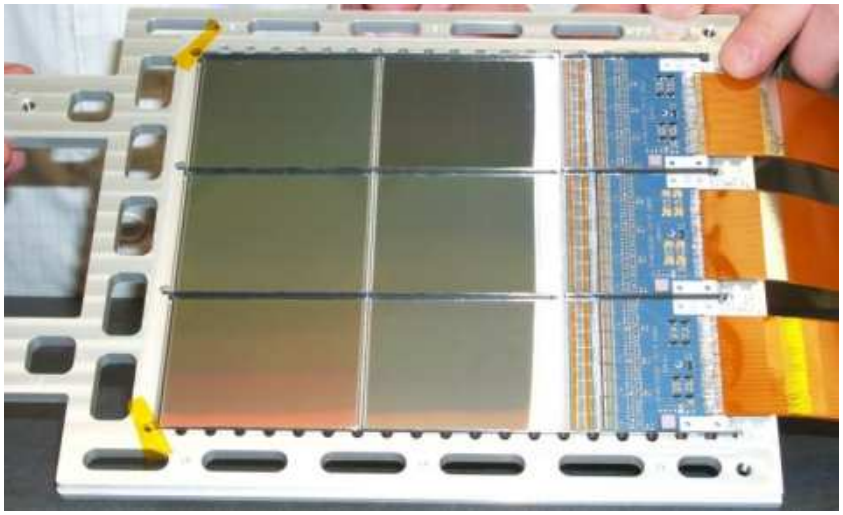

Figure 2.9: A plane of the tracking system, composed of six silicon sensors and their front-end electronics, fixed to an aluminium frame to be inserted in the magnetic structure.

chanical structure of the planes. Each *ladder* in turn is composed by two silicon sensors and an hybrid circuit which contains the front-end electronics. The sensor has a surface of $53.33 \times 70.00\ mm^2$ and is 300 μm thick. Each sensor is a silicon microstrip detector able to measure both the coordinates of the impact point on their surface. This ability is reached using double sided detectors: two sets of silicon strips are implanted on both the sides of the substrate, perpendicularly to each other. On the junction side 2035 p^+ strips are implanted with a pitch of 25 μm, while on the ohmic side there are 1024 n^+ strips with a pitch of 66.5 μm. On the ohmic side an additional p^+ blocking strip is placed between two n^+ strips increasing the interstrip resistance [40]. The decoupling capacitors, for signals running from the wafer to the electronics, are directly integrated on the silicon sensors by separating the implanted strips from the read-out aluminium strips by means of an insulating layer of silicon dioxide. Both the faces of the sensors are covered with a 100 nm thick silicon-dioxide layer. Moreover on the ohmic side an additional 5 μm thick silicon-dioxide layer covers the aluminium deposition. On top of

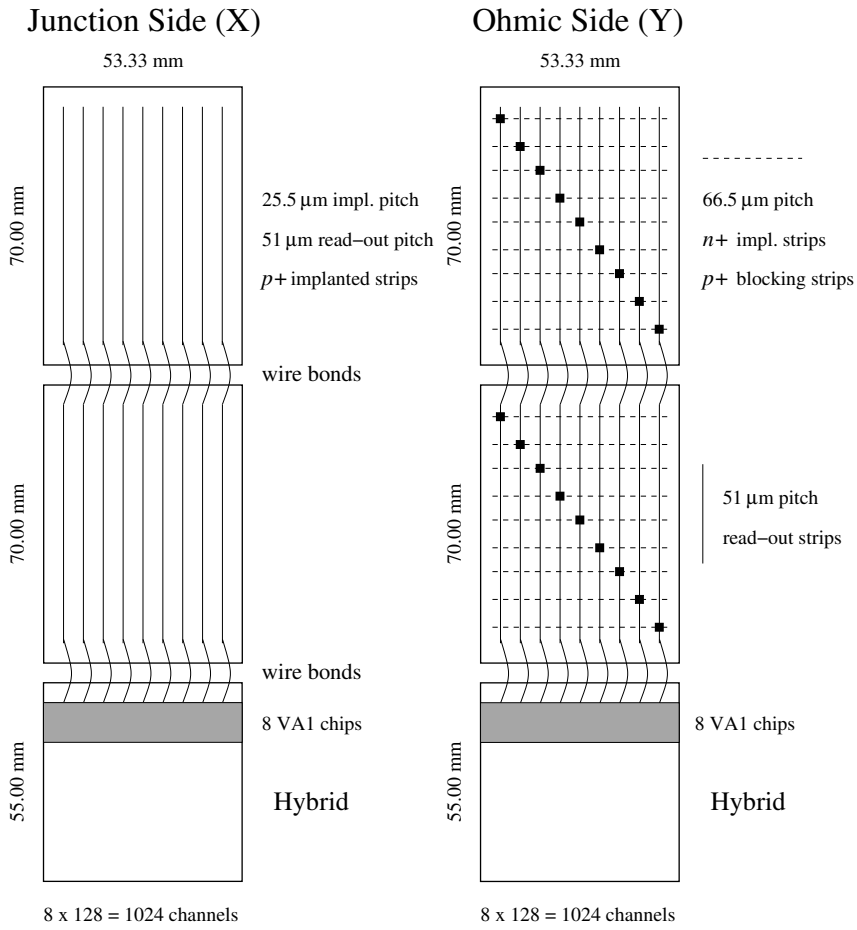

Figure 2.10: Sketch of the strip layout on the two sides of a *ladder* of the tracking system. On the ohmic side the second layer of read-out electrodes, perpendicular to the n^+ strips, and their connections on the diagonal of the sensor are shown.

the second layer of SiO_2 there is an additional set of metallic electrodes positioned orthogonally to the first one; the two sets are connected one-to-one as shown schematically in figure 2.10. By means of the described technique, said *double metalization*, the read-out electrodes on the ohmic side become parallel to the electrodes on junction side; in this way the front-end electronics can be placed on the two faces of a single hybrid so that the mechanical structure of the spectrometer is simplified. The read-out pitch is 50 μm on both sides; thus, on the junction side only one of two strips is read, while on the ohmic side all the strips are read. The sensors inside the spectrometer are oriented in such a way that the strips on the junction side run parallel to the y axis of the PAMELA reference frame, so that they are used to measure the coordinates in the main bending direction. The strips on the ohmic side measure instead the y coordinate. Due to the employed technique there is an ambiguity in the determination of the y coordinate, in fact there are two strips, implanted 7 cm apart, read by the same electronic channel. This ambiguity is solved during the offline data analysis by the track fitting procedure. When it is not sufficient to determine unambiguously which is the correct coordinate, it is possible to take advantage also of the spatial information coming from TOF or calorimeter.

The electronics to read out the collected charge of the silicon sensor has been designed in order to minimize the signal-to-noise ratio, related to the spatial resolution and the power consumption. The front-end electronics is the first stage of the signal acquisition, located on the hybrid. For each ladder side there are 8 VA1 chips, which consist of 128 parallel section, each one is composed by an amplifier, a shaper and a sample-and-hold stage. The VA1 chips are based on C-MOS technology and their main features are the low noise and power consumption. The 128 channels are connected in series with a multiplexer, which sends them to the next stage. The output of the front-end electronics is an analog signal, which is converted by a 12-bit analog-to-digital converter.
Since there are 8 chips for each side of one ladder, for the whole spectrometer the number of channels is $128 \times 8 \times 3 \times 12 = 36864$. This big amount of data cannot be sent to ground because of the limited bandwidth available for the transmission. For this reason for each side of the

tracker planes there is a Digital Signal Processor(DSP) that performs the compression of the signals and calibration. More details about the acquisition procedures implemented in the DSPs will be given in chapter 3.

2.3.2 The calorimeter

The main physics goal of the PAMELA experiment is the measurement of the antimatter abundance. From this follows that the main requirement for the PAMELA calorimeter is the ability to discriminate the signals of antiprotons and positrons in the vast background of electrons and protons. For the physics goal of the PAMELA experiment we must be able to separate electrons from hadrons at a level of $10^5 \div 10^6$. Much of this separation is provided by the calorimeter, but also other detectors can provide additional informations for particle identification. From simulation studies and analyses of test beam data it was proved [39] that, above 10 GeV/c, keeping an efficiency of 90%, a proton rejection factor of about 10^5 can be obtained in selecting positrons and an electron rejection factor of about 10^5 can be obtained in antiproton measurements. The PAMELA calorimeter will be used also to measure the energy of the electrons and positrons with good resolution, independently from the tracker, allowing a cross calibration between the two methods. The procedures used to reconstruct the energy and perform the cross calibration is described in detail in chapters 4 and 5.

The operational principle of all the calorimeters is based on the measurement of the energy deposited by an incident particle interacting inside its volume. Thus, inside a calorimeter, particles have to interact and the energy lost by the interaction products has to be detected. In order to accomplish this task there are two different kinds of configurations: homogeneous and sampling calorimeters. Homogeneous calorimeters consist of only one kind of material, performing both tasks of energy degradation and signal generation. Sampling calorimeters are instead built alternating layers of absorber and active media. The absorber usually is made of a dense material, used to degrade fast the energy of the incident particle, while the active medium is used to measure the detectable sig-

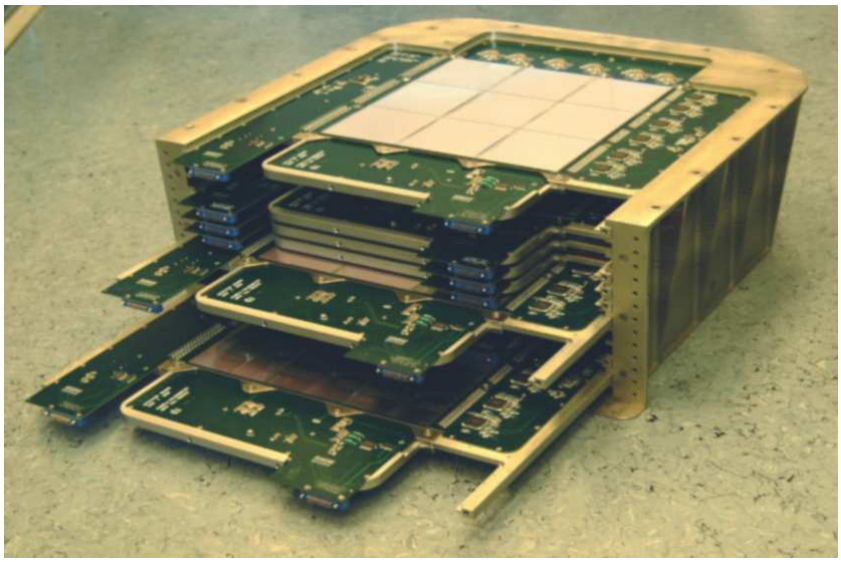

Figure 2.11: The electromagnetic imaging calorimeter, with some of the detecting modules partially inserted.

nal. In this way usually all the energy of the particles is released in the calorimeter volume with the use of a reasonable detector thickness. In space experiments there are strong constraints for mass and size, therefore for the PAMELA experiment a sampling calorimeter was designed. The calorimeter design took advantage of the experience acquired by the collaboration during the past years with other cosmic ray experiments like CAPRICE [41].
The choice of the materials and the design features were done in order to achieve the high identification performances necessary to the PAMELA physics goals. In order to maximize the identification capabilities, the calorimeter has to maximize the electromagnetic shower development while minimizing the probability of hadronic interactions. For this reason the choice of the absorber material has fallen on tungsten, a material with high Z and good mechanical properties.

The choice of silicon as sensitive material is due to several reasons, in particular for a calorimeter is important the fact that in silicon detectors the signal is collected in the form of electric charge, whose production

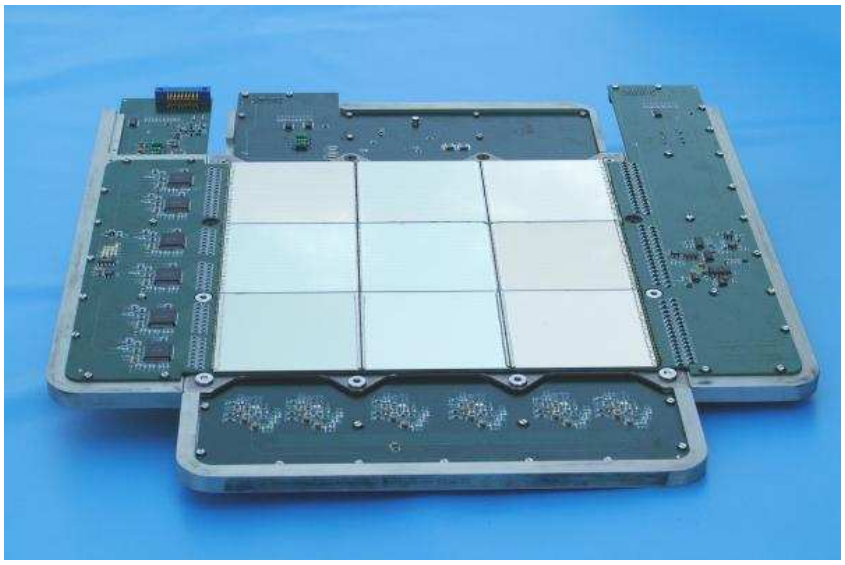

Figure 2.12: One of the calorimeter modules.

and collection is a linear process. Moreover they allow the construction of compact devices thanks to the high density.
The PAMELA calorimeter has a high granularity, both in the longitudinal (z) and in the transversal (x and y) directions. In the z direction, the granularity is determined by the thickness of the layers of the absorbing material; each tungsten layer has a thickness of 0.26 cm, which corresponds to 0.74 X_0, where X_0 is the radiation length. It is an useful quantity to describe calorimeter characteristics and represent the mean distance over which the electron energy is reduced by a factor $1/e$. The total depth is 16.3 X_0, since there are 22 layers of tungsten. Each tungsten layer is sandwiched between two layers of silicon detectors. The silicon detectors are arranged in a square matrix of 3×3 detectors. Since each silicon detector has a surface of 8×8 cm^2, the total sensitive area is 24×24 cm^2. The thickness of the silicon detectors is 380 μm and each one has 32 strips with 2.4 mm pitch. The two adjacent views of each plane have the strips oriented along orthogonal directions and therefore provide transversal spatial information . Each strip is connected to the corresponding ones belonging to the other two detectors of the plane

forming 24 cm long read-out strips. The number of electronics channel per plane is $32 \times 3 = 96$ and the total number of channels is $96 \times 44 = 4224$.

The mechanical structure is based on a modular concept. The basic unit consists of an absorber plate and the two matrices of silicon sensors segmented in opposite directions, i.e. the stratification of a single plane is Si-X/Tungsten/Si-Y. The basic unit contains also the front-end and part of the read-out electronics. Two detection planes form a detection module. In a module, the two detection planes are kept together by a frame to which they are bolted at the edge of the absorber plate. The 12 modules are independent and fully extractable; they are inserted like "drawers" in the main mechanical structure and then locked by a cover. In order to minimize the effect of the gaps present between the silicon detectors on the detection efficiency of non interacting particles, the planes of the calorimeters are not simply put one under another, but a different shift was introduced for the 4 planes forming a calorimeter module. In this way the detector efficiency for non interacting particles is enhanced, in fact, even if the particle passes through a gap in one plane, probably in the subsequent plane the particle passes through a sensitive area.

The current signal of the strips is acquired by CR-1.4 chips, based on a VLSI ASIC. The main design characteristics of this chip are the very large dynamic range (1400 $mips$[1]), the ability to cope with a very large (about 180 pF) detector capacitance, the good noise performance and the low power consumption (< 100 $mW/chip$). Each circuit has 16 channels and each channel comprises a charge sensitive preamplifier, a shaping amplifier, a sample-and-hold circuit and an output multiplexer. On each detector board, the 6 outputs of the chips are connected to a 16-bit ADC. On the read-out boards the collection and analysis of the events, prior to their transmission to the main CPU, is performed. The whole calorimeter is divided, from the point of view of the read-out, into four independent sections: x view odd, x view even, y view odd and y view even. For each section of the calorimeter there is a Digital Signal Processors, which reads and processes the data and controls the

[1] 1 mip is a unit of energy whose value is the mean energy loss by non interacting relativistic particles. For the silicon detectors of the PAMELA calorimeter it amounts to about 100 keV; in section 4.1 more detailed explanations will be given.

acquisition procedure.
The calorimeter will be also used in a self trigger mode to increase the geometric acceptance and to identify high energy electrons and photons. The total calorimeter mass, including electronics and cables, is 110 kg, its total volume is $24 \times 24 \times 18$ cm^3.

2.3.3 TOF scintillator system and S4

The TOF system [42] is composed of a set of scintillator detectors, positioned in the PAMELA apparatus at different heights, shown in figure 2.2. When they are crossed by a cosmic ray a fast pulses arises from the TOF scintillators. The timing information of these signals is used for different purposes. The principal one is the generation of the main trigger signal, which starts the acquisition procedure of the other detectors in PAMELA. The main trigger configurations for the experiment are explained later in section 3.1.1. An additional task of the TOF system is the ability to establish which direction the particle is coming from, by looking at the order in which the scintillators have been hit. This is of fundamental importance when trying to identify antiparticles in cosmic rays, since a particle entering the spectrometer from below (the so-called albedo particles) would mimic the behaviour of its own antiparticle coming from above In fact the sign of the magnetic deflection determines the sign of the charge only if the direction of motion is known, since above 1 GeV the energy loss is negligible and consequently the curvature is constant. Another task of this device consists in measuring the charge absolute value: it can be done in the same way as for the tracking system, by detecting the amount of ionization in the six scintillator layers. In this way the particle charge can be determined up to $Z = 8$.
At last the velocity of incoming particles can be calculated from the time which is needed by the cosmic ray to cover the distance between S1 and S3, the farthest scintillator planes. The value of β is connected to the

momentum and the mass of the particle by the following formula:

$$\beta = \frac{1}{\sqrt{1 + \left(\frac{m\ c^2}{p\ c}\right)^2}} \tag{2.6}$$

This feature can be used to mass resolve protons (antiprotons) from positrons (electrons) for momenta up to about 1 GeV/c.

The TOF system [42] (see figure 2.13) is composed of 3 double planes of plastic scintillator detectors, read-out by photomultiplier tubes: S1, positioned on top of the PAMELA apparatus, S2 and S3, immediately above and below the spectrometer respectively. The distance between S1 and S3 is 77.3 cm. The main requirement of the TOF detectors is the efficient production of output pulses characterized by short delays and small uncertainties with respect to the time of passage of the incident particle, thus achieving on one hand a quick generation of the trigger signal, and on the other hand an high resolution in the determination of the crossing times at each plane. For this reason a plastic scintillator material characterized by prompt response and relatively high light output has been selected and coupled to fast PMT tubes and front-end electronics. Each of the 3 planes S1, S2, S3 is formed by two superposed rectangular scintillator layers, thus having two independent timing measurements. The 6 layers, whose areas match the geometric acceptance window of the spectrometer, are divided into strips whose number and dimensions vary from layer to layer, for a total of 24 strips. At each of the two ends of a strip a light guide conveys the scintillation light toward the input window of a PMT, which transforms the light pulse into an electric current signal, which is then processed by the front-end electronics; a total of 48 PMT are present for the read-out of the 24 scintillator strips. The strips of the upper layer of each plane (S11, S21, S31) are orthogonal to the ones of the corresponding lower layer (S12, S22, S32 respectively), thus coupling to the timing information also a spatial information on the crossing point in the plane. The performances of the TOF system of PAMELA are characterized by a typical delay in the generation of the event signals toward the trigger board of the order of 10 ns and recent

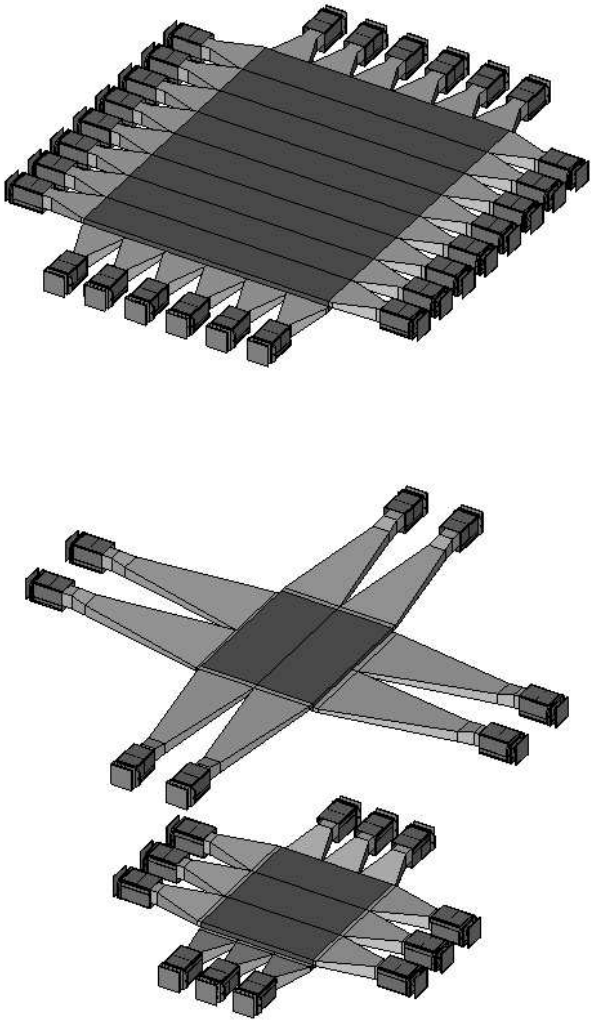

Figure 2.13: Drawing of the time-of-flight system: from top to bottom, the S1, S2 and S3 scintillator planes with their light guides and photomultipliers.

analyses of flight data [43] show an uncertainty in the determination of the instant of particle crossing on a plane of the order of $150 \div 200\ ps$.

Another separate plastic scintillator, not included in the time-of-flight measurement system, is placed directly below the calorimeter, S4 in figure 2.3. It is made of a single piece of polystyrene, with an area of 482 mm^3 and a thickness of 10 mm. Its light output is read by six photomultipliers and it is used to detect the charged component of the shower which can possibly escape the calorimeter in case of very high-energy incident particles. In this way this detector can improve the electron hadron separation performance of PAMELA. The main task of the bottom scintillator is to send the signal of the particles passing through it to the trigger system. It can be used, if required by the trigger configuration, for elaborating the main trigger pulse or, if its signal corresponds to more than 10 mip, it plays the role of trigger for the Neutron Detector

2.3.4 The anticoincidence system

When an event gives a signal which fulfills the TOF trigger conditions, this does not necessarily mean that it corresponds to a "good" event. In fact, particle interactions with the material around the instrument or with the instrument itself can occur, producing in the TOF scintillators signals which mimic a single down-going cosmic ray, some examples are shown in figure 2.14. Indeed, simulations [44] have shown that in space about 75% of triggers are actually expected to be "false", that is to say due to coincidental energy releases in the TOF scintillators by secondary particles generated by cosmic ray interactions in the mechanical structure of the experiment. In order to recognize this kind of events and to exclude them during the offline data analysis, PAMELA is equipped with an anticoincidence system [45]. The spectrometer is shielded from side-entering particles by four scintillator panels surrounding it (Side Anticoincidence Counters, CAS), which have an almost rectangular shape and an area of about $400 \times 388\ mm^2$, while a star-shaped panel with a rectangular opening of about $216 \times 180\ mm^2$ is placed on top of the magnet (Top Anticoincidence Counter, CAT) and is used to tag cosmic rays which enter from above but outside the cavity: in figure 2.15 one of

the side anticoincidence shields and the top one are shown.
Another set of four panels covers the sides of the particle entrance window between the S1 and S2 planes (CARD) as shown in Fig. 2.2.
The material which has been used for these detectors is Bicron BC-448M, and all of them are 8 mm thick. A Light-Emitting Diode (LED) system is used to calibrate and monitor the scintillator performances during flight. The information about whether a section of the anticoincidence detector is hit is recorded in a time window, 1.28 μs long, centered at the time when the trigger signal has been generated. The hit time can be located within this interval with an accuracy of about 80 ns.

2.3.5 The neutron detector

At the bottom of the whole PAMELA instrument a neutron detector is present, which is used to measure the neutron yield in case of hadron-initiated showers in the calorimeter, thus increasing its particle discrimination capabilities. Analysing beams of electrons and protons with energies $20 \div 180$ GeV produced at CERN it was demonstrated that the use of Neutron Detector increases the rejection factor of hadrons from electrons of about ten times [46].
The device is composed of 36 gas proportional tubes filled with ^3He and surrounded by a polyethylene moderator and by a cadmium foil. They are stacked in two planes and cover an area of about 600 mm^2 . The working principle of this detector exploits the properties of the hydrogen-rich polyethylene moderator to slow down neutrons till their energy is low enough for them to have a non-negligible capture cross section when interacting with the gaseous ^3He in the counters. In the nuclear reaction a proton and a ^3He nucleus are produced, and they can be detected as charged particles.

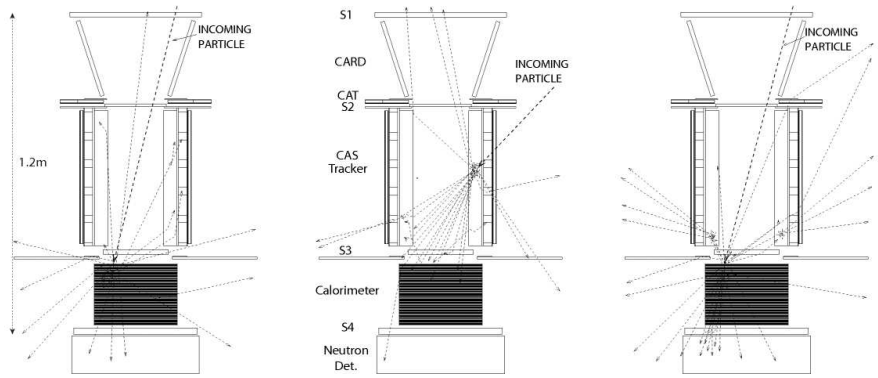

Figure 2.14: Simulation of proton interactions in the detectors. On the left, the incoming particle enters cleanly the acceptance of the instrument and crosses the three TOF planes generating a good trigger without activity in the anticoincidence scintillators; in the center, a cosmic ray enters the magnetic cavity from one side and gives rise to a shower of secondary particles that induce a false trigger: the signal in the side anticoincidence detector allows to reject this event. On the right a good trigger event gives rise to a signal in the anticoincidence detector due to particles backscattered from the calorimeter.

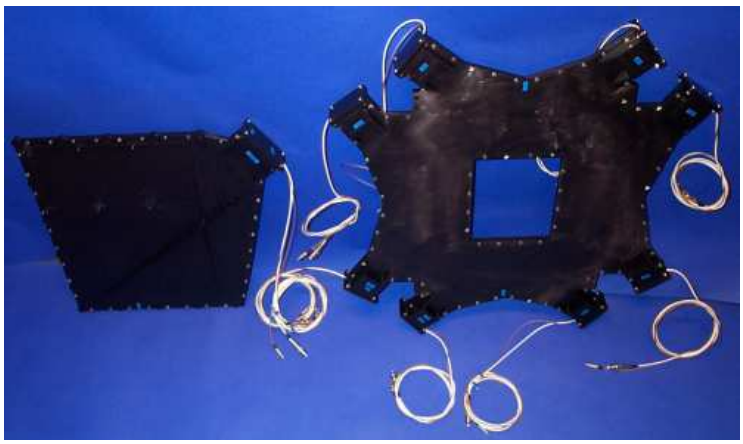

Figure 2.15: The anticoincidence system: one of the panels which surround the spectrometer is shown on the left, while the panel on top of it is shown on the right. The scintillators are enveloped in an opaque wrapping to prevent outside light from reaching them.

Figure 2.16: The neutron detector during the test and assembly phase. Some of the ^{3}He tubes, the polyethylene moderator and the electronic boards are visible.

Chapter 3

Data Acquisition and processing

In this chapter the procedures for the acquisition and reduction of PAMELA spectrometer and calorimeter data are described.
A short description of the acquisition procedure in flight is given, then the online analysis for both the instruments is presented. It consists in the compression of the data and the calibration of the detectors. In fact in both cases there is the need for compression of the data in flight due to the limited bandwidth available for the data transfer toward the Earth. It follows a description of the offline data reduction.
For this work the simulation has been used extensively, therefore at the end of the chapter the main features of the software aimed to simulate the PAMELA detectors are presented.

3.1 Acquisition and online operations

On June 21^{st} 2006 PAMELA has been switched on for the first time. During the first weeks several trigger and hardware configurations were tested and now the experiment is in a nearly continuous data taking mode since July 11^{th} 2006. Until 30^{th} August 2007 the total acquisition time has been $\sim 29.3 \cdot 10^6$ s, corresponding to about 340 days of continuous data taking. The amount of raw data collected is ~ 5.8 TB, corresponding to

more than $7 \cdot 10^8$ triggered event.

PAMELA data acquisition system is based on the PAMELA Storage and Control Unit (PSCU) which handles all in-flight operations, manages the data acquisition and continuously checks for correct operation of the apparatus. The PSCU is composed of a processor and two redundant 2 $GByte$ mass-memory modules, together with interface boards to subsystem and satellite. In case of abnormal conditions, the PSCU can perform an hardware reset of the whole system to recover the system functionalities. For instance, if the temperature conditions are not optimal, the PSCU can power down PAMELA until acceptable working conditions are reached.
The PSCU organizes the data acquisition in *runs*, defined as a continuous period of data taking with constant configurations of detectors and trigger. The detector configurations are defined by the PSCU according to parameters stored in the on-board memory or received from ground. The duration of a run is determined by the PSCU according to the orbital position. The orbital position also determines the trigger configuration, which is different if the satellite is located in high or low radiation environments. Switching between high and low radiation environments can be performed in different ways, usually it is determined fixing a threshold to the counting rate of the S1 scintillator, but it can be determined also according to a fixed time table provided from ground.
The orbital position is derived from the *ascending node* notification issued by the Resurs CPU when the satellite crosses the equator from the southern to the northern hemisphere. The control of the experiment from ground is performed via two different type of commands: *macrocommands*, which are sent to the PAMELA PSCU, and *telecommands*, which are commands sent to Resurs-DK1, handling main power lines. Hundreds of parameters are modifiable through macrocommands, for example the switching on and off of parts of the subdetectors and trigger configurations. Therefore the system is extremely flexible, being able to meet any unknown and unpredictable situation in flight.
During the entire PAMELA observational time some error conditions occurred, mainly attributable to anomalous conditions in the detector electronics. In each of those situations the PSCU was able to recover the

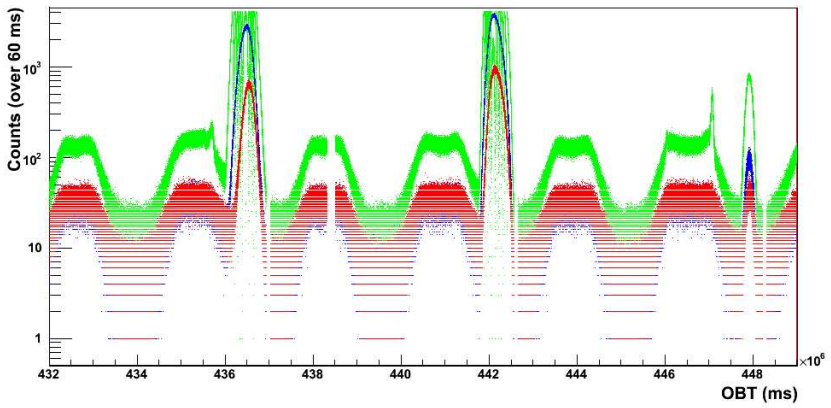

Figure 3.1: Counting rate of S1 (green), S2 (blu), S3 (red).

system functionality and continue the acquisition. The thermal profile of the instrument has been very stable and no power-off due to over-temperature occurred. Furthermore, no radiation dose effects have been observed in the PAMELA sub-detectors.

3.1.1 Trigger configuration

Two operational modes are foreseen for the operation of PAMELA in space, namely *physics mode* and *calibration mode*.
The experiment is in physics mode for a large fraction of the time. During this time the trigger configuration can be chosen among several trigger patterns, given by the OR combinations of the TOF signal, the S4 signal and the calorimeter self-trigger signal. There are 7 different TOF trigger patterns that can be used, obtained with different logical combination of the various scintillator planes, for a total of 31 possible trigger patterns.

A trigger signal is generated when a coincidence of energy deposits is measured in the detectors included in the trigger configuration. The main PAMELA trigger is provided by the TOF system. The following configurations are activated for low and high radiation environment, re-

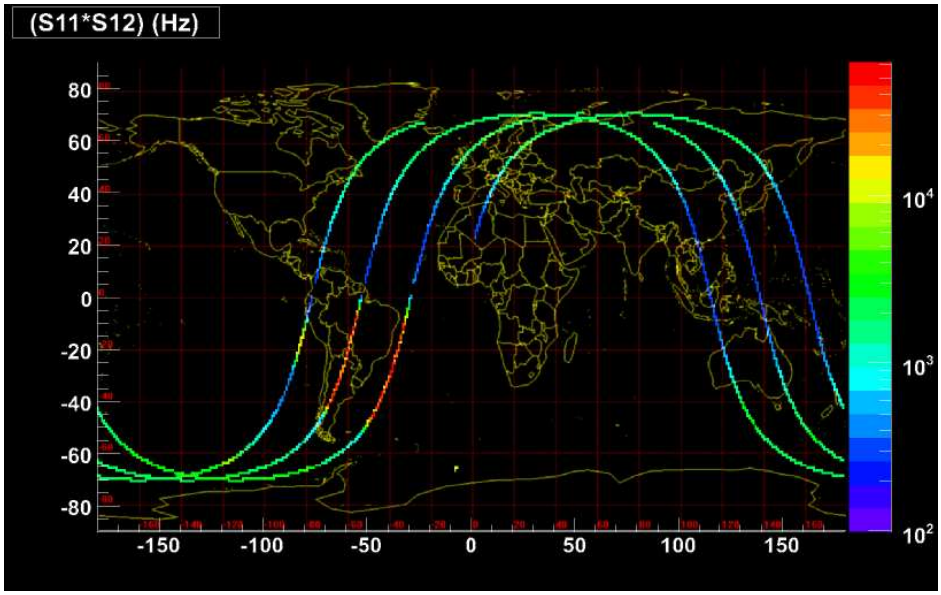

Figure 3.2: Counting rate in the first scintillator for three consecutive orbits (S11 AND S12).

spectively (see section 2.3.3 for the meaning of the symbols):

A : ($S11$ **OR** $S12$) **AND** ($S21$ **OR** $S22$) **AND** ($S31$ **OR** $S32$)
B : ($S21$ **AND** $S22$) **AND** ($S31$ **AND** $S32$)

These TOF conditions are normally used in OR with the calorimeter trigger signal. The TOF configuration B, used generally in high radiation regions, is chosen since the counting rate of the first plane of the TOF system could be saturated by the radiation environment, while S2 and S3 scintillators are more shielded, consequently they are not affected significantly by coincidental hits. This can be seen from the different counts of each scintillator shown in figure 3.1. In the same figure the strong dependence of the trigger rates from the orbital position is evident: the maxima in the counts correspond to passages over the North and South poles, while the minima correspond to the Equator. The sharp peaks are due to the passage close to the South Atlantic Anomaly (SAA), where

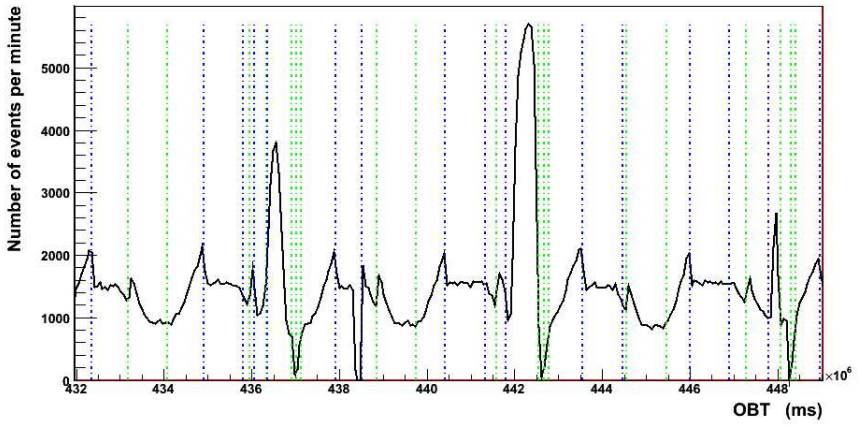

Figure 3.3: Trigger rate during a typical orbit of PAMELA. Mode A (blu) refers to high-radiation regions and it is typical for polar regions and SAA, while mode B (red) holds for low radiation regions like the equator. The calibration is done at every ascending node.

the S1 counter is saturated. Figure 3.2 shows the counting rate in S1 scintillators for three consecutive orbits. It can be noticed that along the orbit the satellite spans different latitudes where the radiation environment is much different: the particle rate increases in the polar regions and in correspondence of the SAA.

The trigger rate along three consecutive orbits is shown in figure 3.3. It is interesting to notice the change of the trigger configuration that happens at each vertical lines. The average trigger rate of the experiment is $\sim 25\ Hz$, varying from $\sim 20\ Hz$ at the equatorial region to $\sim 30\ Hz$ at the poles. In figure 3.4 the PAMELA trigger rate summed over hundreds of orbits is shown, the SAA due to the inner proton radiation belt closer to the earth surface, is clearly seen.

The dead time of the experiment depends on the time needed to read-out the detectors, mainly the calorimeter and the tracker. It is not constant, varies from 10 ms to 50 ms, but depends on the read-out mode (raw or compressed) and on the number of hit strips. In the regions where the particle rate is very intense, such as in the SAA, the trigger rate is fully

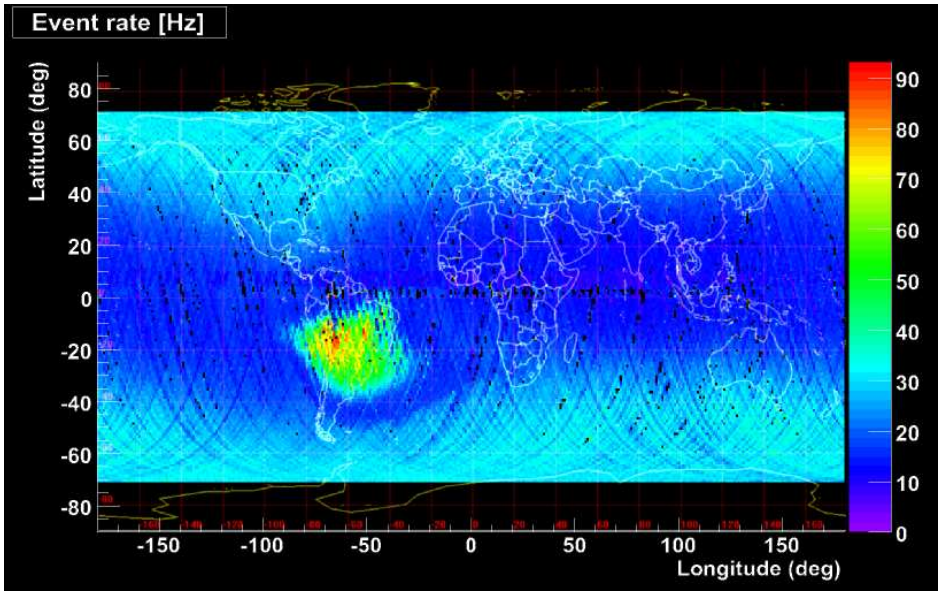

Figure 3.4: Map of the PAMELA trigger rate summed over hundreds of orbits. The colour along the orbit lines is proportional to the rate intensity, as indicated by the palette on the right. The South Atlantic Anomaly is clearly seen.

determined by the dead time. The average fractional live time of the experiment exceeds 70%.
Once for each orbit, every 95 minutes, soon after the ascending node which is the point of lowest trigger rate, physics data acquisition is stopped and PAMELA is set to calibration mode. Also the frequency of calibrations can be modified from ground if it is necessary. The detectors are calibrated sequentially and independently. The calibration procedure for most detectors uses trigger signals generated by a pulse generator, not related to physical particles traversing the apparatus.
The average trigger rate of the experiment is about 25 Hz, as shown in figure 3.3, which means about 100 *Gbyte* for each day. However the experiment is designed to have a typical transfer rate of 10 *Gbyte* per day, as a consequence a data compression procedure has been adopted for the calorimeter and for the spectrometer.

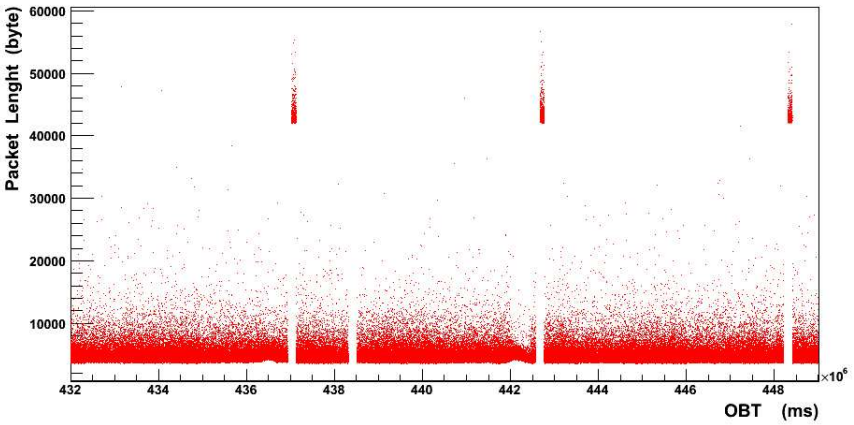

Figure 3.5: Length of the transmitted packets. Physics run are in compressed mode while special run after calibration have bigger size of the packet because the acquisition of the tracker is in full mode.

After each calibration procedure, which takes about 1 minute, a special short acquisition run is performed. While during physics mode the data are compressed, during these special runs the acquisition of the tracker is in raw mode, therefore the amount of data to be transferred is bigger. This can be seen in figure 3.5.

When a trigger is detected, the subdetectors are read out via an appropriate interface. The operation is handled by an Intermediate Data Acquisition System (IDAQ), which sequentially requests information from each of the subdetectors. Data are first stored into then the PAMELA mass memory, then transferred to the satellite on-board memory (download) where they are stored prior to be transmitted to ground (downlink). Downlinked data are received at the ground station in NTsOMZ [47], the Research Centre for Earth Operative Monitoring, located in Moscow, which receives data at a transmission rate of 150 $Mbit/s$. Several downlink windows of about 5-10 minutes are dedicated every day to the PAMELA experiment, which allow to transfer to ground up to 16 $GByte/day$.

Once received at the ground station, data are processed in almost real time to provide information on the engineering and scientific status of the apparatus. Data are then transferred via the GRID network from Moscow to the INFN facility at CNAF (Bologna, Italy), where scientific data analysis is performed, and are accessible to all the people of the PAMELA collaboration.

3.2 Spectrometer data acquisition and reduction

In this section the procedures for the data acquisition and reduction of PAMELA spectrometer are presented. In the following I will describe some of the main aspects of the acquisition procedure, the characteristics of the spectrometer data and their compression algorithm, as well as the calibration procedure performed during data taking. Also the first part of the offline data reduction is presented. The software that has been developed for the offline analysis consists in several routines, coded in FORTRAN, C and C++ languages, which allow to elaborate data coming from the silicon detectors and to extract from them the spatial information about the particle impact points, from which the value of the magnetic deflection of particles is deduced.

3.2.1 The compression algorithm

The spectrometer, with its 36864 electronic channels, is the detector producing the largest output, therefore a data compression is required. The algorithm has to work as quick as possible because it must perform an analysis in flight without increase too much the dead time. The compression is performed by using a software [48] based on a ZOP (Zero-Order Predictor) algorithm, modified to include a peak-identification method. It has been shown during tests with particle beams that this technique allows to obtain a compression factor of about 95%, without any worsening in spatial and momentum resolution.
The ADC value of each strip j belonging to the k-th VA1 chip can be

expressed, for each event i, as the result of the sum of the following contributions:

$$ADC^i_{j,k} = PED_{j,k} + CN^i_k + N^i_{j,k} + S^i_{j,k} \tag{3.1}$$

The true meaningful *signal* induced by the charge produced by a cosmic ray crossing the silicon sensor is indicated as $S^i_{j,k}$. When no particle signal is present, the voltage value $ADC^i_{j,k}$ has a mean represented by $PED_{j,k}$, which is called the *pedestal*. It is a base level which is determined by the characteristics of the detector electronics and it is different for each channel. The pedestal values are almost constant in time and are estimated periodically during online calibration procedures.
In equation 3.1 CN^i_k represents the fluctuation around the pedestal due to the common noise of all the 128 strips of the k-th VA1 at the i-th event. This noise source is equal for all the strips connected to a single VA1 chip, and for this reason it is referred to as *common noise*. Finally $N^i_{j,k}$ is the noise signal due to the electronics and it is uncorrelated to the fluctuations of the others. The standard deviation $\sigma_{j,k}$ of $N^i_{j,k}$ represents the intrinsic noise of the channel j.
When data are acquired in compressed mode, not all the ADC values are stored. For each one of the ladders of the tracking-system planes the value of the first strip is always transmitted, and the decision on whether a following one has to be stored or not is taken on the basis of the variable $C_j = ADC_j - PED_j$, according to the intrinsic noise of the strip. In order to allow the offline event reconstruction we need to know the position of the strips corresponding to the transmitted values. For this purpose the necessary addresses of the strips are transmitted together with the ADC values. Although this compression algorithm is not reversible, since it does not allow to recover the original values of all the strips, but some part of the information is unavoidably lost, the procedure has been optimized in order to do not worsen the spatial resolution and the detection efficiency of the silicon sensors.

3.2.2 Online calibration procedures

The information that is needed during the compression process, namely pedestal and intrinsic noise for each strip, is computed *online* by the DSP software. This is done periodically in the course of the mission when all detectors are calibrated. In fact $PED_{j,k}$ and $\sigma_{j,k}$ for a strip are not strictly constant in time, and periodic calculations of these quantities ensure that proper values are employed in the compression algorithm. The calibration parameters are estimated online by acquiring a set of events, by means of an artificial trigger signal generated by the PSCU. If no particle signal is collected $S^i_{j,k}$ is zero and the pedestal of the generic j-th strip of the k-th VA1 chip can be computed using iteratively equation 3.1 as the average of the ADC counts, after the common noise contribution has been subtracted:

$$PED_{j,k} \;=\; \sum_{i=1}^{N_{ev}} \frac{ADC^i_{j,k} - CN^i_k}{N_{ev}} \,. \tag{3.2}$$

Once the pedestals are known, the common noise of each of the VA1 can be obtained for the i-th event as:

$$CN^i_k \;=\; \sum_{j=1}^{128} \frac{ADC^i_{j,k} \;-\; PED_{j,k}}{128} \,, \tag{3.3}$$

where the sum extends over the 128 strips connected to the k-th chip. Finally the intrinsic noise of each strip is given by:

$$\sigma_{j,k} \;=\; \sqrt{\frac{1}{N_{ev}-1} \sum_{i=1}^{N_{ev}} \Big(ADC^i_{j,k} - CN^i_k - PED_{j,k} \Big)^2} \,, \tag{3.4}$$

since it represents the standard deviation of the signal of each channel around its base level. These quantities are calculated iteratively, first evaluating pedestals from equation 3.2 under the initial assumption $CN^i_k = 0$, then using equation 3.3 to determine the common noise for each event. For each event strips that collected a particle signal are identified and removed from the common noise computation, since they would bias

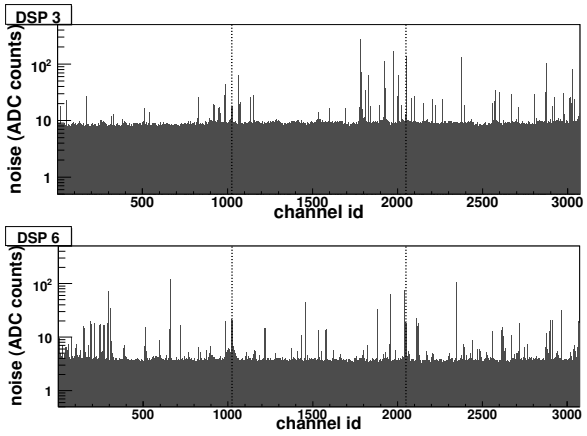

Figure 3.6: Noise profiles for a Y view (DSP 3) and an X view (DSP 6).

it. At each step $\sigma_{j,k}$ is computed from equation 3.4, and strips are classified according to their intrinsic noise: those having a noise more than 5 standard deviations away from the average value calculated for each VA1 chip are labeled as *bad* and they are not considered in the calculations. This procedure is repeated iteratively to get better estimates for the calibration parameters and further strips are marked for exclusion. The final values of pedestals and intrinsic noise, as well as the complete map of bad strips, which typically amount to less than 5% of the total in each ladder, are obtained after repeating the process 8 times on a set of $N_{ev} = 128$ events. In figure 3.6 the noise profile of two planes of the spectrometer are shown. The typical value of σ is about 4 ADC channels for the x side and 9 for the y side, the difference is attributable mainly to the different biasing resistances for the junction and ohmic sides and by the increased capacitance on the ohmic one, also due to the double metalization.

At the end of each calibration these values are stored in the DSP and used to compress data for the acquisition runs which follow. In this way each data set is uniquely associated with a calibration, whose parameters are downlinked to ground, since they are required for uncompressing and for extracting particle signals. If for some reason the calibration procedure fails a standard set of calibration parameters, which have been

stored in dedicated non-volatile solid-state memories, are loaded into the DSP and used instead, in order to be able to compress and transmit data in any case.

3.2.3 Offline signal analysis

The data downlinked from the satellite are analyzed offline. The spectrometer data are extracted and analyzed by dedicated routines which distinguish between calibration and particle runs. The maps of pedestals, intrinsic noise values and bad strips are extracted from calibration packets and stored to be used later to identify clusters. The contents of the acquisition runs are instead unpacked and to each run of data the appropriate set of calibration parameters is associated. In this way the next stage of the reduction process, the uncompression of data, is performed rebuilding for each event the ADC profile of all the 12 detector sides of the tracking system according to the corresponding calibration parameters.

Cluster identification

Once the ADC value of each channel have been reconstructed, the signal analysis can start, in order to isolate the contribution due to the passage of ionizing particles across the sensors. The signal can be obtained from equation 3.1, as:

$$S^i_{j,k} = \pm(ADC^i_{j,k} - PED_{j,k} - CN^i_k) \tag{3.5}$$

the minus sign is applied on the x (junction) side of the silicon sensor, where the signal has opposite sign, since electrons are collected, while on the y (ohmic) sides holes are collected. The common noise for each event is computed again, as it is done during the online calibration phase. After the subtraction of common noise and pedestal the search of the particle signal can start. A *cluster* is defined as a group of contiguous strips that have collected particle signals for a given event. The identification is done on the basis of the signal-to-noise ratio of each channel, by looking

for those strips whose signal is significantly larger than the fluctuations due to intrinsic noise. If a strip satisfies the condition:

$$S^i_{j,k} > C_{seed} \cdot \sigma_{j,k} \tag{3.6}$$

with $C_{seed} = 7$ for the junction side and $C_{seed} = 6$ for the ohmic side, it is classified as the *seed* of a cluster, which is closely related to the cosmic ray impact point. If several consecutive strips pass the seed condition, the one with the maximum signal is chosen. Adjacent strips on both sides of the seed are scanned to check if they pass a similar cut:

$$S^i_{j,k} > C_{incl} \cdot \sigma_{j,k} \tag{3.7}$$

but with a lower threshold $C_{incl} = 4$, and, if so, they are included in the cluster. The values of the cuts have been optimized according to the characteristics of the detectors, by means of several tests on particle beams which have been performed during the preparation of the experiment. The number of strips which pass the inclusion cuts given by equation 3.7 and 3.6, defines the *multiplicity* of the cluster, a quantity related to the way the ionization charge is shared among the different strips involved in the process, and which depends on the implantation pitch, on the thickness of the sensor with respect to the incidence angle of particles and on the capacitive couplings among the strips. For most of the events in PAMELA the multiplicity is 2 for the clusters belonging to the X side and 1 for those of the Y side, due to the larger pitch.

After a cluster has been identified and its multiplicity has been determined, the sum of the signal of all the strips included in the cluster can be calculated. The total signal is a quantity which depends on the energy lost by ionizing particles. To estimate the (dE/dx) we calculate the ratio between the signal of the cluster and the track length in the silicon, which depends on the inclination of the track. The average values obtained with a sample of flight data, normalized to *mip* units, is shown in figure 3.7. The behaviour follows the Bethe Block formula as expected, the (dE/dx) is related to the absolute value of the charge and we can see that elements up to $Z = 5$ can be distinguished. For heavier particles the signal saturates due to the limited dynamical range of the

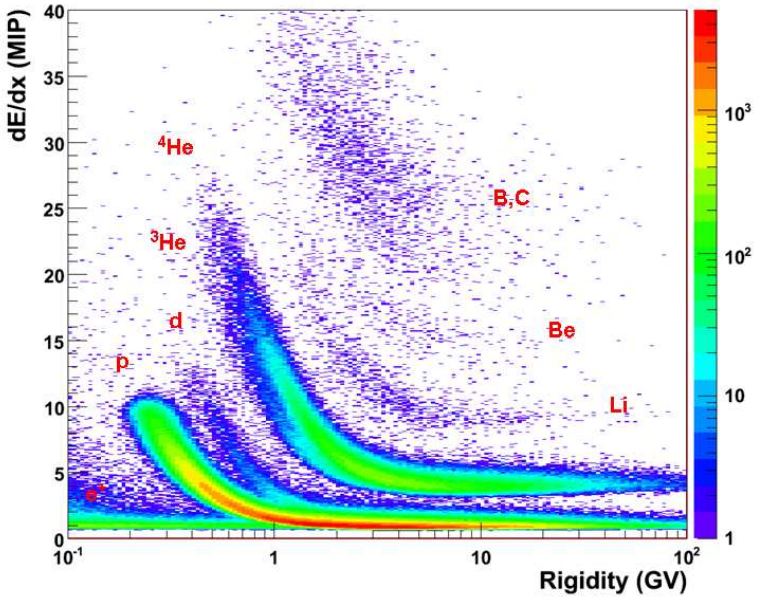

Figure 3.7: Distribution of the mean rate of energy loss in the silicon sensors of tracking system as a function of the tracker measured rigidity.

tracker silicon detectors.

The signal-to-noise ratio of a cluster composed by m strips is evaluated as [58]:

$$(S/N)_{cl} = \sum_{i=1}^{m} \frac{S_i}{\sigma_i}\,, \tag{3.8}$$

This parameter is important since higher values correspond to a better spatial resolution. The distribution of the signal-to-noise ratio is shown in figure 3.8; it can be seen that as expected it is bigger for the x view. At the end of this reduction stage all the quantities related to clusters are stored in data structures which will be used as the starting point for the calculation of the coordinates to be associated to the particle impact points on the tracking system planes.

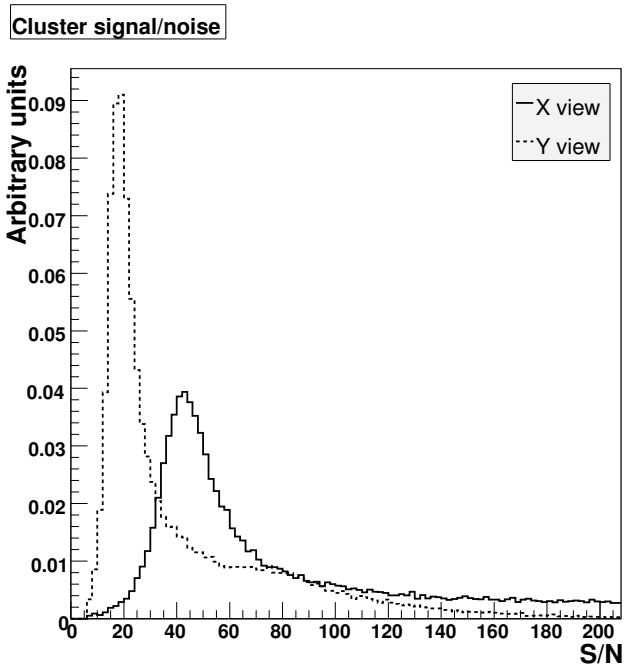

Figure 3.8: Distribution of cluster signal-to-noise ratio for one plane of the tracking system.

Impact-point reconstruction

Before being able to reconstruct the track each cluster has to be associated to a measure of the coordinate of the impact point on the side of the sensor it belongs to. Different position finding algorithms have been developed in order to reconstruct properly the coordinates. The most intuitive approach to such problem consists in associating to the impact point the *center-of-gravity* of the cluster:

$$x_{cog} \;=\; \frac{\sum_{i=1}^{m} S_i \; x_i}{\sum_{i=1}^{m} S_i} \;, \tag{3.9}$$

where m is the cluster multiplicity, x_i the mean of the coordinate of the strip i and S_i its respective signals. In the case of PAMELA the multiplicity is often 1 or 2 and it is convenient to restrict the sum in

equation 3.9 to the two strips with the largest signal in the cluster. Since the noise is about the same for all the channels, if those that have collected a too low signal are excluded, the spatial resolution improves. The method of the two-strip center of gravity gives a good estimate of the true impact point, but only to a certain approximation. In fact, it can be demonstrated [50] that an error is introduced in the reconstructed impact point due to the non-linear effects that occur in the division of the signal among the strips. A method that allows to take into account of this problem is the so-called *non-linear η_2-algorithm* [49].
This approach to the coordinate reconstruction problem provides the best spatial resolution for the sensors of the tracking system of PAMELA, at least in case of particles which hit silicon orthogonally or with not too large angles. In fact, when the incidence angle relative to the vertical direction increases, a larger number of strips may be involved in the charge collection. Therefore the spatial resolution of the detector can be improved if the information carried by further channels is employed: in particular the non-linear η_2-algorithm can be modified in such a way to use 3 or 4 strips. In case of η_3 the strips used are the cluster seed and the two strips on both its sides, in case of η_4 the couple of strips used to compute η_2 and their first neighbours. The detector resolution has been studied for different incidence angles [52], and the procedure which has been chosen as the most satisfactory for the reconstruction of the x coordinate of the impact point consists in using the η_2-algorithm for incidence angles lower than 10°, η_3-algorithm between 10° and 15°, and η_4-algorithm between 15° and 20°, which is the maximum angle on the spectrometer sensors for tracks in the tracker acceptance. In this way the resolution which is achieved in the determination of the x coordinate of the particle in the bending view is lower than 3 μm up to 5° of incidence angles, and lower than 8 μm for larger angles. For the y side the standard η_2-algorithm gives satisfactory results in the whole 0° – 20° range, since the larger implantation pitch causes the charge to be nearly always collected by one or two strips (about 97% of the cases), and a resolution between 8 and 14 μm is obtained. The algorithms have been calibrated with cosmic ray data gathered at ground level in 2005, and a further calibration have been repeated during the flight.

Recently it has been found that a systematic effect arises when the η algorithm is applied to non orthogonal tracks. In this case in fact the asymmetry of the charge packet generated by ionization can result in a shift of the reconstructed impact point in respect to the true one. Reference [53] describes the problem and suggests possible solutions. This kind of correction has been recently implemented [54] and is used together with the appropriate η-algorithm.
However in this study it was very important to avoid systematic errors and, even if the resolution is worse, the standard algorithm of center-of-gravity calculated with four strips was used. With this algorithm a resolution of about 4 μm is obtained with tracks up to 10° of incidence angle [52] and no systematic shifts are present [53].
The physical quantity that we can obtain analyzing the spectrometer information is the value of the rigidity of charged particles passing through the apparatus. It can be obtained using the coordinates of the impact points with a procedure described later in chapter 5.

3.3 Calorimeter data acquisition and reduction

Due to the limitation on the maximum amount of data that the PAMELA experiment can transfer to ground, a compression algorithm has to be applied also to the calorimeter data to reduce the event size. For the calorimeter compression algorithm a standard *zero-suppression* technique is employed: only the signals of those strips with an ADC value that exceed a fixed threshold are stored, along with addressing information. Although this algorithm is good when applied to detectors generating sparse data, its efficiency is reduced in the calorimeters because electromagnetic and hadronic interactions show an energy deposit in several contiguous strips on each layer. An improvement is obtained by grouping the channels and applying the compression only when less than half of the strip detect energy. As already explained for the spectrometer calibration also in this case the calibration parameters are estimated online by acquiring a set of events with an artificial trigger signal generated by

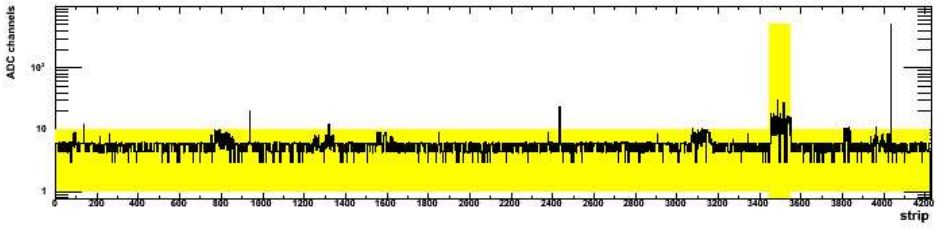

Figure 3.9: Intrinsic noise measured in each one of the calorimeter strip during one of the calibration performed in flight. The yellow region is the range of normal expected value. It can be seen a peak in the strips $3456 - 3552$ due to the presence of a particularly noisy plane (plane number 36).

the PSCU, through a calibration procedure which is performed in several steps with increasing accuracy. These value are used to compress the data of the following acquisition runs. In figure 3.9 the noise profile in each one of the calorimeter strip acquired during one of the calibration performed in flight is shown, typical values are about $3 \div 4$ ADC counts.

3.3.1 Offline signal analysis

The calorimeter information provides a three-dimensional image of the interactions, that can be obtained after decompressing the raw data. The signal collected by each strip of the calorimeter, expressed in ADC values, is obtained from the voltage value read on each strip. This value has to be corrected for the gain factor, which in principle can be different for each channel. Since the front-end preamplifier has a linear response to input signals, a known constant signal can be used in order to determine the gain of each channel. The energy lost by a minimum ionizing particle is a perfect candidate for this purpose, because the most probable value of its distribution is constant (see section 4.1). Moreover a large number of minimum ionizing particles can be found in cosmic rays. Figure 3.10 shows the distribution of signals, in ADC units, collected by a single strip, obtained for a sample of non interacting protons in the range $5 \div 150$ GeV selected from flight data. The gain factor for each channel is

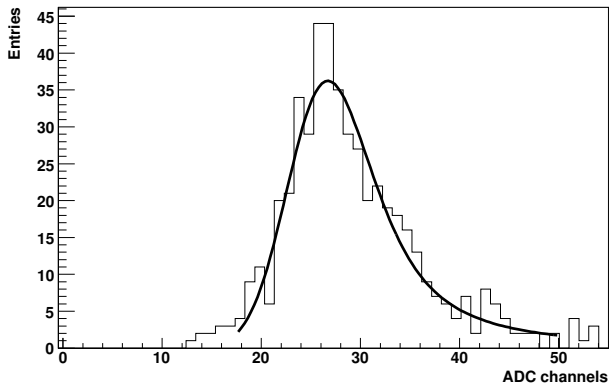

Figure 3.10: Distribution of the charge collected in one of the calorimeter strip for a sample of relativistic protons selected from flight data.

derived from the peak of the experimental distribution of the signal. The fit of the distribution is performed with a Landau function convoluted with a Gaussian function. In fact the energy lost by a relativistic particle in a very thin medium is described by a Landau function but the rise of the distribution up to the maximum is well described with a Gaussian function, which takes into account the electronic noise.
Typical values for the position of the peak are about 25 ADC counts. Considering the values of the noise found from calibrations (see figure 3.9), the resulting signal-to-noise ratio for minimum ionizing particle has a mean value of about 8, showing the good performances of detectors, preamplifiers and analog to digital converter.
The values of the gain factors derived with this procedure are used to normalize the signals detected by each strip to *mip units*. It is important to point out that the values used to perform the conversion from ADC to mip units is not the value of the average charge deposited by a minimum ionizing particle, but is the most probable value of the charge deposited on a single strip. This quantity has been used since it is easy to estimate, being a peak, and allow us to correct the calorimeter image of the shower for the different gains of each strip.

The calorimeter information are then used mainly for two task: reconstruct the energy of electrons and positrons generating electromagnetic showers in the calorimeter and discriminate hadrons from leptons. The explanation of the analyses used for these aims will be given in chapter 4 and 5 respectively.

3.4 Simulation

As usually happens in particle experiments, all the analyses has to be checked with a detailed simulation of the apparatus. For the PAMELA experiment a dedicated Monte Carlo code has been developed to simulate the whole payload geometry, together with the response of all the detectors. This code is based on the *Geant* package [55] version 3.21, which is widely used in particle physics applications. The *Geant* package, whose name is an acronym formed from "GEometry ANd Tracking", provides routines to simulate different kinds of particles and physical processes, particle kinematic, geometrical and physical characteristic of detectors. Furthermore it can be interfaced with other simulation packages such as GHEISHA or FLUKA to simulate hadronic interactions with the nuclei of the traversed matter. The magnetic field in the PAMELA experiment is simulated using the same map of the field employed in the analysis of the experimental data. The simulation of charge diffusion and collection by the strips of the tracker has been performed with a dedicated package [52] interfaced to *Geant*.
The simulation procedure consists in the tracking of every secondary particle, produced by a primary particle interacting with the medium, until a minimum energy is reached.
During the tracking many physical processes in the energy range from 10 keV to 10 TeV are considered in a very accurate way. For example cross sections of electromagnetic interactions are reproduced in *Geant* within a few percent up to a hundred GeV. Concerning hadronic interactions, the range of validity is the one of the hadronic packages used.
The results of the simulation depend critically on the choice of the tracking medium parameters, for example the maximum length of a tracking step, or the maximum number of step allowed or the maximum fractional

energy loss in one step. These parameters can be calculated automatically by the program for each material which compose the detector.
The simulation of a given process is done in the following way:

- the program evaluates the probability of occurrence of the process, depending on the energy and the nature of the particle, by sampling the total cross section;
- the final state after an interaction is generated by sampling the differential cross section of the process;
- to account for continuous processes, such as energy losses or multiple scattering, the mean values of characteristic quantities are computed;
- in case new particles are created, they are followed by the program in the subsequent passages.

The *Geant* structure allows many different choices regarding the kind of interaction with matter that has to be used for any different purposes. In this study electron and positron simulation and the calorimeter information have been extensively used, and special care had to be taken in order to simulate properly electron interactions in the calorimeter. For this reason the detailed description of the calorimeter simulation is presented in the following.

3.4.1 Calorimeter simulation

The control of physics processes is performed using some variables that can be set from the user. In table 3.1 there is a list of the physical processes that can be simulated, together with the value of a control variable set for the PAMELA calorimeter simulation. If the value of the control variable is 0 the process is completely ignored, if it is 1 the process is considered and all the possible secondary particles generated in the interaction are recorded and separately traced later, while if it is 2 the process is simulated but secondary particle are not generated. In case of hadronic interaction the value 4 has been set to specify that an

processes	value
Positron annihilation	1
Bremsstrahlung	1
Cerenkov photon generation	0
Compton scattering	1
Decay in flight	1
Ionization and δ-rays production	1
Hadronic interactions	4
Light absorption	0
Continuous energy loss	1
Multiple scattering (Moliere theory)	1
Muon-nucleus interaction	1
Photon pair production	1
Photoelectric effect	1
Rayleigh effect	0
Synchrotron radiation generation	0

Table 3.1: List of simulated physical processes.

external hadronic package has to be used: for this study GEISHA has been used.

Most of the physical processes that are simulated have some kinetic energy cuts. For example photons produced as secondaries in the interactions are simulated until their energy is above a certain threshold. When their energy reaches the minimum value the tracking stops and all the energy is released in that point. In table 3.2 there is a list of the kinetic energy cuts for the different particles. Different values of the parameter can be set depending on the material where the tracking is performed, in this way one can avoid to spoil to much computation effort in simulating detailed processes in all the materials.

The kinetic energy cuts of secondaries are very important to reproduce the real behaviour of the detectors, especially for a sampling calorimeter. In fact, when a shower develops through the sampling calorimeter simulated for PAMELA, only the energy released in the silicon planes is detected. A kinetic energy cut too high causes the stopping of some

description	default(GeV)	used(GeV)
gammmas	0.001	0.00001
electrons	0.001	0.00001
neutral hadrons	0.01	0.01
charged hadrons	0.01	0.01
muons	0.01	0.00001
electron Bremsstrahlung	0.001	0.00001
muon/hadron Bremsstrahlung	0.001	0.00001
δ-rays by electrons	10^4	0.00001
δ-rays by muons	10^4	0.00001
direct pair production by muons	0.01	0.01

Table 3.2: Kinetic energy cuts.

particles before they can reach the sensitive layer. In fact if the particle reaches the threshold energy when is located in the passive material all the energy is released in that point, and consequently it is lost. On the contrary in the real calorimeter the particle could have continued its propagation until a silicon detecting plane and the total energy measured for the same incident energy would be bigger compared to simulation. Since the simulation has to be used to develop a method for energy reconstruction from the PAMELA calorimeter information, a realistic simulation of the secondaries produced in the shower is needed. For this purpose the best choice is to set low kinetic thresholds. The numerical values are listed in the table 3.2.

The output of a simulation based on *Geant* is the energy deposited in the sensitive layers, expressed in GeV. In order to analyze the simulated events with the same reduction chain used for flight data, the simulation output has to be expressed in the same format of the real data. Consequently a dedicated software has been developed to transform the *Geant* output in the same format of flight data. For what concern the calorimeter, the signal of each strip has to be expressed in ADC units, taking into account the expected noise and the pedestals. In order to determine the conversion factor from GeV to ADC counts a sample of protons was

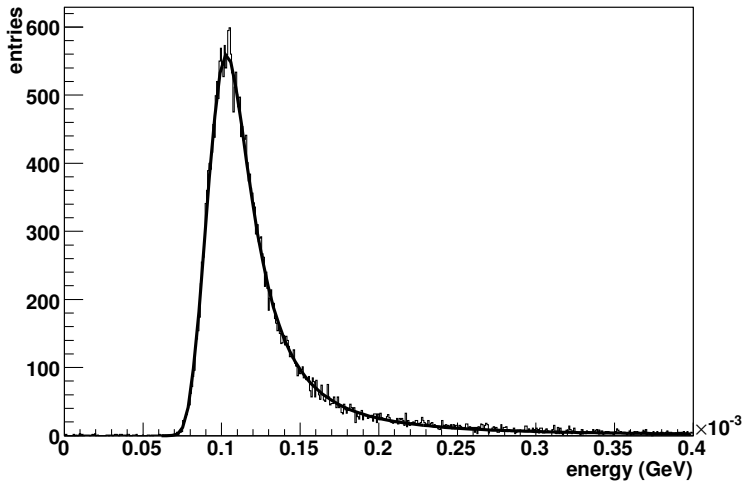

Figure 3.11: Distribution of the energy lost in a calorimeter strip by a sample of relativistic non interacting protons. The energy value is in GeV and is obtained as the output of *Geant* simulation package.

simulated according to cosmic ray spectrum. Figure 3.11 shows the distribution of the energy collected in each strip. As expected, we see a non Gaussian tail due to the fluctuations of energy loss in thin materials; the fit is performed with a Gaussian convoluted with a Landau function and the peak is located at about 103 keV. This value represents one mip unit, as defined in section 3.3.1. Then the conversion from GeV to ADC counts is performed taking into account the measured gain factor G of each strip determined from calorimeter calibrations:

$$S(ADC) = G(ADC/mip) \cdot \frac{1\ mip}{103\ keV} \cdot S_{Geant}(GeV) \tag{3.10}$$

The calorimeter simulation has been used, as explained in chapter 4, to develop and test a procedure to measure the energy of primary electrons and positrons.

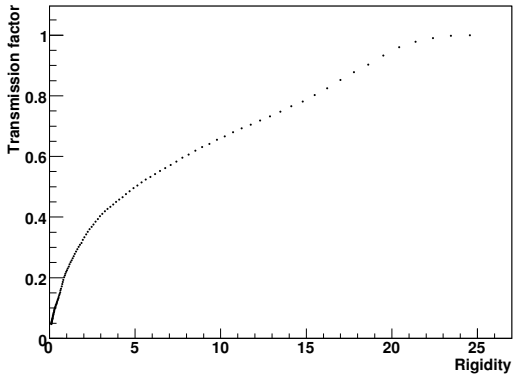

Figure 3.12: Geomagnetic transmission factor used to simulate the cosmic rays fluxes. It has been determined analysing flight data [57].

3.4.2 Description of simulated events

In order to calibrate the instrument and check the analysis code, simulated events have been employed. We simulated electrons and positrons inside the PAMELA detector both with monochromatic and cosmic ray spectrum. The acceptance of the experiment is simulated defining a large square placed above the instrument and generating particles from there with fixed z coordinate, uniform in x and y coordinate and isotropic (uniform in ϕ and in $cos^2\theta$). The electrons momenta are sampled from the following distribution [56]:

$$f = A \cdot \left[\frac{p}{GeV/c} + B\right]^{-\alpha} \cdot \left(\frac{p}{GeV/c}\right)^{\alpha-\gamma} \tag{3.11}$$

$$A = 478. \quad B = 0.71 \quad \alpha = 6.72 \quad \gamma = 3.29$$

In order to reproduce the effect of the geomagnetic cut-off a tabulated transmission factor in function of rigidity, showed in figure 3.12, was applied to the flux expressed by equation 3.11. In order to minimize the time needed to perform the simulation the approach used was to preselect the events in this way: the events generated are tracked inside

the spectrometer with the initial momentum and coordinates, then only those events which cross all the tracker planes are selected.
Some simulation have been performed with a different approach to generate the initial position and momentum of the simulated particles. It consists in using the real data spectrum, after having extrapolated the state vector of each selected event till the top of the payload in order to obtain the initial positions and momentum to be simulated. This procedure has been applied to both electrons and positrons and has been used when it was very important to reproduce a sample comparable with the real data. In chapter 5 this procedure will be explained better.

Chapter 4

Energy reconstruction

The main purpose of the PAMELA calorimeter is the particle identification, namely it should be able to identify the signals of antiprotons and positrons in the vast background of electrons and protons with an efficiency of at least 90% *and a rejection power better that* 10^{-4}. *The calorimeter can also be used to measure the energy of the electrons with good resolution.*
For the PAMELA experiment an electromagnetic sampling calorimeter has been chosen, where the sensitive layers are silicon detectors while the absorbing material is tungsten. Sampling calorimeters are also called "imaging" because of the longitudinal and transverse segmentation. This feature allows to take advantage of the image of the showers development. As we will see through this chapter the knowledge of the shower topology can be used not only to perform particle identification but also to improve the reconstruction of the energy of electrons and positrons.
A brief review of the interaction processes of particles in the calorimeters is presented in section 4.1. Hence the problems related to the reconstruction of the energy of electrons and positrons, as well as the approach used to overcome these problems, are discussed in section 4.2. In section 4.3 and 4.4 there is the description of the calibration of the calorimeter, together with its expected performances determined by means of simulation studies. Finally the cuts to be used to select a good sample of reconstructed electrons and positrons, for alignment purposes, are discussed.

4.1 Particle interactions in the PAMELA calorimeter

Particles can interact electromagnetically with matter in different ways depending on their nature and energy. Charged particles passing through matter lose energy by ionizing and exciting the atoms through inelastic collisions with atomic electrons. In addition they can lose energy by emitting photons when decelerating in the electric field of a nucleus, through the so-called radiation losses. The total energy loss can thus be written as:

$$\left(\frac{dE}{dx}\right)_{tot} = \left(\frac{dE}{dx}\right)_{coll} + \left(\frac{dE}{dx}\right)_{rad} \tag{4.1}$$

The last term in the above equation is due to the so called Bremsstrahlung process. The radiative term is a characteristic of all charged particles, but for particles heavier than electrons its probability is very low and starts to be important only at very high energy. For this reason the discussion for heavy particles is focused only on ionization losses. Hadrons can also interact with different mechanisms in hadronic collision with the material nuclei. The main interaction processes for different kinds of particles will be described in the following.

Interactions of heavy charged particle

At the energies we are interested in, the dominant process through which heavy charged particles lose energy into matter is ionization, due to the interaction with the electrons in the medium. The mean differential energy loss for heavy particles can be described by the well known Bethe-Block [59] formula as a function of his velocity β:

$$-\frac{dE}{dx} = kz^2\frac{Z}{A}\frac{1}{\beta^2}\left[\frac{1}{2}\ln\frac{2m_e c^2\beta^2\gamma^2 T_{max}}{I^2} - \beta^2 - \frac{\delta}{2}\right] \tag{4.2}$$

$$k = 4\pi N_A r_e^2 m_e c^2$$

The parameters, ρ, Z, and A are, respectively, the density, atomic number and atomic weight of the absorber, $I \simeq 16 \cdot Z^{0.9}$ is its effective ionization

potential and δ is a function that takes into account the density effect, z is the charge of the projectile, m_e is the electron mass. T_{max} is the maximum kinetic energy transferred to an electron of the absorber in a single collision:

$$T_{max} = \frac{2m_e c^2 \beta^2 \gamma^2}{1 + 2\gamma m_e/M + (m_e/M)^2} \tag{4.3}$$

The energy loss decreases rapidly for increasing energy, reaching a minimum at $\beta\gamma \sim 3$; when the energy rises further the energy loss increases slowly for $\beta \to 1$, due to the so-called relativistic rise. For solid media the relativistic rise is limited by the density effect δ, therefore for $\beta \gtrsim 0.97$ the energy loss can be considered approximately constant: particles with energy in this zone are called minimum ionizing particles.
In a sampling device only the energy released in the active layers can be detected. If particles do not produce showers in the calorimeter, this energy is directly related to the energy lost by ionization. The choice of silicon detectors as active layers in PAMELA calorimeter is due to the high efficiency and ionization yield, the low voltage operation and a good time stability. The mechanism exploited by these detectors is the production of electron-hole pairs due to the ionization loss of charged particles traversing the silicon; the pairs produced drift very fast (10^6 cm/s) across the depletion zone due to the electric field and a signal is detected. The energy required in silicon to create an electron-hole pair is only 3.6 eV. The mean energy deposited by a minimum ionizing particle in the silicon detector of PAMELA calorimeter, 380 μm thick, is about 108 keV, so 30000 electron-hole pairs are created on average by these particles: this means that it is not necessary a large gain in the preamplifiers to measure the ionization signal, it is another advantage of using silicon detectors.
Using such a kind of detectors it has to be pointed out that equation 4.2 is not exact, due to the presence of δ-rays: secondary electrons produced by the primary interaction with enough energy to ionize in turn. In fact, being the sensors very thin, part of the δ-rays can escape from the sensitive volume without releasing their energy. Therefore the energy loss can be rewritten in term of a maximum energy $T_{cut} < T_{max}$, such that

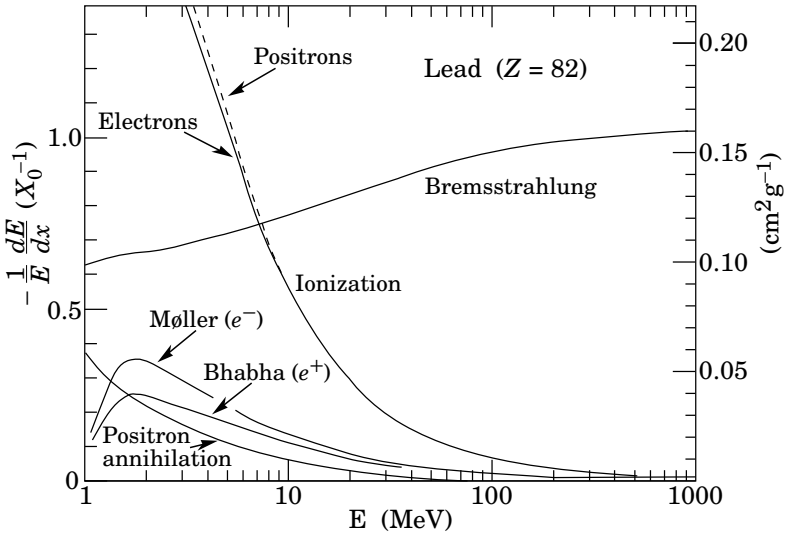

Figure 4.1: Mean energy loss in Lead as a function of particle energy. Main interactions with matter involving electrons and positrons.

secondaries with energies greater than T_{cut} will not be detected:

$$-\frac{dE}{dx} = kz^2\frac{Z}{A}\frac{1}{\beta^2}\left[\frac{1}{2}\ln\frac{2m_e c^2\beta^2\gamma^2 T_{cut}}{I^2} - \frac{\beta^2}{2}\left(1+\frac{T_{cut}}{T_{max}}\right) - \frac{\delta}{2}\right] \quad (4.4)$$

The use of a thin sensor has another important consequence: the distribution of the energy deposited in a medium of thickness δx, $(dE/dx)\delta x$, is not Gaussian as it is for larger δx. This happens because in a thinner medium the energy loss is the result of a small number of collisions, each with a wide range of possible energy transfer, which implies big fluctuations toward high values of energy loss. This feature has to be taken into consideration in order to calibrate the detectors with mip particles, as it was explained in section 3.3.1.

Interactions of electrons and positrons

Also electrons and positrons lose energy by ionization. However the ionization process cannot be described with the Bethe-Bloch formula (equa-

tions 4.2,4.4). In fact, due to the small mass of electrons and positrons, it cannot be assumed that the incident particle remains undeflected during collisions and the maximum energy transfer becomes $T_{max} = T_e/2$, since collisions occur between particles of identical mass. The formula becomes:

$$\frac{dE}{dx} = 2\pi N \frac{Z}{A} r_e^2 mc^2 \left[\ln \frac{\pi^2 m^2 c^4}{I^2(1-\beta)^3} - a \right] \tag{4.5}$$

where $a = 2.9$ for electrons and 3.6 for positrons. Anyway the ionization loss is important only at very low energies. In fact, as it is clear from figure 4.1, when the energy is greater than a certain critical value, radiation losses become more and more important. When a charged particle passes through the electric field of a nucleus its trajectory is deflected and a photon is emitted, this effect is called Bremsstrahlung process.
A useful quantity to describe the Bremsstrahlung process is the radiation length X_0, usually expressed in g/cm^2, which represent the mean distance over which the electron energy is reduced by a factor $1/e$. The value of X_0 depends on the medium in which the electron propagates through its atomic number Z and atomic mass A, it can be expressed according to Rossi [60] as:

$$X_0 = \frac{716.4 \cdot A[1 + 0.12(Z/82)^2]}{Z(Z+1)\ln(183Z^{-1/3})} \tag{4.6}$$

Expressing the thickness t of the traversed medium in units of X_0 it can be shown that, for relativistic electrons, the average rate of energy loss is given by [60]:

$$-\frac{1}{E}\frac{dE}{dt} = \frac{X_0}{E}\frac{dE}{dx} = 1 + \frac{1}{18\ln(183Z^{-1/3})} \qquad t = \frac{x}{X_0} \tag{4.7}$$

The photon emission probability by a particle of mass M, decelerating in the electric field of a nucleus with atomic number Z, is proportional to Z^2/M^2, as a consequence this process is important for low mass particles already at a few tens of MeV, while for charged particles heavier than electrons, for example muons, radiation processes are negligible for energies lower than 100 GeV.

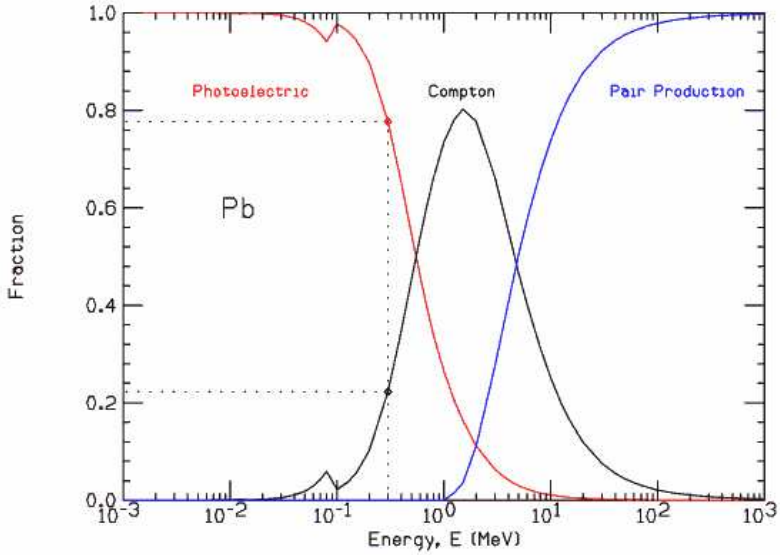

Figure 4.2: Relative contribution of photon interaction with matter as a function of photons energies.

For electrons and positron we can define a critical energy, E_c, at which the radiation losses equal the collision losses; a good approximation of this quantity, valid in solid materials, is [59]:

$$E_c \sim \frac{610\ MeV}{Z + 1.24} \tag{4.8}$$

In order to reach the high identification performances necessary to the PAMELA physics goals, the calorimeter has been designed to maximize the electromagnetic shower development; the choice for the absorber has fallen on tungsten ($Z = 74$), which has a critical energy $E_c \sim 8.1\ MeV$.

Photon interactions

The processes of interaction with matter involving photons are different depending on their energy, as shown in figure 4.2.
At low energy the most important process is the so called photoelectric

effect: it happens when a photon is completely absorbed by an atom with the emission of an electron. This process prevails against the other processes only at energies lower than 1 MeV, being its cross section inversely proportional to the photon energy.
The next process is the Compton effect that consists in the scattering of an incident photon with an atomic electron. It can be shown that, in material of high Z, this is the dominant effect for energies lower than 100 MeV.
At higher energies the most important process that contributes to the photon interaction with matter is the so called pair production induced by the electric field of a nucleus or an atomic electron: in this mechanism of energy transfer the photon undergoes strong field effects and may convert in a positive and negative electron pair. The mean free path of a photon due to this process can be described by $L_{rad} \sim (9/7)X_0$, where X_0 is the radiation length already defined for Bremsstrahlung process, therefore its probability is connected to the material properties in the same way.

Electromagnetic showers

When the photons created by electrons and positrons due to Bremsstrahlung process interact with matter their energy is such that they usually generate electron positron pairs or produce Compton electrons. These new electrons can radiate more photons that produce other electrons in a multiplicative process called cascade shower. This multiplication proceeds until the ionization losses of the secondary particles start to dominate the radiation, dissipating all their energy in excitation and ionization of atoms. All the processes discussed so far contribute to the development of electromagnetic shower induced by e^+/e^- and photons. A qualitative description of the produced cascade is the one showed graphically in figure 4.3. This simplified model assumes that each electron (or positron) in the shower, when traversing one radiation length of material, produces a Bremsstrahlung photon that takes half of its energy. In turn each photon, traversing one radiation length, disappears producing an electron positron pair, each one carrying half of the photon energy. Hence, after

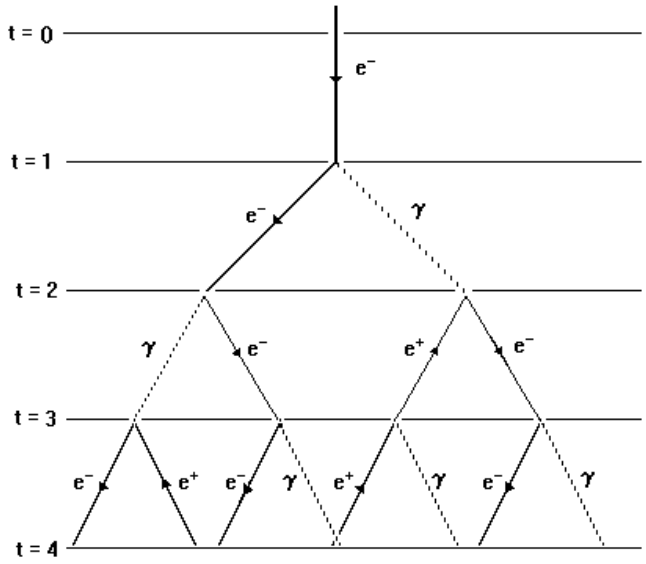

Figure 4.3: The simplified electromagnetic cascade model to describe the shower development. Values of t represent the depth in successive radiation lengths.

a depth nX_0, an electron with initial energy E_0 has produced $N = 2^n$ secondaries, of energy $E = E_0/N$ each. When the energy of the secondaries reaches the critical value below which the collision loss prevails, the cascade stops its multiplication and the number of particles starts to decrease. The maximum number of particles will be $N_{max} = E_0/E_c$, reached after $n_{max} = \frac{\ln(E_0/E_c)}{\ln 2}$ radiation lengths. This model is obviously simplified, but can help to understand some properties of electromagnetic showers that are valid even in more detailed descriptions. In particular it demonstrates the most important features of electromagnetic showers generated by particles of original energy E_0: the number of particles at the maximum of the shower is proportional to E_0 and the location of the shower maximum changes logarithmically with E_0.

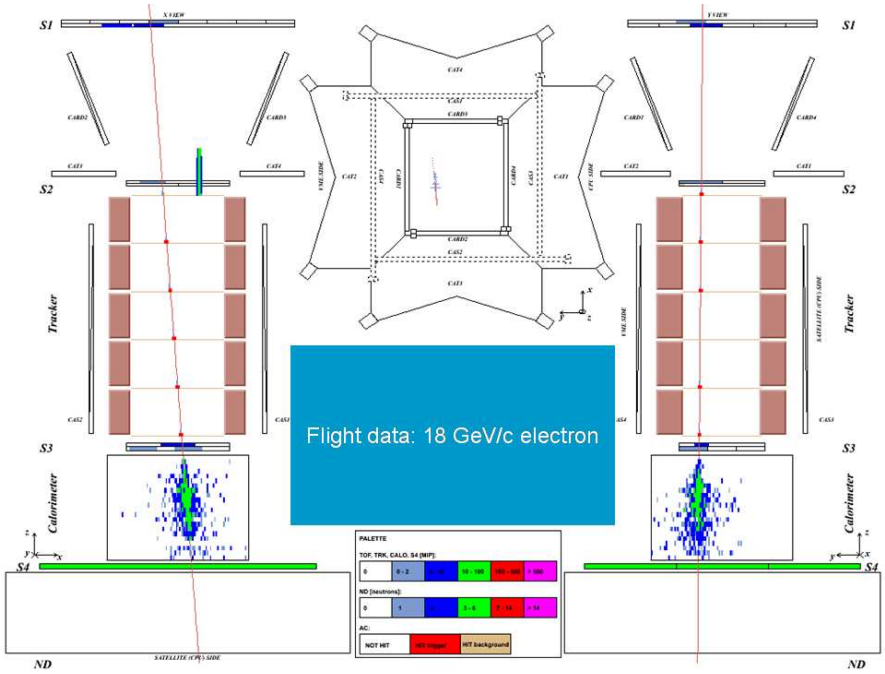

Figure 4.4: Electron selected from flight data with rigidity $-18\ GeV/c$.

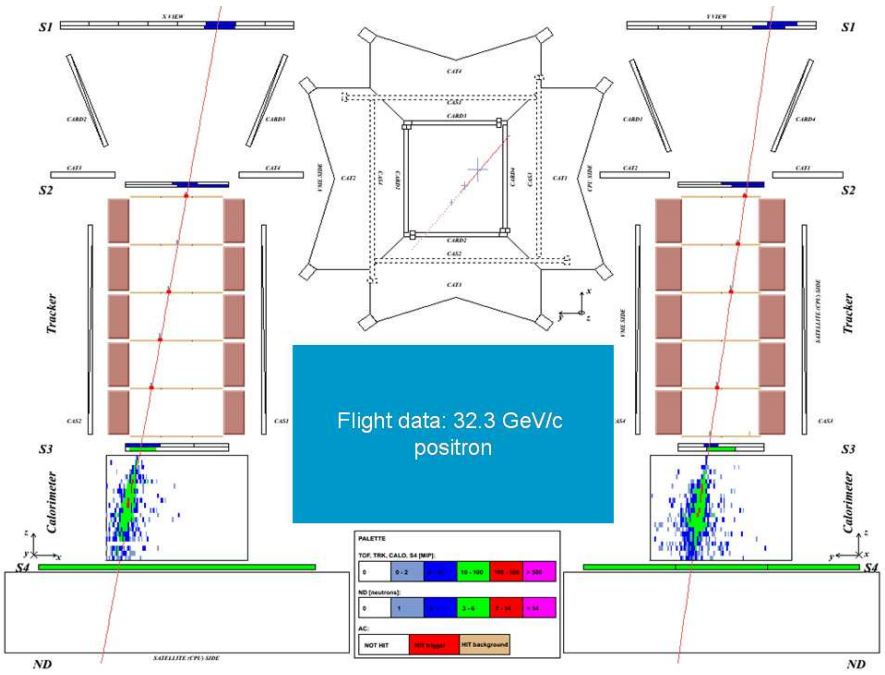

Figure 4.5: Positron selected from flight data with rigidity 32.3 GeV/c.

A more detailed description of the longitudinal development is for instance that of "Rossi's approximation B"[60]. From his model it follows that, for shower induced by e^+/e^-, the maximum of the shower is approximately located at:

$$T_{max} \simeq 1.01 \left(\ln \frac{E_0}{E_c} - b \right) \tag{4.9}$$

where $b = 1$ for electrons and $b = 0.5$ for positrons, and the maximum is in unit of X_0. It can be shown also that on average the cascade deposits 98% of its energy within a length[61]:

$$T_{98\%} \sim T_{max} + 13.6 \cdot X_0 \tag{4.10}$$

Regarding the lateral development, about 99% of the shower energy is contained inside a cylinder of radius 3.5 R_M, where:

$$R_M \sim \frac{21\ MeV\ X_0}{E_c} \tag{4.11}$$

is a useful quantity called Moliere radius.
As already said the PAMELA calorimeter has a total depth of $16.3X_0$, thus in many cases some of the shower energy will be lost because the particles of the cascade exit from the bottom of the calorimeter, in this case we say that the shower is not completely contained or that there is longitudinal leakage.
Even at energies lower than 10 GeV, where the shower is mostly contained according to formula 4.10, we should check event by event if the containment is satisfactory because the electromagnetic shower development is a process with great statistical fluctuations and often the shower maximum falls quite far from the expected value.
At last it can be noticed that, in the case of the PAMELA calorimeter, the Moliere radius is $\sim 9\ mm$, that is equivalent to 4 strips, thus the shower is usually well contained laterally.
In figures 4.4 and 4.5 there are two examples of showers developing in the PAMELA calorimeter initiated by electrons and positrons selected from flight data. The 18^{th} silicon plane of the x view is not functioning,

it is visible in the left picture of figure 4.5.

The longitudinal shower profiles and their lateral development in various media have been studied extensively both experimentally and through simulation. A detailed analytical description of the longitudinal development has been used in this work in order to reconstruct the energy of electrons with calorimeter information, as it will be shown in the following section 4.3.1.

Hadronic interactions

Also hadronic particles can interact with a nucleus of the traversed medium generating a shower. However, differently from electromagnetic showers, no simple analytic description of the cascade is available for its development. In fact the cascade is the result of different inelastic nuclear reactions which give rise to a shower with large fluctuations in energy loss and particle production from cascade to cascade. Usually a great part of the energy is carried by one or more particles travelling along the direction of the primary particle, while the rest of the energy is distributed among the secondaries, which are produced with an average transverse momentum of $\sim 350\ MeV/c$. The consequence is that the hadronic shower tends to be more spread out laterally than the electromagnetic one. The secondary particles produced in the hadronic interactions are pions, protons and neutrons with large emission angles. On average about 30% of the incident energy is released as electromagnetic energy; in fact, at an incident energy of 10 GeV, a considerable part of the secondaries are neutral pions, which decay in two photons ($\pi^0 \rightarrow \gamma\gamma$) which in turn induce electromagnetic showers. A non negligible amount of the initial energy is converted into excitation or break-up of the medium nuclei, of which only a fraction will result in detectable energy, while the binding energy used to break-up the nuclei and the energy carried by neutrinos are lost. The non visible energy amounts to about 20% of the incoming particle energy.

From what said till now it is clear that the measurement of the energy of interacting hadrons cannot be done efficiently with the calorimeter, nonetheless a description of the longitudinal shower development is useful for discrimination purpose.

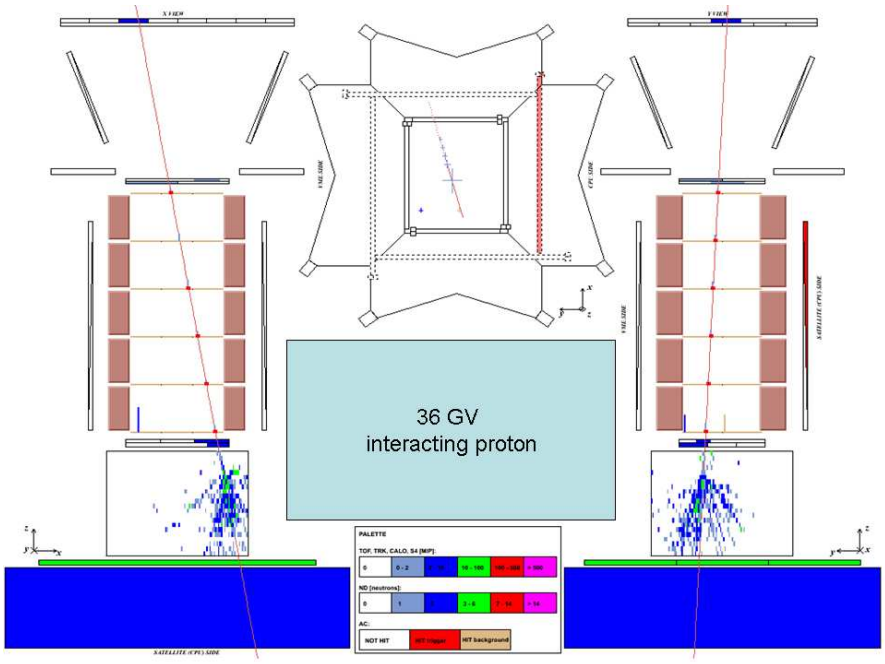

Figure 4.6: Proton selected from flight data with rigidity 36 GeV/c.

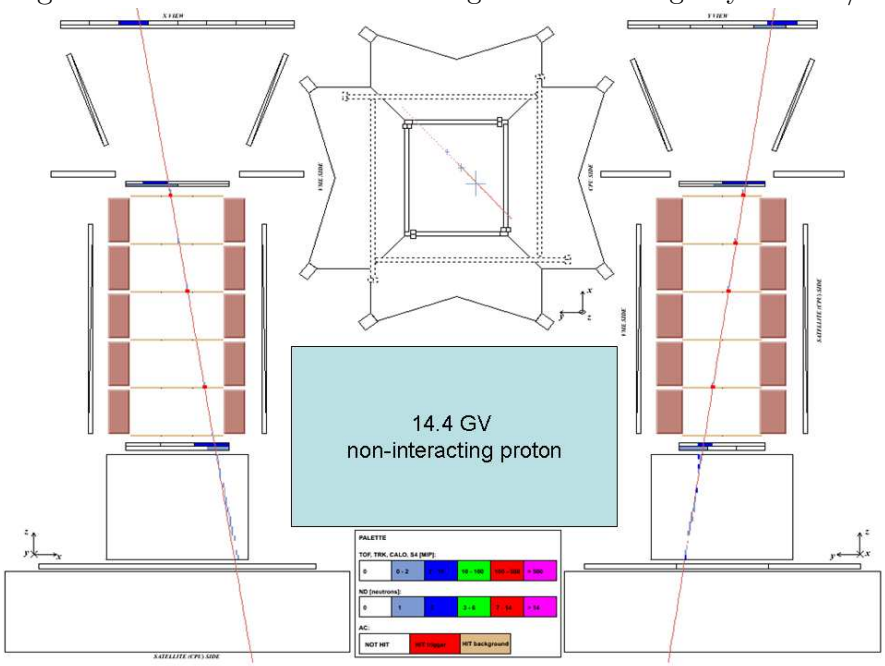

Figure 4.7: Proton selected from flight data with rigidity 14.4 GeV/c.

The probability of an inelastic hadron-nucleus interaction in a length dx of the traversed medium is given by $n\sigma dx$, where n is the number of nuclei per unit volume in the material and σ is the cross section for inelastic reactions. Consequently we can define a unit length that characterizes the longitudinal development of an hadronic cascade, as already done for electromagnetic showers. This quantity is called nuclear absorption length and can be expressed very roughly by [59]:

$$\lambda_0 = \frac{1}{n\sigma} \simeq 35\ A^{1/3}\ g/cm^2 \tag{4.12}$$

It is practically independent on the energy and the type of interacting particle, while it depends on the atomic weight A of the medium. When an hadronic interaction takes place, the longitudinal profile of the shower rises fast in the early phase due to the electromagnetic component, reaching a maximum, in unit of λ_0, at [59]:

$$T_{max} \sim 0.2 \cdot \ln E(GeV) + 0.7 \tag{4.13}$$

After the maximum the cascade is dominated by the hadronic component and the profile decreases slowly with a weak energy dependence. The longitudinal development is described by the attenuation length, λ_{att}, and the containment of 95% of the shower can be approximated by [61]:

$$L(95\%) \sim T_{max} + 2.5\lambda_{att} \qquad \lambda_{att} \sim \lambda_0 \cdot [E(GeV)]^{0.13} \tag{4.14}$$

The lateral profile of hadronic shower increases almost linearly with the longitudinal depth; there is a central core close to the shower axis which decays quickly, and a peripheral component, caused by the large emission angle of the secondary particles, which brings a large fraction of the energy away from the axis. On average about 95% of the shower energy is contained in a cylinder of radius $R = \lambda_0$.

For the PAMELA calorimeter the requirement is to minimize the probability of hadronic interaction, in order to optimize its identification performances, thus a suitable material for the absorber should be one with high Z. The absorption length in tungsten is $\lambda_0 \sim 10.3\ cm$; since the PAMELA calorimeter has a total thickness of 5.72 cm of tungsten,

its value is such that the whole calorimeter represents only $\sim 0.6\lambda_0$. This means that in many cases hadrons will not interact.
In figures 4.6 and 4.7 there are two examples of interacting and non interacting protons in the PAMELA calorimeter. It is evident that in case of interacting hadron the shape of the shower is quite different from that of the electron showers (compare with figures 4.4 and 4.5). This topological feature is used to discriminate electrons and positrons from hadrons. Moreover in case of hadronic interactions neutrons can be produced. An example is visible in figure 4.6 where the Neutron Detector box is blue having detected some neutrons.

4.2 Electrons and positrons energy reconstruction

The energy of the primary electron or positron[1], which generate an electromagnetic shower, can be determined by a measurement of the energy lost by the particles of the cascade produced in the calorimeter. In homogeneous calorimeters the energy of a fully contained particle is given by the total deposited energy, and consequently an excellent energy resolution can be achieved. On the contrary with sampling calorimeters it is possible to measure only the energy lost in the active layers. This has the consequence that the energy resolution of sampling calorimeters is in general worse than that of homogeneous calorimeter, owing to the sampling fluctuations produced by the absorber layers interleaved with the active layers. On the other hand sampling calorimeters have usually a better spatial resolution because they can be easily segmented both in longitudinal and radial directions. Another advantage of sampling calorimeters is that they provide enough interaction lengths with a reasonable detector thickness, so that a good shower containment can be obtained with a small apparatus, which is needed for space missions.

Nevertheless, if the response of the detector is linear with the energy loss, a linear relation can be obtained between the energy of the primary

[1]In the following of this chapter the term "electrons" will be used to indicate both electrons and positrons, otherwise it will be explicitly remarked.

particle and the charge collected in the calorimeter active layers. The linearity follows from the fact that the instrument measures the ionization loss in the silicon detectors produced by the secondaries, and that their number is proportional to the initial energy. It has to be noticed that, even if the linearity is valid, most of the energy is lost in the passive layers and this energy vary statistically from event to event, leading to the so-called sampling fluctuations, which have considerable influence on the energy resolution. Moreover this linear relation holds only if the whole shower is contained inside the calorimeter, both longitudinally and laterally. In the following it will be shown that this condition is not always satisfied in the case of PAMELA calorimeter and some corrections have to be done in order to maintain the linear relation for each event, otherwise, for some of the events, the total charge collected in the calorimeter and consequently the reconstructed energy is underestimated. In order to reconstruct the energy of electrons a calibration of the calorimeter has to be performed: it implies converting the output of the electronic channels of the calorimeter, that is a digital signal in ADC counts, to the energy of the primary particle. The calibration can be divided in two different steps. First of all one has to relate the signal of each strip with the energy lost by charged particles; this implies the knowledge of the gain factor of each calorimeter channel and has already been treated in section 3.3.1. Once performed this conversion, we know the amount of energy deposited by a particle traversing the calorimeter on each strip expressed in mip units. In case of interacting particles the sum of the charge collected by all the channels, treated in the correct way, can be related to the primary energy by means of a second step of calibration.

4.2.1 The leakage problem

The most important problem to be addressed, in order to reconstruct the energy of electrons and positrons by means of calorimeter information, is the leakage of the showers out of the PAMELA calorimeter. A useful way to understand the effect of the energy leakage is to analyze simulated events.
Figure 4.8 shows the distribution of the total charge, Q_{tot}, detected in

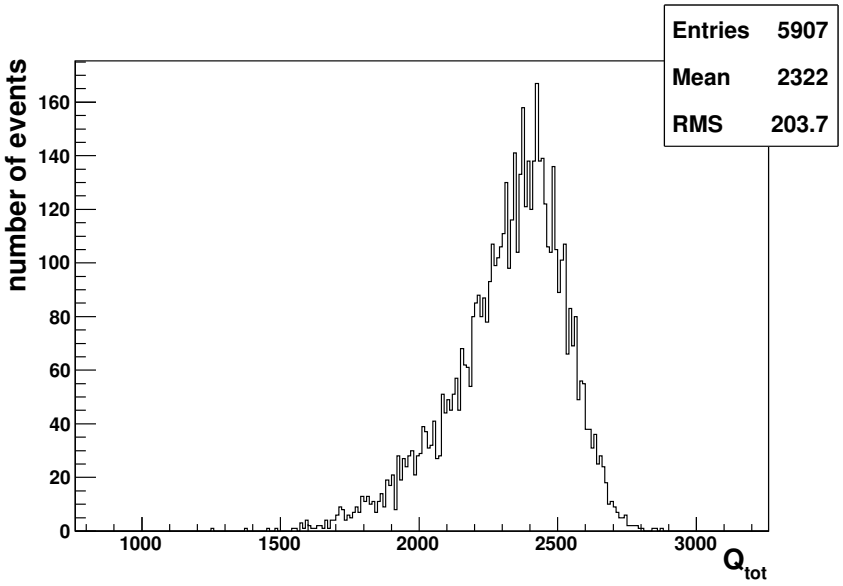

Figure 4.8: Distribution of the total charge collected in the calorimeter (in *mip* units) for a sample of simulated events with fixed energy (10 GeV) and isotropic distribution in the PAMELA acceptance.

the calorimeter for simulated electrons with energy equal to 10 GeV:

$$Q_{tot} = \sum_{j=1}^{44} q_{totj} \tag{4.15}$$

This quantity is the sum of the charge collected by each one of the calorimeter planes q_{totj} (22 for the x view and 22 for the y view). The distribution is not symmetric and shows a non-gaussian tail towards lower values of collected charge. This effect can be addressed to the fact that sometimes the number of interaction lengths over which the shower is contained is greater than those corresponding to the whole calorimeter, therefore the shower is not completely contained in the calorimeter. If the value of the total detected charge is plotted as a function of the shower maximum depth, a clear correlation appears, as it is evident in figure 4.9. The problem of longitudinal leakage is clearly more important at high

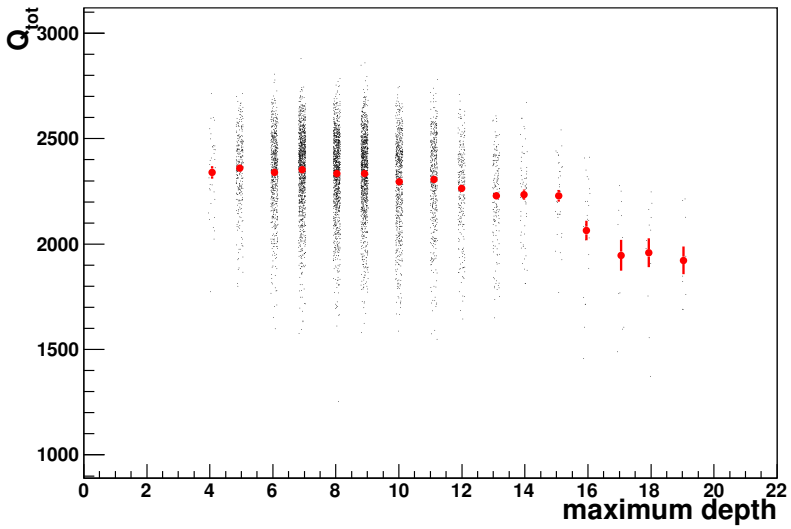

Figure 4.9: The total charge collected in the calorimeter showed as a function of the depth of shower maximum, in term of traversed tungsten planes, for the same sample of figure 4.8. The red points are the average charge collected by events with the maximum in the same plane.

energies because the maximum of the shower and its total depth increase with the energy (see equations 4.10 and 4.9); however, due to the big fluctuations present in the shower development, it could be significant even at lower energy.

There is another fact that bring to underestimate the energy released in the calorimeter, that is the presence of gaps between the silicon detectors. Figure 4.10 shows a schematic view of one of the calorimeter's plane, together with the projection of the shower crossing the plane; it is clear that, if the shower axis crosses the planes near to the gap or to the side, part of the shower energy will be lost. In order to have a precise reconstruction of the electron energy this effect has to be taken in to account. In fact from figure 4.11 it is clear that the total collected charge is correlated to the position of the shower maximum.

In order to overcome the leakage problems that has been described, it

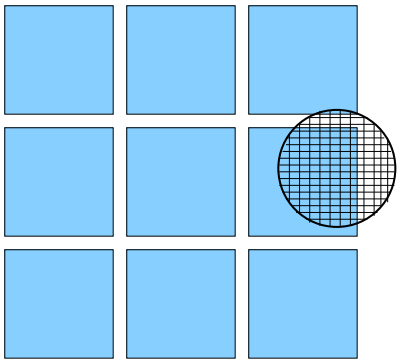

Figure 4.10: Schematic view of one of the calorimeter's plane from the top. The black grid represent the intersection between the shower and the plane.

is useful to take advantage of the longitudinal and lateral segmentation of the PAMELA calorimeter, which provides a good description of the shower shape. In fact the observed shape, when dealing with showers generated by electrons or positrons, can be compared with that expected according to the theoretical description.

Many studies can be found in literature regarding the development of electromagnetic showers, based on both theory and simulation, which provide useful relations to describe longitudinal and radial profiles of showers initiated by electrons. The shower parametrization was extensively studied by Grindhammer and Peters [63], with the aim to speed up the calorimeter simulations: in fact a parametrization of the shower can be used, instead of the individual particle tracking of all secondary particles produced in the showers, when the computing time has to be reduced. Our objective is to precisely describe the shower in order to correct event by event the collected charge in the calorimeter planes. The correction is performed looking at the profile that fits the best with the charge collected in any layer. It will be shown in the following sections that such a fit is a useful way to overcome the leakage problem.

The spatial distribution of the deposited energy in electromagnetic showers can be described by using three normalized probability-density functions characterizing the longitudinal, radial and azimuthal energy

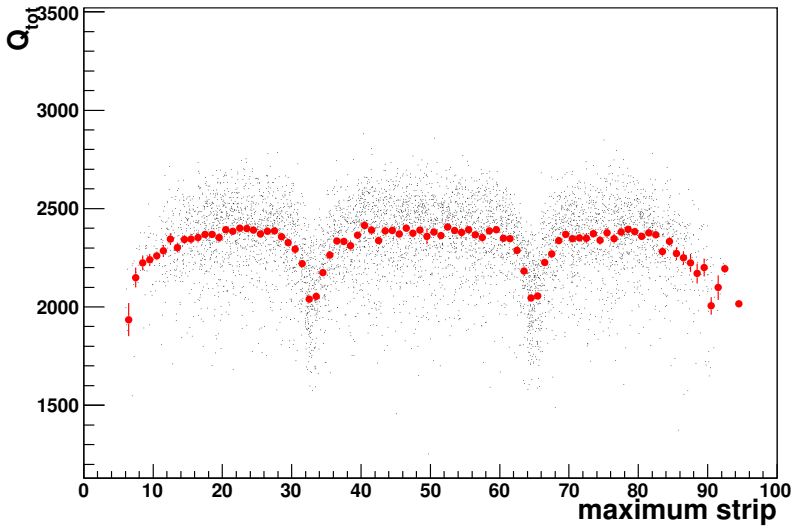

Figure 4.11: Total charge collected in the calorimeter as a function of the x-coordinate of shower maximum for the same sample of figure 4.8. The red points are the average values of the charge distribution. A similar behaviour is observed on the y view.

distributions:

$$dQ(\vec{r}) = Q \cdot f_l(t)dt \cdot f_r(r,t)dr \cdot f_a(\phi)d\phi \tag{4.16}$$

where t is the longitudinal shower depth in units of radiation length, r is the radial distance from the shower axis and ϕ is the azimuthal angle. One can assume that the energy is uniformly distributed in ϕ, so that $f_a(\phi) = 1/2\pi$.
In the following a detailed description of the distributions f_l and f_r will be given, together with the method by which these distributions are used to determine the shower energy. The over-all procedure consists in:

1) evaluating the average shape of the radial distribution of electromagnetic showers by analysing selected samples of simulated and real events;

2) calculating event-by-event the total charge collected by the calorimeter and correcting its value according to the expected parameterized shape;

3) performing an event-by-event fit of the longitudinal development of each shower and evaluating a factor to correct the total charge collected for longitudinal leakage;

4) finding the relation between the measured shower charge, corrected for lateral and longitudinal leakage, and the energy of the primary particle at the entrance of the apparatus, by means of simulated electrons;

5) using the calibration between the simulated energy and the charge collected in the calorimeter to calculate the energy of electrons and positrons selected from flight data.

Some comments have to be done on the described procedure. The method developed to reconstruct the energy of electrons and positrons is based on the simulation. A different approach could have been to perform this calibration with the real instrument, using the data acquired during the test with beams of electrons of known energies. This was not possible because, when the test was performed, in 2003, the acquisition electronics was not complete. However the simulation of the calorimeter is tuned by analysing the test data. Moreover the other instrument that provides an energy measurement for electrons is the spectrometer. It cannot be used directly to calibrate the calorimeter because, as will be explained in detail in the next chapter, the rigidity measured by the spectrometer is affected by the Bremsstrahlung effect. However a cross calibration between the two detectors can be performed and a correction to the calibration factor found with simulation studies can be found. This will be treated in chapter 5.

4.3 Lateral profile

The transverse size of an electromagnetic shower is mainly determined by the process of multiple scattering of electrons and positrons away from

the shower axis, in addition to the emission angle of Bremsstrahlung photons. It can be shown that the radial profile does not depend on the energy of the primary particle but it depends on the longitudinal position in the shower. In order to describe the radial profile a new variable, $\tau = t/T_m$, has been introduced, which expresses the position along the shower relative to the maximum. The following two-component function has been used to describe the normalized average radial profile of electromagnetic showers [63]:

$$\langle \frac{dQ(t,r)}{Q\ dr} \rangle = f_r(r,\tau) =$$

$$= \frac{1}{2\pi} \left[p(\tau) \frac{2r R_C^2(\tau)}{(r^2 + R_C^2(\tau))^2} + (1 - p(\tau)) \frac{2r R_T^2(\tau)}{(r^2 + R_T^2(\tau))^2} \right] \qquad (4.17)$$

In fact the radial profile can be seen as the sum of two distinct components that vary in different ways with increasing shower depths; one of the component describes the core of the distribution, the other describes the tails. In equation 4.17 the parameters $R_C(\tau)$ and $R_T(\tau)$ are connected to the width of the core and tail components, while the parameter $p(\tau) \in (0,1)$ gives the relative weight of the two. The above equation has been introduced to describe the radial profile of showers developing in homogeneous calorimeter. However it was demonstrated [63] that the exact geometry of the calorimeter has a rather small influence on radial energy profiles, as a consequence equation 4.17 has been used to describe the shower development inside the PAMELA calorimeter, even if it is a sampling calorimeter.

As discussed in the previous section, in order to have an unbiased reconstruction of the energy, we must take into account that, on each plane, part of the shower is not detected because its energy is lost in the gaps or from the side. In order to evaluate the charge that would have been collected in an ideal calorimeter, our approach has been to estimate the fraction of charge deposited on the dead area and to correct accordingly the measured charge. At the energies we are interested in, the charge deposited in each single plane is too low, especially in the first planes, so that it is impossible to perform an event by event fit of the radial

charge distribution. Therefore we decided to use an average profile to correct the experimental values of the charge on each single plane. From equation 4.17 follows that the profile has different parameters depending on the longitudinal position in the shower. A dedicated procedure has been developed to derive these parameters from data itself and it has been applied to both simulated and flight data. In the following the parametrization of the average radial profile is described and the lateral leakage correction discussed.

4.3.1 Parametrization of radial profile

In order to study the lateral distribution of electromagnetic showers we used a set of simulated electrons generated with a cosmic ray spectrum in the energy interval $5 \div 10\ GeV$, as was explained in section 3.4.2. Furthermore simulated data sets of both electrons and positrons with fixed energies have been used in order to address specific features of the lateral profiles.
The goal is to describe the average radial profile of the shower and to use this information to correct the energy detected in each plane. Since the radial profile depends on the longitudinal position, the approach was to create 12 different distributions of radial profiles, ranging from $\tau = 0$ to $\tau = 3$, in order to cover the most significant intervals of depth, where most of the shower energy is contained. The distributions have been determined by analyzing a set of selected showers in the following way:

- the depth of the maximum, T_m, is determined as the depth of the plane which collected most charge;
- for each plane j, the quantity $\tau_j = t_j/T_m$ is calculated,
- the shower axis is determined by extrapolating in the calorimeter the particle trajectory resulting from the spectrometer; for each plane j, the coordinate (x_a, y_a) of the intersection of the shower axis with the plane is calculated;
- the distance of each strip from the shower axis is calculated as $d_i = x_i - x_a$ if the considered plane is an x view, or $d_i = y_i - y_a$ if is an y view;

- the fraction of charge, w_i, collected by the strip i relative to the total charge collected by the plane is calculated as $w_i = q_{ij}/q_{totj}$, where q_{ij} is the charge collected by the strip i of the plane j and q_{totj} is the total charge collected by the plane j;

- the distribution of the corresponding τ-bin is populated with the quantity d_i weighted with w_i.

In order to determine the average shape of the radial profiles, showers well contained laterally that do not lose energy in the gaps or from the sides, have to be selected. Since the profile depends only on the depth, and the correction is applied independently to each plane, the selection is applied plane by plane, not to the whole event. This choice allows to increase the statistic of the sample used to create the lateral distributions. The definition of a fiducial area in the plane is critical from the point of view of the statistics. In fact, if the requirement was to use only showers fully contained laterally, the shower axis in each plane should be at least 3 *cm* far from the gaps. However, if the sample is isotropically distributed, the efficiency of this selection is too drastic. One opportunity would be to simulate showers that hit the calorimeter on a restricted zone, such that the showers develop mostly inside a fiducial volume. Obviously this can be done only for simulated events while we would like to apply the same procedure to the real data in order to compare the shower profiles and to take into account possible differences between the real apparatus and its simulation. As a consequence it is necessary to reach a compromise between having enough statistics and in the same time obtaining an appropriate description of the lateral distribution. The final choice has been to use only planes where the shower axis is located at least 4 strips far from the gaps and 10 strips far from the side. With this selection the resulting distributions are adequate to describe the shower core. In fact, the correction is clearly more important if the gap is near to the core of the shower, where the distribution is quite sharp, and it is more important to have a good parametrization of the most central part of the shower than of the tails.
The PAMELA calorimeter is constructed in such a way that each plane collects the charge deposited along each strip; so the observed distri-

bution cannot be compared to equation 4.17. The right formula for the measured distributions is instead obtained integrating equation 4.17 along the coordinate parallel to the detecting strip, for example in case of an x view:

$$f_P(x;\tau) = \int_{-\infty}^{+\infty} f_r(x,y;\tau)dy \tag{4.18}$$

where the integrand function is:

$$f_r(x,y;\tau) = \frac{1}{\pi}\left[\frac{p(\tau)\cdot R_C^2(\tau)}{(x^2+y^2+R_C^2(\tau))^2} + \frac{(1-p(\tau))\cdot R_T^2(\tau)}{(x^2+y^2+R_T^2(\tau))^2}\right] \tag{4.19}$$

Since the radial distribution is uniform in ϕ, the result of the integral is the same integrating over x or y and the following function has been used to perform a fit of the obtained distributions in both x and y views:

$$f_P(x;\tau) = p(\tau)\frac{R_C^2(\tau)/2}{(x^2+R_C^2(\tau))^{3/2}} + (1-p(\tau))\frac{R_T^2(\tau)/2}{(x^2+R_T^2(\tau))^{3/2}} \tag{4.20}$$

The values of the parameters, for each τ-bin, are obtained by fitting the experimental distribution with the function defined by equation 4.20. Figure 4.12 shows the average lateral profiles, in different τ-bin obtained for planes in the x view, together with the described fit.

Three different sets of parameters have to be determined due to the geometry of the calorimeter. This was necessary because the radial charge profiles depend on the distance between the absorber, where the shower develops, and the detecting silicon planes. In fact the particles of the shower have to propagate from the bottom surface of each tungsten block to the silicon detector, so that the lateral distribution of secondaries widens and the width increases for increasing distances between the two surfaces. Figure 4.13 shows a schematic view of the first and second module of the calorimeter. It can be seen that all the x planes are located at the same distance from the tungsten; the y planes are more distant, moreover odd and even planes are located at different distances from the corresponding tungsten plane. For example the planes X_0 and Y_1 correspond to the same τ-bin, being the quantity of radiation length traversed almost the same, but they have a different radial

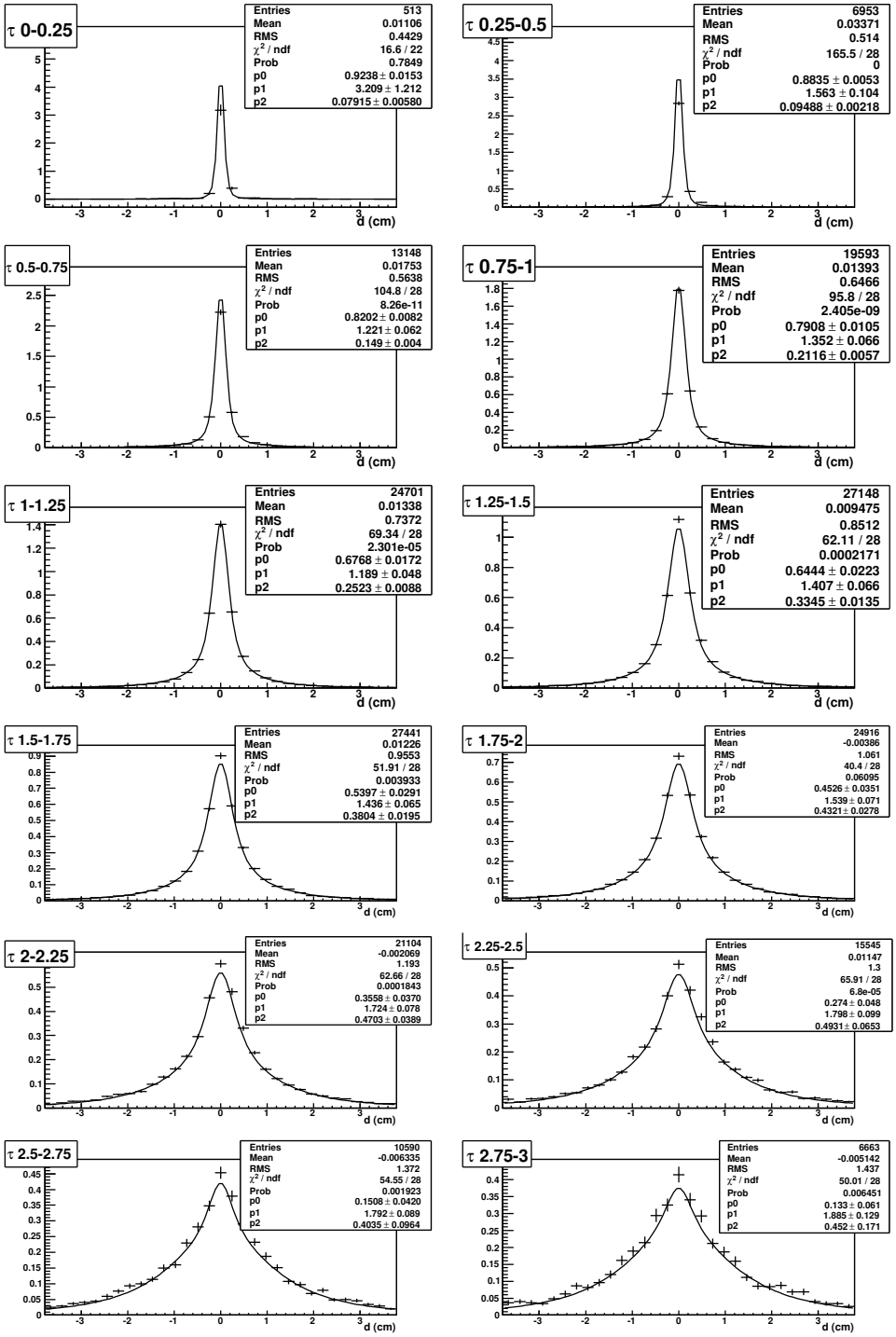

Figure 4.12: Lateral profiles, in different τ-bins on the x view, obtained with simulated electrons with cosmic ray spectrum and energies in the interval $5 \div 10\ GeV$.

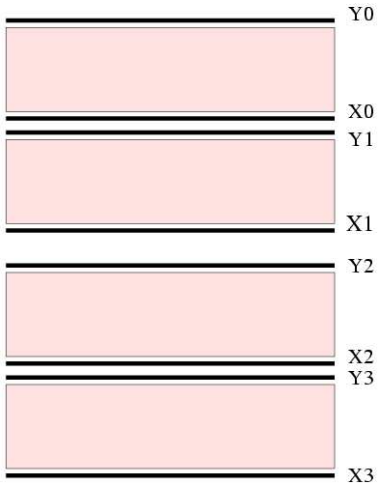

Figure 4.13: Schematic view of the first end second module of the calorimeter, the shaded area represents the tungsten. The plane Y1 is located 0.228 *cm* below X0, while the plane Y2 is located 0.428 *cm* below X1. The same structure is repeated 22 times.

profile. Consequently the average lateral profile has been evaluated independently for the three cases, namely x, y_{odd} and y_{even} views. The three sets of parameters R_C,R_T and p as a function of τ are shown in figures 4.14. The behaviour of these parameters can be explained qualitatively: at the beginning of the shower secondary particles are located near to the shower axis, while when the shower develops through the calorimeter the particles are more spread out. In fact it can be seen in the figures 4.14 that the weight of the core component, p, decrease with increasing τ, and its average value, R_C, increases almost linearly with τ. Moreover what was discussed above regarding the charge distributions in the x, y_{odd} and y_{even} view is confirmed by the results. In fact looking at the plot on the right, one can notice that the relative contribution of the core is lower for the y views than for the x view because the particles of the shower propagate a greater distance before they are detected

from the silicon planes. The difference between the average radial profiles obtained from the x, y_{odd} and y_{even} views in the most significant τ-bin, $\tau \in (1, 1.25)$, are shown in figure 4.15.

As already pointed out, the same analysis has been performed on real data. For this purpose a set of electrons have been selected from flight data. To perform the electron selection the requirement was only to have negative particles interacting in the calorimeters. Actually much more refined cuts have been implemented in order to distinguish between calorimeter showers generated by hadrons or leptons. They are explained in details in chapter 5, they have not been used here because the contamination of hadron at this energy is made only of interacting antiprotons, consequently it is very low, on the contrary the strongest cuts have to be used to select positrons, since there is a larger number of protons that could contaminate the sample.
In this case the same geometrical cuts on the shower track, explained before for the simulation, have been applied and finally three analogous sets of parameter have been found, as shown in figure 4.16. Figure 4.17 shows the comparison between the parameters calculated for flight data and simulation. One can notice that the global behaviour as a function of τ for simulated and real data is similar. However some small differences can be observed especially at small shower depths. The most significant differences concern the width of the tail component, for example in figure 4.18 a comparison between the distributions obtained for real data and simulation is shown; it seems that the tail is more spread for simulation than for real data. A possible explanation could be that the simulation of the secondary particles with lower energies, that affect the shape of the tails, is not well optimized, so a better fine tuning of the interactions in the calorimeter simulation could be necessary. To take into account of these differences the parameters calculated from the real data are used for flight data analysis.

Before going on with the explanation of the method used to correct the detected charge some general considerations on the radial profiles can be done by using the simulation. First of all a comparison between the distributions measured with two different fixed electron energies has been performed in order to check that that there is no clear dependence

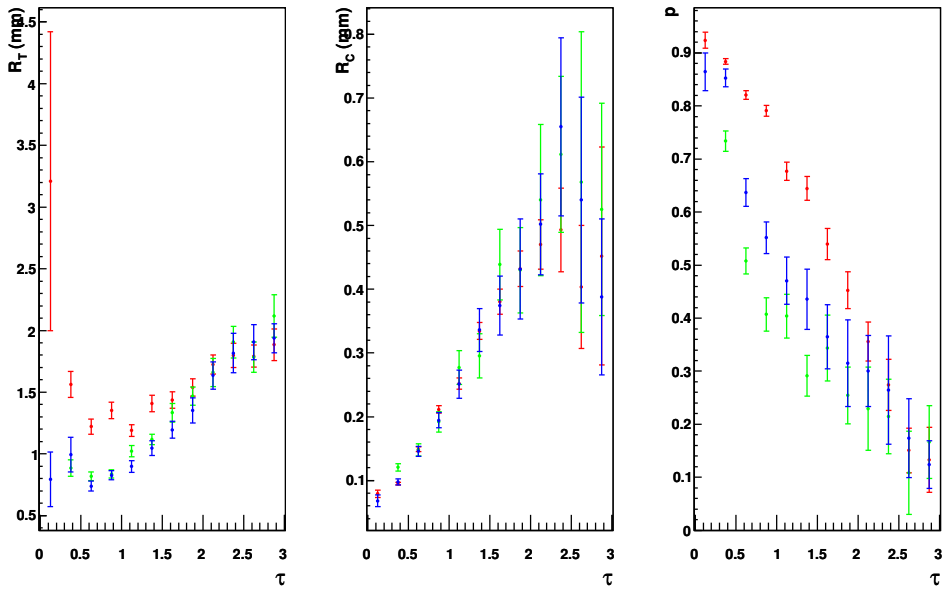

Figure 4.14: R_C,R_T and p as a function of τ; red points for x view fit, green for y_{even} and blue for y_{odd}. These values come from the fit of radial profiles of simulated data with uniform direction distribution and cosmic ray spectrum in the energy range $5 \div 10\ GeV$.

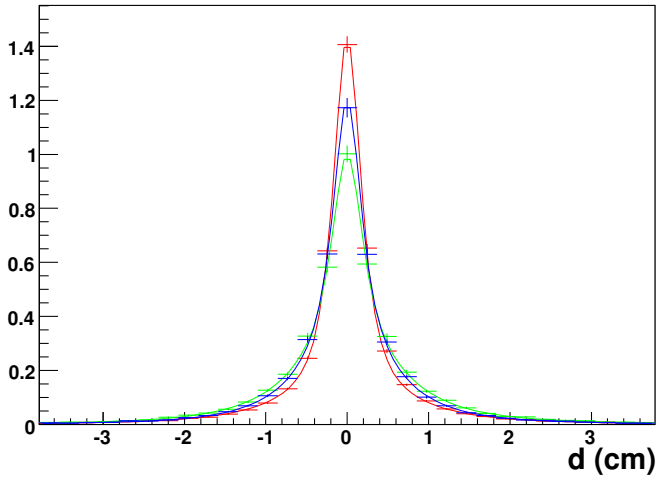

Figure 4.15: Radial profiles in the most significant bin ($\tau = 1 \div 1.25$), red for x view, green for y_{even} and blue for y_{odd}.

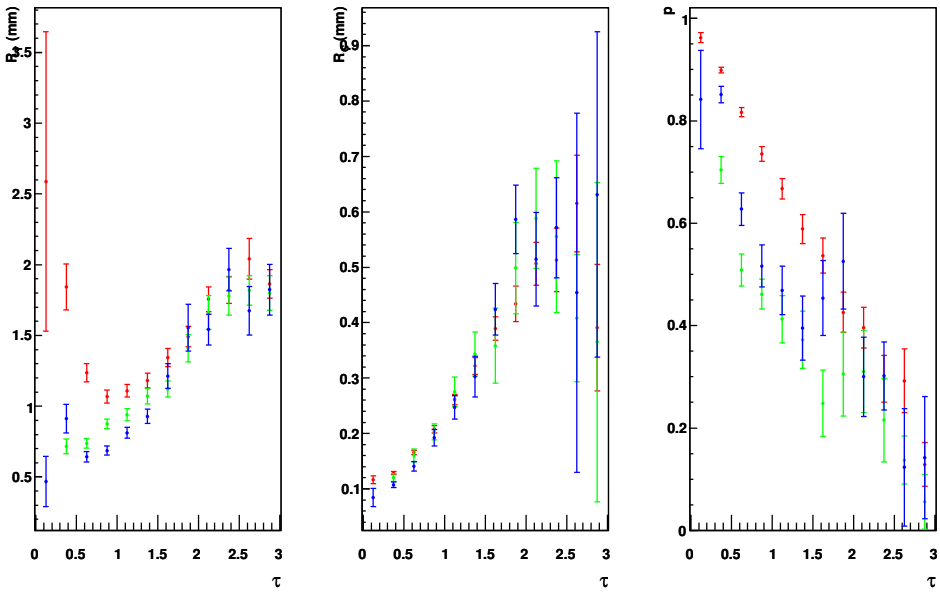

Figure 4.16: R_C,R_T and p as a function of τ; red points for x view fit, green for y_{even} and blue for y_{odd}. These values come from the fit of radial profiles of real data.

on the shower energy, as expected from equation 4.17. The result for the most significant τ-bin is shown in figure 4.19, from which is clear that the basic assumption of the independence of the radial profile on the shower energy is satisfied. This justifies the choice to evaluate the radial parametrization with a sample of events with energies ranging from 5 to 10 GeV. This allows to apply the same procedure to real data, in order to evaluate the best parameters to be used for the flight-data analysis.

It is necessary to make few considerations on the determination of the shower axis coordinates (x_a, y_a) which are determined by means of an extrapolation of the particle trajectory, measured with the spectrometer [2]. If the electron emits a Bremsstrahlung photon in the material above the

[2]The algorithm [64] used for this task takes into account also the not constant residual magnetic field that is present out of the spectrometer.

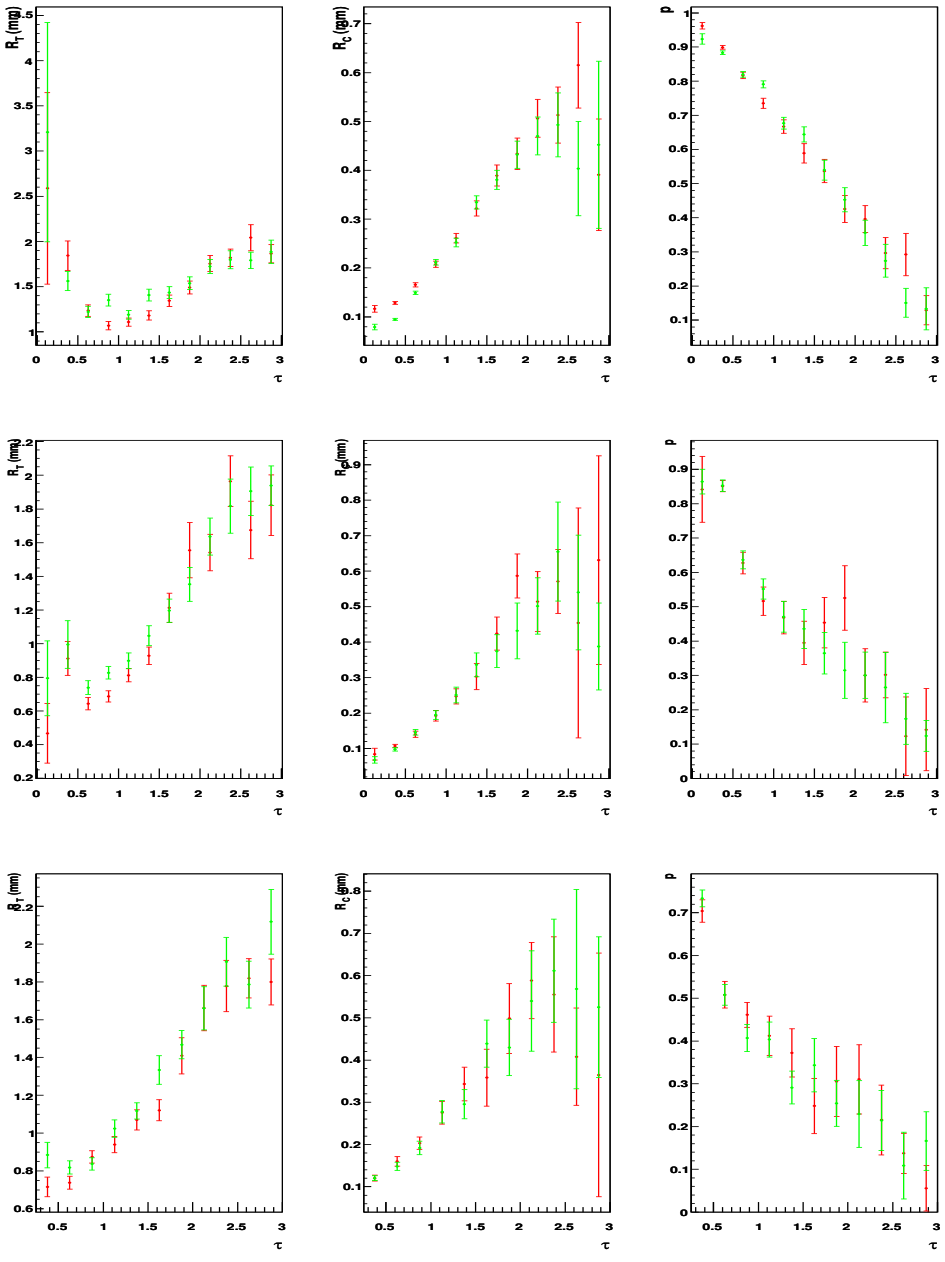

Figure 4.17: Comparison between simulation (green) and real data (red) parameters R_C,R_T and p as a function of τ, upper graphs for x view, middle for y_{even} and lower for y_{odd}.

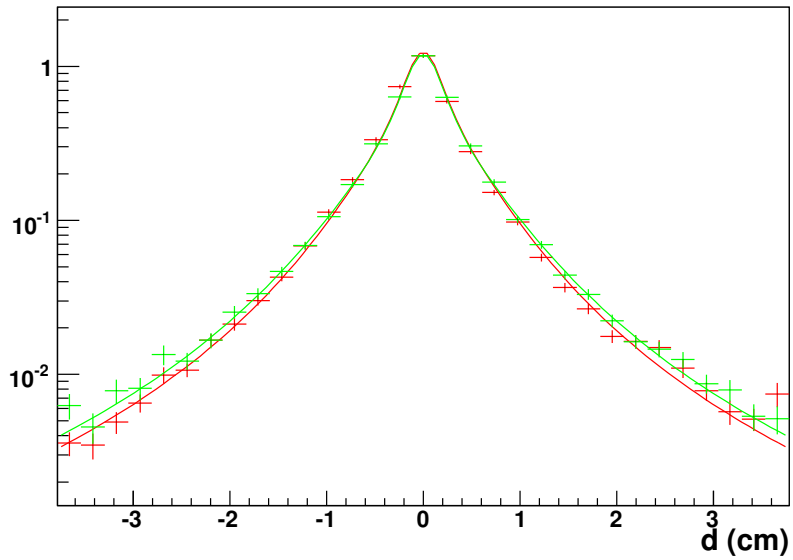

Figure 4.18: Radial profiles in the most significant bin ($\tau = 1 \div 1.25$) for the y_{even} view. Comparison between simulation (green) and real data (red) distributions.

spectrometer the track measured by the spectrometer matches the axis of the electromagnetic shower generated in the calorimeter by the electron only; on the other hand, the pattern observed in the calorimeter consists in the superposition of both the showers initiated by the secondary photon and the primary electron. As a consequence the coordinates of the shower axis determined by using the spectrometer track are consistent with the real axis of the shower only when there is no Bremsstrahlung emission. On the x view the electron trajectory is curved by the magnetic field and the two showers are slightly separated. This causes an asymmetry in the lateral charge distribution, if this is evaluated relative to the electron trajectory. This effect is negligible on the y view because, being the magnetic field directed mainly along y axis, the electron and photon trajectories are almost the same and the two showers overlap. In order to study this feature a sample of positrons has been simulated with

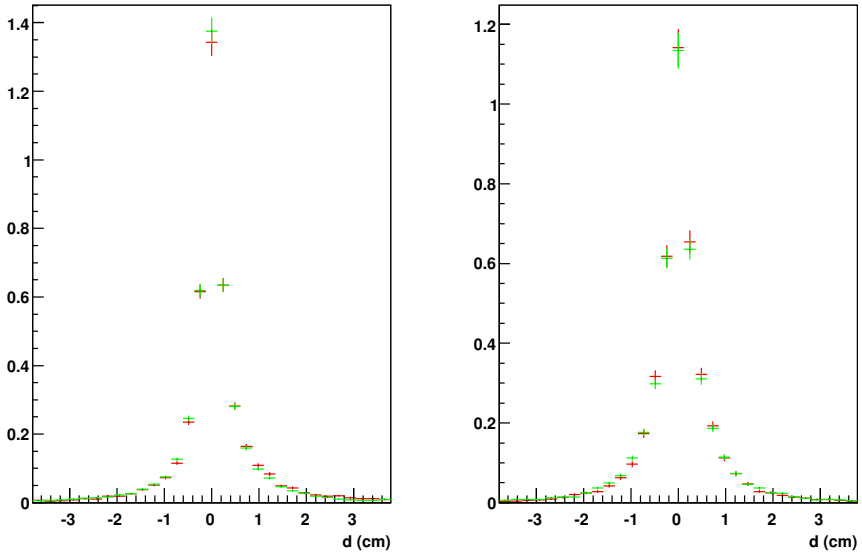

Figure 4.19: Comparison between lateral distributions of simulated electrons with energy 5 GeV(red) 10 GeV(green), on the x view(left) and y view (right) and for $\tau = 1 \div 1.25$.

fixed energy. In fact the asymmetry should emerge for showers generated by both electrons and positrons, but in opposite directions. In figure 4.20 one can notice that the asymmetry is present, as expected, only in the x view and is in opposite direction for e^+ and e^-. This effect is more visible in the tails of the distribution and has been neglected in this study.

For flight data analysis, an additional systematic uncertainty in the determination of the shower axis comes from the relative misalignment between the tracking system and the calorimeter. On the contrary the axis intersection coordinates determined from a calorimeter stand-alone fit would not be affected by this problem but, when the shower develops near a gap, the result of the calorimeter fit is biased, while the extrapolated spectrometer track is not affected by the gaps. However it is important to remark that the calorimeter position resolution is poorer than the tracker one (mm instead of μm). A procedure to evaluate the

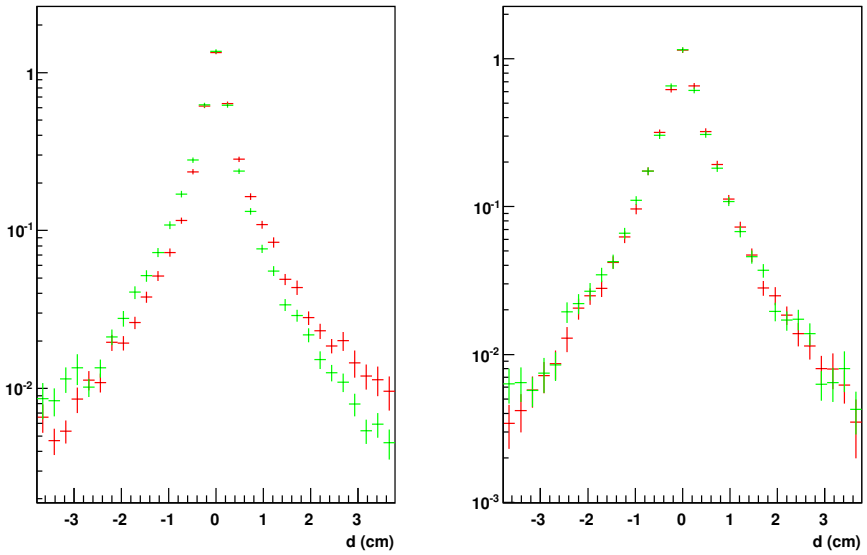

Figure 4.20: Comparison between distributions of simulated electrons(red) and positrons(green) of energy 5 GeV; Lateral distribution in x view(left) and y view(right) for $\tau = 1 \div 1.25$.

alignment parameters between the two detectors has been developed using non interacting relativistic particles. The errors on these parameters are negligible compared with the calorimeter resolution. The final decision was to use the extrapolation of the spectrometer track both for parametrization and correction purpose.

Concerning the lateral profile of very inclined showers, it is important to notice that their development is in principle different from vertical ones. In fact, from equation 4.17 follows that the charge distribution is symmetric around the shower axis, and depends on the shower depths. In case of inclined showers the sampling planes are not orthogonal to the axis, as a consequence the charge distributions measured by each silicon plane should be described by a superposition of different radial profiles at different depths. This effect is more important at the end of the shower development, because at small depths the particles are

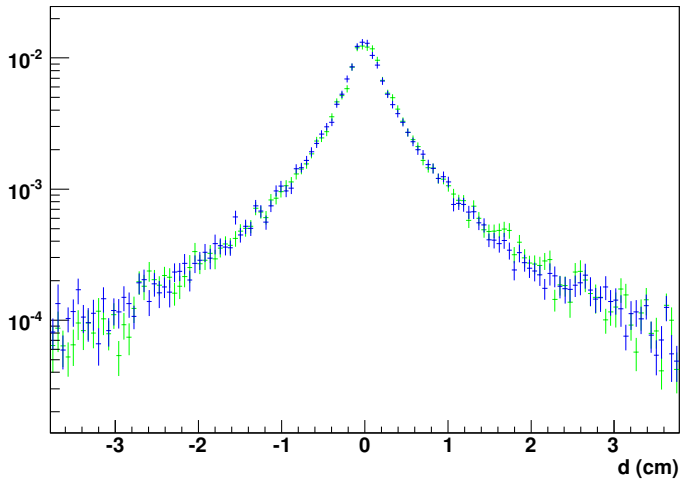

Figure 4.21: Comparison between distributions of simulated electrons of energy $5 \div 10\ GeV$ with the projected angle in the x view greater than 0 (green) or lower than 0 (blue) for $\tau = 1 \div 1.25$.

concentrated near the axis and there is not much difference. However, as it is clear in figure 4.21, the difference is negligible for our purpose so that the effect has been neglected and the average lateral profiles have been described with a symmetric function.

4.3.2 Lateral leakage correction

The lateral parametrization was used to calculate the fraction of energy lost, on each plane, due to the gaps existing between the detectors and to the lateral leakage (see figure 4.10). The following procedure is applied to every single event:

- the charge collected by each single plane is evaluated as:

$$q_j = \sum_{|d_i|<d_m} q_{ij} \tag{4.21}$$

where the sum is extended to every strip that has distance d_i, de-

fined previously in section 4.3.1, to the shower axis coordinate lower than a fixed cut d_m;

- the depth of each plane, determined as $\tau_j = t_j/T_m$, is used to determine the parameters (R_C, R_T, p) that better describe the lateral profile, according to the lateral parametrization described in section 4.3.1;

- for each plane the correction is calculated by means of the following integrals:

$$I_t = \int_{\xi<d_m} f_P(\xi, \tau_j) d\xi \qquad I_d = \int_{\xi<d_m\ \xi\in\mathcal{S}} f_P(\xi, \tau_j) d\xi \tag{4.22}$$

where $\mathcal{S}$ is the sensitive area. I_d corresponds to the fraction of detected charge, while I_t to the value measured with an ideal calorimeter without gaps; hence the correction factor, F_r, and the corrected charge on each plane, q'_j, are calculated as:

$$F_r = \frac{I_t}{I_d} \qquad q'_j = F_r \cdot q_j \tag{4.23}$$

To understand how this procedure works, it is useful to study the distribution of the total measured charge from simulated particles of fixed energy, whose shower is well contained longitudinally. It has to be noticed that for this analysis, since the longitudinal development has not been considered till now, only those events whose track intersect the last calorimeter plane inside its sensitive area have been considered. The total charge is calculated before and after the lateral correction in this way:

$$Q_0 = \sum_{j<j_m} q_j \qquad Q_1 = \sum_{j<j_m} q'_j \tag{4.24}$$

where j_m is the index of the maximum plane which is considered to calculate the total charge. In figure 4.22 the distributions of Q_0 and Q_1 are shown; the distribution of Q_0 has a tail at lower values, while the Q_1 distribution is more symmetric. Moreover, as shown in figure 4.23, the dependence of the total charge on the position of the strip traversed by

the shower maximum is strongly reduced, as expected, after the correction. However in the same figure a slightly overestimation of the charge after the correction is visible for some events with the strip of the maximum signal near the gaps. This effect could be a consequence of the lateral cut applied when the distributions are created. Due to this cut the weight of the tails is slightly underestimated and, since each lateral distribution is normalized, the core will result overestimated.

The total charge in each plane is calculated according to equation 4.21, where a cut on the distance between the considered strip and the shower axis coordinate is introduced ($|d_i| < d_m$): this cut has been applied in order to minimize the effect of noisy strips. The maximum distance has been set as $d_m = 4\ cm$, which assures that on average 98% of the energy is collected.

For the same reason, in order to evaluate the total charge in equation 4.24 only the planes until a certain maximum plane are considered. Studying the average development, we found a good compromise if the considered planes are those with $t < 5T_m$.

4.3.3 Q_1-energy calibration

In this section the calibration between the total measured charge after lateral correction and the particle energy is described. To find this relation several sets of 10000 monochromatic isotropic electrons, in the interval $5 \div 16\ GeV$, were generated. For each event the lateral correction was applied and the distribution of the total collected charge Q_1 was fitted with a gaussian function: the resulting parameters are then used to estimate the value and the error of the average energy deposited in the calorimeter for each sample of simulated electrons. Figure 4.24 shows the average values of Q_1 as a function of the simulated energy, E_0, together with the fit with the function $Q_1 = p_0 + p_1 \cdot E_0$. The fit was performed in different energy ranges in order to understand when the linear relation starts to fail due to the longitudinal leakage. The conclusion is that a further correction to account for the longitudinal leakage is necessary already at $10\ GeV$. The electron energy reconstructed after lateral leakage correction is E_1, defined as $E_1(Q_1) = \frac{1}{p_1} \cdot Q_1 - \frac{p_0}{p_1}$.

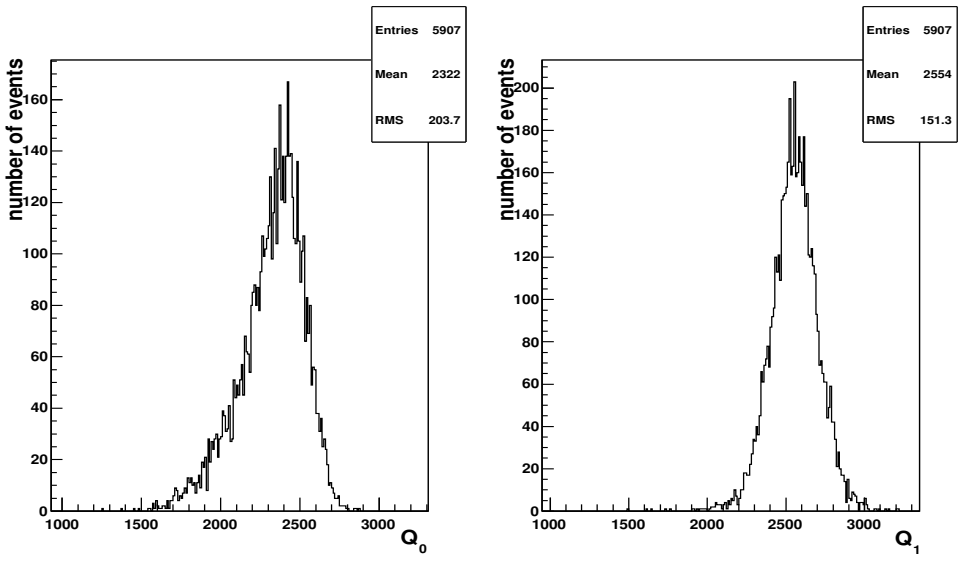

Figure 4.22: Distribution of the total collected charge for events simulated with fixed energy (10 GeV). The distribution on the left is without any correction, on the right after the correction for lateral leakage.

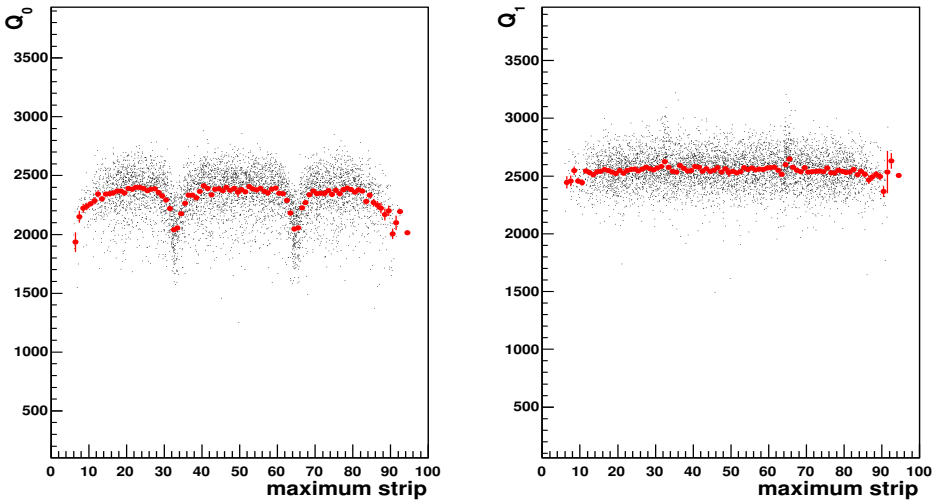

Figure 4.23: The total collected charge shown as a function of the position of the shower maximum before and after lateral correction. Same data sample of figure 4.22.

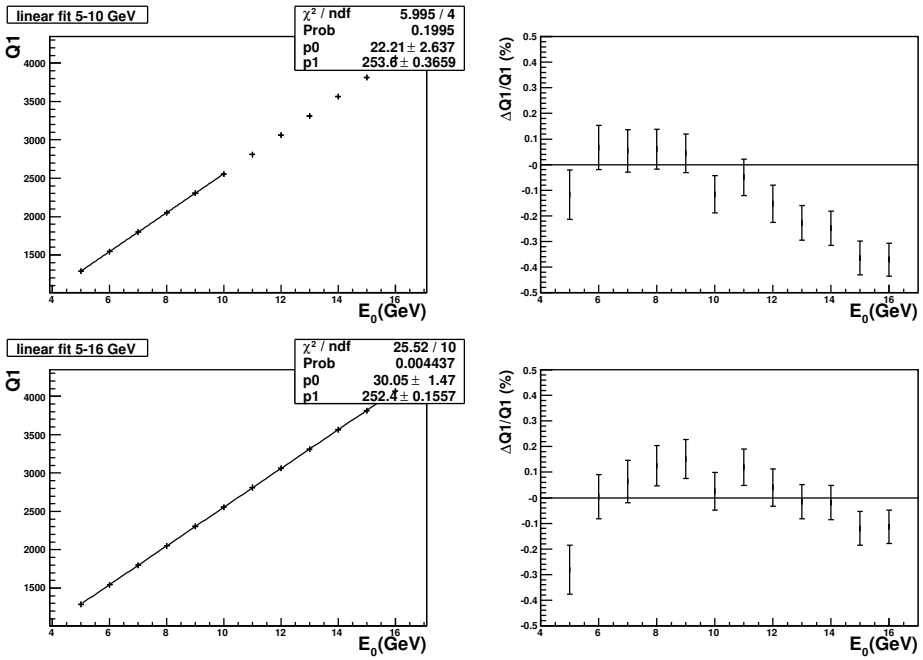

Figure 4.24: The plots on the left show the the linear fit of the average value of Q_1 as a function of the simulated energy performed in different energy interval. In the plot on the right there is the relative difference between the result of the fit and the average charge: $\frac{Q_1 - Q_1^{fit}}{Q_1}$.

The estimated resolution for the reconstruction of the energy of electrons, $\sigma(E_1)/E_1$, obtained after the lateral correction is shown in figure 4.25.

For an ideal calorimeter the energy resolution depends only on the statistical fluctuations in the number of secondary particles produced in the electromagnetic shower. Assuming a poissonian-like distribution, the average number of secondaries N_m has an associated error of $\sqrt{N_m}$. It follows that:

$$\frac{\sigma(E)}{E} \sim \frac{\sigma(N_m)}{N_m} \sim \frac{1}{\sqrt{N_m}} \propto \frac{1}{\sqrt{E}} \tag{4.25}$$

Actually the energy resolution depends on other factors and it can be

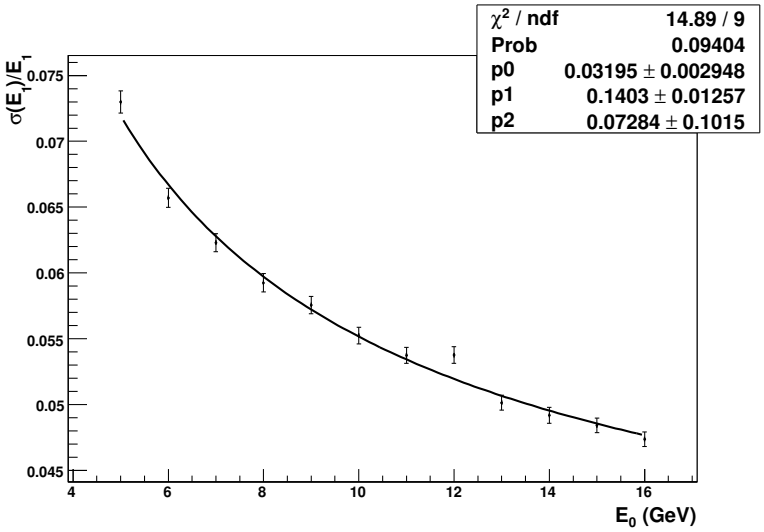

Figure 4.25: Energy resolution after lateral leakage correction shown as a function of simulated energy. The function used for the fit is : $\sqrt{p_0^2 + \frac{p_1^2}{E_0} + \frac{p_2^2}{E_0^2}}$, according to equation 4.26.

written as the sum of three different term [62]:

$$\frac{\sigma(E)}{E} = \frac{a}{\sqrt{E}} \oplus \frac{b}{E} \oplus c \tag{4.26}$$

where the symbol $\oplus$ indicates a quadratic sum. The first term on the right-hand side is due to the stochastic nature of the process of shower development, which has intrinsic fluctuations; the second term is due to the electronic noise of the readout chain and is important at low energy; the last constant term includes contributions that do not depend on the energy of the particle and is important only at very high energy.

4.4 Longitudinal profile

It has been shown in the previous section that a longitudinal correction has to be applied in order to obtain an unbiased reconstruction of the

energy above 10 GeV.
It is well known that the average longitudinal shower profile can be described by a gamma distribution [65] with shape parameter α and scaling parameter β:

$$\langle \frac{dQ(t)}{Q\ dt} \rangle = f_l(t) = \frac{(\beta t)^{\alpha-1}\beta e^{-\beta t}}{\Gamma(\alpha)} \tag{4.27}$$

where $t = 0$ is the space point where the first Bremsstrahlung process occurs and the shower starts to develop. Since the radiation length in tungsten is 0.35 cm we made the assumption that the beginning of the shower coincides with the beginning of the calorimeter.
We assumed also that individual profiles can be approximated by a gamma distribution. The center of gravity, $\langle t \rangle$, and the position of the shower maximum, T, can be expressed in terms of the parameters α and β in the following way:

$$\langle t \rangle = \frac{\alpha}{\beta} \qquad T = \frac{\alpha - 1}{\beta} \tag{4.28}$$

The depth of the shower maximum is proportional to the logarithm of primary energy, it is therefore convenient to use T instead of β to describe longitudinal profiles, together with the parameters Q and α.
Thus the following form has been used to describe the longitudinal profiles of the showers:

$$\frac{dQ(t)}{dt} = f_l(t; Q, \alpha, T) =$$

$$= Q\frac{\alpha - 1}{T \cdot \Gamma(\alpha)} \left(\frac{(\alpha - 1)t}{T} \right)^{\alpha-1} e^{-(\alpha-1)t/T} \tag{4.29}$$

This description of the shower is the result of analytical calculations valid for the longitudinal development of electromagnetic showers in homogeneous media. In sampling calorimeters the inhomogeneous distribution of materials modifies the behaviour of the showers. However, in the energy range of interest for this study, the description of the shower obtainable through equation 4.29 is adequate in order to calculate a correction.

4.4.1 Longitudinal leakage correction

The approach used to perform the longitudinal correction is to perform an event-by-event fit of the longitudinal profile and to correct the total charge detected according to the result of the fit. This approach is different from the one used to account for lateral leakage, in fact it will be shown in the following that the fluctuations in the longitudinal development of the showers are quite significant and, as a consequence, a parametrization of the average development would not be very useful. Moreover usually most of the shower is contained, at least till the maximum, and the collected charge is enough to perform an event by event fit.
In order to perform a longitudinal correction, the values of the charge in each plane, already corrected for lateral leakage, q'_j, as a function of the depths in units of radiation length, t_j, are interpolated with the function f_l defined by equation 4.29. The fit is performed by minimizing the following function:

$$\chi^2 = \sum_{i=1}^{n} \left(\frac{f_l(t_j; Q, \alpha, T) - q'_j}{\sqrt{q'_j}} \right)^2 \tag{4.30}$$

where Q, α and T are the free parameters. The fit is performed using the *Minuit* package [66]. The result of the fit is very sensitive to the parameter initialization and in some cases, if the initialization is not optimal, the minimization does not converge. To solve this problem the minimization is performed twice: the first time bounding the parameters with reasonable physical limits, then the fit is performed again releasing the limits, but starting with parameters found by the previous fit.
It is interesting to notice that particles with the same energy can develop with showers very different from each other, due to fluctuations. The examples in figure 4.26 show the described fit applied to showers generated by 50 GeV simulated electrons: it is evident that the fluctuations are quite important, with the parameter T varying from the value 5.6 to 8.9.

In order to study the distributions of the fit parameters as a function of the energy of the particles generating the showers, the longitudinal

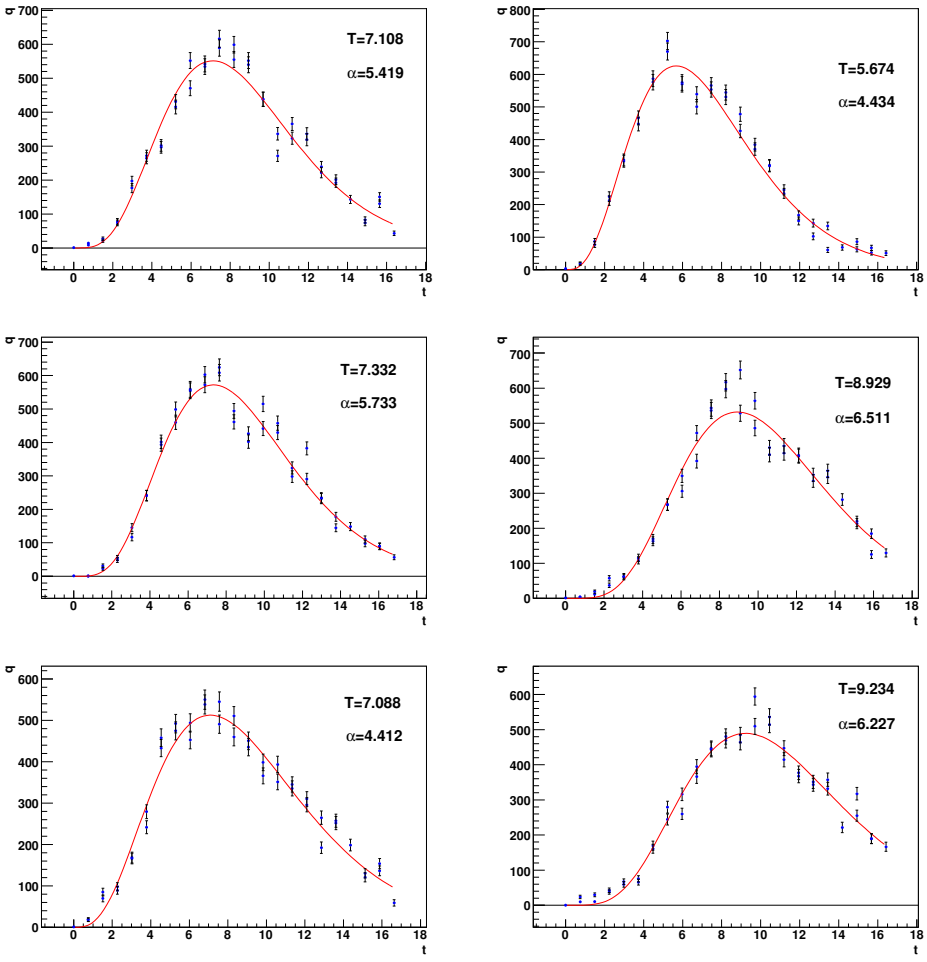

Figure 4.26: Individual profiles of showers generated by 50 *GeV* simulated electrons. The blue points are the experimental values of the charge collected on each plane, after the lateral leakage correction, the red line is the result of the fit.

fit was applied to different samples of simulated electrons with constant energy. The results for 10 GeV electrons are shown in figure 4.27. The logarithm of the parameters has a quite gaussian distribution. Particularly interesting is the correlation between the logarithm of the shape parameter and the logarithm of the shower maximum. This feature is very important because it depends weakly on the energy, as shown in figure 4.28, where it can be seen that the logarithm of T increases with the energy but the slope is almost constant. Figure 4.29 shows the correlation between the parameter Q and $\ln(T)$: it can be seen that the fluctuation of the shower maximum decreases with increasing energy, as expected from theoretical studies of electromagnetic shower development.

The parameters found after the minimization $(\tilde{Q}, \tilde{\alpha}, \tilde{T_m})$ are used to correct the measured energy for the longitudinal leakage. The correction is evaluated as the ratio between the integral of the longitudinal profile function between $t = 0$ and $t = 5T_m$ and the integral calculated over the whole depth of the calorimeter:

$$F_l = \frac{\int_0^{5T_m} f_l(t; \tilde{Q}, \tilde{\alpha}, \tilde{T_m})dt}{\int_0^{t_{calo}} f_l(t; \tilde{Q}, \tilde{\alpha}, \tilde{T_m})dt} \tag{4.31}$$

where t_{calo} is the longitudinal depth of the last calorimeter plane.
The total collected charge after this correction, Q_2, is evaluated as $Q_2 = F_l \cdot Q_1$. In principle the upper limit on the integral at the numerator in the previous equation should be ∞, but, as anticipated in section 4.3.1, in order to minimize the effect of noisy strips, the total collected charge in the calorimeter is evaluated considering only a limited number of planes. Consequently, if $5T_m$ falls outside the calorimeter ($t_{calo} < 5T_m$), the total charge is evaluated summing up the charge of all the planes and the correction for the longitudinal leakage is applied. Otherwise the planes corresponding to a depth greater than $5T_m$ are discarded and no longitudinal correction is applied.

Another consideration has to be done on the method used to correct the collected charge. To correct for lateral leakage a first estimate of the shower maximum, given by the depth of the plane that collects more

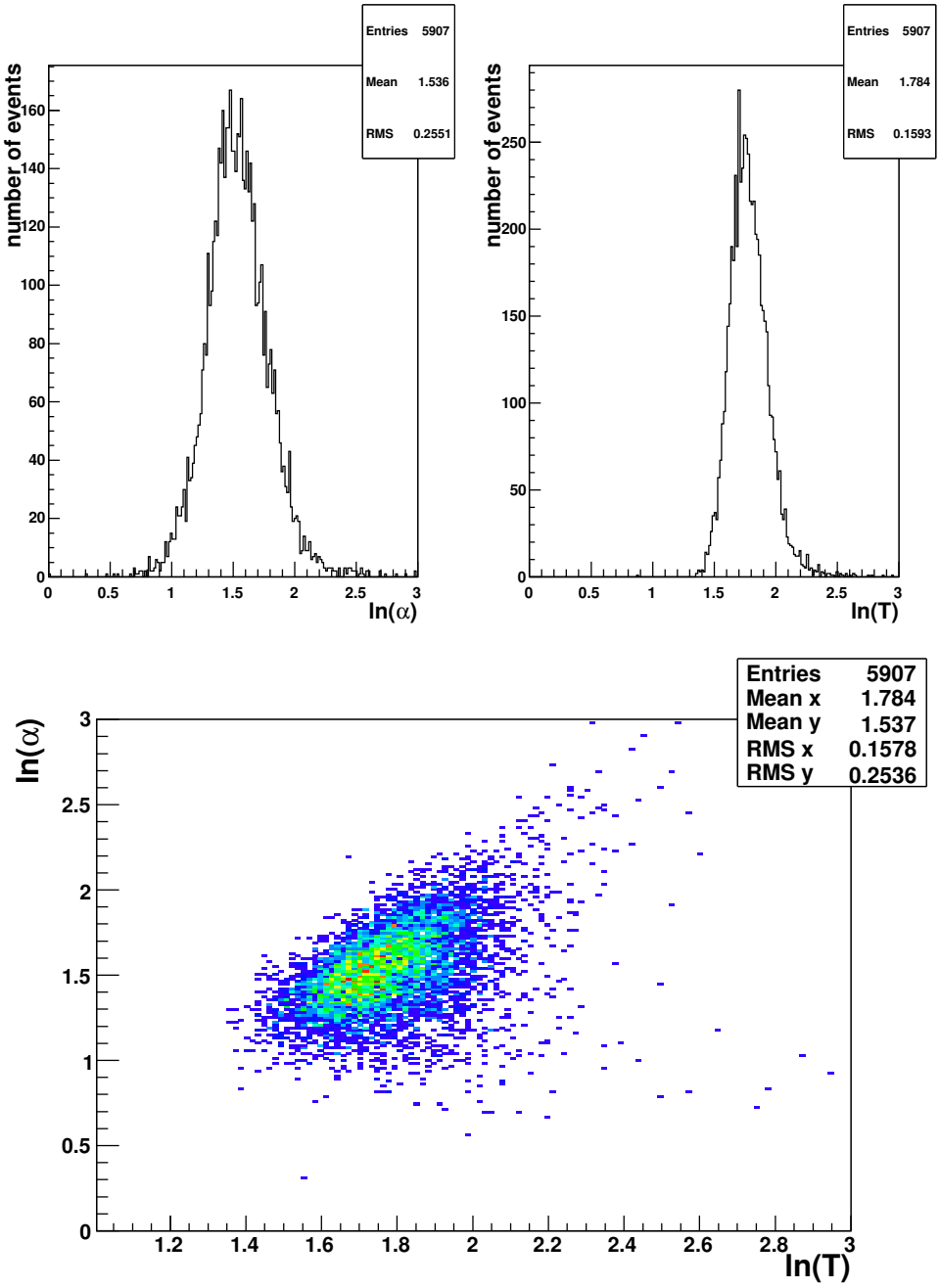

Figure 4.27: Fit parameter's distribution and their correlation. Same analyzed sample of figure 4.22.

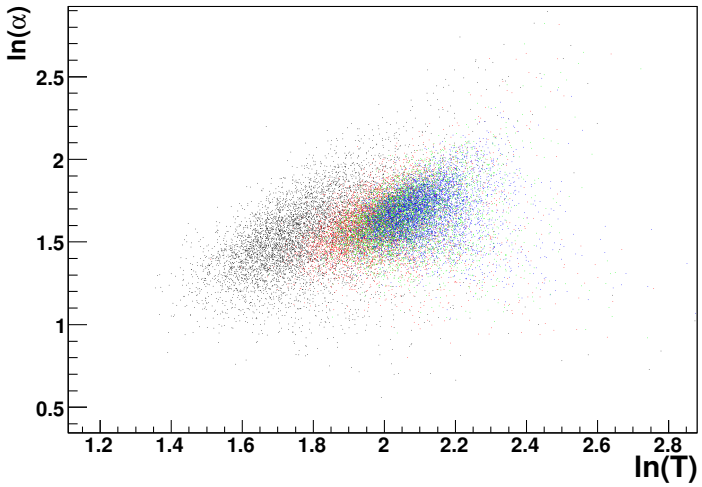

Figure 4.28: Correlation between $\ln(\alpha)$ and $\ln(T)$. Each color is obtained from a sample of events generated with different energies: 10(black),40(red),70(green),100(blue) GeV.

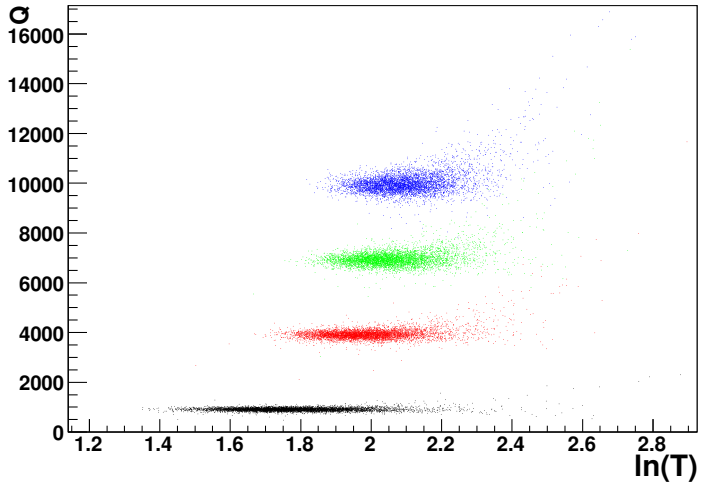

Figure 4.29: Correlation between Q and $\ln(T)$. Each color is obtained from a sample of events generated with different energies: 10(black),40(red),70(green),100(blue) GeV.

charge, has been used to describe the expected lateral distribution. This procedure could be affected by a significant error if the shower maximum is badly estimated, for example for very inclined showers that propagate out of the calorimeter from lateral walls. Showers whose axis does not intersect the last calorimeter planes are have been excluded from the calibration sample. However the developed method will be applied to any shower and the above cut in general will be removed. In case the shower maximum obtained from the longitudinal fit is significantly different from the previously estimated value, the lateral correction is applied again after the new calculation of the τ-bin corresponding to each plane.

The result of applying the longitudinal correction is to recover the effect of the energy leakage as is evident in figure 4.30; the distribution of the charge Q_1 has a quite important tail at lower values, which is recovered after longitudinal correction, in fact the distribution of Q_2 is more gaussian.

4.4.2 Q_2-energy calibration

The final calibration, after both steps of leakage correction, has been performed with the same approach described previously for the Q_1-energy calibration, but the event were simulated in the energy interval $10 \div 120\ GeV$. Figure 4.31 shows the average values of Q_2 as a function of the simulated energy together with the fit with the function $Q_2 = p_0 + p_1 \cdot E_0$. As expected the linear relation holds in the whole energy range, confirming that the longitudinal correction works properly.
The electron energy reconstructed after both lateral and longitudinal leakage correction is E_2, defined as $E_2(Q_2) = \frac{1}{p_1} \cdot Q_2 - \frac{p_0}{p_1}$. Figure 4.32 shows on the right a comparison of the resolution, obtained after applying both lateral and longitudinal corrections and after lateral correction only. The same figure on the left shows the behaviour of the resolution in the whole simulated energy range, the resolution improves with increasing energy.

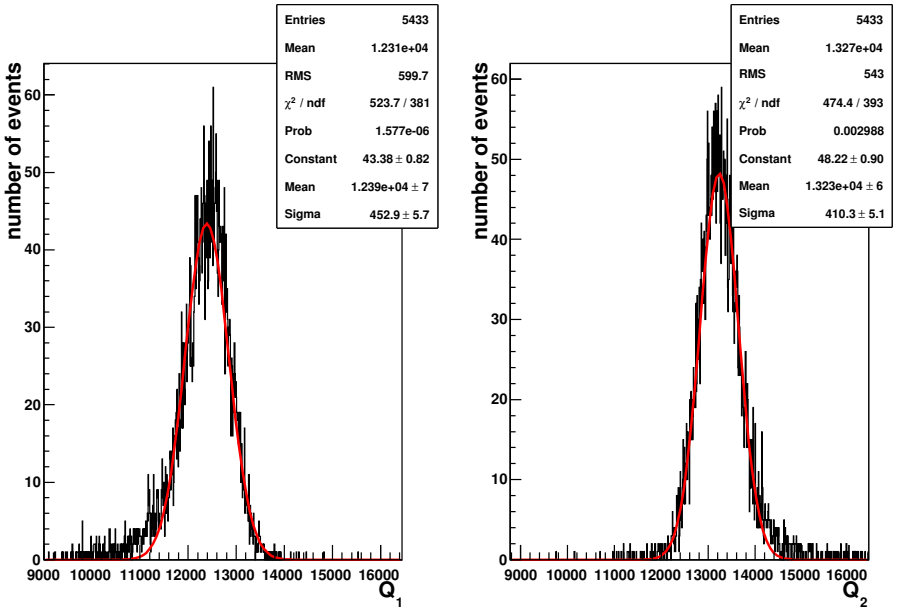

Figure 4.30: Distribution of the total charge collected for events simulated with fixed energy (50 GeV). The distribution on the left is with lateral correction only, on the right after the correction for longitudinal leakage.

4.4.3 Selection of a high-quality sample

In the next chapter the procedure for the alignment of the spectrometer is explained. For this task it is necessary to extract the momentum of electron and positrons from the calorimeter information. For alignment purpose, the reconstruction of the energy has to be performed with a resolution lower then 10%, and in particular one has to be sure that there are no events affected by systematic errors. In this section the specific quality cuts that have been developed to select events to be used for alignment purpose are explained.

The results of the described correction procedure are shown if figure 4.33: the effect of the longitudinal leakage on the reconstruction is recovered in most of the cases. However for some of the events it brings an overestimation of the reconstructed energy, in particular when the

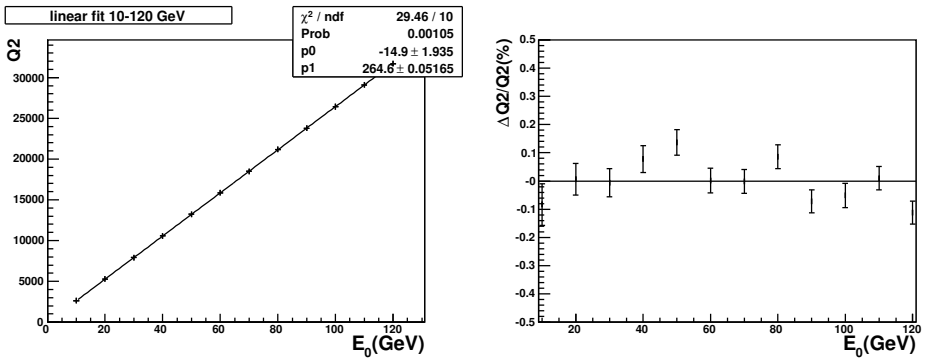

Figure 4.31: The plot on the left shows the linear fit of the average value of Q_2 as a function of the simulated energy. The plot on the right shows the relative difference between the result of the fit and the average charge: $\frac{Q_2 - Q_2^{fit}}{Q_2}$.

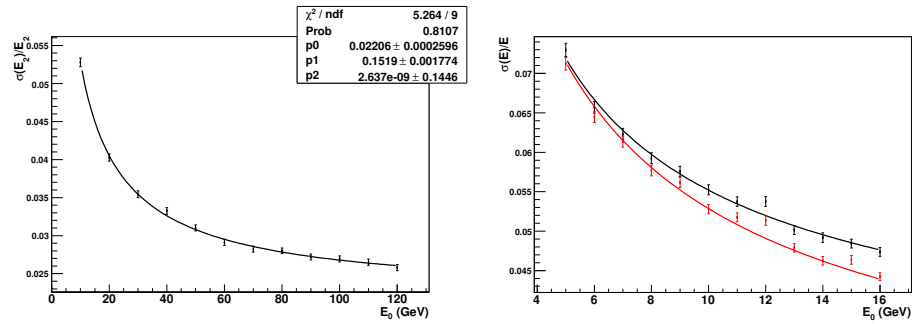

Figure 4.32: Energy resolution obtained after lateral and longitudinal correction shown as a function of simulated energy, in the whole simulated energy range. The function used for the fit is $\sqrt{p_0^2 + \frac{p_1^2}{E_0} + \frac{p_2^2}{E_0^2}}$ according to equation 4.26. On the right the comparison between the resolution after lateral correction only (black) and after lateral and longitudinal corrections (red) is shown.

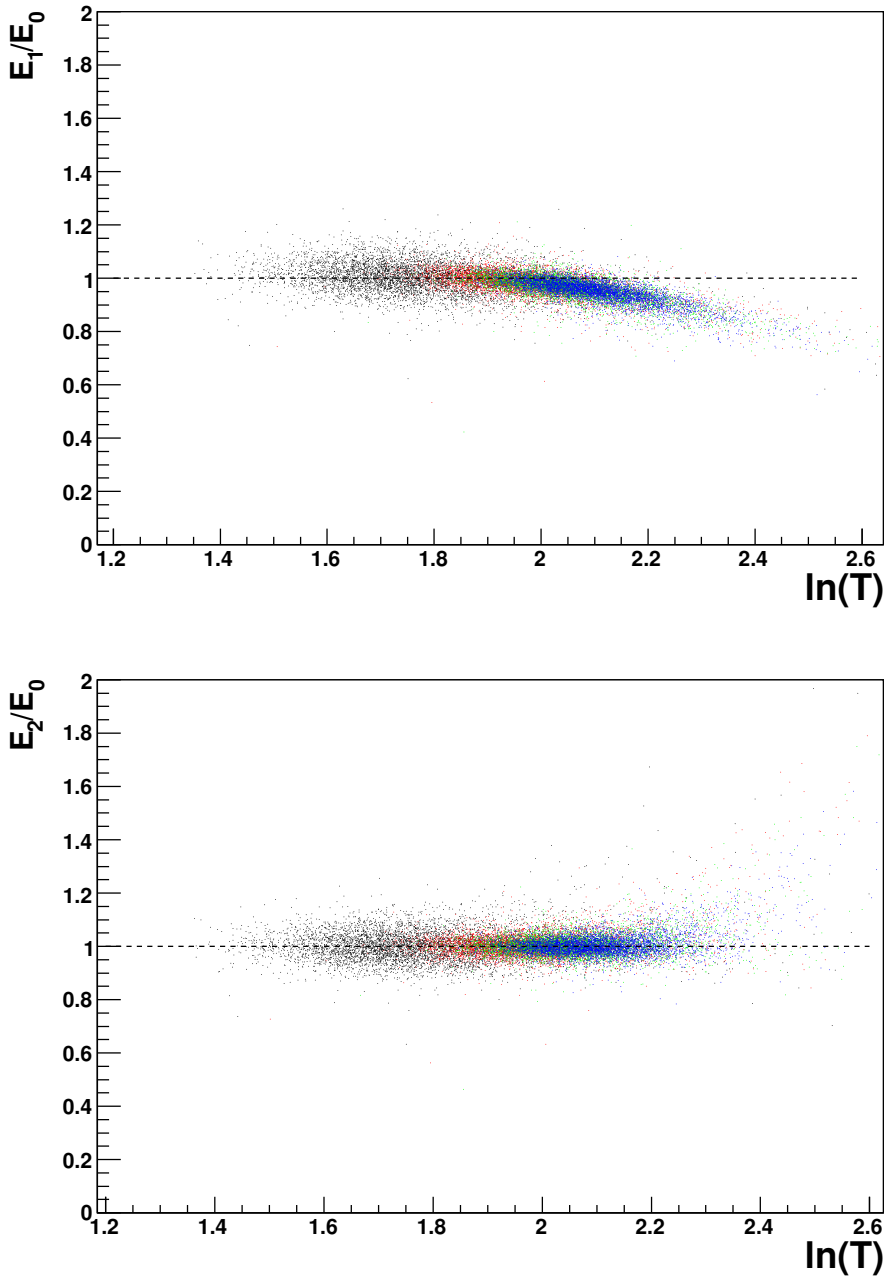

Figure 4.33: Ratio between the reconstructed energy and the original energy as a function of the maximum of the shower. In the upper part the energy was reconstructed applying only lateral correction, in the bottom applying both lateral and longitudinal corrections. Each color is obtained from a sample of events generated with different energies: 10(black),40(red),70(green),100(blue) GeV.

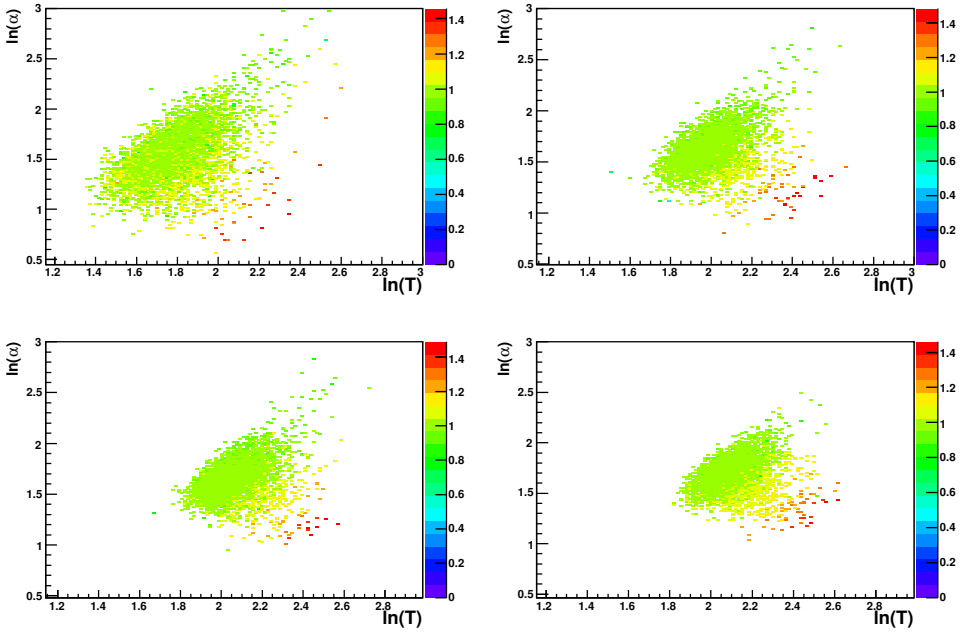

Figure 4.34: The correlation between $\ln(\alpha)$ and $\ln(T_m)$ is shown weighted with the ratio E_2/E_0. Each plot is obtained from a simulated sample of electrons with energy 10,40,70,100 GeV.

shower maximum is located in the last part of the calorimeter. The overestimated energies can be connected with those events where the longitudinal parameters lie far from the correlation zone, as is evident from figure 4.34.

To explain this effect is useful to analyze some examples. In figure 4.35,4.36 the longitudinal development, together with the fit of two events simulated with energy 50 GeV, is shown; in the upper plot the shape parameter α has a value lower than the expected average value, which means a flatter distribution of the signal. In this case the charge deposited outside of the calorimeter is overestimated and consequently by applying the longitudinal correction the reconstructed energy is overestimated.

The performances of the calorimeter energy reconstruction have been

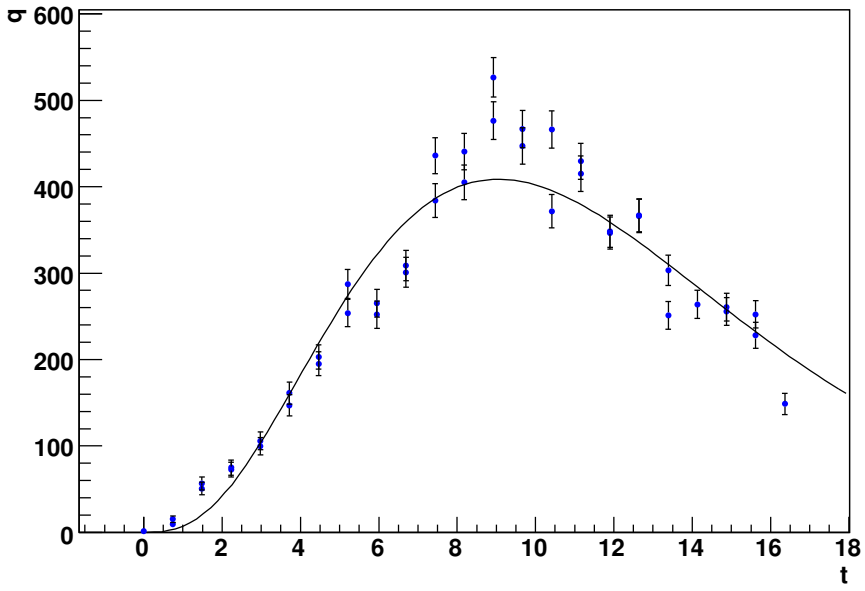

Figure 4.35: Example of an event with parameters out of the correlation zone ($\alpha = 4.13$, $T = 9.04$). Simulated energy 50 GeV, reconstructed energy 45 GeV,after longitudinal correction($F_l = 1.25$) 54 GeV

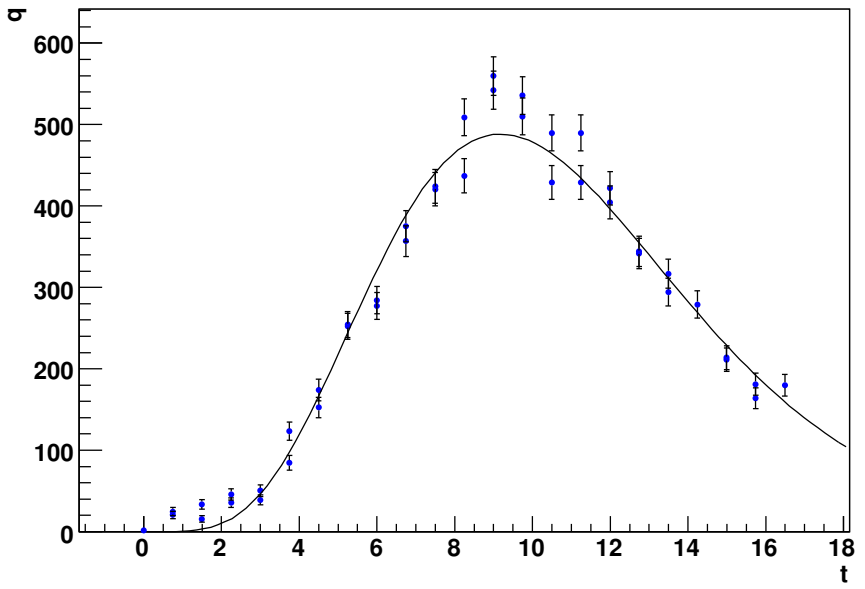

Figure 4.36: Example of an event with correlated parameters ($\alpha = 6.3$, $T = 9.1$). Simulated energy 50 GeV, reconstructed energy 46.2 GeV,after longitudinal correction($F_l = 1.12$) 49.69 GeV

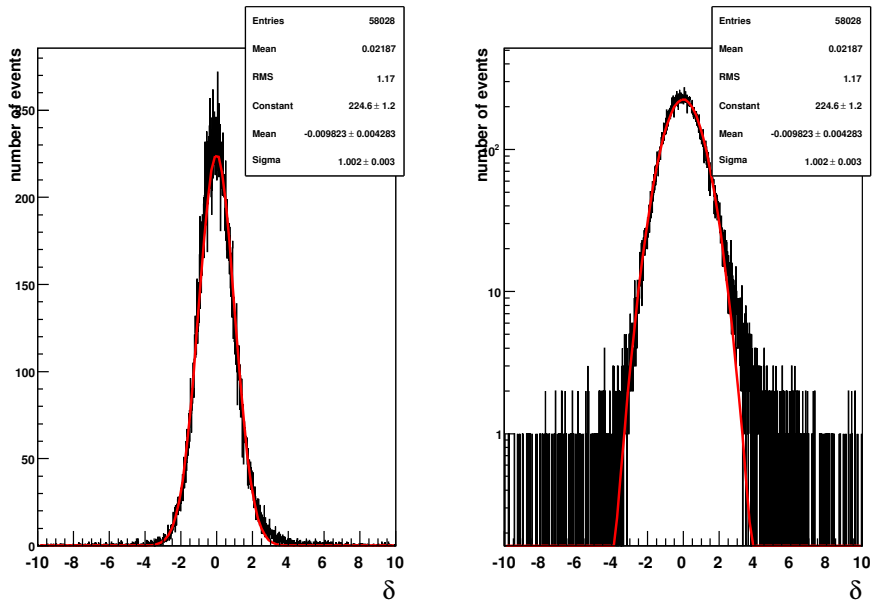

Figure 4.37: Distribution of the quantity δ on linear (left) and logarithmic (right) scale.

studied using the variable $\delta = \frac{E_2 - E_0}{\sigma(E_2)}$. The distribution of this quantity is shown in figure 4.37 together with a gaussian fit. There are non-gaussian tails that have to be removed for alignment purpose.
The tail on the right is due to events for which the longitudinal correction is overestimated. It has been shown that these events are those for which the parameters α and T, resulting from longitudinal fit, lay out of a correlation zone. The correlation between the logarithm of the parameters α and T is a feature common to all the energies and has been used as a topological criterion to select unbiased events among those used for the alignment procedure. The correlation zone has been determined phenomenologically and is shown in figure 4.38, the selected events have to satisfy the condition:

$$1.3 < \ln(T) < 2.3 \qquad AND \qquad |\ln(\alpha) - 0.92 \cdot \ln(T)| < 0.5 \qquad (4.32)$$

At this energy the efficiency of this cut is about 95%. After applying this cut the non-gaussian tail on the right disappears, its effect is shown in figure 4.39.

However the tail on the left remains, and it is due to events where the calorimeter energy is underestimated. They are caused by events where the difference between the extrapolated spectrometer track is far from the main shower in the calorimeter, this could happen when the energy lost by the primary particle above the spectrometer due to Bremsstrahlung process is very high; one of these events is shown in figure 4.40. This kind of shower will be excluded by means of other cuts, aimed to exclude showers with a development different from the development of purely electromagnetic showers. These cuts are called *hadronic cuts*, and are explained in detail in chapter 5. The distribution obtained after applying this ulterior cut is shown in figure 4.41.

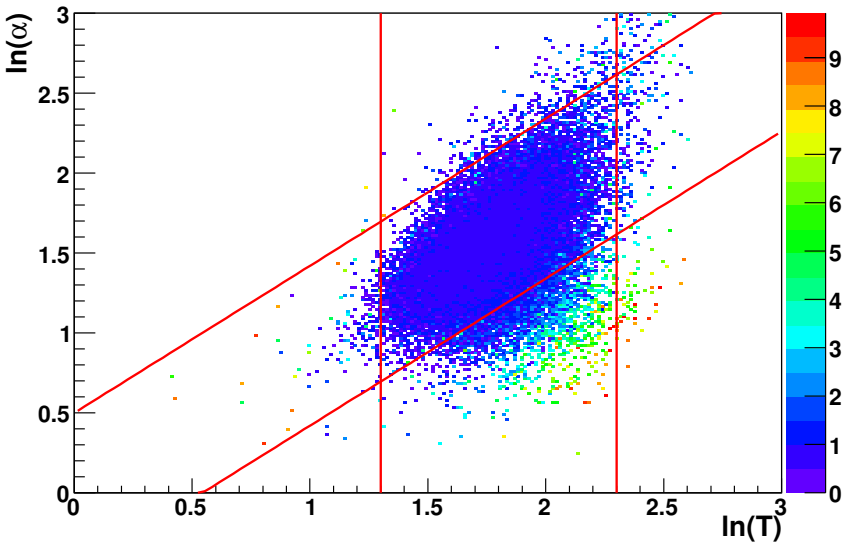

Figure 4.38: The selected events are those inside the correlation zone identified by the red lines.

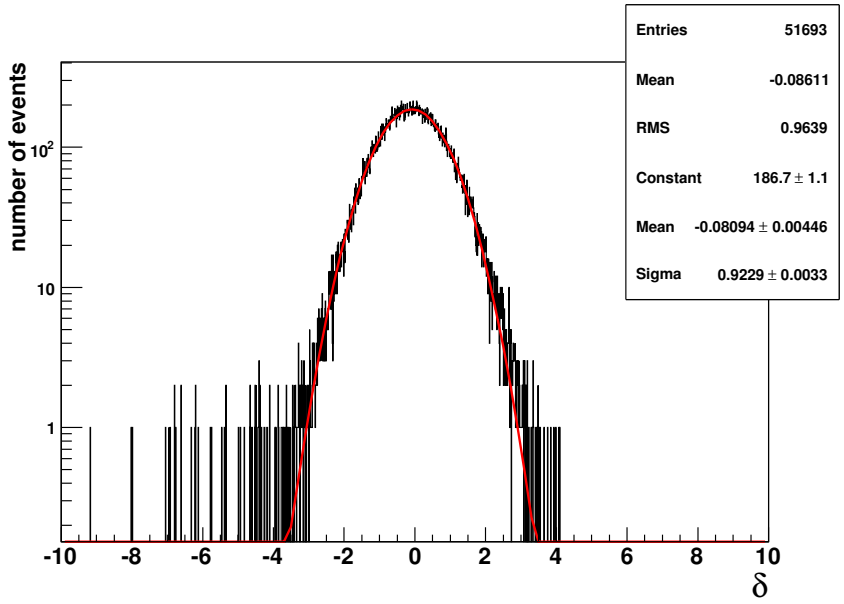

Figure 4.39: Distribution of the quantity δ after applying the cuts defined in figure 4.38.

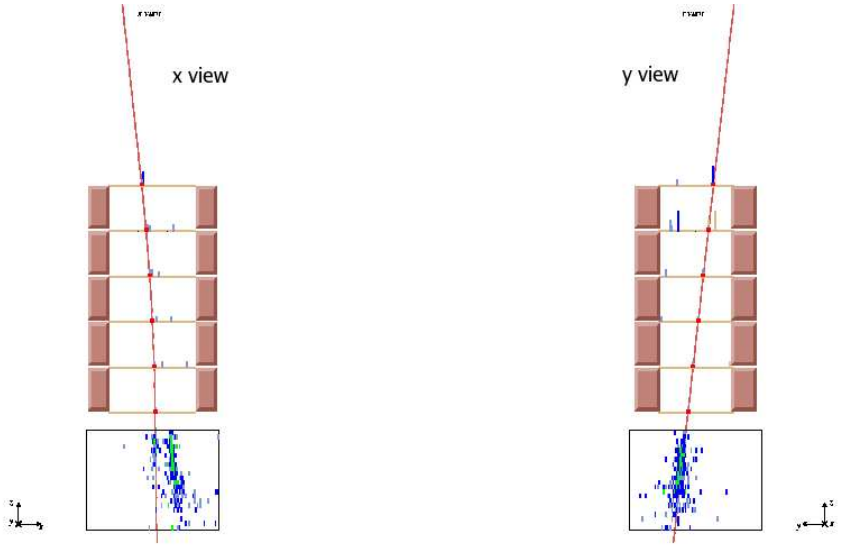

Figure 4.40: Example of a simulated electron with emission of Bremsstrahlung photon. $E_0 = 8\ GeV$, $E_2 = 6\ GeV$, $Rigidity = -0.684\ GeV$.

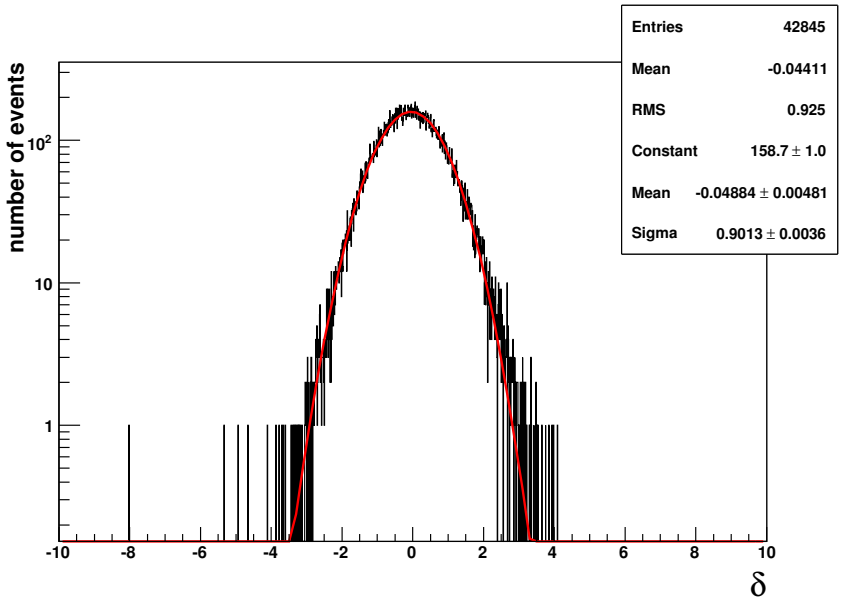

Figure 4.41: Distribution of the quantity δ after applying the cuts defined in figure 4.38 and the hadronic cuts.

Chapter 5

Spectrometer alignment

The most important objective of the PAMELA experiment is the precise determination of the flux of cosmic rays in a large energy interval, with much more statistics and accuracy than previous experiments. This task needs an exact calibration of all the detectors involved in the measurement. As already stated before, PAMELA was conceived in such a way that the system is redundant, that is the same information can be extracted from different detectors, even if only in some energy intervals and with different accuracy. Thanks to this feature, in order to perform the calibration of the detectors, it is possible not only to rely on simulation, but also to perform a cross calibration among different detectors.
The tracker calibration is very important because the spectrometer is in charge to provide an unbiased measurement of the momentum of charged particles. To obtain this information, starting from the ADC values recorded in each strip of the silicon planes, the following steps have to be performed: first it is necessary to uncompress the flight data, then to identify among them the cluster of signals generated by particles, to reconstruct the impact points, to recognize the points belonging to a physical track and finally to perform the fit to establish the deflection. All the above passages have been studied extensively by the PAMELA collaboration. It is very important to be able to measure with small uncertainties the coordinates of the impact points on the silicon sensors which compose the tracking system. The procedure that allows to accomplish this task has been described briefly in section 3.2.3, where it has been shown the

possibility to obtain a very high spatial resolution, better than 3 μm on the bending plane, for perpendicularly incident cosmic rays. Nonetheless, at the same time such a high resolution in identifying the impact points is not really useful in measuring particle deflection if the mutual positions of the silicon sensors are not known. In fact, in order to perform the track fitting, the coordinates of the impact points have to be expressed in a general frame of reference, common to the whole spectrometer. It is important to develop a method to determine the correct transformation, from the reference frame of each silicon detectors to the general frame of reference, which requires the precise knowledge of the positions of each sensor. The procedure to determine these parameters is referred to as "spectrometer alignment".
The explanation of the algorithms used to recognize a track generated by a particle in the spectrometer and to calculate its rigidity is given in section 5.1. In section 5.2 the basic principle of the alignment method is described. In section 5.3.1 the procedure that has been applied to align the system on ground before the launch of the satellite is described, while in section 5.3.2 the different approach used for flight analysis is explained. The alignment procedure can be divided in two parts, named "coherent" and "incoherent" alignment. In section 5.4 the incoherent procedure is described and the results of its application to flight data are shown. In section 5.5 the coherent procedure is explained; to use this algorithm it is necessary to know the particle momentum independently on the spectrometer: the calorimeter can provide this information by means of the reconstruction of electron energy, as explained in chapter 4.

5.1 Spectrometer deflection measurement

In order to calculate the deflection of charged particles detected by the spectrometer many studies have been performed in the past. Before explaining the method used to fit the track I will describe briefly the way in which a candidate track in the spectrometer is recognized among all the possible tracks.

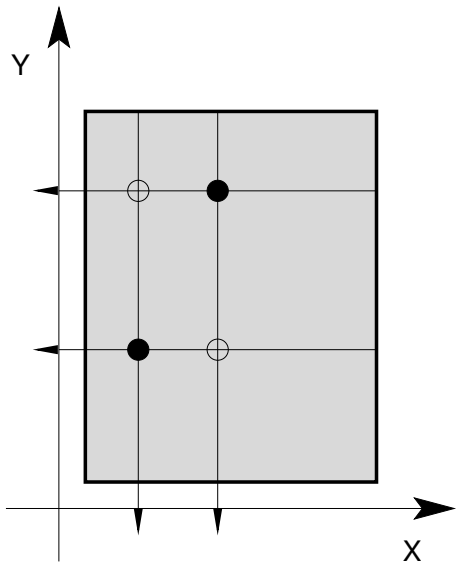

Figure 5.1: Sketch of a silicon sensor on which two clusters have been identified both on the x and on the y side. The coordinates reconstructed from the information on the hit strips are represented by the markers on the axes: they can be associated in two different configurations of impact points, indicated by the pairs of open and filled circles.

5.1.1 Track recognition

For each group of strips with signal it is possible to identify a cluster, generated by the passage of a particle, with an associated coordinate, as was explained in section 3.2.3. Before being able to fit a curve through a set of measured points and to reconstruct the track of the particle, the clusters and their associated coordinates for the two sides of each plane, that till now have been treated as independent measurements, have to be paired into a physical point of incidence. Hence, such points have to be grouped as belonging to a track.

If more than one cluster is present both on the x and y sides of a sensor, there is not a unique way to associate them to a physical impact point, as it can be seen from figure 5.1. The connection between them can

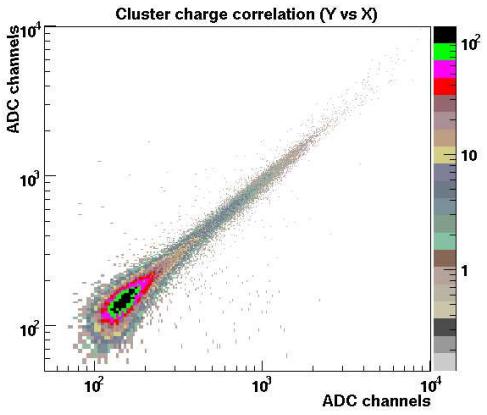

Figure 5.2: The correlation between the amplitude of the cluster signal measured on the x and y view is shown for a sample of tracks from flight data.

be done on the basis of the amplitudes of the cluster signals, since those generated by the same particle are correlated, as shown in figure 5.2. Those points, representing pairs of x and y clusters that are likely to be due to the same amount of ionization charge, carry both the x and y coordinate information of an impact point; for this reason they are called *couples* and they are used in the following track recognition phase. On the contrary, the unpaired clusters that have been excluded by means of dedicated cuts on the charge correlation, are called *singlets*. In this case only the value of one coordinate can be extracted and they are included only at the end of the track fitting if an impact point is missing on some plane. A remark has to be done about the ambiguity issue due to the way the read-out electrodes are built on the ohmic side of the ladders, as explained in section 2.3.1. In principle, the y coordinate of each reconstructed impact point has an intrinsic indetermination due to the fact that the electronic channels read the signals coming from both the strips implanted on the two sensors of a ladder, which are ~ 7 *cm* apart. At this stage, for the purpose of forming couples, each cluster that belongs to the y side of a plane is considered twice, as if two distinct clusters were present in the event. As illustrated in figure 5.3, the real combinations associated to the physical impact points of the particle are

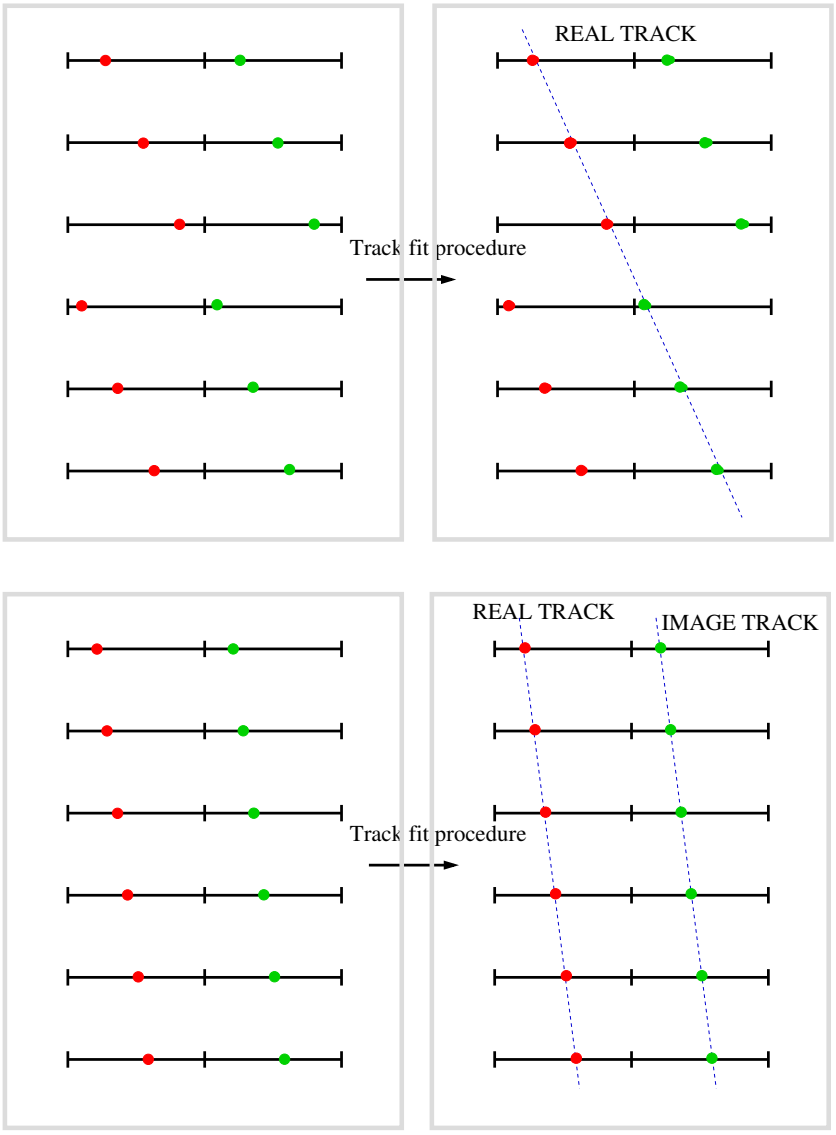

Figure 5.3: Schematic representation of the y-z projection of the spectrometer, showing the ambiguity in the coordinate determination on the y side of the silicon sensors. Each y cluster which has been identified is duplicated on both sensors, 7 cm apart (red and green dots). In most cases the indetermination is resolved as part of the normal process of track fitting, as shown in the upper part of the picture. In case a track is completely contained in a vertical set of sensors the ambiguity has to be resolved by means of the spatial information coming from the other detectors of PAMELA (lower part of the picture).

determined during the reconstruction of the track, since in general if the wrong sensor is chosen the quality of the fit will be worse. In case of a track completely contained in a vertical set of sensors (bottom picture in figure 5.3) the spatial information coming from the TOF or from the calorimeter is used in order to resolve the ambiguity.

Up to this stage the coordinates of the couples identified for each event are referred to the intrinsic x and y axes of the sensor they belong to. Then the information of all the planes has to be merged together to obtain the complete representation of tracks in the three-dimensional space. The coordinates have to be expressed in a frame of reference common to the whole spectrometer. The chosen reference frame is the one shown in figure 5.4, which has its origin at the geometrical center of the magnet, the z axis pointing upward, the y axis opposite to the main component of the magnetic field, and the x axis directed consequently to have a right-handed set of coordinates. At a first order of approximation the positions of the 36 silicon sensors forming the tracking system are known from the mechanical design of the spectrometer, so this change of reference frame can be done simply through a translation of the coordinates of the impact points. However their true positions and orientations in space are not known *a priori* at the level required in order not to spoil the very high spatial resolution of the detector, which is of few micrometers, while the mechanical position uncertainties are of the order of 500 μm. Moreover the misalignments from their design configuration could change in time, due for instance to mechanical stresses on the device. For this reason a procedure to determine *a posteriori* the actual positions of the sensors from the analysis of the flight data has been developed and will be explained in detail in this chapter.

Once the misalignments of the sensors have been taken into account and the coordinates of the couples have been expressed in a general reference frame, the real recognition procedure which groups them into potential tracks can start. The principle is to recognize which are the clusters associated with the physical track generated by the cosmic ray. For this task it is necessary to find the clusters closer to the expected trajectory.
The curve which a relativistic charged particle follows, while moving in

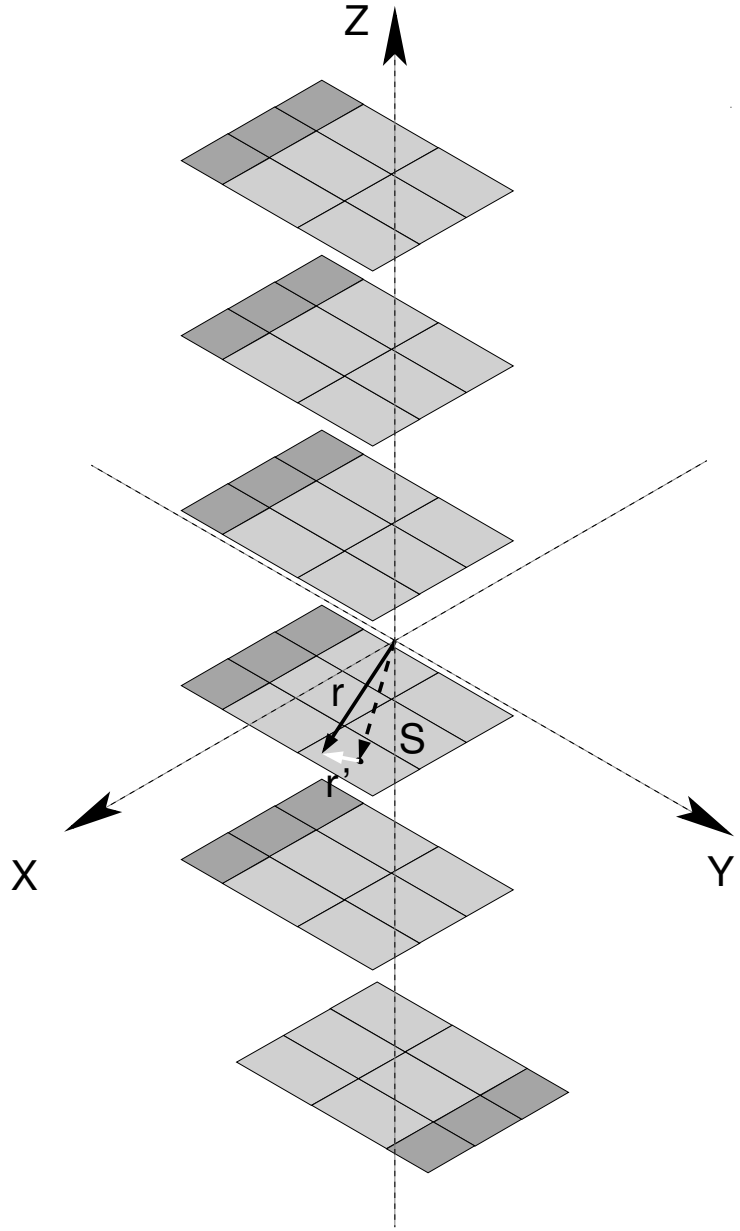

Figure 5.4: Sketch of the ideal configuration of the tracking system. The silicon sensors are arranged in six planar configurations of six sensors with aligned strips, and their positions with respect to the origin of the coordinate system are known from the mechanical design of the spectrometer. The coordinates of a point on a sensor (represented by the $\vec{r}'$ vector) can be expressed in the general reference frame (as the vector $\vec{r}$) simply through the translation of the point according to the vector $\vec{S}$ which identifies the position of the center of that sensor.

a known magnetic field, can be obtained by integrating the equation of motion:

$$m\gamma \frac{\mathrm{d}^2\vec{r}}{\mathrm{d}t^2} = q\left(\frac{\mathrm{d}\vec{r}}{\mathrm{d}t} \times \vec{B}\right) . \tag{5.1}$$

By introducing the path length $l = \beta ct$ and using $p = m\gamma\beta c$, from $\eta = 1/R = q/p$ it follows that, since $\beta = vc$ is a constant, this equation can be rewritten as:

$$\frac{\mathrm{d}^2\vec{r}}{\mathrm{d}l^2} = \frac{q}{m\gamma\beta c}\left(\frac{\mathrm{d}\vec{r}}{\mathrm{d}l} \times \vec{B}\right) = \eta\left(\frac{\mathrm{d}\vec{r}}{\mathrm{d}l} \times \vec{B}\right) . \tag{5.2}$$

The track of the particle inside the spectrometer is completely defined by a set of six numbers, namely the components of the initial position and velocity vectors. An equivalent choice of the track parameters, convenient for our experimental set up, consists in considering a fixed reference plane which is crossed by the particle and assigning a vector, which is called the *state vector* of the track. In our case the plane is expressed as $z = z^* = const$ and is placed above the spectrometer, and the chosen state vector is:

$$\vec{\alpha} = (x^*, y^*, \sin\theta^*, \varphi^*, \eta) \tag{5.3}$$

where (x^*, y^*) are the coordinates of the intersection point of the track on the reference plane, θ^* and φ^* the polar incidence angles, and η the magnetic deflection of the particle. It has 5 components, since one spatial coordinate of the initial position has been fixed. A certain vector $\vec{\alpha}$ corresponds to one and only one trajectory of a particle in the magnetic field. The track reconstruction process consists in finding the state vector that gives the best approximation of the experimental points on the silicon planes of the spectrometer. The task of the recognition phase is to identify all the possible particle tracks in each event and to provide an initial estimate for their state vectors, which will be used as a starting point for the fitting procedure.

During the track-recognition phase, in order to reduce the computation time, a simplified magnetic configuration has been employed: the field is considered uniform along the y direction, with an intensity corresponding to the average value $\langle B \rangle = 0.43\ T$. Consequently the particle

trajectories can be approximated as straight lines on the y-z plane and as an arc of circumference on the x-z plane. The analysis is carried on independently for the x-z and y-z projections using an algorithm based on a combinatorial implementation of the so-called method of the *Hough transform* [67]. It is a general feature-extraction technique which allows to detect and isolate a pattern or a shape in a complex arrangement of objects. Here it is used to recognize all the possible straight lines and circumferences that can be associated reasonably well to y and x clusters generated by a cosmic ray. In this way, two of the five track parameters are extracted from the parameters of the line and the remaining three from those of the circle. The complete vector $\vec{\alpha}$ is obtained by merging the information from any suitable combination of them and a *track candidate* is obtained; its state vector will be used as the initial condition in the complete fitting procedure, explained in the next section.

5.1.2 Track fitting

The trajectory of the particle inside the spectrometer is calculated through an iterative procedure. From the analysis of the clusters that potentially belong to a physical track by means of the Hough transform a first guess of the state vector $\vec{\alpha}$ is obtained, and used as the initial condition to solve the equations of motion 5.2. Whereas during the track-recognition phase a simplified magnetic configuration is employed, here the real $\vec{B}$ field is used. The map of the magnetic field has been obtained from a sampling of the field components in a three dimensional grid of points inside the magnetic cavity; the value of the field in each point of the track is extracted from the measured values using a three-dimensional linear interpolation. To solve the equations of motion with a non constant magnetic field the Nyström algorithm [64] is used, which is based on the stepwise numerical integration of the equations with the Runge-Kutta method, as it has been coded in FORTRAN in the CERN software libraries [68]. This method allows to obtain the trajectory starting directly from the system of second-order differential equations of motion without the need of the intermediate step of reducing them to a first-order system, thus resulting in a high computational efficiency. The impact points

that are obtained from the intersection between the trajectory and the planes of the spectrometer are then compared with the measured ones: a χ^2-function, which states how much the fit differs from the actual physical track is calculated:

$$\chi^2(\vec{\alpha}) \;=\; \sum_i^{N_x} \left(\frac{x_i - \tilde{x}_i(\vec{\alpha})}{\sigma_{x_i}} \right)^2 + \sum_i^{N_y} \left(\frac{y_i - \tilde{y}_i(\vec{\alpha})}{\sigma_{y_i}} \right)^2 \tag{5.4}$$

In the above equation (x_i, y_i) represents the measured coordinates of the points on the i-th plane, and the coordinates obtained from the fit for a certain state vector $\vec{\alpha}$ are defined as $(\tilde{x}_i, \tilde{y}_i)$. If some singlets are present in the track the number of planes included in the track on the x-view, N_x, can be different from the number of planes on the y-view, N_y. The uncertainties on the coordinates, σ_{x_i} and σ_{y_i}, have been studied by means of simulation [49]. It was demonstrated that the uncertainties depend on the estimated angle of the track and on the algorithm used to reconstruct the measured points. Moreover a correction on the uncertainties is performed taking into account the "quality" of the cluster, that is the noise of the strips which compose it. By minimizing equation 5.4 as a function of the components of $\vec{\alpha}$, the values of the initial conditions of integration that result in impact points nearer to the experimental ones are found. The minimization is performed with an iterative procedure, based on an analytical approach [69]. To minimize the function 5.4 the following system of partial derivatives has to be solved:

$$\frac{\partial}{\partial \alpha_k} \left(\chi^2(\vec{\alpha}) \right) \;=\; 0 \,, \qquad k \;=\; 1 \ldots 5 \,. \tag{5.5}$$

Starting from the χ^2 evaluated for a given initial guess $\vec{\alpha}_0$, the function at a nearby value $\vec{\alpha} = \vec{\alpha}_0 + \Delta\vec{\alpha}$ is obtained by means of a second-order Taylor series expansion:

$$\chi^2(\vec{\alpha}) \;\simeq\; \chi^2(\vec{\alpha}_0) + \sum_{h=1}^{5} \left. \frac{\partial \chi^2}{\partial \alpha_h} \right|_{\vec{\alpha}_0} \Delta\alpha_h \;+\; \frac{1}{2} \sum_{h,l=1}^{5} \left. \frac{\partial^2 \chi^2}{\partial \alpha_h \partial \alpha_l} \right|_{\vec{\alpha}_0} \Delta\alpha_h \Delta\alpha_l \,, \tag{5.6}$$

in which the sums are on the five components of the $\vec{\alpha}$ vector. When this expression replaces $\chi^2(\vec{\alpha})$ in the minimization conditions (5.5), it gives:

$$0 + \sum_{h=1}^{5} \left.\frac{\partial \chi^2}{\partial \alpha_h}\right|_{\vec{\alpha}_0} \frac{\partial \Delta\alpha_h}{\partial \alpha_k} + \frac{1}{2} \sum_{h,l=1}^{5} \left.\frac{\partial^2 \chi^2}{\partial \alpha_h \partial \alpha_l}\right|_{\vec{\alpha}_0} \frac{\partial}{\partial \alpha_k} (\Delta\alpha_h \Delta\alpha_l) \simeq 0 \quad (5.7)$$

with $k = 1 \ldots 5$. Now, since:

$$\frac{\partial \Delta\alpha_h}{\partial \alpha_k} = \delta_{hk} , \quad (5.8)$$

where δ_{hk} is the Kronecker delta, equation (5.7) becomes:

$$\left.\frac{\partial \chi^2}{\partial \alpha_k}\right|_{\vec{\alpha}_0} + \sum_{h=1}^{5} \left.\frac{\partial^2 \chi^2}{\partial \alpha_h \partial \alpha_k}\right|_{\vec{\alpha}_0} \Delta\alpha_h \simeq 0 , \qquad k = 1 \ldots 5 . \quad (5.9)$$

By introducing the first-derivative vector $\vec{V}$ and the second-derivative matrix Z, both calculated in $\vec{\alpha}_0$:

$$(\vec{V})_k = \left.\frac{\partial \chi^2}{\partial \alpha_k}\right|_{\vec{\alpha}_0} \qquad (\mathsf{Z})_{h,k} = \left.\frac{\partial^2 \chi^2}{\partial \alpha_h \partial \alpha_k}\right|_{\vec{\alpha}_0} \quad (5.10)$$

equation (5.9) can be rewritten as:

$$\vec{V} + \mathsf{Z} (\vec{\alpha} - \vec{\alpha}_0) \simeq 0 , \quad (5.11)$$

and the improved vector is:

$$\vec{\alpha} \simeq \vec{\alpha}_0 - \mathsf{Z}^{-1} \vec{V} . \quad (5.12)$$

This value of the state vector is used as a new set of initial conditions for integrating equation 5.2, and the procedure is repeated until the desired degree of convergence is reached.

Extensive studies of the spectrometer performances have been done before the launch. The results of measurements performed in 2003 at the CERN SPS beam with protons of known momentum are shown in figure 5.5, where the uncertainties on the rigidity is shown as a function

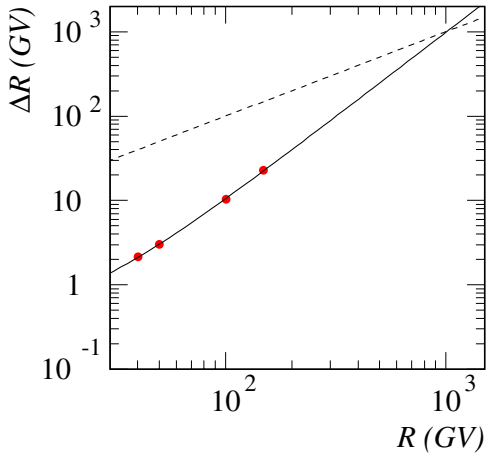

Figure 5.5: Results of the spectrometer rigidity resolution obtained from the measurements performed in 2003 at the CERN SPS beam.

of the rigidity. The dashed line is the bisector $\Delta R = R$. The fit to the four experimental points (solid curve) assumes a contribution from multiple scattering ($\Delta R_{ms} \propto R$) and a contribution from spatial resolution ($\Delta R_{sr} \propto R^2$). The intersection of the two curves gives the maximum detectable rigidity of the spectrometer, MDR, which is defined as the value of the rigidity which corresponds to a 100% uncertainty on its measurement. The results of figure 5.5 show that an MDR of about 1 TeV can be achieved.

5.2 Alignment

The task of the alignment procedure is to determine at a micrometer level the positions of the silicon-sensor in a general frame of reference common to the whole spectrometer. Before going on with the detailed explanation of the alignment method, the transformation used to find the real position of the tracker sensors will be clarified. The real position and orientation in three-dimensional space of each silicon sensor in the PAMELA reference frame can be unambiguously defined by a set of six numbers, which represents the components of a vector of translation

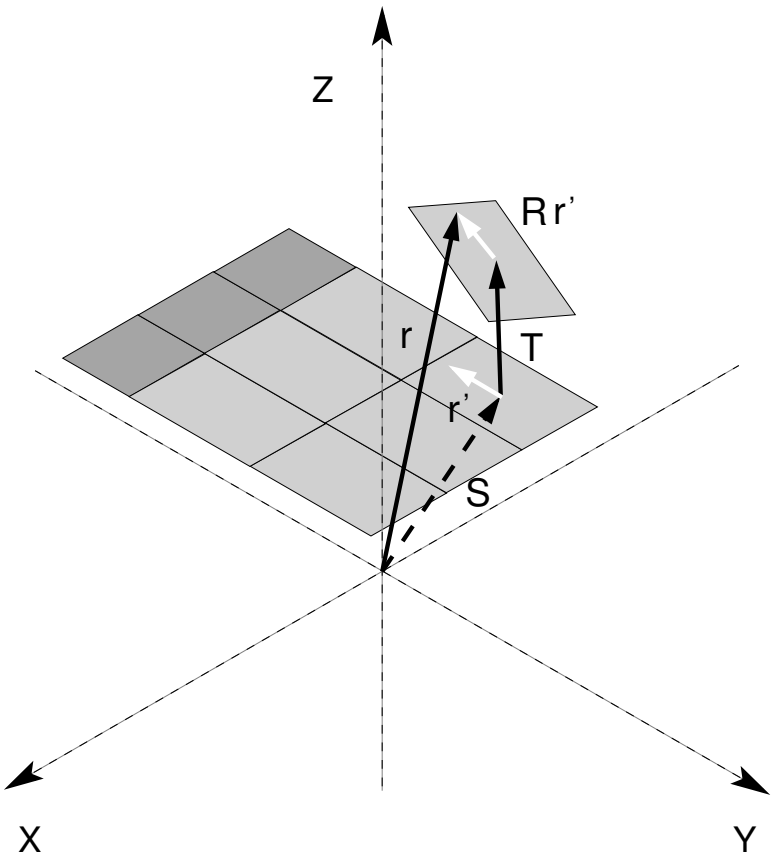

Figure 5.6: Sketch of the transformation of frame of reference which corrects for the misalignment of the sensors. The vector $\vec{r}'$ contains the coordinates of a point as measured in the silicon sensor frame. Before translating the vector according to the sensor position in the mechanical design (vector $\vec{S}$), the sensor has to be rotated by the matrix R and translated by the vector $\vec{T}$ to account for the misalignment. The final position of the point in the general reference frame is identified by the vector $\vec{r}$ given by equation 5.13.

and three angles of rotations in respect to the ideal configuration given by the mechanical design of the instrument. For the alignment purpose, each sensor is considered as a perfectly rigid body with the shape of a rectangular parallelepiped. The convention which has been chosen to define this transformation of reference frame, consists in using in turn the rotations ω, γ and β along the z, y and x orthogonal coordinate axes passing through the center of the ideal sensor, and the translations Δz, Δy and Δx along those three axes which shift the sensor from its design position to the real one.
As shown in figure 5.6, if the vector $\vec{r}' = (x', y', 0)$ represents the coordinates as measured in respect to the center of the sensor, then the coordinates $\vec{r} = (x, y, z)$ in the PAMELA reference frame after the rototranslation from the ideal to the real position can be expressed as:

$$\vec{r} \;=\; \left(\mathsf{R}\,\vec{r}' \;+\; \vec{T}\right) \;+\; \vec{S}\,, \tag{5.13}$$

where $\mathsf{R}(\omega, \gamma, \beta)$ is the rotation matrix, $\vec{T}(\Delta x, \Delta y, \Delta z)$ the translation vector, and $\vec{S}$ is the vector which defines the position of the center of the sensor that the point belongs to, as known from the mechanical project. In the hypothesis that the rotations are small, a first-order approximation can be used and the matrix R reduces to:

$$\mathsf{R} = \begin{pmatrix} 1 & -\omega & \gamma \\ \omega & 1 & -\beta \\ -\gamma & \beta & 1 \end{pmatrix}\,. \tag{5.14}$$

The translation vector $\vec{T}$ is instead simply given by:

$$\vec{T} \;=\; (\Delta x, \Delta y, \Delta z)\,, \tag{5.15}$$

and the vector $\vec{S} \;=\; (X, Y, Z)$ contains the known coordinates of the center of the sensor in the reference frame of PAMELA, according to the mechanical design.
Using previous equations, the rototranslation (5.13) which provides the real coordinates $\vec{r} \;=\; (x, y, z)$ as a function of those measured on the

sensor $\vec{r}' = (x', y', 0)$ becomes:

$$\begin{cases} x &= x' &- \omega\, y' &+ \Delta x &+ X \\ y &= \omega\, x' &+ y' &+ \Delta y &+ Y \\ z &= -\gamma\, x' &+ \beta\, y' &+ \Delta z &+ Z \end{cases} . \tag{5.16}$$

In this framework, the alignment issue reduces to identify for each sensor the six parameters $\vec{A} = (\beta, \gamma, \omega, \Delta x, \Delta y, \Delta z)$.

Before the launch of PAMELA a big effort has been put to determine accurately the right position of each sensor (for the details see [70]). The quality of the alignment procedure can be evaluated from the distribution of the differences between the set of measured coordinates and those determined by the intersection of the fitted track with the sensors, the so-called *residuals*. We expect that if the tracker sensors are not properly aligned the residual distributions are not centered on zero and their width is wider in comparison to what is expected from the analysis of the impact point reconstruction. See for example in figure 5.7 the residuals obtained, using the nominal position known from the mechanical design, for a sample of events with fixed energy taken from beam test data: the discrepancies between measured and fitted point are up to several hundred of micrometers. A set of alignment parameters was determined [70] and figure 5.8 shows the resulting residual distributions after the transformation. It is evident by comparing with the previous distributions that now the residuals are very well centered to zero and also that their widths are lower.
This demonstrates that with the alignment of the system on ground a very good level of accuracy was obtained. However, after the stress of the launch the alignment parameters could have changed. In fact, by analysing the residuals for a set of events acquired in flight, it seems that the positions of the sensors are changed. This is proved by the distribution of the residuals, shown in figure 5.9, obtained for protons selected from flight data. These data were analyzed with the position-finding-algorithm $COG4$, consequently their width is larger than the nominal resolution expected with the non-linear η-algorithm. The unbiased algorithm $COG4$ was used in the alignment procedure in order to be sure of

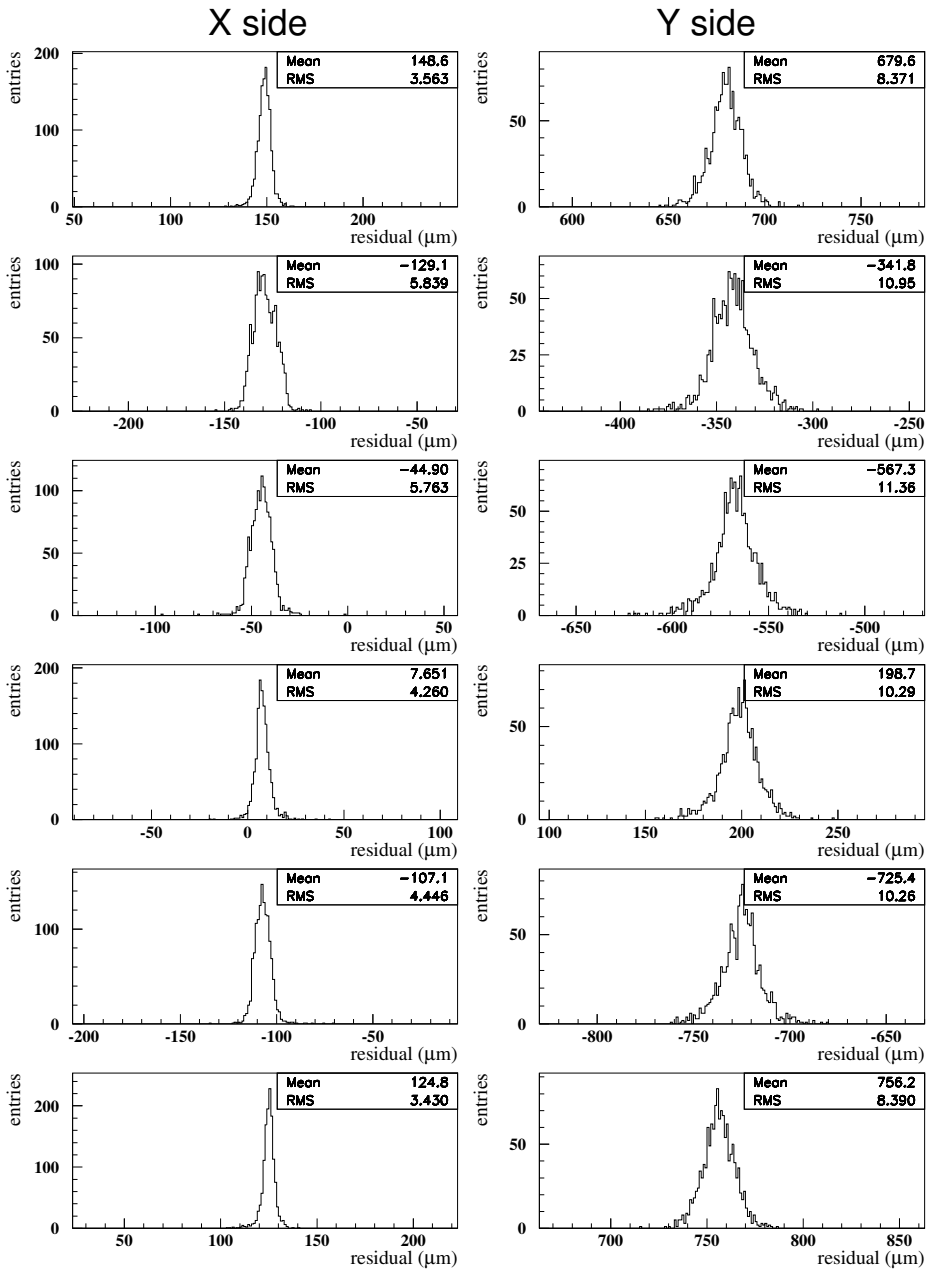

Figure 5.7: Distributions of the spatial residuals for a column of sensors, for a sample of tracks from test-beam data.

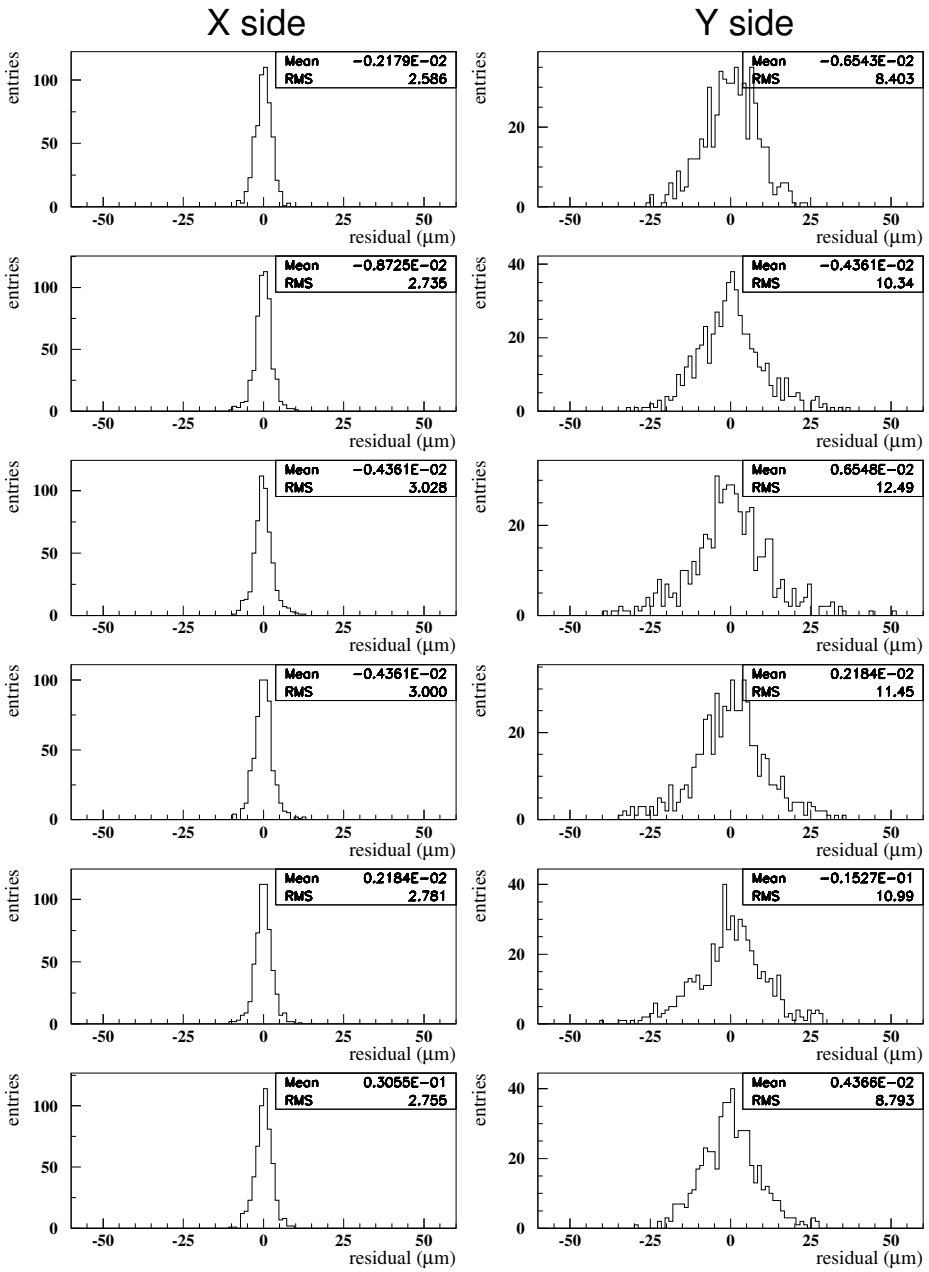

Figure 5.8: Distributions of the spatial residuals for a column of sensors after the alignment with test-beam data.

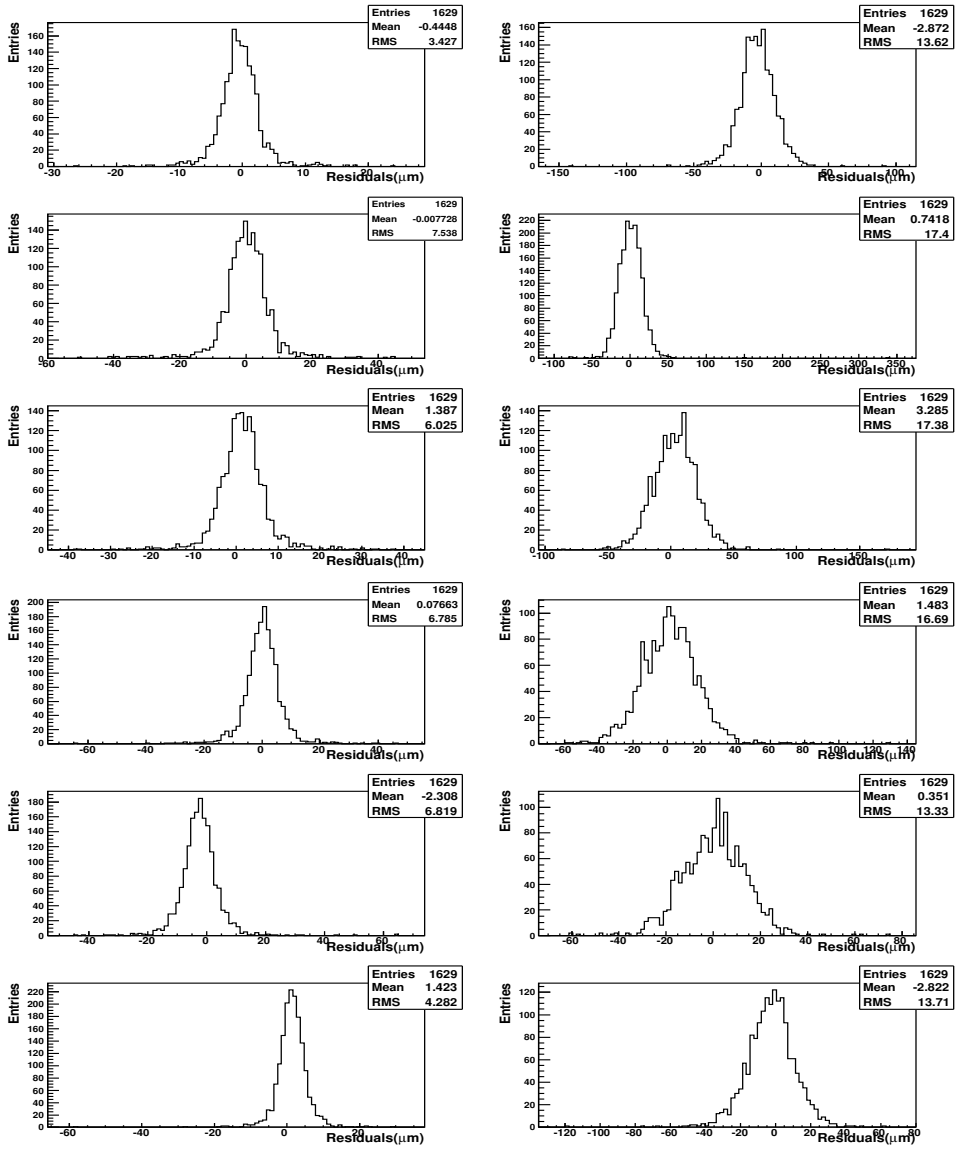

Figure 5.9: Distributions of the spatial residuals for a sample of proton tracks selected from flight data, analyzed by applying the test-beam alignment parameters.

avoiding systematic errors. When the flight data are analyzed using the set of alignment parameters found previously from ground data analysis a misalignment effect of some micrometers appears, as can be seen from the mean values of the distributions in figure 5.9. Therefore it is necessary to develop a procedure in order to find how to correct the alignment parameters using flight data.

The alignment principle

The rototranslation parameters which give the right position of the sensors are those that generate the residuals distribution that we expect, namely centered in zero with the width resulting from the impact point resolution. In other words the right parameters are those generating reconstructed coordinates of the points of the track as much similar as possible to the measured ones. To clarify how to use this feature it is useful to look at some pictures. In figure 5.10, on the left, a set of measured impact points are shown, according to the ideal configuration of the planes. If the two external sensors are kept fixed as reference, the correct positions of the others can be found by requiring that the points lie on the reconstructed trajectory of the particle. It is clear that if the deflection, and consequently the *shape* of the track, is not known a priori, there are infinite combinations of different positions and curvatures which comply with the measured points. On the contrary, if the shape of the track is correctly reconstructed on the basis of its known deflection, and two positions in space are determined on the reference planes, the comparison between the other measured points and the expected ones results in a unique configuration of the sensor positions.
This comparison mathematically can be done through the minimization of a χ^2 function that contains the difference between the measured coordinates of the impact points $\vec{r}_{ij}(\vec{A})$ and the corresponding reconstructed coordinates $\tilde{\vec{r}}_{ij}(\vec{A},\vec{\alpha})$, for each plane i and event j. Both the sets of coordinates depend on the alignment-parameter set $\vec{A}$, but the reconstructed coordinates depend also on the vector $\vec{\alpha}$, in fact as explained in section 5.1 the trajectory of a cosmic ray in the magnetic field is determined unambiguously by a certain vector $\vec{\alpha}$. Consequently the function

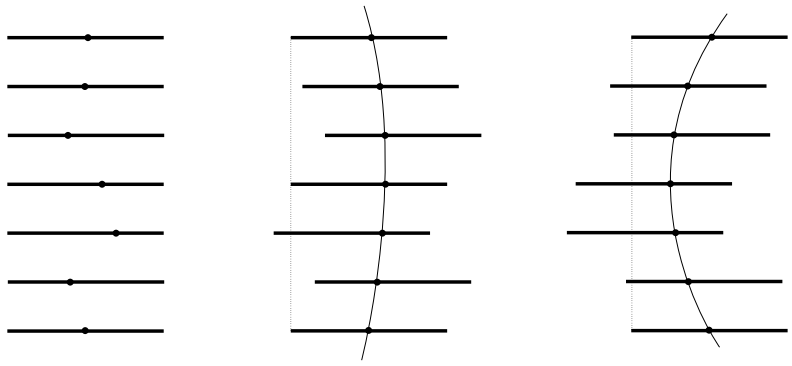

Figure 5.10: Schematic description of the alignment principle. The pictures represent simplified two-dimensional sketches of a column of sensors. In the left picture a set of measured impact points are shown, according to the ideal configuration of the planes. In the center and right pictures two of the infinite possible combinations of positions that comply with the measured points are shown.

to be minimized (see also equation 5.4 for the meaning of symbols) is a global χ^2 given by the sum of the χ^2 of equation 5.4 for each single track, in details:

$$\chi^2(\vec{A}) = \sum_{j=1}^{N_{ev}} \left[\sum_{i=1}^{N_x} \left(\frac{x_{ij}(\vec{A}) - \tilde{x}_{ij}(\vec{A}, \vec{\alpha})}{\sigma_{x_i}} \right)^2 + \sum_{i=1}^{N_y} \left(\frac{y_{ij}(\vec{A}) - \tilde{y}_{ij}(\vec{A}, \vec{\alpha})}{\sigma_{y_i}} \right)^2 \right] \tag{5.17}$$

For each one of the N_{ev} events the residuals on each plane are calculated and then, with an iterative procedure, the minimum of the global χ^2 is found, by varying the value of the alignment parameters $\vec{A}$.
With simulation studies has been found that not all the 6×36 parameters which identify all the spectrometer sensors, can be let free in the minimization, in fact the procedure does not converge because there is not a unique minimum in all the parameters. The consequence is that only a relative alignment is possible. In principle an absolute frame of reference exists to which positions could be referred to: in fact the presence of a non-uniform magnetic field causes the space around the sensors to be not isotropic, so that the coordinate axes could be oriented, and the origin placed, according to its shape. However in practice the inhomogeneities

of $\vec{B}$ have proved to be too small for the method to be sensitive enough to them. In order to clarify the procedure, let us consider separately each group of six detecting elements one under another along the cavity of the spectrometer. In this case two of the sensors are taken as reference and they are assumed as being really placed according to their ideal design configuration: this means that their rotations β, γ, ω and translations Δx, Δy, Δz are set to zero and kept constant during the minimization process.
A consequence of this kind of approach to the misalignment problem is that the incoming direction of particles can be affected by a systematic error, of the order of the precision in knowing the mechanical position of the two reference sensors, since their reciprocal positions cannot be determined. In spite of this uncertainty in the identification of the angle of incidence of cosmic rays, the effect, at a first approximation level, does not interfere with a correct measurement of their momentum, which is the real quantity of interest.
The best choice for the two elements to be kept fixed is the pair of most external sensors, since in this way the indetermination on the incoming direction of particles would be minimized. However the bottom plane of the tracking system differs from the others in its geometric configuration: in fact, as it is represented in figure 5.4, the plane is turned upside down by means of a rotation around a line parallel to the x axis. For this reason the aluminium frame that contains the silicon detectors is attached to the structure of the magnet in a different way, and the mechanical location of the last plane is affected by a greater uncertainty. Therefore to align the spectrometer on ground the plane located above the bottom one has been chosen as reference. Now the task is to find the new set of alignment parameters, but starting from a system that has already been aligned with the parameters set found on ground. In this case there is no reason from which the last plane should now be worse than the others, and the alignment of the single columns has been performed fixing the two most external sensors.

It is convenient to remark that to determine unambiguously the right set of alignment parameters the shape of the track has to be fixed in the minimization of the $\chi^2(\vec{A})$ in equation 5.17. This means that the

deflection of the particle has to be known a priori, independently on the spectrometer reconstruction that can be affected by a misalignment error. In other similar experiments with spectrometers the most common way to perform the alignment of the system is to collect a certain set of particles without the magnetic field, because in this case the track is straight, and its shape is perfectly known a priori. This strategy cannot be adopted in our case because, as described in chapter 2, the PAMELA experiment has a permanent magnet. This implies that the alignment procedure is more complex because we have to use curved tracks, and their shape has to be found by using the value of the deflection obtained without the spectrometer information.
It has to be noticed also that a big computational effort is necessary for this procedure. In fact for each variation of the vector $\vec{A}$, all the tracks of the sample have to be fitted again in order to reconstruct the trajectories that result from the new configuration of sensors; the algorithm used to fit the tracks is similar to the one explained in section 5.1, but with a fixed value of the deflection.

5.3 The alignment method

5.3.1 Alignment at ground

From the previous explanation of the general alignment principle should be evident that, in order to align our system, it is necessary to know the shape of the analyzed tracks. During ground data analysis the set of alignment parameters was found using a sample of 50 GeV/c proton tracks selected from data acquired during a beam-test session at the CERN SPS facility in 2003. The set-up was such that a proton beam with a momentum $p = 50\ GeV/c$ hits in turn each of the six sensors on the top plane of the spectrometer perpendicularly. Moreover, the moving support which PAMELA lay on with its longitudinal axis parallel to the floor, was inclined in respect to the beam, first in the x-z plane in order to have particles crossing the sensors with an angle of about 2°, then in the y-z plane with an incidence angle of about 5°. The importance of having non-orthogonal trajectories of particles available for the alignment pro-

cedure will be better explained later in this section. Since protons do not emit Bremsstrahlung photons and at this energy the ionization losses are negligible, they are expected to cross the spectrometer with energy equal to the energy of the beam. This implies that the deflection of the particles is exactly known independently on the tracker measurement, and was fixed to the nominal value during the minimization of function 5.17. Before going on with the discussion regarding the flight data, some issues on the alignment parameters and the method used to perform the minimization will be analyzed. These considerations are valid also for the flight data alignment.

Among the three coordinates of the particle impact points on the silicon planes, only those that are actually measured, namely x and y, appear in the expression given by equation 5.17 for the χ^2. The parameters which are contained directly in the correction for the misalignment of x and y (see equations 5.16) are only Δx, Δy and ω, while β, γ and Δz get involved exclusively as higher-order corrections, through z, in the calculation of the fit-reconstructed coordinates $\tilde{x}$ and $\tilde{y}$. For this reason the method is less sensitive to variations of the rotations around the x and y axes and of the translations along z. In particular, it is necessary that the event sample which is used for the alignment, contains not only perpendicular trajectories of particles with respect to the sensors, but also inclined ones. In fact, for instance, in case all the tracks were orthogonal to the planes, a variation of Δz would not make the coordinates $\tilde{x}$ and $\tilde{y}$ resulting from the fit vary, and likewise the χ^2. For a similar reason, in order to increase the sensitivity to rotations, impact points are required to be spread on the sensors over an area as large as possible.

The approach used to align the whole spectrometer was to divide the detector in different columns of silicon sensors and apply the alignment procedure independently on each single column. This approach was necessary because the test was performed with particles incident on each column of sensor in turn. However, in order to measure the deflection of particles in all the acceptance of PAMELA, the information about the positions of the six columns has to be merged together, and an alignment

of the whole tracking system is required. A procedure has been developed, which employs particles whose trajectory go across the columns, and which allows to determine the mutual positions of all the 36 silicon sensors of the spectrometer. Before the launch of PAMELA, cosmic rays have been acquired on ground. Among these events tracks that intercept the spectrometer in all its acceptance are present and they have been used to optimize the alignment algorithm.

5.3.2 Alignment in flight

In order to perform a similar analysis with flight data we need a sample of events whose deflection is known without spectrometer information: the only candidates for such an analysis are electrons and positrons because their energy can be measured with a high degree of accuracy with the calorimeter, as explained in chapter 4. There are two problems that prevent us to use the same method used for ground alignment, by simply substituting the sample of protons from the beam with the sample of $e^{\pm}$ selected from flight data.
The first problem is a matter of statistics. In fact the procedure to find the minimum value of the χ^2 function by varying the set of parameters $\vec{A}$ needs at least about 1000 event on each column to converge properly, obtaining a statistical error lesser than the required accuracy. The expected flux of electrons, in the energy range where the calorimeter resolution is adequate, is too low to obtain the required statistics.
The second problem relies on the reconstruction of the electron and positron energy: unfortunately, as will be explained better in section 5.5.1, these particles lose some of their energy due to the Bremsstrahlung effect passing through the material above the spectrometer. Since the spectrometer measures the deflection of charged particles, its information is related only to the energy of electrons and positrons, on the contrary the calorimeter measures the total initial energy because it usually collects also the energy carried by the Bremsstrahlung photons. This implies that a difference arises between the deflection calculated from the calorimeter output and the deflection of the charged particle in the spectrometer. A simulation study has demonstrated that, if the minimization algorithm

is applied by using the deflection measured by the calorimeter, the positions of the sensors after the alignment have systematic errors of about $5 \div 10\ \mu m$.

For this reason an alternative approach has to be used: a different algorithm that uses electrons, positrons and protons has been developed. The principle is to separate the procedure in two different steps named *incoherent* and *coherent* alignment. In fact we can think that there is a component of the relation between the real position of the detectors and the nominal position, due to random displacements around the track (incoherent), and another component which can be expressed as a change in the track curvature (coherent). These two components are depicted in figure 5.11 and figure 5.12.

The first step of incoherent alignment is aimed to align the system around the reconstructed track by using protons. However if there is a combination of misalignments that simulates a curvature, in the approximation of constant magnetic field, this causes a constant error on deflection, independently on the energy of the particle. This systematic deflection error cannot be detected with the incoherent alignment procedure, which uses in the minimization of equation 5.17 the deflection measured by the tracker itself. On the contrary, an independent evaluation of the momentum can be used to put in evidence possible systematic errors for the tracker. This second step is the essence of the coherent-alignment procedure: for this purpose electrons and positrons are used.

The random sensor displacements, not correlated from sensor to sensor, generate the incoherent misalignment, that does not change the track curvature, while the coherent misalignment comes from those movements of the sensors correlated with the movement of the other sensors. Mathematically the whole set of alignment parameters can be written, as a first-order approximation, in the following way:

$$A_i = A_i^0 + \frac{\partial A_i}{\partial \delta\eta} \cdot \delta\eta \tag{5.18}$$

for each one of the alignment parameter[1] $i = 1, 204$.

[1]As previously explained not all the parameters of the 36 sensors can be deter-

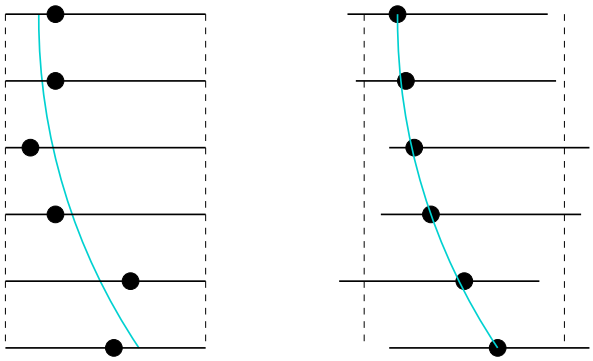

Figure 5.11: Schematic description of the incoherent misalignment. The curvature of the fitted track is the same before and after moving the sensor. The residual of the measured points are much lower after the correction for the incoherent alignment.

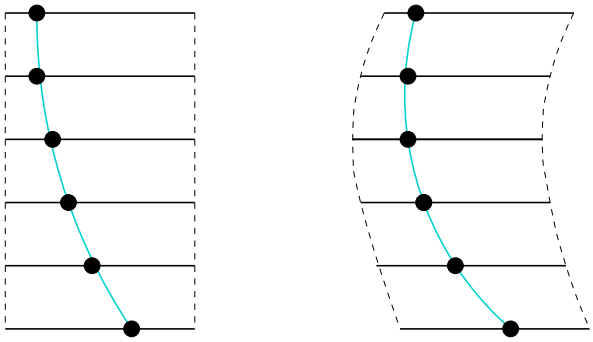

Figure 5.12: Schematic description of the coherent misalignment. The set of parameters that corrects this misalignment results in a fixed change of the curvature. The residuals of the measured points remain the same after the correction for the incoherent alignment.

The first term on the right is the incoherent alignment parameter, which is not connected with a deflection shift. It can be found minimizing the χ^2 function described by equation 5.17, by using high energy proton tracks selected from flight data, with the deflection value fixed to the one measured by the spectrometer ($\eta_{fix} = \eta_m$). The method used for this procedure, the selection cuts and its final results are presented in the next section 5.4.
The second term on the right of equation 5.18 is the coherent parameter, connected with a deflection shift $\delta\eta$, that has been determined by means of electrons and positrons analysis, described in detail in section 5.5. It was proved from simulation studies that the A_i values, at a first order approximation, are linear with the deflection shift, with a coefficient that can be determined in the following way:

$$\frac{\partial A_i}{\partial \delta\eta} = \frac{A_i^0(\Delta\eta) - A_i^0(0)}{\Delta\eta} \tag{5.19}$$

where the values of $A_i^0(\Delta\eta)$ are those determined by applying the incoherent alignment procedure to protons with the deflection fixed to a value different from the measured one, namely $\eta_{fix} = \eta_m + \Delta\eta$.

5.4 Incoherent alignment

The incoherent alignment parameter determination is performed by minimizing the χ^2 function in 5.17. The sample of tracks used consists in protons selected from flight data; since the available statistics of protons is very high, strong cuts can be applied to be sure to avoid errors due to bad tracking or any other effect that could prevent us to determine the alignment parameters with the desired precision. First of all a basic set of cuts was applied in order to select cosmic rays crossing the apparatus within the detector acceptance. It consists in the following conditions:

- single track in the spectrometer;

mined independently, two of the sensors have to be fixed as reference position; the rototranslation of each one of the sensor is described by 6 parameters, so the total number of parameters to be determined is $6 \times (36 - 2) = 204$

- one and only one hit paddle for each plane in the TOF;
- no hits in AC;
- no albedo ($\beta_{TOF} > 0$);
- events acquired out of the radiation belts;
- calorimeter geometric consistency[2].

Another set of cuts has been applied in order to select only non-interacting protons:

- no interaction in calorimeter[3];
- positive deflection measured by the tracker;
- energy release in the silicon tracker planes $(dE/dx) < 3\ mip$;

Some other cuts have been developed expressly for alignment purpose and have been applied in order to select only good tracks in the spectrometer:

- no bad strips in the cluster on the first and last spectrometer plane;
- spectrometer data compressed with the corresponding online calibration parameters;
- 6 hits both in x and y view;
- track fit procedure converged with a number of steps lower than 100;
- rigidity from tracker greater than 7 GV/c, otherwise multiple scattering effects can spoil resolution;
- rigidity from tracker lower than 100 GV/c, to perform rigidity reconstruction with resolution better than 10%.

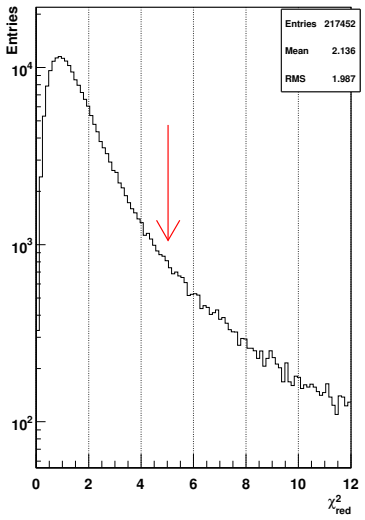

Figure 5.13: Distribution of χ^2_{red} for a sample of flight data events, the red arrows is the cut applied for alignment purpose.

After these selections applied on about 300 days of data we collected 48124 events. Starting from this sample further track-quality cuts have been applied. The distribution of the reduced χ^2_{red} from the tracking is shown in figure 5.13: all the events with $\chi^2_{red} > 5$ were rejected. Furthermore the spatial residuals between measured and fitted coordinates are computed and the events with at least one hit out of 5 times the width of the residual distribution were discarded as well.
It is useful to point out that cuts which depend on the alignment condition of the system could induce a bias in the results. In particular since the residual distributions are obtained with a system not perfectly aligned the χ^2 cut could exclude tracks which hit the more misaligned sensors. To avoid this effect the excluded events are reinserted after the

[2]It means that the distance between the track fitted in the calorimeter and the extrapolated spectrometer track has to be lower than 2 *cm*.

[3]To identify non interacting particles in the calorimeter a cut is applied on the fraction of energy collected around the trajectory of the particle inside the calorimeter, as obtained extending the spectrometer track.

first minimization and the procedure is repeated iteratively.

Due to the high number of parameters to be determined, care has to be taken to optimize the computation time and keep it reasonable, in fact the time needed to minimize a function with N free parameters is approximately proportional to N^3 [71]. For this reason each group of six detecting elements one under another along the cavity of the spectrometer has been considered separately: to such set, the name of *column* of sensors is given. In this way the incoherent alignment procedure is composed of 2 steps: first each column is aligned in respect to two reference sensors by using the technique described previously; then the whole tracking system is considered and the mutual positions of the columns are obtained. In fact after the determination of the alignment parameters for each one of the 6 columns of sensors we can correctly measure, apart from the coherent shift, the deflection of particles that cross only one column. However the cosmic ray flux is isotropic, consequently, to measure the deflection of particles in all the acceptance of PAMELA, the information about the position of the 6 columns has to be merged together and an alignment of the whole tracking system is required.

Single column alignment

In order to align each column we have selected, starting from the previously described sample, events that cross only a single column. Hence the selected tracks, with the deflection value fixed to the measured one, have been used to minimize the χ^2 function of equation 5.17 and to find the 24 parameters of the column. Since any of the six columns that compose the tracking system is equivalent to the others for the alignment purposes, the procedure has been applied independently to each of them. In order to test whether the alignment procedure works properly it is useful to look at the residuals of the coordinates obtained using the new alignment parameters. In fact the incoherent misalignment influences the residuals distribution, while the coherent one has no influence. In figure 5.14 the residual distribution obtained for one column using the new alignment parameters calculated with the single alignment procedure is shown. The misalignment effect, that was present for the same sample analyzed with ground alignment parameter (see figure 5.9), disappears: in fact the av-

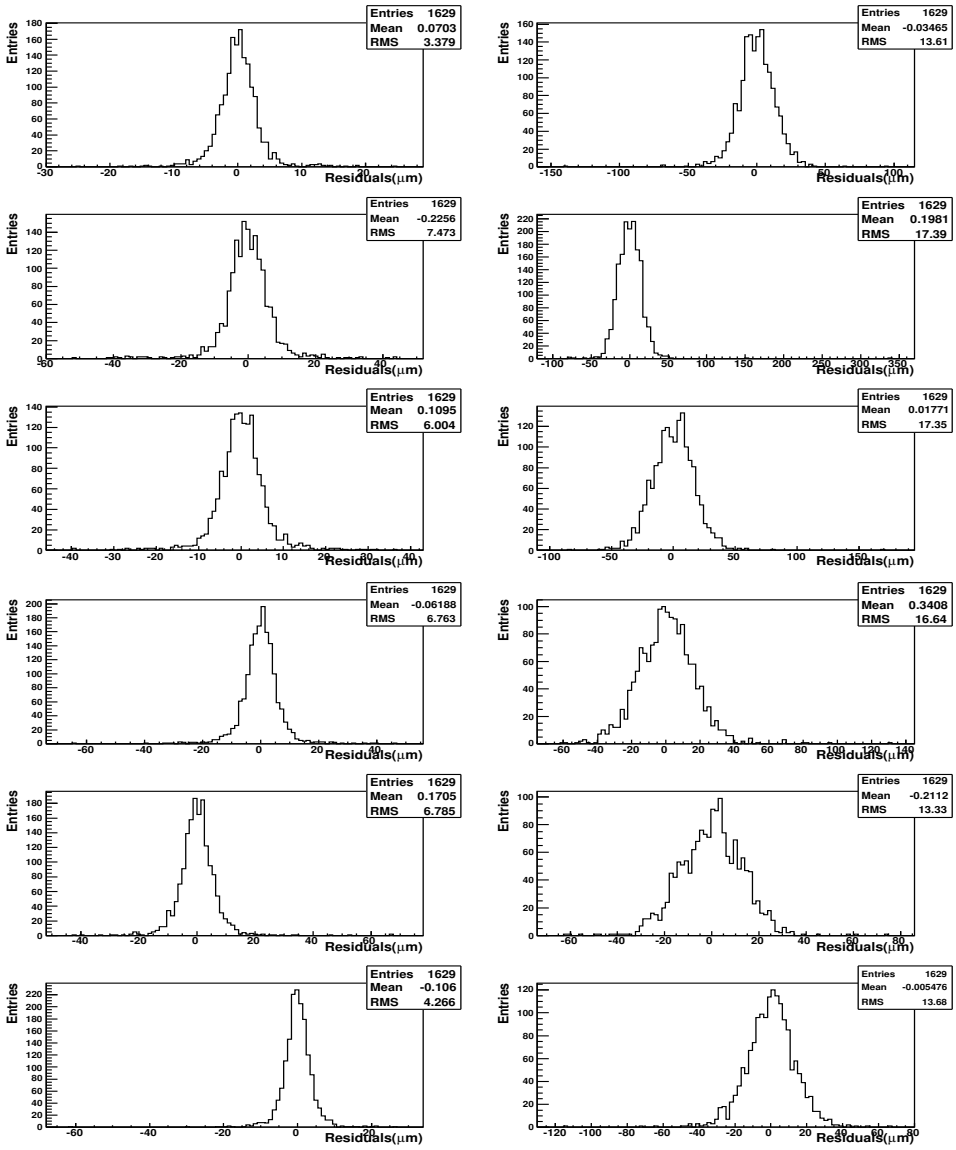

Figure 5.14: Distributions of the residuals after the incoherent alignment with single column flight data (same sample of figure 5.9). The misalignment effect disappears, in fact the mean values of the distributions for every plane and view are lower than 1 μm (x-view on the left, y-view on the right, data analyzed with the position finding algorithm COG4).

erage values of the residuals are for every plane and view lower than 1 μm.

Whole tracker alignment

At the end of the single column alignment a set of 24 parameters for each column of sensor is available. These parameters can be used only to analyze tracks whose points belong to the same column. We have to remind that there is still a possible coherent misalignment, which causes a shift of the measured deflection that could be different for each single column. The determination of the alignment parameters responsible for this shift is the task of the coherent alignment procedure. However this procedure cannot be applied to each column independently. The reason is that the coherent alignment makes use of electrons and positrons, which are much less abundant in cosmic rays than protons, so the statistics in this case is a crucial point and the numbers of electrons and positrons detected in each single column would be insufficient. Thus, an inter-columns alignment is applied first. Since this alignment procedure is performed relative to one column, chosen as reference column, the systematic deflection error propagates accordingly and the next coherent alignment algorithm will be valid for the whole detector. The procedure to perform the inter-column (or whole tracker) alignment is still based on the minimization of the χ^2 function. The procedure can be better explained with the help of some pictures. Let us assume that the column number 1 is chosen as reference (figure 5.16); the procedure consists in modifying the position of the sensors of the other columns in order to align them to the reference one. First, the columns 0,2 and 4 are aligned relative to column 1. Figure 5.15 shows the selection criteria used to select the sample of events for the alignment between column 0 and column 1: the events selected are protons with the same quality checks defined previously in this section, that pass across only column 0 or both column 0 and 1. The selected tracks are used to minimize the habitual χ^2 function with the important difference that the curvature is not fixed a priori: in this way the coherent misalignment of column 1 will be propagated to column 0. In fact by fixing the rototranslation parameters of the sensors of the reference column to the values previously found with the single column alignment,

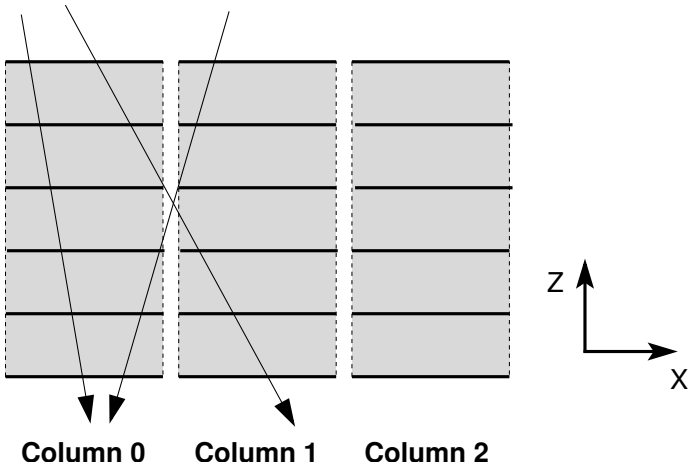

Figure 5.15: Tracks selection criteria for the inter-column incoherent alignment procedure.

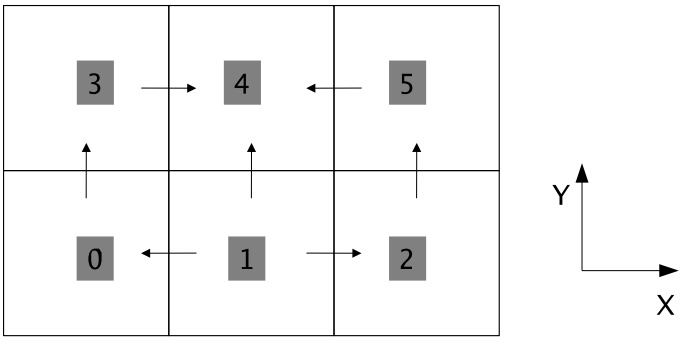

Figure 5.16: Schematic description of the inter-column incoherent alignment procedure.

the measured points on column 1 do not change. On the contrary all the parameters of column 0 are free. The parameters previously found from the single column alignment of column 0 can be used to initialize the free parameters in the minimization. At the end 36 parameters for column 0 will result from this procedure. The same procedure is applied to columns 2 and 4. The next step consists in aligning column 3 relative to 0; now the reference column is 0, its parameters are fixed to the values found by aligning column 0 respect to 1 and tracks that pass through column 3 only or both columns 3 and 0 are used. Hence the same procedure was applied to align column 5 respect to 2, as shown in figure 5.16. Finally we apply the algorithm to column 4, using tracks which intersect columns 1,3 and 5.
The whole procedure can be done starting from column 4 instead of 0; the alignment parameters in this case are different because of the remaining coherent alignment parameters to be determined, but the residuals have the same distribution.
The residual distributions after the inter-column alignment procedure are shown in figures 5.17, 5.18. They are compared with the results obtained from the simulation of a perfectly aligned system. The mean values of the distributions are lower that 1 μm and there is a good agreement with simulation. Some differences can be seen mostly in the shape of the residuals of the 6^{th} plane, an hypothesis for this, currently under investigation, is a disagreement in the z coordinate of this plane between simulation and the real apparatus.

5.5 Coherent alignment

The coherent alignment parameters are those whose effect is to change the deflection value. The simplest kind of coherent misalignment, evident from the sketch in figure 5.12, causes a deflection shift that does not depend on the particle energy. Therefore the true particle deflection is given by the measured deflection plus a constant shift $\eta = \eta_m + \delta\eta$. In order to find the deflection shift $\delta\eta$ we have used particles whose energy can be determined independently with the calorimeter, namely electrons and positrons, measuring their energy according to the procedure de-

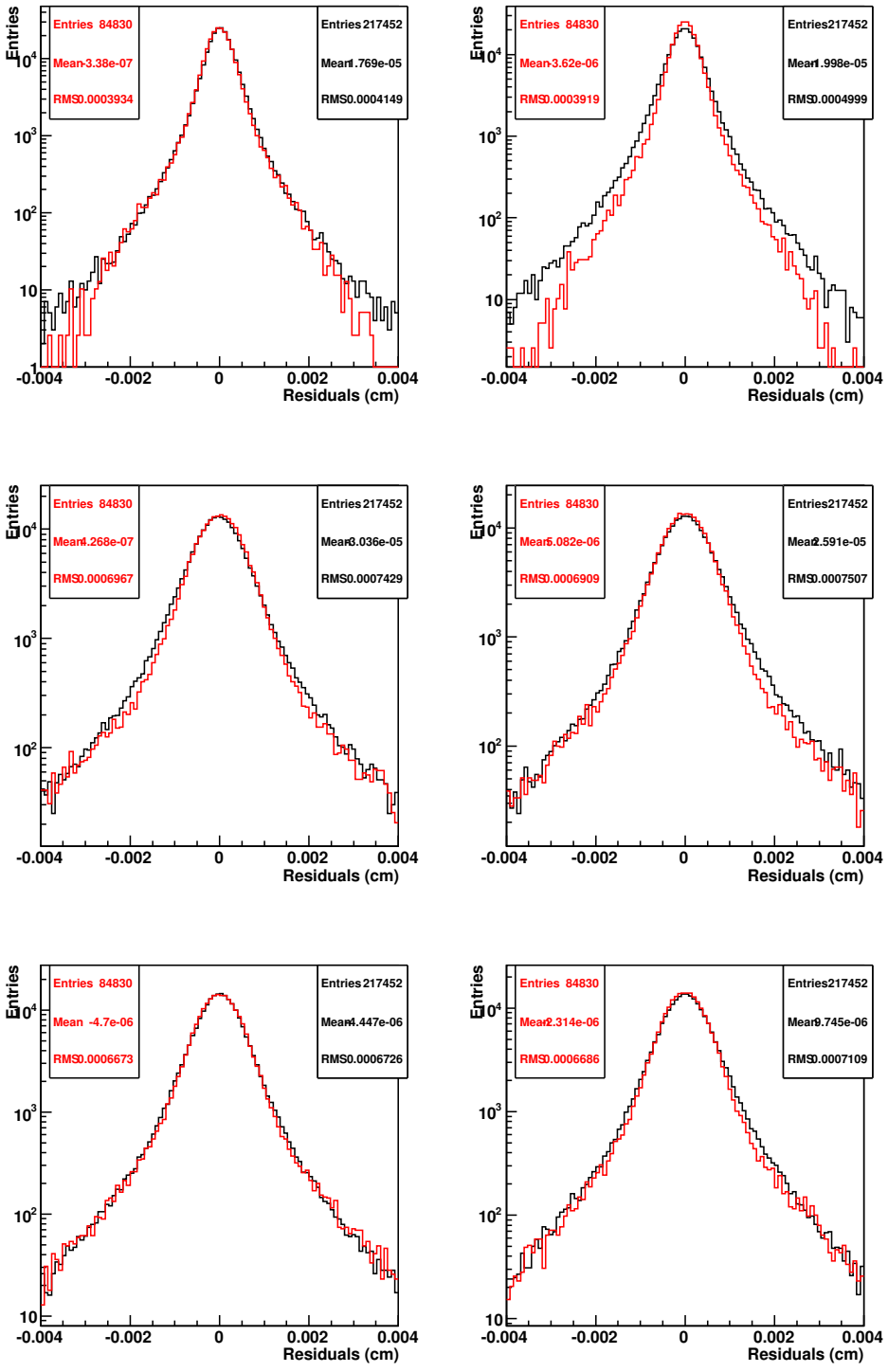

Figure 5.17: Comparison between residuals of simulation (red) and flight data residuals after the incoherent whole tracker alignment (black) in the x-view. On the left, from top to bottom, for the planes 1,2,3 and on the right 6,5,4.

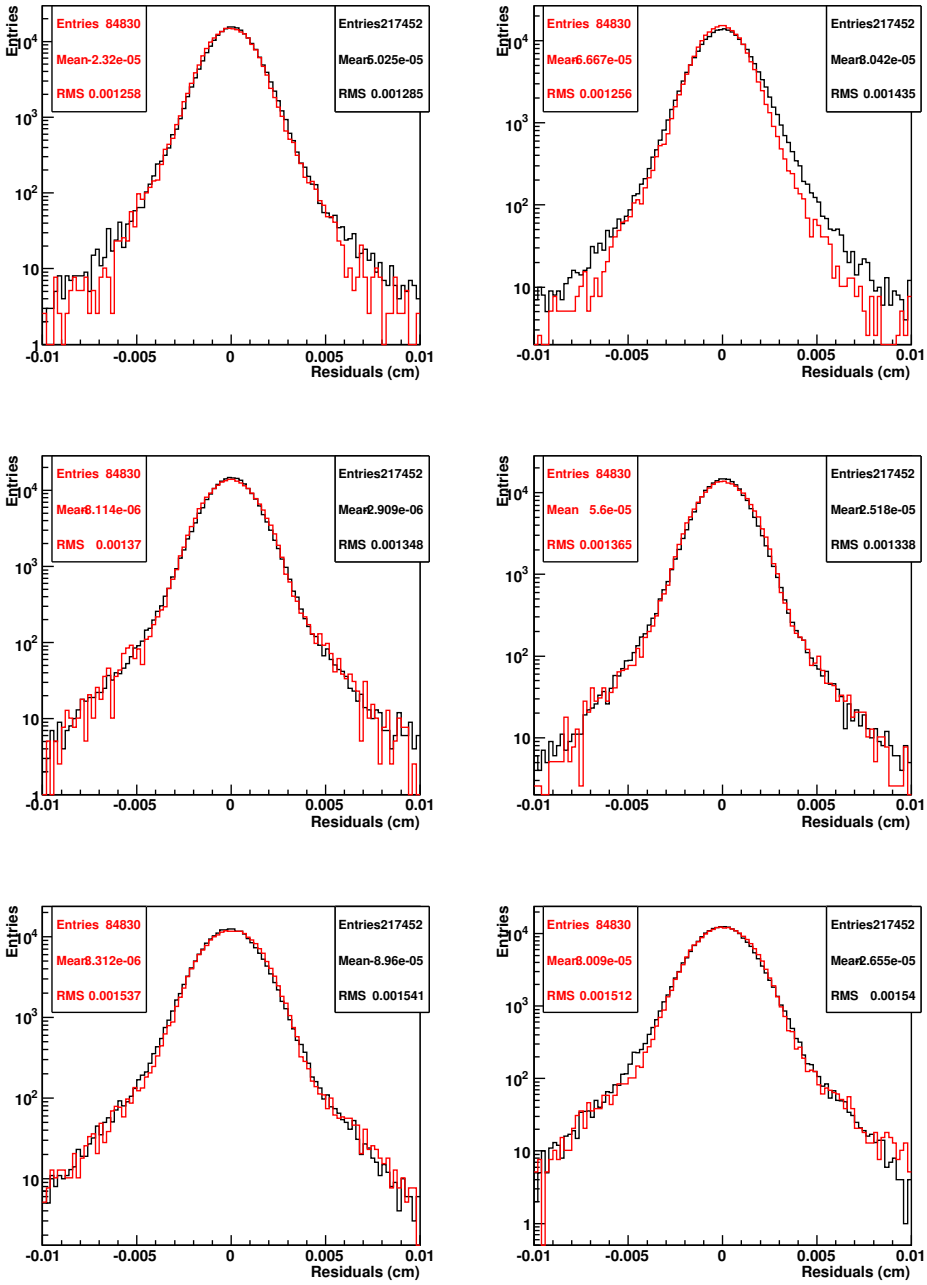

Figure 5.18: Comparison between residuals of simulation (red) and flight data residuals after the incoherent whole tracker alignment (black) in the y-view. On the left, from top to bottom, for the planes 1,2,3 and on the right 6,5,4.

scribed in chapter 4.
If the Bremsstrahlung process could be neglected, the deflection shift caused by the coherent misalignment would arise naturally by comparing event by event the measured spectrometer deflection to the deflection derived from the calorimeter. By applying again the incoherent alignment procedure with the corrected deflection, it would be possible to find the complete alignment parameters (A_i in equation 5.18). However, due to the fact that the Bremsstrahlung process is a stochastic phenomenon, the comparison cannot be performed event by event but only by using distributions. Before describing the algorithms used to determine the deflection systematic error, I will explain better the effect of the Bremsstrahlung process and how we can handle it in the PAMELA experiment. Furthermore I will explain the cuts applied to select electrons and positrons from flight data, since these particles have been used for the coherent alignment procedure.

5.5.1 Bremsstrahlung process

Electrons and positrons interact with the material of the apparatus and lose energy in different ways: ionization and excitement of atomic electrons, Cerenkov light generation and emission of Bremsstrahlung photons due to the interaction with the nuclear Coulomb fields. In the energy range of interest, the most important process is the last one. Since the nucleus is much heavier than the electrons it can acquire any amount of energy. As a consequence the Bremsstrahlung photon spectrum, emitted by a particle of energy E_0, is continuous in the interval $[0, E_0 - m_e c^2]$, where m_e is the electron mass. The distribution of the Bremsstrahlung photon energy can be seen from figure 5.19, where the ratio between the energy of simulated electrons after traversing the material above the spectrometer and the initial energy is shown. This distribution is peaked at 1 with a long tail at lower values, which means that usually the fraction of energy lost is small but occasionally it can be greater than 50%.
There is a well known model to reproduce the distribution of the energy lost developed by Bethe and Heitler [72]: the variable used to describe it is the ratio between the momentum of the particle after the Bremsstrahlung

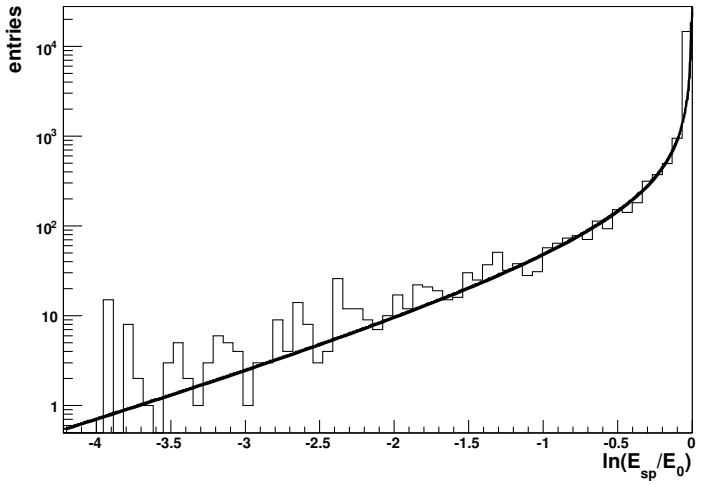

Figure 5.19: Logarithm of the ratio between the energy of simulated electrons on the first silicon tracker plane, E_{sp}, and their original energy, E_0. The line is the function obtained according to Bethe and Heitler with the parameter $c = 0.012$.

loss and the initial one, $z = p_f/p_0$. The distribution of z depends on the thickness of material t, measured in units of radiation length X_0, through which the particle has to pass. The function describing the distribution of z is:

$$f_{BH}(z) = \frac{(-\ln z)^{c-1}}{\Gamma(c)}, \qquad c = t/\ln 2, \qquad 0 < z < 1 \tag{5.20}$$

where $\Gamma(c)$ is the Gamma function and the parameter c has to be lower than 1, such that equation 5.20 is valid only for thin layers. In this model the z distribution does not depend on the original energy of the electrons. In the case of the PAMELA experiment cosmic rays pass through different materials before their detection by the tracker and calorimeter; if during this passage a particle loses a certain fraction of its energy, the spectrometer measures a deflection corresponding to a momentum lower than the original one. In fact the spectrometer detects only charged

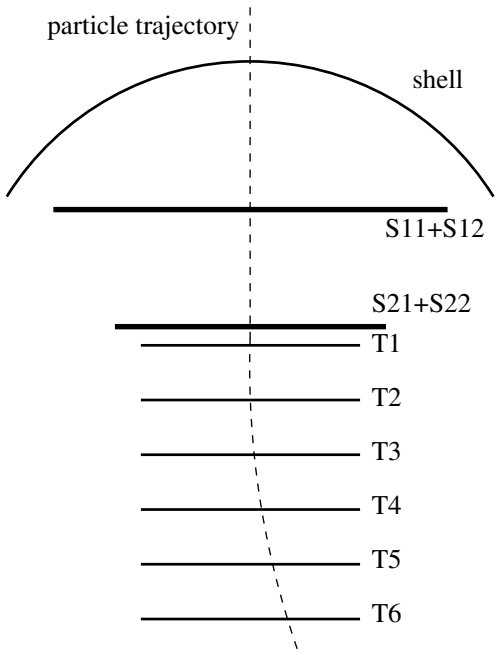

Figure 5.20: Schematic drawing of the materials traversed by a particle in the spectrometer acceptance. Only those materials for which the thickness in terms of radiation length is important for Bremsstrahlung process are shown.

particles, whose deflection is determined from the curvature of the track in the magnetic field. On the contrary the calorimeter measurement is not affected by this effect because it collects also the energy deposited by the Bremsstrahlung photons, thanks to the electromagnetic shower that they can generate. In fact the angular distribution of the emitted radiation has a small angle in respect to the trajectory of the particle. The average emission angle is $\theta \sim \frac{m_e c^2}{E_0}$, therefore in most of the cases the photons enter the calorimeter acceptance together with the electron. The consequence is that the calorimeter spectrum is different from the tracker spectrum. We can estimate the Bremsstrahlung effect expected in PAMELA from the parameter $c = \frac{t}{\ln 2}$ of the theoretical distribution 5.20, by calculating the quantity and the type of material traversed by a particle along its passage through the apparatus. A sketch of the apparatus

	material	$X_0(g/cm^2)$	$\rho(g/cm^2)$	thickness	$t(X_0)$
Shell	$AMg6M$	24.01	2.7	2 mm	0.022
S1+S2	$H^{11}C^{10}$	43.34	1.032	24 mm	0.0572
	Mylar	39.95	1.39	0.1 mm	0.0035
Tracker	Silicon	21.8	2.33	1.8 mm	0.02

Table 5.1: Principal materials traversed above the calorimeter.

with the significant materials in terms of radiation length is shown in figure 5.20. The particles pass through the protective shell which contains the PAMELA apparatus; then they pass two elements of the TOF detector, that is four scintillator (S11, S12, S21, S22) surrounded by a Mylar shell. Table 5.1 lists the numerical values [59] of the radiation lengths, of the densities and of the thickness of each material, together with the calculated thickness in units of radiation lengths.

Summing up all the contributions the result is that a particle entering the PAMELA apparatus perpendicularly to the detecting planes, before being detected by the tracker, passes through a thickness $t \sim 0.084$ in unit of radiation lengths. With this value the parameter c of the Bethe-Heitler distribution of equation 5.20 is $c = t/\ln 2 \simeq 0.12$. From the parameter c we can calculate the average fraction z due to Bremsstrahlung effect, in fact the momentum around zero of the distribution $f_{BH}(z)$ have the simple form $E_k = \mathbf{E}(z^k) = (k+1)^{-c}$. It means that the mean value of z is connected to c by the formula $\mathbf{E}(z) = \overline{z} = 2^{-c}$, therefore $\overline{z} \sim 0.92$ and the mean fraction of energy loss before entering the spectrometer is about 8%. The same quantity has been studied also by using the simulation and the result is in good agreement with theoretical expectations (see figure 5.19 where the distribution obtained from a simulated electron sample is shown together with the theoretical one).

There is another contribution to be considered, that is the material traversed inside the spectrometer. As already said in chapter 2 the tracker design was performed in order to minimize the particle interaction; nonetheless particles pass in the spectrometer through six silicon planes, each one 0.3 mm thick, which in units of radiation length is $t_{sp} \sim 0.02$. Consequently $t_{tot} \sim 0.1$, $c_{tot} \sim 0.145$ and $\overline{z}_{tot} \sim 0.9$, so the

average value of z at the bottom of the spectrometer is about 10%.

5.5.2 Electrons and positron separation from hadron

Calorimeter information has to be used to select positrons and electrons among the large background of hadronic particles present in cosmic rays. This is true in particular for the positron identification for which the hadronic background consists of protons; on the contrary the hadronic background of electrons, mainly antiprotons, is very low. Both $e^{\pm}$ and hadrons can interact with the calorimeter material and produce cascades of particles. As described in section 4.1 there are some topological differences between hadronic and electromagnetic showers, which can be used to select $e^{\pm}$ initiated showers among events interacting in the calorimeter.
The identification cannot rely only on calorimeter, additional information comes from the comparison between the total detected energy and the rigidity measured by the spectrometer; in fact the charge deposited by an electromagnetic shower, if it is well contained in the calorimeter, is strongly related to the energy of the primary electron. It is convenient to notice that the use of the spectrometer rigidity measurement is possible for this aim even if it is still affected by an error due to the misalignment, because it is lower than the resolution needed for a comparison with the charge collected by the calorimeter.
The problem of electron and positron separation from hadrons is critical for experiments aimed to study the cosmic ray antimatter components that use a calorimeter as main identification instrument. This method to discriminate hadronic and electromagnetic events has been developed for the calorimeter of the CAPRICE experiments [41] and can be applied with some changes also to our experiment, since the two calorimeters are very similar. These cuts have been optimized with the use of simulation and test beam data and are based on phenomenological considerations on the distribution of some calorimeter variables [73].

The features of the electromagnetic shower, that are useful to separate electromagnetic from hadronic showers are:

- the fraction of detectable energy;

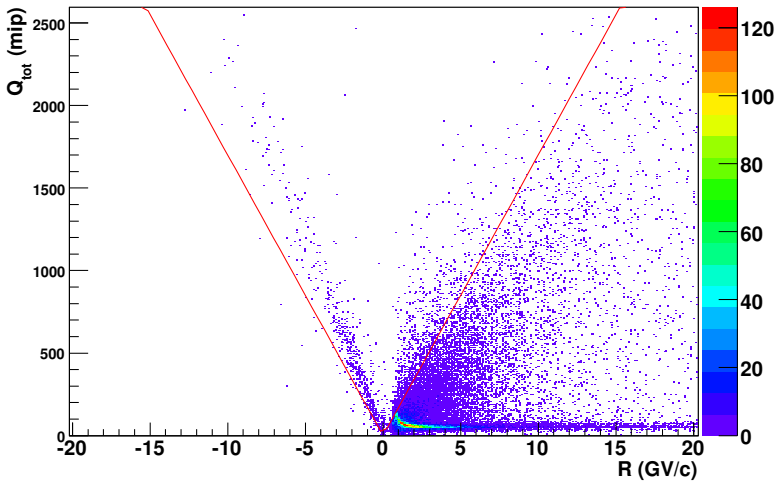

Figure 5.21: Total charge collected in the calorimeter as a function of particle rigidity for a sample of events selected from data. Only the events above the red line are selected as $e^{\pm}$.

- the starting point of the shower;
- the longitudinal profile;
- the lateral profile.

Fraction of detectable energy

The electromagnetic showers, if well contained in the calorimeter, have a total charge strongly related to the energy of the primary particle which generated the shower. To be more precise this quantity depends linearly on the energy, as shown in chapter 4. To exploit this feature the total charge detected in the calorimeter (Q_{tot}) and the charge detected within 4 strips from the track [4] (Q_{tr}) are compared with the rigidity (R) measured by the spectrometer and the following cuts are applied:

[4]This track is the one obtained extrapolating the spectrometer track in the calorimeter.

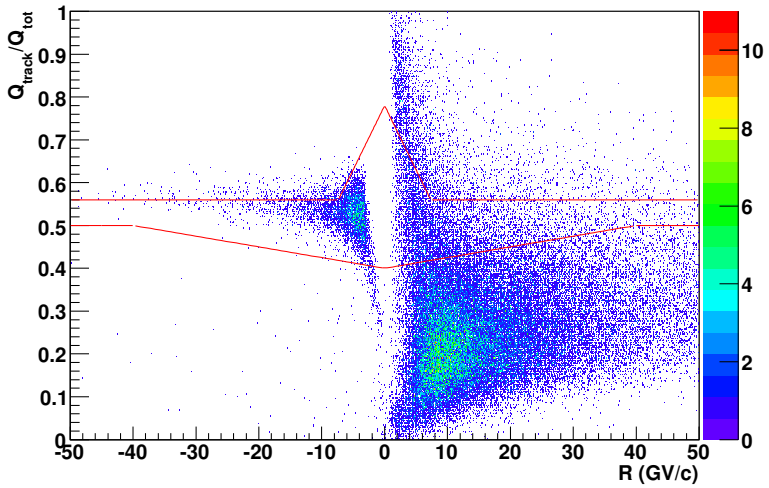

Figure 5.22: Ratio between Q_{track} and Q_{tot}, defined in the text, as a function of particle rigidity for a sample of interacting particles selected from data by requiring $Q_{tot} > 800$. Only the events within the red lines are selected as $e^{\pm}$.

$Q_{tot} > c_{tot}$	$\lvert R\rvert < 147;\ c_{tot} = 170 \cdot \lvert R\rvert$ $\lvert R\rvert > 147;\ c_{tot} = 25000$
$Q_{tr} > c_{tr}$	$\lvert R\rvert < 50;\ c_{tr} = 150 \cdot \lvert R\rvert$ $\lvert R\rvert > 50;\ c_{tot} = 32142 \cdot \left(1 + 1.0301 \cdot e^{-0.0059\lvert R\rvert}\right)$

In figure 5.21 the quantity Q_{tot} is shown as a function of the particle rigidity together with the applied cut. The sample is selected from flight data by requiring $\left(\frac{dE}{dx}\right)_{trk} < 3$ to exclude low-energy protons and nuclei. For negative rigidities the linear behaviour is evident, in fact almost all the selected events are interacting electrons. On the contrary, among positively charged particles, non-interacting protons are evident; they have an almost constant charge deposit in the calorimeter. At low energy the charge deposit increases linearly till a peak, located at the minimum energy needed for non-interacting protons to pass through all the calorimeter, then it decreases toward a constant value,

In order to put better in evidence the difference between electromagnetic and hadronic showers, in the following we have applied also the

cut $Q_{tot} > 800$. In fact by requiring a high energy deposited in the calorimeter all non interacting particles are removed.

By defining Q_{track} as the charge deposited in the strip closest to the track and the neighboring strip on each side, the ratio between Q_{track} and Q_{tot} is another important variable; in fact this ratio is 1 for non interacting particles, while it is very low for hadronic showers, since their lateral development is much more spread out. For electrons this quantity is instead almost constant and is about ~ 0.55. This behaviour can be clearly seen in figure 5.22. The following cuts have been applied to select electromagnetic showers:

$\frac{Q_{track}}{Q_{tot}} < c_1$	$\|R\| < 7.3;\ c_1 = -0.03 \cdot \|R\| + 0.78$
	$\|R\| > 7.3;\ c_1 = 0.56$
$\frac{Q_{track}}{Q_{tot}} > c_2$	$\|R\| < 40;\ c_2 = 0.0025 \cdot \|R\| + 0.4$
	$\|R\| > 40;\ c_1 = 0.5$
$\frac{Q_{tr}}{Q_{tot}} > c_3$	$\|R\| < 3;\ c_3 = 0.1 \cdot \|R\| + 0.4$
	$\|R\| > 3;\ c_3 = 0.7$
$\frac{Q_{track}}{Q_{tr}} > c_4$	$\|R\| > 10;\ c_4 = 0.62\left(1 - 0.15e^{-0.015\|R\|}\right)$
	$5.665 < \|R\| < 10;\ c_4 = 0.028 \cdot \|R\| + 0.272$
	$\|R\| < 5.665;\ c_4 = 0.55$

Starting point of the shower

Since the radiation length X_0 in tungsten is 0.35 cm, the probability for an electromagnetic shower to start developing in the first three planes is greater than 89%. On the other hand for an hadronic shower λ is 9.59 cm, consequently many hadrons do not produce any shower and the starting point of interacting hadrons is uniformly distributed through the calorimeter. A useful quantity to characterize the starting point of the shower is:

$$N_{int0} = \sum_{j=1}^{2} \sum_{i=1}^{22} \theta_{ij} \cdot i \tag{5.21}$$

where $\theta_{ij} = 1$ if the i-th plane of the j-th view has a cluster along the track, that is a group of contiguous strips less than 4 mm away from the track with a deposited energy typical of a proton, $\theta_{ij} = 0$ otherwise. It

can be expected that hadrons have high values for this variable, up to a maximum of 506 for a straight proton track with hits on all the planes, while for electromagnetic showers it assumes low values.
Another variable connected to the starting point of the shower is the ratio between Q_{presh} and n_{presh}. They are defined as the charge and the number of hit strips in a cylinder of radius two strips around the track in the first four planes of the calorimeter. The cuts exploiting these feature are:

$$\begin{array}{|c|}\hline N_{int0} < 5 \cdot \left(1 + 33 \cdot e^{-2.2|R|}\right) \\ \hline \frac{Q_{presh}}{n_{presh}} > 2 \\ \hline \end{array}$$

Longitudinal profile

One of the characteristics of the longitudinal profile of electromagnetic showers is that its energy deposit decreases fast and spatially broadens

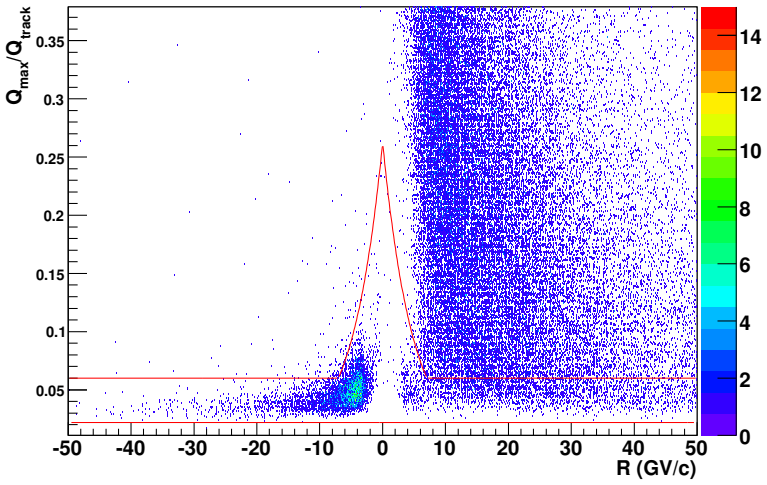

Figure 5.23: Ratio between Q_{max} and Q_{track}, defined in the text, as a function of particle rigidity for a sample of interacting particles selected from data by requiring $Q_{tot} > 800$. Only the events within the two red lines are selected as electrons or positrons.

after the shower maximum. As a consequence a variable that can be used to select $e^{\pm}$ among interacting hadrons is the fraction of charge detected within a cylinder of radius $4R_M$ in the last four calorimeter planes (Q_{last}), since it has lower values in case of electromagnetic showers than for hadronic shower.
Another interesting feature that can be used is that the charge collected by the strip with the highest detected signal (Q_{max}) is related to the number of electrons at the shower maximum and thus to the energy of the incident particle, for electromagnetic showers. Figure 5.23 shows the ratio between Q_{max} and Q_{track}: it can be seen that for interacting hadrons the spread of Q_{max}/Q_{track} is much larger than for $e^{\pm}$, in fact the maximum charge can be of the order of hundreds of mips in case of the breaking of a silicon nucleus whose fragment lose all their energy in a strip.
To exploit these features the following cuts have been applied:

$\frac{Q_{last}}{Q_{tot}} < c_5$	$\|R\| > 13;\ c_5 = 0.07 + 0.01 \cdot \|R\|$
	$\|R\| < 13;\ c_5 = 0.2$
$\frac{Q_{max}}{Q_{track}} < c_6$	$\|R\| > 7;\ c_6 = 0.2 \cdot e^{-0.21(\|R\|-1.3)}$
	$\|R\| < 7;\ c_6 = 0.06$
$\frac{Q_{max}}{Q_{track}} > c_7$	$c_7 = 0.022$

Lateral profile

The high transversal segmentation of the calorimeter sensitive areas makes it possible to exploit the difference between the lateral profiles of hadronic and electromagnetic showers. In case of electrons most of the total detected energy should be contained in a cylinder of radius $4R_M$ around the shower axis, while for hadrons the lateral distribution is more spread out. The variable used to employ this feature is the ratio between the number of hit strips within 8 strips from the track (n_{cyl}) and the total number of strips with signal (n_{strip}).
Another useful quantity is the fraction of the total charge which is not deposited in clusters around the track; in fact, for electromagnetic showers many clusters are produced close to the track, while for hadronic

showers the clusters will be fewer and further away from the track. By defining Q_{tx} and Q_{ty} as the charge released in clusters along the track in the x and y view respectively, the variable used to exploit this behaviour is $\frac{Q_{tot}-Q_{tx}-Q_{ty}}{Q_{tot}}$. The distribution of these quantities as a function of particle rigidity is shown in figures 5.24 and 5.25, together with the applied cuts, described in the following table:

$\frac{n_{cyl}}{n_{strip}} > c_8$	$c_8 = 0.8 - 0.0047 \cdot \lvert R \rvert$
$\frac{Q_{tot}-Q_{tx}-Q_{ty}}{Q_{tot}} < c_9$	$\lvert R \rvert < 11;\ c_9 = 0.6 \cdot \lvert R \rvert^{-0.75}$ $\lvert R \rvert > 11;\ c_9 = 0.1$

5.5.3 Coherent alignment parameters

A set of coherent movements of the sensors that cause a systematic deflection error can be evaluated if we have an independent measurement of the particle momentum. If we neglect the effect of the Bremsstrahlung process, a set of electrons or positrons whose energy has been measured by the calorimeter and whose rigidity has been measured by the spectrometer is enough to determine the parameters which account for this misalignment. However it was demonstrated in section 5.5.1 that the Bremsstrahlung process cannot be neglected for the alignment purpose, with the consequence that calorimeter and tracker measurement are not expected to be the same, and the distribution of the fraction of energy loss for electrons and positrons is the one approximately described by the Bethe-Heitler model.

From what was explained so far it is evident that the best variable to be used to take into account the Bremsstrahlung process is the fraction z of the particle energy after the Bremsstrahlung emission, because its distribution is independent on the initial energy of the particle. The distribution of z is found by selecting electrons and positrons from flight data and by calculating for each event the value $z = \frac{1}{|\eta_m| \cdot p_C}$, where η_m is the deflection measured by the tracker and p_C is the momentum calculated using the energy measured in the calorimeter.

We do not expect the z distribution of the selected sample to reproduce exactly the Bethe-Heitler distribution, because it is affected by

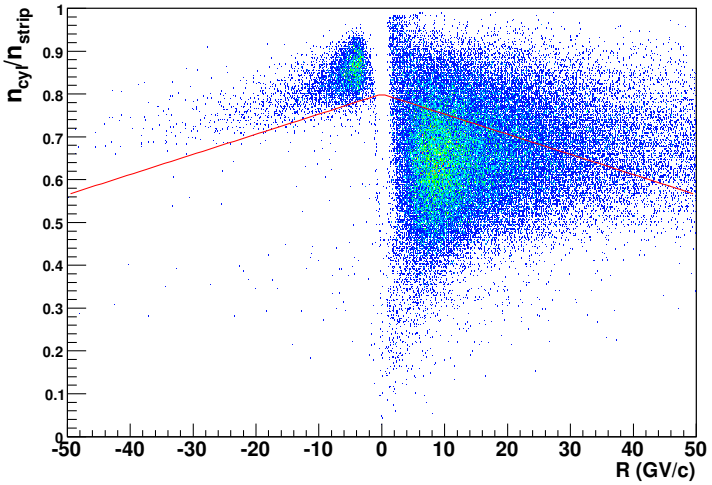

Figure 5.24: Ratio between n_{cyl} and n_{strip}, defined in the text, as a function of particle rigidity for a sample of interacting particles selected from data by requiring $Q_{tot} > 800$. Only the events above red line are selected as electrons or positrons.

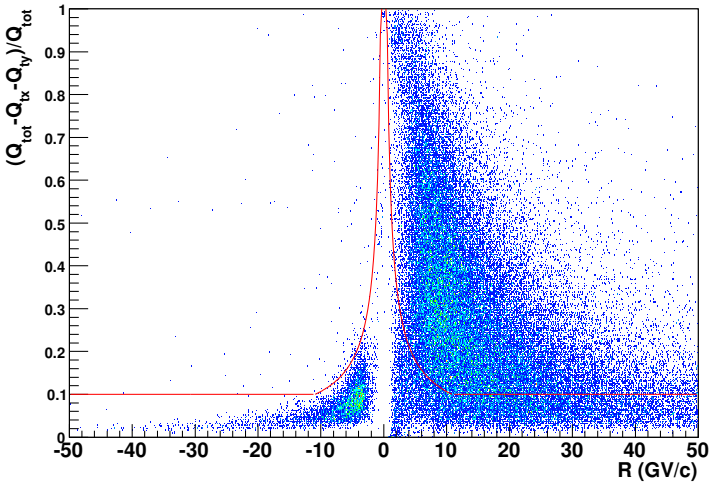

Figure 5.25: Ratio between $Q_{tot} - Q_{tx} - Q_{ty}$ and Q_{tot}, defined in the text, as a function of particle rigidity for a sample of interacting particles selected from data by requiring $Q_{tot} > 800$. Only the events within the two red lines are selected as electrons or positrons.

the cuts that have been applied to select $e^{\pm}$. As was explained in the previous section, the cuts applied to reject hadronic events, are based mostly on the topological development of the showers in the calorimeter: hadronic events with a big fraction of energy deposit have a topological distribution of charge in the calorimeter much different from a single pure electromagnetic shower and can be tagged as hadronic events. Most of the events with a large fraction of energy converted in Bremsstrahlung photons appear in the calorimeter as double showers, with a development much different from a single pure electromagnetic shower and they are excluded by the hadronic cuts. An example of an event of this type was shown in the previous chapter in figure 4.40. Even if we do not know the real distribution expected for the variable z, we can say that it should be the same for electrons and positrons, because the Bremsstrahlung process acts in the same way for both kind of particles. Obviously this is true only if the same selection cuts are applied for electrons and positrons. Moreover the z distribution does not depend on the energy spectrum of the particles, as a consequence we can compare the electron and positron z distributions even if their energy spectra are different. A coherent misalignment, which mimics a certain curvature, causes a systematic error on the absolute value of the electron deflection that is opposite in sign to the systematic error on the absolute value of the positron deflection. This concept can be understood better with the example shown in figure 5.26. As a consequence if a coherent misalignment is present we expect to observe different z distribution for electrons and positrons. By considering a constant shift $\delta\eta$ due to the coherent misalignment, we can think that the true deflection that the spectrometer should have measured is given by $|\eta| = |\eta_m| - \delta\eta$ for electrons and $|\eta| = |\eta_m| + \delta\eta$ for positrons, in the hypothesis that the systematic deflection error $\delta\eta$ is small. The algorithm developed to calculate the coherent parameter $\delta\eta$ relies on the fact that the positron and electron z-distributions are in principle the same. In this case also the mean value of the electron z-distribution $\langle z\rangle_-$ has to be equal to the mean value of the positron z-distribution $\langle z\rangle_+$. As a consequence, by using the above definition of η, we obtain:

$$\langle z\rangle_+ = \langle z\rangle_- \qquad \rightarrow \qquad \langle \frac{1}{p_C(|\eta_m| + \delta\eta)} \rangle_+ = \langle \frac{1}{p_C(|\eta_m| - \delta\eta)} \rangle_- . \quad (5.22)$$

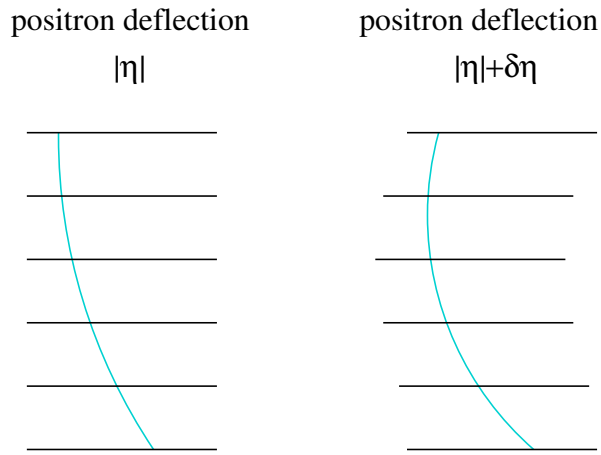

(a)

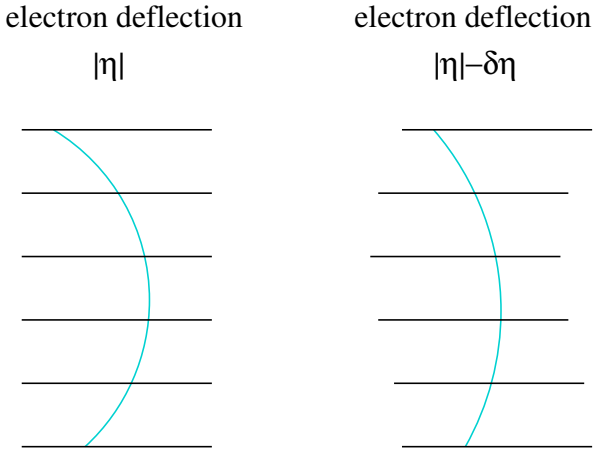

(b)

Figure 5.26: A coherent misalignment of the six silicon planes results in a systematic deflection error, $\delta\eta$; if we consider particles with opposite charge, the same deflection error goes in opposite directions. (a)Sketch of a track due to a positively charged particle: after accounting for the misalignment the curvature is higher then the measured one. (b)Sketch of a track due to a negatively charged particle: in this case the true curvature is lower then the measured one.

Since the systematic deflection error, as will be verified later, is $\delta\eta \ll |\eta_m|$, the following approximation can be done to calculate the value of z:

$$\frac{1}{p_C(|\eta_m| + \delta\eta)} = \frac{1}{p_C|\eta_m|}\left(1 + \frac{\delta\eta}{|\eta_m|}\right)^{-1} \simeq \frac{1}{p_C|\eta_m|}\left(1 - \frac{\delta\eta}{|\eta_m|}\right). \quad (5.23)$$

By using this approximation for electrons and positrons we find:

$$\langle z\rangle_+ = \langle\frac{1}{p_C|\eta_m|}\rangle_+ - \delta\eta\langle\frac{1}{p_C\eta_m^2}\rangle_+ \quad (5.24)$$

$$\langle z\rangle_- = \langle\frac{1}{p_C|\eta_m|}\rangle_- + \delta\eta\langle\frac{1}{p_C\eta_m^2}\rangle_- \quad (5.25)$$

By substituting in equation 5.22 we can find at last a simple formula for the deflection shift $\delta\eta$:

$$\delta\eta = \frac{\langle\frac{1}{p_C|\eta_m|}\rangle_+ - \langle\frac{1}{p_C|\eta_m|}\rangle_-}{\langle\frac{1}{p_C\eta_m^2}\rangle_+ + \langle\frac{1}{p_C\eta_m^2}\rangle_-} \quad (5.26)$$

We have selected electrons and positrons from 14 months of data acquired by PAMELA from July 2006 to August 2007.
The cuts applied to select these events are the basic cuts already discussed in section 5.4 for the incoherent alignment procedure and the hadronic cuts discussed in section 5.5.2. Hence further cuts have been applied in order to use well reconstructed tracks in the spectrometer and a good energy measurement in the calorimeter:

- at least 4 hits in x view and 3 hits in y view;
- track fit procedure converged with number of steps lower than 100;
- total charge measured in the calorimeter greater than 800;
- rigidity measured from tracker lower than 20 GV/c;
- high-quality sample from longitudinal fit (see section 4.4.3);

These cuts have been developed purposely for the coherent procedure since we must be able to reconstruct the energy of electrons and positrons

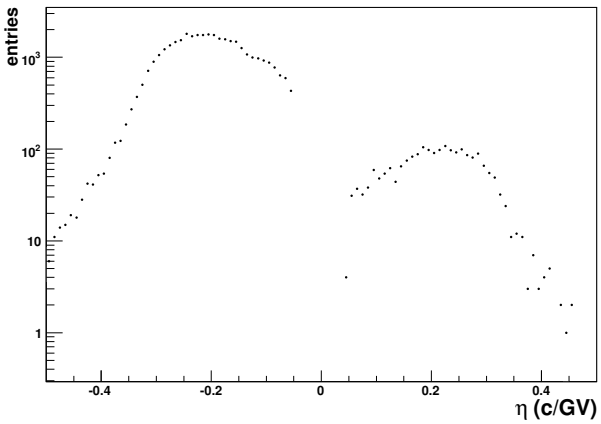

Figure 5.27: Deflection distribution of the sample of events selected for the coherent alignment.

with resolution better than 10% and in particular without systematic errors. In this condition the number of selected electrons is about 35000, while the number of selected positrons, about 2000, is much lower. The distribution of the deflection of the selected events is shown in figure 5.27. The z distribution of the selected sample of electrons and positrons, shown in figure 5.28, can be interpreted as the result of the convolution of the Bremsstrahlung effect with spectrometer and calorimeter resolutions, for this reason it is different from what expected theoretically according to the Bethe-Heitler distribution. It can be noticed that the mean values of the two distributions are different. In order to compare two experimental distributions a statistical test can be used, in this study we have applied the Kolmogorov Test [74]. The result of the test is a number $K_t \in (0, 1)$, that is near to 0 when two distribution are not compatible. In the case of the electron and positron distributions in figure 5.28 the result of the Kolmogorov Test is much less than 1, suggesting that the two distributions are not compatible.
By using the measured values η_m and p_C the terms needed to obtain the deflection shift $\delta\eta$ from equation 5.26 have been calculated. The terms calculated from electrons and positrons are affected by different errors

because the statistics of the two samples are very different. After the propagation of these uncertainties we have found the following value for the systematic shift in deflection:

$$\delta\eta = (-0.0013 \pm 0.0002)\ c/GV \tag{5.27}$$

We have used this value of the parameter $\delta\eta$ to calculate the new deflection of electrons and positrons as $|\eta| = |\eta_m| \mp \delta\eta$. The new z-distribution that have been obtained are shown in figure 5.29. The mean values are now the same and the Kolmogorov test in this case suggest that the two distributions are compatible. The electron and positron z-distributions before and after the coherent correction are directly compared in figure 5.30.
Due to the fact that to solve equation 5.22 we had to make an approximation, it is useful to apply this procedure iteratively. The same algorithm was applied after the first step of coherent correction to the deflection measurement and we found that the further correction has a value $\delta\eta' = -4.36 \cdot 10^{-7}\ c/GV$. This value is negligible since it is lower than the error on $\delta\eta$, as a consequence we can say that one step of the procedure is enough. This result is reasonable since the hypothesis used to made the approximation in equation 5.23, $\delta\eta \ll |\eta_m|$, is satisfied. In fact the events used for this analysis, whose η distribution is shown in figure 5.27, have an average deflection $\langle|\eta|\rangle \simeq 0.2$, so $\delta\eta/\langle|\eta|\rangle \sim 0.007 \ll 1$.

5.5.4 Final calorimeter calibration

At the end we would like to show that the same approach can be useful in order to optimize the calorimeter energy reconstruction. This can be done by using the cross calibration between calorimeter and tracker, together with dedicated simulations.
As explained in chapter 4, the calibration from mip to GeV was performed by means of simulation. An improvement of this calibration can be obtained by assuming that the real value of p_C could be different from the measured one, p_m. If there is an error in the calorimeter calibration we should write $p_C = k \cdot p_m$. For the coherent alignment this was not a

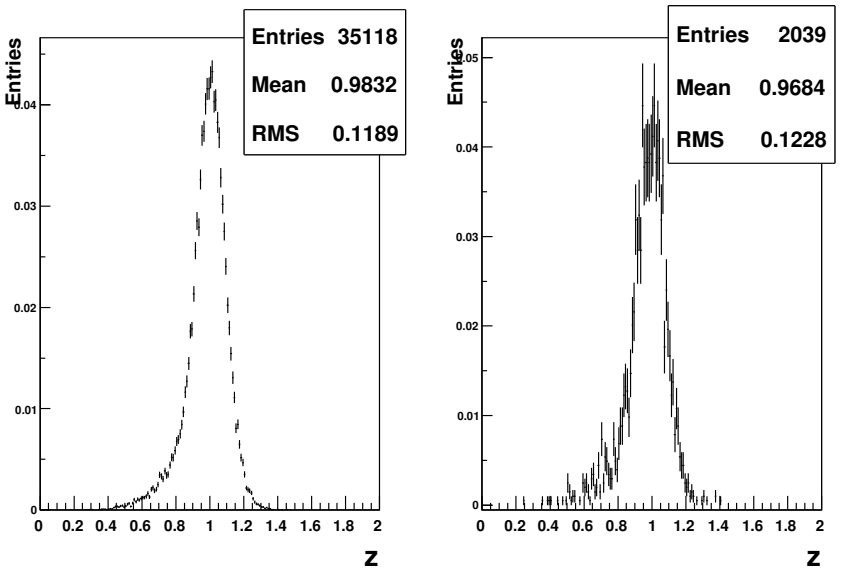

Figure 5.28: Distribution of the experimental value of the variable $z = \frac{1}{p_C \cdot |\eta_m|}$ for a sample of electrons (left) and positrons (right) selected from flight data.

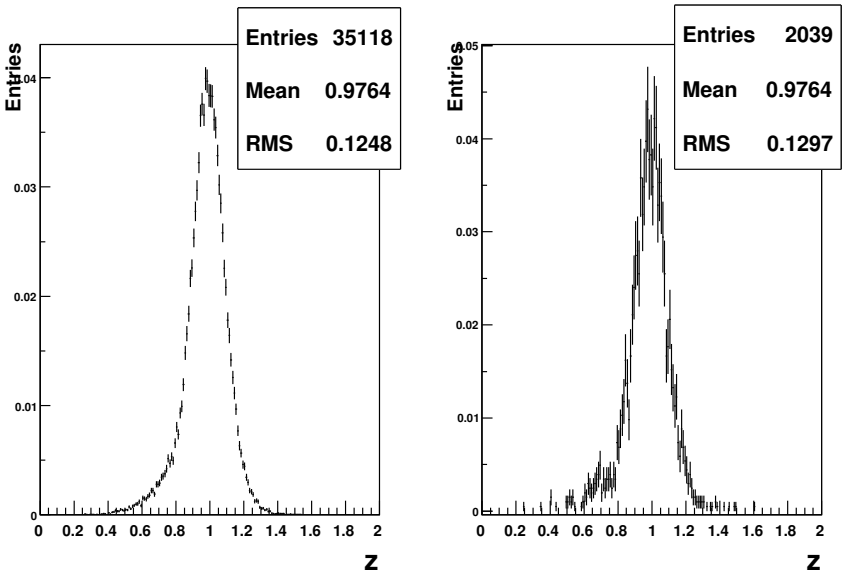

Figure 5.29: Distribution of the corrected value of the variable $z = \frac{1}{p_C \cdot (|\eta_m| \mp \delta\eta)}$ for the same sample of figure 5.28.

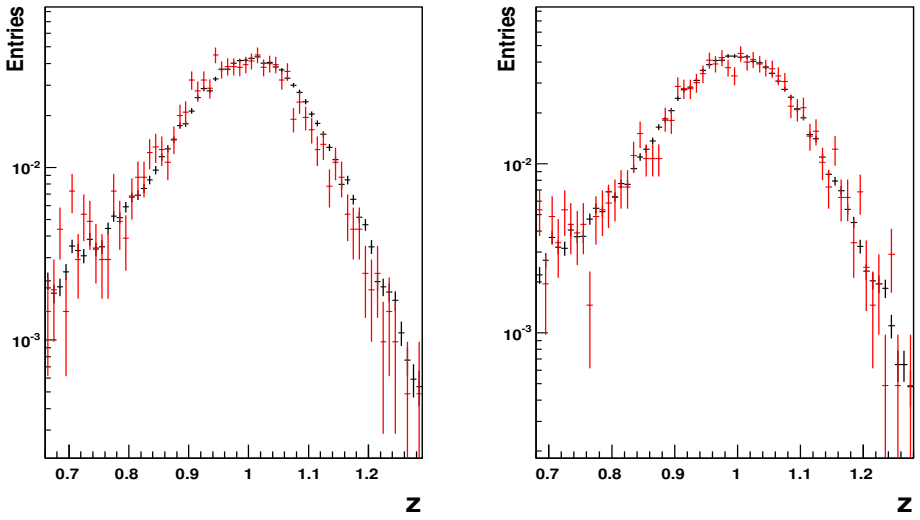

Figure 5.30: Same distributions shown in figure 5.28 (left) and figure 5.29 (right). The red distributions are for electrons, blue for positrons. The logarithmic scale shows that the electron and positron z-distributions are more similar after the coherent alignment. This is supported by the results of the Kolmogorov test: before the alignment $K_t = 4.3 \cdot 10^{-6}$, after the correction it becomes $K_t = 0.77$.

problem because for electrons and positrons the factor k is the same and we can assume $k = 1$.

After the determination of the coherent-alignment parameter $\delta\eta$ we have an unbiased reconstruction of the deflection with the spectrometer: $\eta(e^{\pm}) = \eta_m + \delta\eta$. After the correction the two z-distributions have the same shape and mean value, which should be consistent with those obtained with simulation, too. If there is a difference it can be addressed to a wrong calibration of the calorimeter, such that the real calorimeter energy is connected to the measured one by $p_C = k \cdot p_m$. The value of k can be found by comparing the z distribution of real and simulated data.

For each selected real event we found the state vector, we propagated it back till the entrance of the apparatus to have the initial positions and momentum vector, then we generated from there 10 electrons and prop-

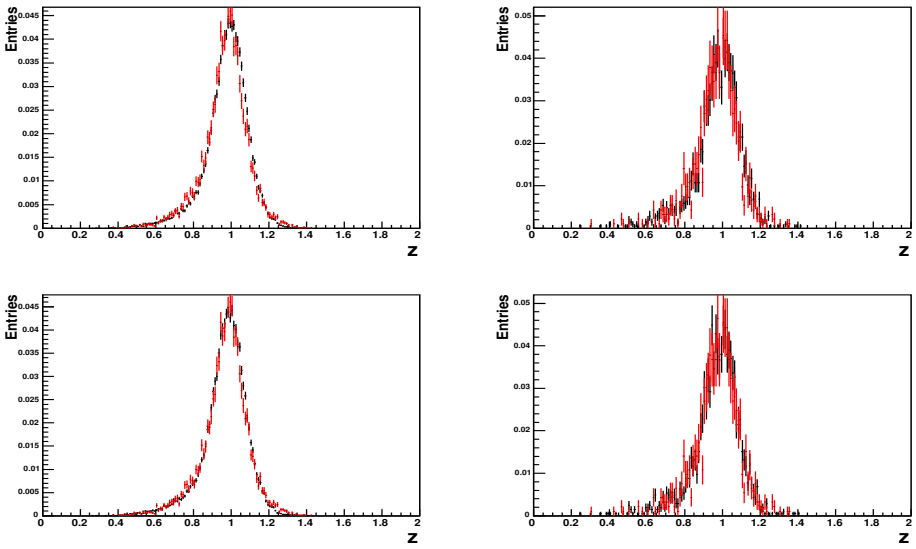

Figure 5.31: Distribution of the corrected value of variable z for a sample of electrons (left) and positrons (right) selected from flight data (black distribution). Superimposed in red is the same distribution for simulated electrons and positrons. On the top, p_m is the result of standard calorimeter energy reconstruction. On the bottom, the correction $k = 1.0082$ has been applied to p_m, for the flight data calorimeter energy reconstruction.

agated them with the simulation program developed for the PAMELA experiment. This procedure has been applied in order to simulate events with initial conditions as much similar as possible between real and simulated data. At the end we have applied the same cuts used for real data, in order to deal with a simulated sample with a spectrum as much as possible comparable with real data. To compare the z distribution again we have calculated the mean of the distributions. Since the calorimeter calibration is based on simulation and the simulated spectrometer is perfectly aligned, the mean of the z distribution for simulated data is given by:

$$\langle z \rangle_{S_\pm} = \langle \frac{1}{p_C |\eta|} \rangle_{S_\pm}. \tag{5.28}$$

On the contrary the z distribution for real data is given by:

$$\langle z \rangle_{\pm} = \langle \frac{1}{k \cdot p_m(|\eta_m| \pm \delta\eta)} \rangle_{\pm}. \tag{5.29}$$

By simply equalizing the two expressions above, independently for the two samples of electrons and positrons, we have obtained two values of k:

$$k^{(-)} = \frac{\langle \frac{1}{p_m(|\eta_m| - \delta\eta)} \rangle_-}{\langle \frac{1}{p_C|\eta|} \rangle_{S_-}} \qquad k^{(+)} = \frac{\langle \frac{1}{p_m(|\eta_m| + \delta\eta)} \rangle_+}{\langle \frac{1}{p_C|\eta|} \rangle_{S_+}} \tag{5.30}$$

We have verified that both the equations give the same result within the errors:

$$k^{(-)} = (1.0084 \pm 0.0015) \qquad k^{(+)} = (1.0063 \pm 0.0049) \tag{5.31}$$

where it is clear that the error on $k^{(+)}$ is bigger because we have much less statistic of positrons than electrons. In figure 5.31 the z-distribution obtained before and after the calorimeter-calibration correction are shown, together with the simulated distributions. The consistency between the values $k^{(+)}$ and $k^{(-)}$ can be considered also as a test of the correctness of the coherent alignment algorithm.

5.5.5 Next steps of the alignment procedure

The next stage of the alignment procedure is to use the value of $\delta\eta$ to find the correct alignment parameters of each sensor, A_i in equation 5.18. For this aim the alignment procedure will be applied to a proton sample where the deflection value is the one measured by the spectrometer corrected for the systematic effect $\delta\eta$.

It must be pointed out that other kinds of coherent misalignment could be present. For example another kind of coherent misalignment can be due to a coherent twist of the spectrometer around the z axis, which can cause a deflection shift proportional to the y coordinate. If we look at the distribution of z as a function of the average y coordinate of the track, shown in figure 5.32, a small correlation is visible, suggesting the presence of this kind of coherent misalignment.

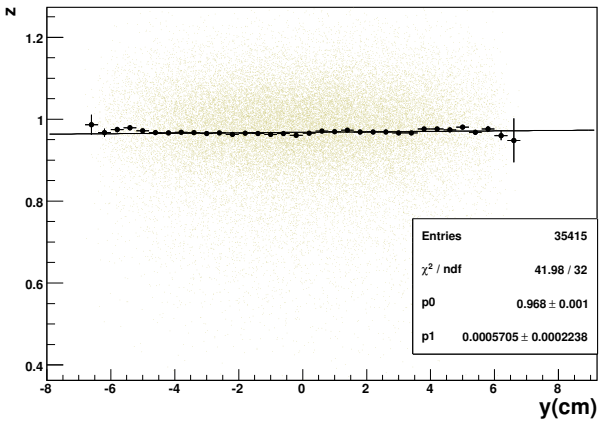

Figure 5.32: The electron z distribution is shown as a function of the average y coordinate of each track. The parameters in the box are the results of the linear fit: $z = p_0 + p_1 \cdot y$.

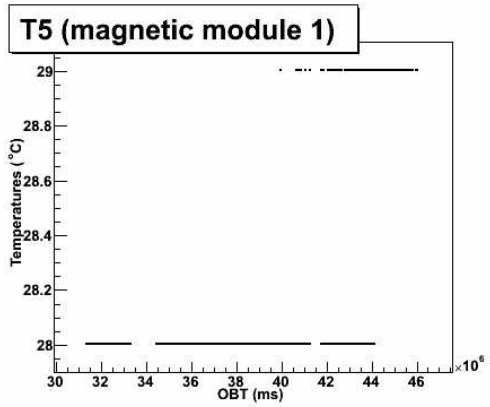

Figure 5.33: Temperature measured by one of the sensors located on the magnetic modules.

At last it is necessary to discuss whether the alignment parameters found so far represent the final calibration or not. In fact due to some satellite movements the position of the silicon sensor could change again. Moreover the position measurements depend also on the temperature of the sensors. Till now we have verified that the temperature should not be a problem because it is stable within 1° (see figure 5.33): the temperature linear dilatation coefficient of the silicon sensor is $2.6 \cdot 10^{-6}/°C$, so the maximum shift is less than 1 μm. However we verified that 1 year of data is enough to perform the alignment procedure and it will be repeated to see if something has changed.

5.6 Galactic positron fraction

The analysis of the data collected by the PAMELA experiment is currently under progress. Much effort has been done during the previous years in order to calibrate the instruments and optimize the algorithms developed for the analyses. However at present not all the calibrations of the instruments are completed. For example an important part of the work that has still to be done consists in the analysis of the efficiencies of the selection procedures. As a consequence what will be presented in the following is only a preliminary attempt to analyze some of the results.

In order to determine the fluxes of the various cosmic ray components an analysis of the live time and the acceptance of the experiment and especially of the efficiencies is needed. Since all efficiencies can be reliably assumed to be the same for electrons and positrons, they do not appear in the ratio, as a consequence it is experimentally easier to calculate the ratio instead of the absolute flux. For this reason more experimental data exist on the positron fraction than on the flux.

In figure 5.34 a collection of most recent experimental results regarding the positron fraction collected in the previous years is shown.
In the same figure we have shown also the positron fraction expected near the Earth, considering also the solar modulation, on the basis of the secondary $e^{\pm}$ calculations according to some theoretical models of Stephens [81] and Moskalenko [82]. The dashed line is the theoretical expectation calculated using a diffusive halo model for Galactic cosmic

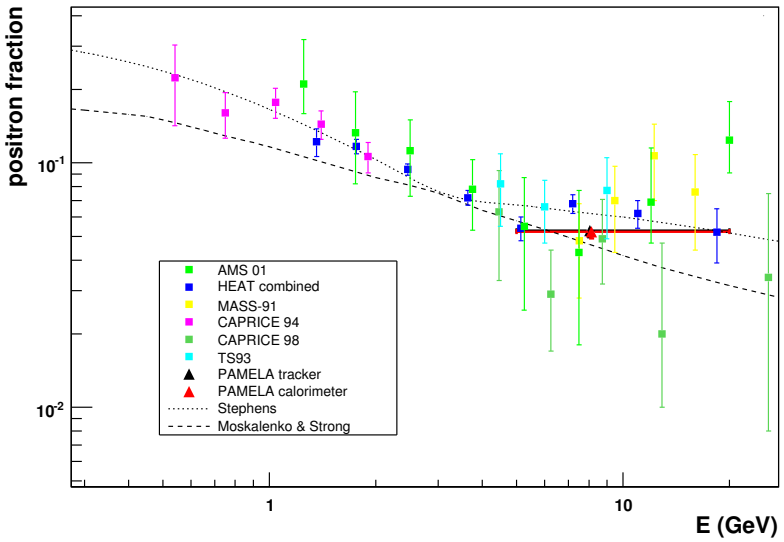

Figure 5.34: The positron fraction measured by PAMELA (this work) and several other experiments: AMS01 [75], HEAT [76], MASS91 [77], CAPRICE94 [78], CAPRICE98 [79], TS93 [80]. The dashed and dotted lines are two of the theoretical calculations for the secondary positron fraction [81, 82].

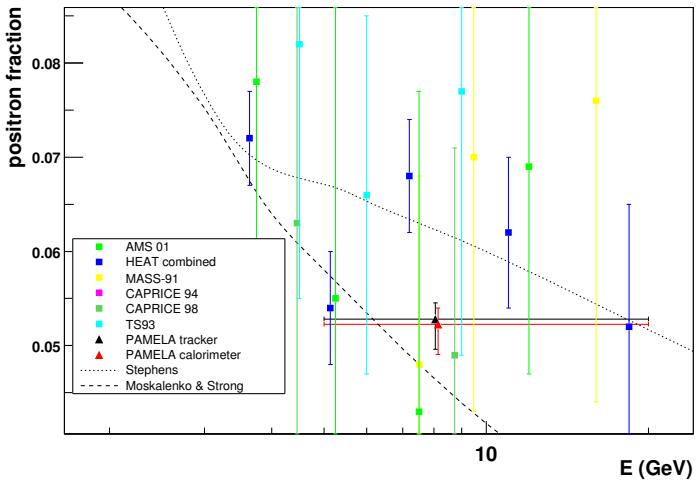

Figure 5.35: Same data of the previous figure shown in linear scale on an limited energy range.

ray propagation, the dotted line is instead obtained using the Leaky-box model. Apart from different cosmic ray propagation models, the theoretical ratio depends also on the flux of primary electron and on the interstellar nucleon spectra. Moreover at energies lower than few GeV many differences among the models could be present due to the solar modulation, that affects largely both fluxes of electrons and positrons. Some models predict a sign charge dependence of this modulation which has been invoked to explain the positron fraction and the electron spectrum. As a consequence there are still strong uncertainties on the evaluation of the secondary positron fraction.
The data taken by the various experiments are in agreement with each other within the error bars, which are however still quite large. In fact almost all the past experiments were performed with balloon flights and due to their limited time duration the positron statistics is quite poor. Due to the rapidly falling flux, the previous experiments were able to measure the positron spectrum only up to approximately 30 GeV and with rather large error bars. Moreover large systematic errors are present due to the difficulty to identify positrons in the vast background of protons and due to the fact that the atmospheric secondary positrons have to be subtracted properly. The only one among the past experiments that acquired cosmic rays out of the atmosphere is AMS-01, which was flown on the Space Shuttle Discovery for a ten days mission. It consisted of a cylindrical permanent magnet and a silicon tracking device with a large acceptance but without any subdetector devoted to hadron/lepton separation. In order to select positrons in the vast proton background a particular technique was used, based on the identification of the bremsstrahlung emission through photoconversion above the tracking system. This method has a low efficiency and consequently also with this experiment the available positron statistic is very poor.

The HEAT collaboration claims from its measurements that there is an excess between 5 and 7 GeV at the level of $\sim 3\sigma$ over the prediction of the propagation model of Moskalenko. Also other experiments have found a positron fraction too high compared to the theoretical secondary production. This caused the proliferation of many theories about exotic positron sources. For example this excess could be due to a contribution

Detector	$\langle E \rangle$	positron fraction	σ_{stat}	σ_{sys}
Spectrometer	8.05 GeV	0.0528	± 0.0017	-0.0015
Calorimeter	8.14 GeV	0.0523	± 0.0017	-0.0015

Table 5.2: Measurements of the positron ratio with calorimeter and spectrometer, σ_{stat} and σ_{sys} represent the statistic and systematics errors respectively.

to the positron spectrum coming from dark matter annihilations, as was explained in chapter 1. However no conclusion could be reached since the results are affected by significant uncertainties.

Regarding the results of the PAMELA experiment we have calculated a preliminary esteem of the positron fraction in the energy range $5 \div 20$ GeV, independently with calorimeter and spectrometer information. In this energy range the resolution of both the instruments is better than 10%. The values of these ratio with the errors and the corresponding average energies are shown in table 5.2 and reported in figures 5.34 and 5.35 together with the other measurements. In the second plot they are shown in linear scale with a zoom to put better in evidence the error bars and the difference between calorimeter and tracker results. It can be seen that the value of the ratio, third column in table 5.2, is the same within the errors, but the plot it is centered on a different point. In fact the center of the bin is calculated as the average of their energy distribution, reported in the second column of the table 5.2. This difference is reasonably attributable to the Bremsstrahlung effect, in fact it has extensively pointed out through this chapter that the spectrometer measurements of electrons and positrons are underestimated due to the Bremsstrahlung photons emitted above the spectrometer.
It can be noticed that the statistical errors, σ_{stat} in the table, are very little because the number of detected positrons is much higher compared with other experiments, even if we have collected till now only 1 year of data. Since the experiment is planned to be active for at least 3 years these results will be improved significantly.
Finally one can notice that also a systematic contribution, σ_{sys} in the table, to the positron fraction measured with PAMELA has been included. Being a ratio of particle fluxes, most of the sources of systematic error,

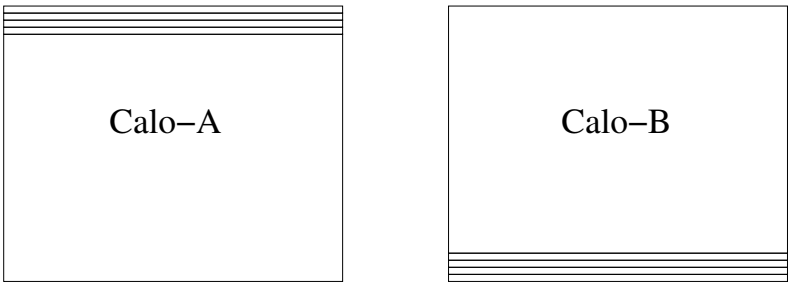

Figure 5.36: Sketch of the two calorimeters used for the *pre-sampler* method [83].

such as detector acceptance or trigger efficiency, naturally cancel out for the positron ratio because they are the same for electrons and positrons. The contribution from possible background sources is instead different because for positrons it consist of protons, while for electrons mainly of antiprotons. The proton contamination in the positron sample has been evaluated by analyzing flight data with the so called *pre-sampler* method [83]. This method takes advantage of the high segmentation of the PAMELA calorimeter and of the high number of radiation lengths of which it is composed. The whole calorimeter is made with 22 tungsten layers but a reduced calorimeter can be used to analyze a sample of particles identified as protons by requiring that they do not interact before the first 4 layers of tungsten. The reduced calorimeter used for this aim is composed by the last 18 tungsten layers and is shown in the left picture (*Calo-A*) of figure 5.36. Then the hadronic cuts are applied to this set and from the number of events that pass these cuts the fraction of protons that are misidentified as positrons can be calculated. Then the same analysis can be applied to a sample of positively charged particles using a different reduced calorimeter, composed by the first 18 tungsten layers: *Calo-B* in figure 5.36. If the same hadronic cuts are applied to select positrons the contamination of protons in this sample can be estimated. From this analysis the proton contamination in the positron sample in the energy range $5 \div 20\ GeV$ is estimated of about 3% and the fraction of protons that pass the hadronic cut is estimated as less than $2 \cdot 10^{-5}$. It means that the systematic error in the positron fraction is

about $-1.5 \cdot 10^{-3}$.

We have seen that in order to understand better many important astrophysical items there is the need of measurements with greater precision and at higher energy. The preliminary analyses are very promising in this direction and PAMELA will provide, in the near future, significant improvements to the measurements on the cosmic ray positron fraction, thanks to its large acceptance and long exposure time and to its better energy resolution and discrimination capability compared to the previous experiment. The total electron and positron flux will be found with the final analyses, together with the detailed positron fraction extending till much higher energies.

Conclusion

The PAMELA apparatus was integrated inside the Russian Resurs-DK1 Earth-observation satellite that has been put into orbit around the Earth on the 15^{th} June 2006.

The PAMELA experiment is equipped with different subdetectors, whose information can be used to measure the energy of the particles detected by the apparatus. This work has been mainly focused on the cross calibration between calorimeter and spectrometer.
For what concern particles interacting in the calorimeter and generating electromagnetic showers, namely electrons and positrons, the energy can be evaluated by using the information on the energy collected by the silicon planes of the sampling calorimeter. This quantity has to be corrected, in order to optimize the energy reconstruction and avoid systematic errors, by taking into account the energy lost due to the leakage effect from the side or the bottom, as well as the energy lost in the gaps present among the silicon detectors. By using samples of simulated electrons a method to reconstruct the energy of electrons and positrons has been developed and the calorimeter calibration has been performed. It has been demonstrated that the resolution achievable with this method above 5 GeV is better than 10%, improving till values lower than 4% when the energy is greater than 20 GeV up to about 100 GeV where the longitudinal energy leakage cannot be properly recovered . This reconstruction method has been applied to flight data and, after the final spectrometer calibration, a comparison of the spectrometer and calorimeter energy measurement between simulated and real data has been used to correct the calorimeter calibration.
The particle rigidity can be measured for all the kinds of particles by

using the spectrometer information. In fact from the coordinates of the track intersection points on the different planes of the tracking system, the magnetic deflection of the particles can be measured by fitting them with an appropriate curve in three-dimensional space. The fitting is performed by integrating the relativistic equations of motion of the charged particles in the magnetic field. In order to correctly relate the spatial information of the different silicon sensors in a common frame of reference, their absolute positions have to be known. Due to the very high resolution in impact-point reconstruction, an accurate alignment procedure is needed to find the true configuration of the detectors. A first set of alignment parameters was found before the launch with an algorithm applied to tracks generated by a proton beam. When this set was used to analyze data acquired in flight it was evident that during the launch the sensors suffered further displacements. For this reason the alignment procedure had to be performed again by using cosmic-ray tracks collected in flight. The alignment procedure needs tracks with known curvature, that is particles of known energy. For flight data an energy measurement independent on the spectrometer is not available for protons and a different procedure, that uses also electrons and positrons has been developed. For this aim the misalignment of the sensors has been divided in two components: a set of random displacements and a set of movements that generate a systematic error on the measured curvature. The first set has been evaluated with a procedure similar to the one used at ground, by using flight protons and the curvature measured by the spectrometer. The second set has been instead found comparing the calorimeter and spectrometer measurements for electrons and positrons selected from flight data.

At last a new set of alignment parameters has been found and the calorimeter and spectrometer calibration has been finalized. After this calibration the analysis of flight data provides the first scientific results. In this work a preliminary estimation of the positron fraction in the energy range from 5 GeV to 20 GeV has been presented.

Bibliography

[1] V. Hesse, Physik Zeitschr. **13**, 1084 (1912).

[2] S. Eidelman et al., *Review of Particle Physics*, PL, B 592 (2004) http://pdg.lbl.gov

[3] E. Fermi, Phys. Rev. 75, 1169 (1949).

[4] The Pierre Auger Collaboration, *Correlation of the Highest-Energy Cosmic Rays with Nearby Extragalactic Objects* Science 318 (5852), 938.(9 November 2007)

[5] T. Kobayashi et al., Adv. Space Res., 27, 653 (2001).

[6] J. M. Clem et al., Journal of Geophysical Research, Vol.105, A10, 23,099 (2000)

[7] M. S. Longair, *High energy astrophysics*, Cambridge University Press (1981).

[8] A.D. Sakharov, JETP Lett. 5, 24 (1967).

[9] A.G. Cohen, A. De Rjula and S.L. Glashow, Astrophys. J. 495, 539 (1998),

[10] C. Bambi and A.D. Dolgov, Nucl.Phys.B784:132-150 (2007)

[11] Y. Asaoka et al., Phys. Rev. Lett. 88 (2002) 051101; Y. Asaoka et al., Phys. Rev. Lett. (2001). astro-ph/0109007.

[12] M. Aguilar et al., Phys. Rep. 366 (2002) 331.

[13] M. Boezio et al., Astrophys. J. 561 (2001) 787; M. Boezio et al., Astrophys. J. (2001). astro-ph/0103513.

[14] S. Orito et al., Phys. Rev. Lett. 84 (2000) 1078.

[15] G. Basini et al., in: Proc. 26th International Cosmic Ray Conference, Salt Lake City, vol. 3, 1999, p. 77; M. Hof et al., Astrophys. J. 467 (1996) L33.

[16] M. Boezio et al., Astrophys. J. 487 (1997) 415.

[17] J. Mitchell et al., Phys. Rev. Lett. 76 (1996) 3057.

[18] M. Simon et al., Astrophysical J. 499 (1998)250

[19] L. Bergstrom et al., Phys.Rev. D 59 (1999) 43506

[20] P. Ullio et al., astro-ph/9904086 (1999)

[21] R.L. Golden et al., Astrophys. J. 457 (1994) L103.

[22] D. Muller et al., Astrophys. J. 312 (1987) 183.

[23] J.M. Clem et al., Astrophys. J. 464 (1996) 507.

[24] R.L. Golden et al., Astrophys. J. 436 (1994) 769.

[25] R.L. Golden et al., Astrophys. J. 457 (1994) L103.

[26] S.W. Barwick et al., Astrophys. J. 498 (1998) 779.

[27] M. Boezio et al., Astrophys. J. 532 (2000) 653;

[28] G. Barbiellini et al., Astron. Astrophys. 309 (1996) L15.

[29] J. Alcaraz et al., Phys. Lett. B 484 (2000) 10.

[30] M. Boezio et al., Adv. Space Res. 27 (2001) 669.

[31] J.J. Beatty et al., Phys. Rev. Lett. 93 (2004) 241102; J.J. Beatty et al., Phys. Rev. Lett. (2004). astro-ph/0412230.

[32] R. J. Protheroe et al., Astrophysical J. 254 (1982) 391

[33] I. V. Moskalenko and A. W. Strong, Astrophysical J. 493 (1998) 694

[34] P. Baltz et al., Phys.Rev. D 61 (2000) 02351

[35] H. Aizu et al., Phys. Rev. 121 (1961) 1206; G.F. Smoot et al., Phys. Rev. Lett. 35 (1975) 258; G.D. Badhwar et al., Nature 274 (1978) 137; A. Buffington et al., Astrophys. J. 248 (1981) 1179; R.L. Golden et al., Astrophys. J. 479 (1997) 992; J.F. Ormes et al., Astrophys. J. Lett. 482 (1997) L187; T. Saeki et al., Phys. Lett. B 422 (1998) 319; J. Alcaraz et al., Phys. Lett. B 461 (1999) 387; M. Sasaki et al., Nucl. Phys. (Proc. Suppl. B 11) (2002) 202.

[36] M.Aguilar et al.,Physics Reports 366, 331 405 (2002).

[37] K. G. Begeman, A. H. Broeils, R. H. Sanders, Mon. Not. R. Astron. Soc. **249**, 523 (1991).

[38] Y. Sofue, V. Rubin, Annu. Rev. Astron. Astrophys. **39**, 137 (2001).

[39] P. Picozza et al, Astro Phys. 27, 296 (2007)

[40] A. Peisert, *Silicon Microstrip Detector*, in *Instrumentation in High Energy Physics*, ed. Fabio Sauli, World Scientific (1992).

[41] M. Boezio, *Positrons and Electrons in the Cosmic Radiation Measured by the CAPRICE94 experiment*, Phd Thesis, University of Stockholm (1998).

[42] G. Osteria et al., *The TOF and Trigger systems of the PAMELA experiment: Performances of the Flight Model*, Proc. of the 29th International Cosmic Ray Conference (2005), submitted for publication; see also http://icrc2005.tifr.res.in

[43] W. Menn *The TOF system of the PAMELA Experiment: In-orbit performance* 30th ICRC, OG.1.5, 2007

[44] J. Lund, *A study of the PAMELA anticoincidence system*, Licentiate thesis, Stockholm, 2002.

[45] S. Orsi et al., 35th COSPAR Scientific Assembly, Paris (2004), to be published in Adv. Sp. Res.

[46] Y.I. Stozhkov et al. *About Separation of Hadron and Electromagnetic Cascades in the PAMELA Calorimeter* International Journal of Modern Physics A Vol. 20, No. 29, 67456748 (2005)

[47] *http://eng.ntsomz.ru*

[48] M. Badi, *Algoritmi di compressione per il rivelatore tracciante dello spettrometro PAMELA*, Tesi di Laurea, Università degli Studi di Firenze (2001).

[49] S. Straulino, *Simulation of silicon microstrip detectors for a cosmic ray experiment*, Università degli Studi di Bologna (2003).

[50] G. Landi, Nucl. Instr. and Meth. A 485, p. 698 (2002).

[51] G. Landi, Nucl. Instr. and Meth. A 497, p. 511 (2003).

[52] S. Straulino et al.,*Spatial resolution of double-sided silicon microstrip detectors for the PAMELA apparatus*, Nucl. Instr. and Meth. A556, 100-114 (2006).

[53] G. Landi, Nucl. Instr. and Meth. A 554, p. 226 (2005).

[54] E. Vannuccini, *In-flight performances of the PAMELA magnetic spectrometer*, Vertex 2007 - 16th International Workshop on Vertex detectors - Lake Placid, Ny, Usa.

[55] R. Brun et al., *Detector Description and Simulation Tool*, CERN program library (1994).

[56] F Giambi *Calibrazione e allineamento dell'esperimento PAMELA su satellite*, Tesi di Laurea, Università degli Studi di Firenze, (2003).

[57] E. Vannuccini, private communication.

[58] R. Turchetta, Nucl. Instr. and Meth. **A335**, 44 (1993).

[59] Particle Data Group: W.-M. Yao et al., J. Phys G 33, 1 (2006).

[60] B.Rossi, *High-energy particles*, Prentice-Hall, New York (1952).

[61] C.W.Fabjan, *Calorimetry for particle physics*, CERN EP85-54 (1985).

[62] C.W.Fabjan anf F. Giannotti, Rev. Mod. Phys. 75, 1243 (2003)

[63] G.Grindhammer, S.Peters,*The parametrised simulation of electromagnetic showers in homogeneous and sampling calorimeters* Int.Conf. on Monte Carlo Simulation in High Energy and Nuclear Physics, 1993.

[64] National Bureau of Standards, procedure 25.5.20.

[65] E.Longo,I.Sestili, Nucl. Instrum. Methods 128, 123 (1975).

[66] F. James, Reference Manual Version 94.1, *Function Minimization and Error Analysis*, Computing and Networks Division, CERN Geneva, Switzerland

[67] H. Bischof and R. Frühwirth, NIM A 419, 259 (1998)

[68] CERNLIB, web page: http://cern.ch/wwwasd/cernlib

[69] R. L. Golden et al., *Performance of a balloon-borne magnetic spectrometer for cosmic ray studies*, NIM A 306, 366 (1991)

[70] M.Bongi, *Data analysis of cosmic rays at ground level with the PAMELA experiment.* Phd Thesis, University of Florence 2005.

[71] H William, Saul A Teukolsky *Numerical recipes in C: the art of scientific computing* Brian P Flannery (1992).

[72] H.A.Bethe,W.Heitler, Proc.Roy.Soc. London A 146, 83 (1934).

[73] M. Boezio et al., Astroparticle Physics 26 (2006) 111118

[74] Chakravarti, Laha, and Roy, *Handbook of Methods of Applied Statistics*, Volume I, John Wiley and Sons, 392 (1967)

[75] M. Aguilar et al., Physics Letters B 646 (2007) 145

[76] S.W.Barwick et al., Astrophys. Journ., 482 (1997) 191

[77] Grimani et al., Astron. and Astroph. 392 (2002) 287

[78] M. Boezio et al., Astrophys. Journ. 532 (2000) 653

[79] M. Boezio et al., Adv. Sp. Res. 27 (2001) 669

[80] R.L.Golden et al., Astrophys. Journ. 457 (1996) 103

[81] S.A. Stephens, *Origin of cosmic ray electrons*, Adv. Space Res. 27 (4) pp. 687 (2001).

[82] I. V. Moskalenko and A. W. Strong, Astrophysical J. 493 (1998) 694

[83] Mirko Boezio, private communication (2007)

Acknowledgements

Prima di tutto vorrei dire che questi tre anni appena trascorsi sono stati per me forse i più difficili della mia vita, per tantissimi motivi, e proprio per questo l'aiuto di tutte le persone vicine (e lontane) è stato fondamentale per lo svolgimento di questo lavoro di ricerca. Mi rendo conto che interagire con me non deve essere stato facile, nonostante tutto ci avete provato e solo adesso mi rendo conto di quanto è stato importante.
Prima di tutto vorrei ringraziare tutto il gruppo di ricerca di PAMELA di Firenze per avermi sopportato e aiutato e spronato non solo scientificamente ma anche come persone amiche. Per iniziare Sergio, che mi ha fatto conoscere per primo i nostri amati raggi cosmici, e poi Paolo, Massimo, Davide, Lorenzo, Sergio R. e Oscar: grazie per aver creduto in me anche quando io non ci credevo per niente, ma soprattutto Elena, penso che senza la fiducia che mi hai dato non avrei davvero scritto neanche una riga! Inoltre un ringraziamento sincero va a Mirko ed Emiliano, sempre disponibilissimi per discussioni e consigli sul nostro caro calorimetro.
Poi ci sono tante persone che pur non sapendo niente di raggi cosmici sono state egualmente importanti. Prima di tutto Barbara, Rosa e Luciana, tre donne diverse ma tutte speciali e bellissime, nonostante le circostanze sono stata veramente contenta di avervi conosciuto. E vorrei ricordare anche i'Cambi e tutti quelli che ci lavorano! E anche i miei nonni, mi state insegnando molto più di quanto crediate, un abbraccio! E poi c'è la mia grande passione, la danza, grazie Manuela e Mark, che mi avete fatto scoprire molto del mio corpo e delle mie emozioni.. anche troppo!
E poi i miei amici, tutti, non vi elenco perchè già lo sapete e sicuramente mi dimenticherei qualcuno (però non posso non mandare un bacione all'Anto, alla Costy, alla Francy!). Devo dire che per me è stato

molto difficile vedere le persone andare via una ad una da Firenze, ma la lontananza non diminuisce l'affetto fortunatamente, che sento fortissimo per tutti voi. Un abbraccio fortissimo va al mio grande amico 'più', il più lontano di tutti, che è riuscito a starmi veramente vicino in ogni momento e anche a capirmi a volte nonostante la mia chiusura.
E per finire vorrei ricordare le persone che mi amano incondizionatamente, senza volere niente in cambio dal primo momento che ho visto la luce, mamma e babbo, siete veramente speciali, grazie!